UNIVERSITY OF CANTERBURY
Te Whare Wānanga o Waitaha
CHRISTCHURCH NEW ZEALAND

Hygrothermal Effects on the Mechanical Behaviour of All-cellulose Composites

Mokhtar Bin Mat Salleh

A thesis submitted in partial fulfilment of the requirements for the

Degree of Doctor of Philosophy in Mechanical Engineering,

University of Canterbury

August 2017

Table of contents

ACKNOWLEDGEMENTS

Praise to Allah, the most gracious and merciful

Firstly, I would like to thank my supervisor, Associate Professor Dr Mark P. Staiger for his guidance and motivation during my study. To my co-supervisors, Prof Shusheng Pang and Dr Kevin Magniez, thanks for the inputs and critical comments on my work.

I would also like to thank Kevin Stobbs, Mike Flaws, all-cellulose composite (ACC) group members, and all of my friends who assisted with experimental works, result analysis, and provided useful input on my thesis.

I also would like to thank the Ministry of Higher Education (MoHE) Malaysia, and University Malaysia Perlis (UniMAP) for granting a sponsorship for my study.

I thank my family for all of their advice and encouragements.

Lastly, I would like to express my deepest gratitude to my beloved wife, Rohana Mohamed Yusof, and my wonderful children, Miswani Raihan Hamidah, Muhammad Umar Haziq, and Maryam Zulaikha for their love, patience, unconditional support, and sacrifice during my study.

Terima kasih !!!

ABSTRACT

Cellulose is an excellent resource for bio-based materials production due to its high strength, high stiffness, low density, availability, and biodegradability. An incompatibility issue experienced by many of the bio-composites has led to the development of a new class of bio-based materials *aka* all-cellulose composite (ACC). ACC is produced from cellulose for both reinforcement and matrix phases. Non-derivatising solvents and coagulants are used to dissolve and regenerate cellulose, respectively. The excellent mechanical properties of ACCs compared to other bio-based materials have been reported. Recently, solvent infusion process (SIP) has shown a promising processing route for ACCs production. As a result, extensive scientific research has been focussed on investigating the best processing route for ACCs production. Hygrothermal effects are the effects of water/moisture, temperature or the combination of both factors on the structures and properties of bio-based materials. A potential problem for ACCs is their propensity for absorbing water due to the use of cellulose for both reinforcement and matrix phases. Cellulose is known to have numerous hydroxyl groups, resulting in strong cellulose-cellulose and cellulose-water interaction. There are very limited studies of hygrothermal effects on the mechanical properties of ACCs. Hence, the aim of the present study was to investigate hygrothermal effects on the structure and properties of ACCs.

This thesis investigated the production of ACCs using two types of solvents (BmimAc and NaOH/urea) and a precursor cellulose (woven rayon textile). Both types of ACCs were manufactured using SIP. A design of experiment methodology (DOE) and a statistical analysis based on the Taguchi approach were used to study the multivariable control factors including the dissolution time (t_d), dissolution temperature (T_d), pressure at hot press (P_{HP}), and pressure

at SIP (P_{SIP}) incorporated with a wide range of its levels during SIP. The effect of control factors on the mechanical properties of ACCs was investigated using the DOE Taguchi approach, resulting in the best combination of control factors and their levels in maximising the mechanical properties of ACCs. Multiple regression analysis (MRA) was used to determine the accuracy of the experimental and theoretical mechanical properties. Interestingly, t_d was the most significant control factor for both ACCs, followed by P_{HP}. The effect of t_d on phase characterisation, viscoelastic properties, density and microstructure was also investigated.

The water absorption behaviour of ACCs was investigated. The effects of water bath temperature and t_d on the water absorption behaviour were examined. The water absorption behaviour was also associated with the changes in the structure and phase composition of ACCs. The relationship between experiments and theory for water concentration (M_t/M_m) and thickness swelling (TS) was investigated. Finite element-based simulation work using ANSYS was used to (i) determine the effect of water bath temperature on M_t/M_m at different thicknesses, and (ii) observe the correlation of saturation time between theoretical calculations and experimental data.

The effect of varying water contents on the mechanical properties, glass transition temperature (T_g), and structural changes of ACCs were studied. The tensile testing, differential scanning calorimetry (DSC), dynamic mechanical analysis (DMA) and Fourier-transformed infrared spectroscopy (FTIR) were used for ACC characterisation. A decreasing Young's modulus (E) and ultimate tensile strength (UTS) were observed with an increasing water content of ACCs. An increase in the strain to failure (ε_f) was also observed with the increasing water content. A higher water threshold associated with increasing freezing bound water was found in ACCs produced *via* NaOH/urea than that produced *via* BmimAc. The presence of free water was

observed beyond the water threshold for both types of ACC. A decrease in T_g was also observed due to plasticisation effects, caused by softening of the amorphous phase in ACCs. The experimentally determined values of *E* were within ±15% of the theoretical value of *E* as calculated from the C-O-C region in the FTIR spectrum. Interestingly, the structural changes in the C-O-C and OH regions were observed to affect the mechanical properties of ACCs due to the increasing strain.

The hygrothermal effect on the creep performance of ACCs was investigated. The time temperature superposition (TTS) principle was used to construct master creep curves using short-term creep tests. The results of experimental long-term creep testing was compared with the TTS master curve in order to investigate the physical aging of ACCs. The Bürgers model for creep could be used to describe the experimental creep of ACCs. Increasing creep strain in ACCs was also observed with the increasing water content and temperature. Higher creep strains were observed for ACC produced *via* NaOH/urea compared with BmimAc due to slippage effects. The results suggest that physical aging in all of the ACCs took place at the temperature of 30 °C. Physical aging was negligible at temperatures between 150 and 200 °C. As a conclusion, t_d was found as the most significant control factor in ACCs production *via* SIP method. The optimum t_d for ACCs produced *via* BmimAc and NaOH/urea were 30 and 15 min, respectively. A higher water diffusivity was found in the ACCs as compared with other bio-based composite materials due to cellulose being used for both the reinforcing and matrix phases. Furthermore, a decrease in the mechanical properties was reported with the increasing absorbed water into the ACCs. These results were due to the presence of bound and free water at a lower and higher water content, respectively. An increase in creep strain was also observed at a higher water content that was due to the decreasing hydrogen bonding density and increasing molecular-level slippage effects.

List of Figures

List of Tables

List of abbreviations

ACC	All-cellulose composite
AmimCl	1-Allyl-3-methylimidazolium chloride
ANOVA	Analysis of variance
ATR-FTIR	Attenuated total reflectance-Fourier transform infrared
BmimAc	1-Butyl-3-Methylimidazolium Acetate
BmimCl	1-Butyl-3-Methylimidazolium Chloride
c	Cellulose concentration
CrI	Crystallinity index
CS_2	Carbon disulphide
D	Water diffusion coefficient
DMA	Dynamic mechanical analyser
D_o	Diffusivity index
DOE	Design of experiment
DSC	Differential scanning calorimetry
E	Young's modulus
E'	Storage modulus
E''	Loss modulus

E_a	Activation energy
E_K	Elastic modulus of the Kelvin-Voigt spring
E_M	Elastic modulus of the Maxwell spring
EMC	Equilibrium moisture content
EmimAc	1-Ethyl-3-Methylimidazolium Acetate
ε	Creep strain
ε_f	Strain to failure
f	Degrees of freedom
F	*F*-ratio
f	Frequency
F_{crit}	*F* critical
FEA	Finite element analysis
FE-SEM	Field emission scanning electron microscope
h	Thickness
HDPE	High density polyethylene
IL	Ionic liquid
K_{sr}	Swelling rate
l	Length
LiCl/DMAc	Lithium chloride/*N,N*-Dimethylacetamide

LVR	Linear viscoelastic region
M_b	Mole of bound water
M_{ba}	Mole of bound water at amorphous region
MCC	Microcrystalline cellulose
MFC	Microfibrillated cellulose
MRA	Multiple regression analysis
M_t/M_m	Water concentration
NaOH	Sodium hydroxide
NMMO	N-Methylmorpholine N-oxide
NMR	Nuclear magnetic resonance
OA	Orthogonal array
OH	Hydroxyl
P	Percentages of contribution
PBS	Polybutylene succinate
PE	Polyethylene
P_{HP}	Pressure at hot press
PLA	Poly(lactic) acid
PLLA	Poly(L-lactic) acid
PP	Polypropylene

P_{SIP}	Pressure at SIP
PVC	Polyvinyl chloride
R	Universal gas constant
RH	Relative humidity
RT	Room temperature
S	Sum of squares
S/N	Signal to noise ratio
SIP	Solvent infusion process
SPCs	Single polymer composites
T	Temperature
TCI	Total crystalline index
T_d	Dissolution temperature
t_d	Dissolution time
T_g	Glass transition temperature
TS	Thickness swelling
TTS	Time temperature superposition
UTS	Ultimate tensile strength
V	Variance
VARTM	Vacuum assisted resin transfer moulding

V_f	Fibre volume fraction
V_m	Matrix volume fraction
vol.	Volume
V_v	Void volume fraction
w	Width
WAXD	Wide angle X-ray diffraction
W_c	Water content
WLF	William-Landel-Ferry
W_{nf}	Weight of non-freezing bound water
W_{P1}	Weight of free water
W_{P2}	Weight of freezing bound water
wt.	Weight
XRD	X-ray diffraction
η_K	Viscosity of Kelvin-Voigt dashpot
η_M	Viscosity of Maxwell dashpot

Chapter 1

Introduction

1.1 Introduction to bio-based material

Bio-based composites are processed materials that are derived from living organisms. Bio-based composites consist of two or more different components that function as reinforcing and matrix phases. Generally, bio-based composites are placed into one of two different categories: (i) biocomposites or (ii) green composites. Biocomposites consist of a combination of natural cellulose fibres, man-made cellulose fibres or wood particles as the reinforcing phase and a petrochemically-derived polymer that acts as the matrix phase (*e.g.* polyethylene, polypropylene, epoxy resin, etc.) [1, 2]. In contrast, green composites consist of a natural fibre reinforcement and a naturally-derived polymer (or bio-polymer) that acts as the matrix phase (*e.g.* polylactides, palm oil-based resin, starch, etc.) [1, 2].

The modern day usage of cellulosic fibres in a polymer matrix composite dated back to the early 1970s and 80s [3, 4]. Since then, the development of cellulosic or natural fibre-reinforced polymer composites has had a huge resurgence in interest with well over 3000 studies now published in the literature (Compendex Engineering Village, 03.03.2016). More recently, the research and development of cellulose-based materials have been supported by governments and industries worldwide. The US Department of Energy is aiming to make all basic chemical building blocks that consist of at least 10% plant-derived renewable resources by 2020, with projections of up to 50% by 2050 [1]. Cellulosic fibre-reinforced polymer matrix composites have found numerous applications in the automotive industry in Europe. Jute and sugar cane

fibres are used in low cost housings in India and South America [5]. Natural fibres that are commonly used in composite and other bio-based materials include wood, jute, hemp, and flax fibres [4, 6-10]. Natural fibres have several advantages over glass fibres including biodegradability, higher specific tensile strength and stiffness, less hazardous to handle, lower cost, and less energy required during processing [4, 11, 12]. In addition, natural fibres sequester carbon dioxide during their production [4, 11, 13, 14]. However, natural fibres have less consistent fibre properties compared to glass fibres due to variations in the growing and harvesting conditions [4]. Hence, quality control during the processing of natural fibres is especially important for the production of consistent material properties [4].

The problems with bio-based materials include poor fibre-matrix interfacial adhesion, low degradation temperatures, and poor resistance to moisture ingress, making the use of natural fibres less favourable than synthetic fibres (*e.g.* glass, carbon or aramid fibre) [11, 15]. Strong interfacial interaction between the fibre and matrix is required to obtain efficient mechanical reinforcement in a composite material. Improvements in fibre-matrix adhesion is usually achieved by fibre surface or matrix modifications, with the addition of compatibilisers or coupling agents [11, 16]. However, these modifications typically increase the processing time and cost of bio-based composites [16]. Recently, all-cellulose composites (ACCs) have been proposed as an alternative approach to conventional bio-based composites with the aim of eliminating chemical incompatibilities between the reinforcement and matrix phases by utilising cellulose for both phases [4, 17].

1.2 All-cellulose composites

ACCs consist of a matrix of a dissolved cellulose, while the reinforcement is undissolved or partially dissolved cellulose [18-20]. ACCs will impart chemical compatibility between the reinforcement and matrix phases, resulting in an efficient stress transfer due to strong adhesion at the fibre-matrix interface [20]. ACCs are also known to be fully biodegradable [18-22]. The

modern day concept of an ACC was first explored by Nishino *et al.* [4, 19]. ACCs can be categorised as a bio-derived monocomponent composites or single polymer composite. The underlying objective of the ACC concept is to improve chemical bonding at the reinforcement and matrix interface to produce a material with outstanding mechanical properties [4, 17-19, 21, 23-25].

1.2.1 Processing routes of all-cellulose composites

Cellulose does not melt due to extensive intra- and intermolecular hydrogen bonding [17, 19]. However, cellulose can be dissolved with the appropriate solvents and then resolidified (or regenerated) by removing the solvents [17]. The processing of ACCs may be carried out by partially dissolving the cellulose after which the partially dissolved portion regenerated to form a matrix *in situ* (*i.e.* adjacent to the undissolved portion) [17, 18]. Recently, a process known as solvent infusion processing (SIP) has been successfully applied to produce ACCs [17]. SIP results in improved tensile strength and stiffness, presumably due to a more uniform distribution of the solvent through the cellulose precursor. The applied vacuum pressure during SIP also minimises contact with air, reducing water uptake by the fibre and solvent. The important of the applied vacuum pressure during SIP will help to reduce the void content of ACCs through a homogeneous solvent dispersion into the fibres. Huber *et al.* have described several processing variables that should be considered when producing ACCs including (i) dissolution time (t_d), (ii) dissolution temperature (T_d), (iii) coagulant medium, and (iv) drying conditions [4]. However, there has been a lack of systematic research to quantify the importance of these control factors on the final mechanical properties of ACCs. In the present study, a design of experiment (DOE) approach was used to optimise the control factors of ACCs. The significant control factors were then analysed according to the Analysis of Variance (ANOVA) and signal to noise (*S/N*) ratio.

1.2.2 Hygrothermal effects on all-cellulose composites

Hygrothermal effects in conventional composites have an impact on mechanical properties, viscoelastic properties, and creep behaviour. Cellulose is highly hydrophilic due to the presence of numerous hydroxyl (OH) groups within the macromolecular structure. Moisture uptake typically decreases the stability and degrades the mechanical properties of polymeric materials. Currently, there is lack of studies on the effects of moisture and temperature (or their combined effects) on the mechanical properties of ACCs. As a first step in the present study, a relationship between t_d and water absorption behaviour of ACCs was reported. The research then focusses on the hygrothermal effect on the mechanical properties of ACCs, with an emphasis on understanding the relationship between the cellulose structure and end-properties. Finally, the hygrothermal effect on the creep behaviour of ACCs was examined.

1.3 Research questions

The primary research questions that this study attempts to answer are as follows:

- What is the dominant control factor in processing to achieve the optimal mechanical properties for ACCs?
- What is the water absorption behaviour of ACCs?
- How do the mechanical properties of ACCs change as a consequence of hygrothermal effects?
- How is the creep behaviour of ACCs influenced by hygrothermal effects?

1.4 Research objectives

The objectives of this study are as follows:

- To optimise SIP control factors to achieve the optimal mechanical properties of ACCs.
- To determine the water absorption behaviour of ACCs.
- To observe the mechanical properties of ACCs due to the hygrothermal effect.

- To examine the creep behaviour of ACCs due to the hygrothermal effect.

1.5 Thesis outline

Chapter 2 presents a literature review on bio-based materials including ACCs. The chapter begins with a discussion of the structure, properties and sources of cellulose. Following this, the fabrication and processing of ACCs are reviewed including the preparation pathways, solvents, processing parameters, and regeneration and drying. Previous research on hygrothermal effects on cellulose-based materials and creep behaviour in cellulose composites are outlined.

Chapter 3 explains the research methodology for ACCs. This chapter covers the fabrication of ACCs including the selection of materials and solvents, SIP procedures, and other experimental procedures.

Chapter 4 establishes a processing-property relationship of ACCs. The importance of the control factors of ACCs production are analysed using Taguchi DOE. The ANOVA and *S/N* ratio approaches are used to analyse the experimental data. The processing-property relationship is determined using multiple regression analysis (MRA). The parametric dependency of each mechanical property outputs are analysed in terms of the power series equation. As a result, a combination of control factors is known to achieve the optimal mechanical performance of ACCs. The validation test is also performed to validate the results.

Chapter 5 discusses the water absorption behaviour in ACCs. This chapter covers the kinetic of water absorption, nonlinear regression analyses, and Arrhenius law analyses. The effects of water bath temperature and t_d on the water absorption behaviour are observed. ANSYS software is used to estimate the saturation time, predict the water content at various times and thicknesses, and observe a relationship between theoretical and experimental saturation times.

Chapter 6 discusses the hygrothermal effect on the mechanical properties of ACCs. The water threshold is also determined. The bound and free water effects on the mechanical properties of ACCs are also evaluated and discussed. The prediction of Young's modulus (E) is performed based on information regarding molecular deformation.

Creep behaviour for ACCs is discussed in Chapter 7. This chapter investigates the creep performance in ACCs. The determination of linear viscoelastic region (LVR) is performed to ensure that the creep test is conducted within the LVR. The effects of temperature and water content on the ACCs creep behaviour are studied. The application of time-temperature superposition (TTS) principle is investigated by constructing a master curve from the short-term creep test data. Physical aging effects in ACCs as observed in long-term creep testing is also discussed.

Chapter 8 presents a general discussion, conclusion and suggested future works for this present study.

Chapter 2

Literature review

2.1 Bio-based materials

The societal demand for environmentally-friendly materials is increasing as a result of worldwide environmental issues. The usage of many petrochemically derived materials has had negative effects on the environment due to their non-biodegradable nature. As a result, there is increasing focus on the development of new biomaterials based on renewable resources. An example of a renewable material that has the potential to replace petrochemically-derived polymers is natural fibre. The advantages of natural fibre include low cost compared to synthetic fibres, sustainability, degradability, and availability in a variety of forms [5, 26]. Many researchers have focussed on the use of cellulosic fibres (flax, hemp, ramie, sisal, jute or kenaf fibres) as a replacement for glass fibres in polymer composites [7, 13, 27-52].

Single polymer composites (*aka* self-reinforced polymer composites) have been introduced as an environmentally-friendly polymer composite [53]. For instance, fully recyclable all-polypropylene composites (all-PP) have been suggested as alternatives to the conventional glass fibre reinforced plastics in various applications such as in the automotive industry [53-59]. A class of single polymer composite (SPCs) known as all-cellulose composites (ACCs) have recently emerged through the pioneering work of Nishino *et al.* [19].

2.2 All-cellulose composites

In general, an all-cellulose composite, or ACC, refers to an SPC that has the reinforcement and matrix phases based on non-derivatised cellulose [17]. This concept was originally applied to thermoplastic polymer composites to simplify the recycling process [17, 60]. ACCs may exhibit excellent mechanical properties compared to traditional biocomposites, depending on the types of fibre [4, 17, 53]. The mechanical properties of ACCs and biocomposites will be discussed in subsequent subchapter (2.2.3.4).

2.2.1 Natural and man-made fibres

Natural fibre may be divided into two main groups: (i) organic, and (ii) inorganic. Plant and animal-based fibres are organic fibres, whereas mineral fibres are inorganic fibres [61]. The classification of various natural fibres is illustrated in Figure 2.1 [61].

Man-made cellulose fibre (*e.g.* viscose) is an industrially processed fibre, derived from natural resources. The term viscose originates from highly viscous cellulose solution obtained during the dissolution process [62]. The viscose process involves the derivatisation of cellulose I to create a wet-spinnable cellulose solution. Generally, regeneration of the dissolved cellulose in a water bath results in non-derivatised cellulose II fibres [17].

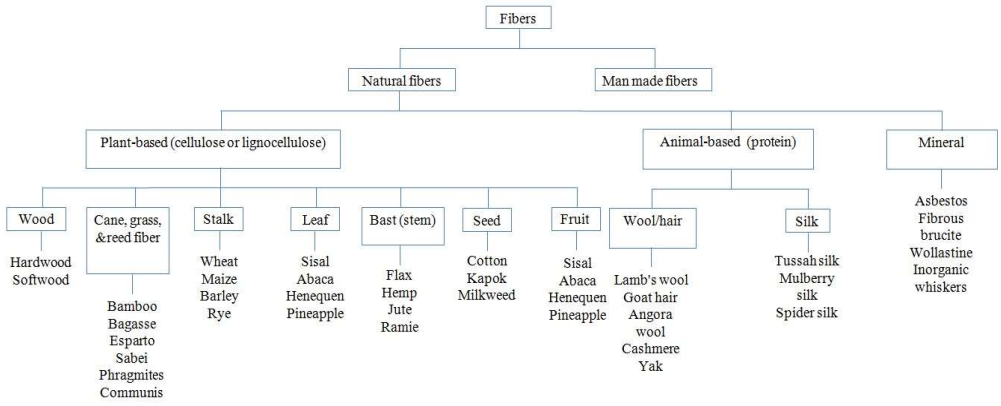

Figure 2.1 The classification of various natural fibres [61].

Viscose rayon textile is a man-made cellulose fibre. This textile is produced by a variation of the viscose processes, involving a dissolved natural cellulose pulp in a sodium hydroxide (NaOH) and carbon disulphide (CS_2) solution [14]. Viscose rayon textile production reduces the variation associated with natural fibres while still using a naturally derived feedstock [14, 63]. The viscose dope is filtered, degased, and extruded into a coagulation bath to generate cellulose fibre [14, 64]. A major drawback of the rayon process is the contamination of wastewater by CS_2 and other polluting sulphur by-products of the cellulose derivatisation step [62].

2.2.2 Chemical structure of cellulose

Cellulose is the most abundant biopolymer on Earth, with approximately 1.5×10^{12} tons of cellulose produced a year, representing a huge source of biodegradable raw material [24, 65, 66].

Cellulose was first discovered and isolated from green plants by Anselme Payen (1795-1871) [65, 67, 68]. It is a rigid linear polysaccharide, that consists of many repeat units in the cellulose chain known as anhydroglucose units (Figure 2.2) [69, 70]. Two anhydroglucose units linked together by a β-1,4-glycosidic linkage are known as cellubiose [69, 70].

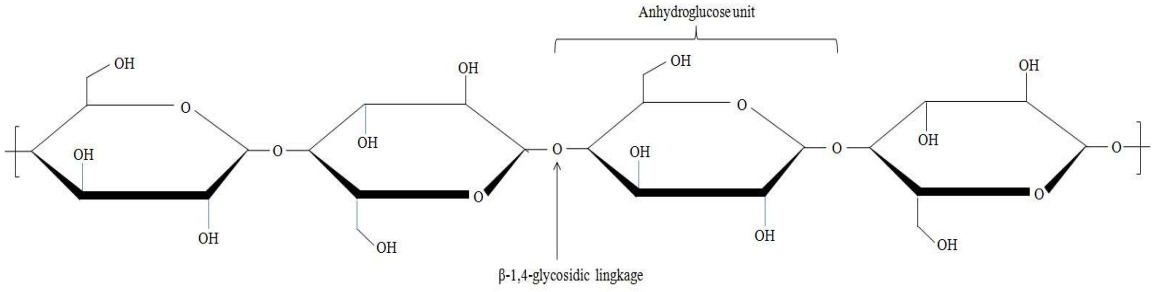

Figure 2.2 Polymeric chain structure of cellulose showing the β-1,4-glycosidic linkage and one anhydroglucose unit [69, 70].

A single glucose unit (hexose) is arranged as either an α or β structure, depending on the position of the hydroxyl (OH) groups. Individual cellulose chains are highly hydrophilic due to the presence of the OH groups. Four allomorphs of cellulose are described and known as cellulose I, II, III, and IV. Cellulose I (*aka* native cellulose) is the most crystalline type, composed of two structural forms: I_α (triclinic unit cell) and I_β (monoclinic unit cell) [71]. The proportion of I_α and I_β regions varies according to the source of cellulose. Lower plants (*e.g. Valonia*) and higher plants (*e.g.* cotton cellulose) are predominantly I_α and I_β, respectively [72]. The hydrogen bonding arrangement of cellulose I_α differs from cellulose I_β such that I_α is less stable than I_β [73]. The bond angles for both intermolecular and intramolecular bonds in I_β are closer to 180° compared with that of I_α [74, 75]. The crystallographic structure and hydrogen bonding pattern for both types of cellulose differentiate the properties of cellulose fibres. The intrachain O2H-O6 bond distances in I_α are shorter than I_β, while the interchain O6H-O3 bond distances in I_β are shorter than I_α [76]. The hydrogen bonding structures of I_α and I_β are shown in Figure 2.3.

Cellulose II is formed by the mercerisation or regeneration of cellulose I. Cellulose II is considered the most thermodynamically stable form of cellulose [77]. Cellulose II is the main component of man-made cellulose fibres such as rayon and Lyocell. Cellulose II exhibits anti-parallel packing of the cellulose chain, meaning half of the reducing ends of the cellulose chain can be found on both ends of the crystal [78].

Cellulose III is formed from either cellulose I or II by a treatment with liquid ammonia to generate either the cellulose III_I or III_{II} structure. Cellulose IV_I and IV_{II} can be prepared from the corresponding form of cellulose III by heating it in glycerol [4, 79]. The transformation of cellulose to different allomorphs is illustrated in Figure 2.4.

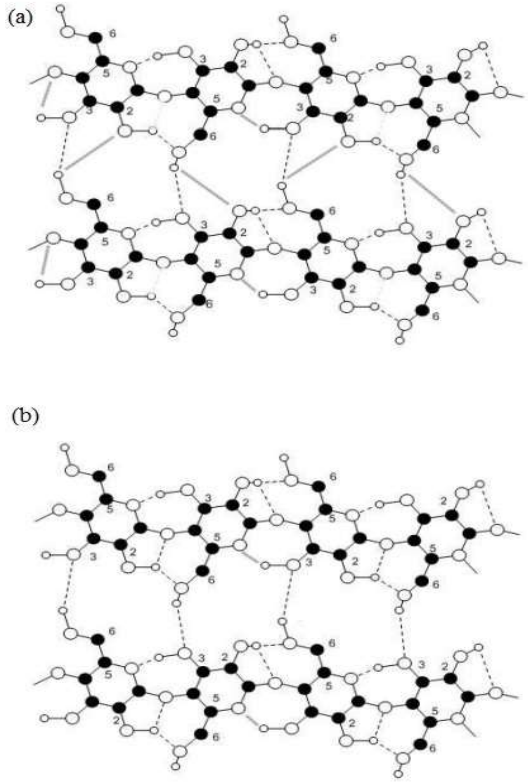

Figure 2.3 Hydrogen bonding pattern (dotted lines) in cellulose: (a) I_α and (b) I_β [69].

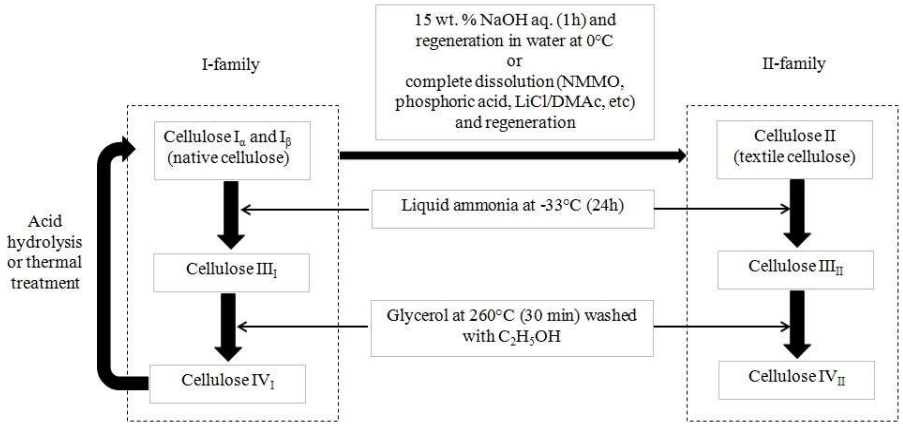

Figure 2.4 Transformation process of cellulose [80].

The mechanical properties of the cellulose allomorphs vary due to the differences in the molecular structure [4]. Cellulose I is semicrystalline in nature, with the amorphous regions present as a thin layer between single microfibrils aligned with the longitudinal axis of the fibre (*aka* micellar model or fringe fibrillar model). The structure of amorphous cellulose is unstable in the presence of moisture such that it may be recrystallised into cellulose II [81, 82].

The basic element of the molecular structure is formed by the parallel arrangement of crystalline chains in native cellulose. The structure of the crystal is formed by intermolecular and intramolecular hydrogen bonding of OH group at the cellulose chain, in combination with stiff and strong cellulose molecules [83]. Many crystals are linked together in long molecular segments which are known as elementary fibril. Figure 2.5 shows the chain conformations of cellulose I and II [69].

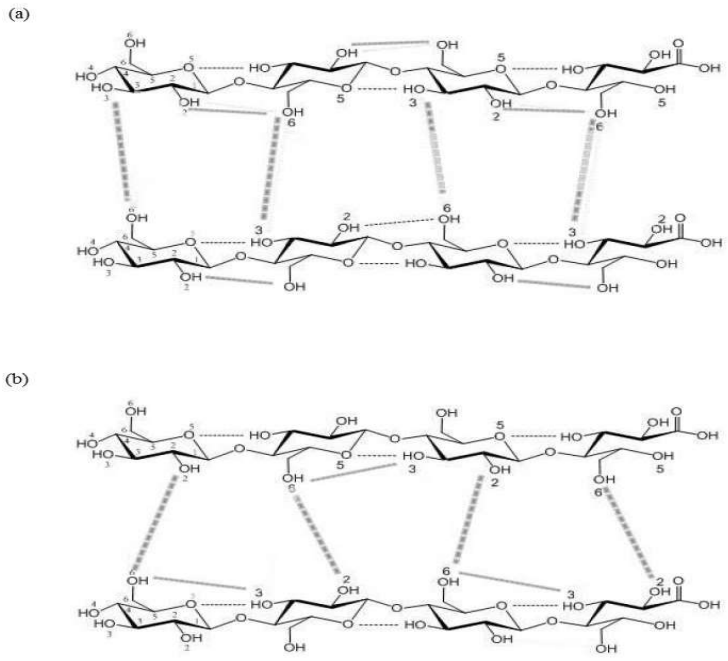

Figure 2.5 The chain conformations of (a) cellulose I, and (b) cellulose II. The dotted and solid grey lines represent inter- and intramolecular hydrogen bonding, respectively [69].

Hydrogen bonding in cellulose I and II occurs at different positions. Intramolecular hydrogen bonding takes place at O(3)H-O(5) and O(2)H-O(6), and intermolecular hydrogen bonding takes place at O(3)H-O(6) in cellulose I. In contrast, cellulose II forms intramolecular hydrogen bonds at O(3)H-O(6) and O(3)H-O(5), and intermolecular hydrogen bonding at O(2)H-O(6). The O(3)H-O(5) intramolecular hydrogen bonds exist in both cellulose I and II, leading to the linear and rigid chain structure of cellulose. The difference between cellulose I and II appears in the interchain bonding where the dominant hydrogen bond for cellulose I is at O(3)H-O(6) while that of cellulose II is at O(2)H-O(6).

2.2.3 Preparation of all-cellulose composites

One of two methods can be used for the producing ACCs (Figure 2.6): (i) 2-step method [19], or (ii) 1-step method [18]. In the 2-step method, a portion of cellulose is completely dissolved in a solvent and then regenerated in the presence of undissolved cellulose. An example of this method was first given by Nishino *et al.* [19] in which Kraft fibre was fully dissolved and then regenerated in the presence of ramie fibres. The 1-step method involves partially dissolving cellulose, and then regenerating the dissolved portion such that it surrounds the undissolved portion, forming a matrix phase *in situ*. An example of this method was first reported by Gindl *et al.* [18]. The partially dissolved cellulose I results in relatively high volume fractions (V_f) of the reinforcement phase ($\leq$ 90%) that is embedded in a small amount of cellulose matrix phase ($\geq$ 10%). The dissolution of cellulose is followed by removal of the solvent (regeneration) with a coagulant and then final drying to remove the coagulant [4].

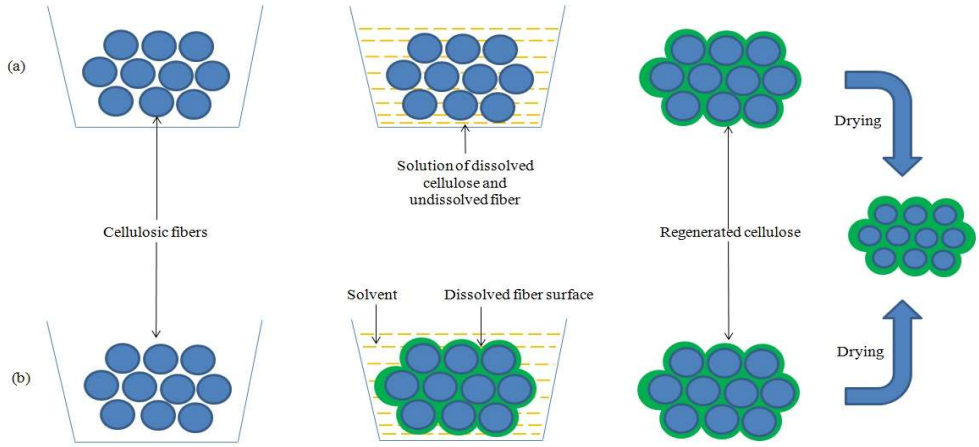

Figure 2.6 Schematic representation of ACCs preparation (a) 2-step method, and (b) 1-step method [4].

Huber *et al.* [24] partially dissolved woven textiles using an IL, demonstrating the process of hand impregnation and compression moulding (Figure 2.7). However, this method has two disadvantages, including excessive void formation and incomplete fibre wetting, leading to lower mechanical properties and fibre-matrix interfacial adhesion. Alternatively, vacuum is used to infuse the reinforcement with a solvent, serving as a basis for the process known as vacuum assisted resin transfer moulding (VARTM) [80]. The advantages of VARTM include: (i) high V_f (60-70 wt.%), (ii) low void content (V_v) (< 1%), (iii) high specific mechanical properties, (iv) volatile-free processing, (v) low cost investment, (vi) reduced manual labour, (vii) high cost-efficiency for small production runs, and (viii) large and highly integrated fabrication of structures [61, 84]. Solvent infusion processing (SIP) was developed by Huber *et al.* [17] based on the concept of VARTM. SIP can be divided into five stages (Figure 2.8): (i) solvent infusion, (ii) temperature-triggered partial dissolution of the surface of the fibres while under pressure, (iii) infusion of a coagulant (distilled water), (iv) the washing process, and (v) drying under pressure.

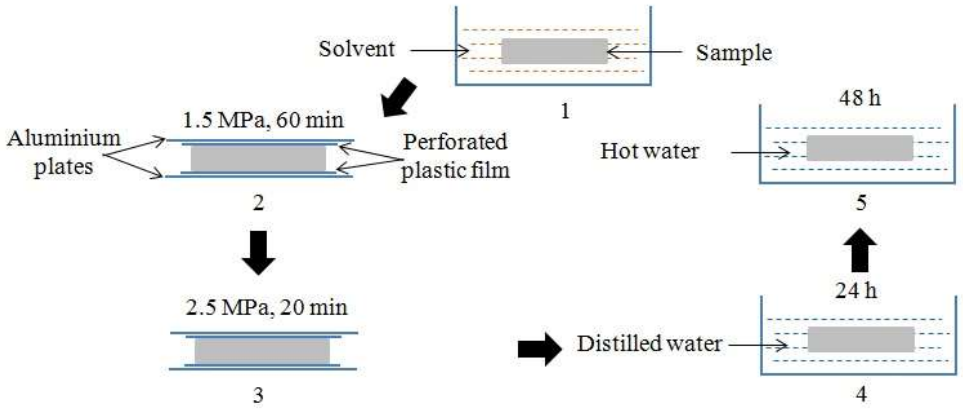

Figure 2.7 Hand impregnation and compression moulding process: (1) hand impregnated process, (2)-(3) hot pressing, (4) regeneration of cellulose in distilled water, and (5) removal of residual solvent in hot water [24].

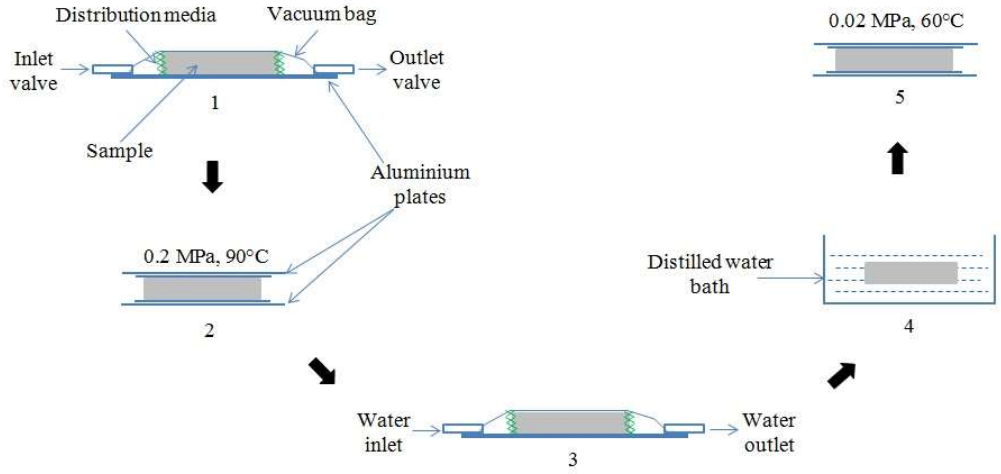

Figure 2.8 Schematic process of SIP method (1) solvent infusion, (2) partial dissolution at hot press, (3) regeneration of cellulose, (4) washing process, and (5) drying process [17].

2.2.3.1 Cellulose solvent

A limited number of solvents can be utilised to dissolve cellulose including *N*-methylmorpholine *N*-oxide (NMMO), NaOH, lithium chloride/*N,N*-dimethylacetamide (LiCl/DMAc) and various ionic liquids (ILs). Duchemin *et al.* discussed the advantages and disadvantages of various types of solvents (Table 2.1) [68].

Table 2.1 The advantages and disadvantages of various types of solvents

Solvents	Advantages	Disadvantages	Ref.
NMMO	Good solvent, industrially used, non-toxic, recyclable,	Expensive, special handling, degradation reaction	[68]
NaOH	Eco-friendliness, safest, easy to use, nontoxic, cheap,	Does not efficiently dissolve all cellulose sources like both LiCl/DMAc and NMMO.	[4, 68]
LiCl/DMAc	Ability to complete high molecular weight of cellulose	Pretreatment step, expensive, time consuming, highly toxic, corrosive, volatile, and high healthy and safety issues	[4]
IL	High cellulose dissolution rates, easy to use, low vapour pressure, recyclable, safe to handle.	High toxicity, expensive	[4]

2.2.3.1.1 Ionic liquid

In general, ILs are molten salts that have a melting point below 100 °C. More specifically, room temperature ionic liquids (RTILs) are ILs that are a liquid at room temperature [85]. Some ILs have the ability to dissolve cellulose due to their high polarity. In 1934, Charles Graenacher was the first to discover an IL solvent system for cellulose [86]. More recently, a number of RTILs have now been discovered to dissolve non-derivatised cellulose [87-93]. The most successful RTILs in dissolving cellulose are composed of an allyl-, ethyl- or butyl-methylimidazolium or methylpyridinium cation core, and anion based on chloride, acetate or formate [94, 95].

Swatloski *et al.* and Zhang *et al.* found that the solubility of cellulose decreased with increasing the size of the cations (*e.g.* increasing the size of the alkyl group substituted on the imidazolium ring) [87, 88]. In comparison, allyl-methylimidazolium has a smaller cation than butyl-methylimidazolium due to the three carbon atoms and double bond in the N-substituted methylimidazonium cation of AmimCl. An intensive interaction with cellulose occurs in salt

solutions with small, strong and large polarising cations/anions [88, 96]. Small cations are speculated to favour the attack of the oxygen atom on the hydroxyl groups of cellulose.

The most effective RTILs for dissolving cellulose include butyl-imidazolium chloride (BmimCl), butyl-imidazolium acetate (BmimAc), and ethyl-imidazolium acetate (EmimAc). BmimCl is observed to dissolve up to 25 wt.% of cellulose when heated to 100 °C by microwave irradiation, resulting in a clear and highly viscous solution [87]. BmimCl has a relatively high melting point (65 °C), and high in viscosity. EmimAc and BmimAc are ILs that will also dissolve cellulose but produce lower viscosity solutions compared with BmimCl [97].

A large number of intermolecular hydrogen bonds are disrupted during cellulose dissolution. The reacting parts of the cellulose molecules are the oxygen and hydrogen atoms of cellulose-OH. The cellulose oxygen and hydrogen atoms act as the electron donors and electron acceptors, respectively, while the cation and anion in the IL work as the electron acceptor and donor, respectively [88]. Above the critical temperature of 100 °C, the ion pairs in the IL separate into individual cations and anions [87]. Free anions ($[Ac]^+$) are associated with the cellulose OH proton, and the free cations ($[Bmim]^+$) are associated with the cellulose OH oxygen. The disrupted hydrogen bonding in cellulose led to the dissolution of the cellulose (Figure 2.9).

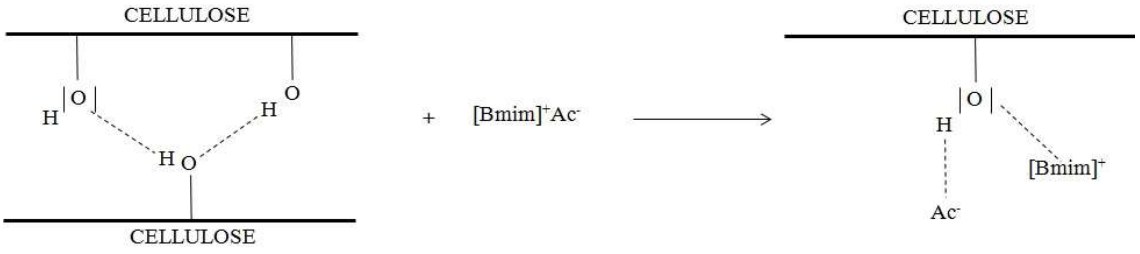

Figure 2.9 Possible dissolution mechanism of cellulose in BmimAc [88].

2.2.3.1.2 Sodium hydroxide

Aqueous NaOH solution is able to swell or dissolve the cellulose at high concentration [98]. NaOH has been used to dissolve cellulose due to its low processing temperature, cost effectiveness, low toxicity, and ease of handling [99, 100]. Recently, it was shown that a more efficient solvent is created by adding urea and/or thiourea to an aqueous NaOH solution [68, 100-102]. Urea acts to interrupt the intramolecular and intermolecular hydrogen bonding of cellulose [103]. However, the aqueous NaOH solvent system is not as efficient in dissolving cellulose as LiCl/DMAc or NMMO.

Recently, a new complex aqueous solvent consisting of NaOH, urea, and thiourea has been found to rapidly dissolve cellulose when cooled in the temperature range of -8 to -12 °C [99]. At low temperature, the solvent encases the cellulose macromolecules in the aqueous solvent, interrupting the cellulose chains and resulting in the dissolution of cellulose [100]. A 7 wt.% NaOH and 12 wt.% urea aqueous solution is a low cost solvent system that may easily dissolve cellulose. In addition, the dissolution of cellulose at a low temperature can be considered as an environmentally-friendly process since this reduces evaporation of the solvent system when compared with other more volatile organic solvents that require elevated temperature to dissolve cellulose [100].

2.2.3.2 Processing parameters

The 3 primary processing parameters that affect cellulose dissolution using ILs include dissolution time (t_d), dissolution temperature (T_d), and pressure at hot press (P_{HP}) [17, 87]. The dissolution rate is higher in the initial stages of cellulose dissolution. However, a decrease in the dissolution rate is observed after a period of time once the amorphous phases have been dissolved and only crystalline phases remain. The dissolution rate decreases since the crystalline phases are not easily dissolved by solvents such as ILs [87]. Extending t_d contributes to further dissolution of the cellulose until a maximum solubility is attained [87].

Cellulose dissolution is also influenced by T_d. Cellulose can be dissolved in the range of 90 to 130 °C [104]. At a certain temperature (20°C), cellulose cannot be dissolved by 1-ethyl-3-methylimidazolium acetate (EmimAc) due to the increasing viscosity, resulting in a decreasing dissolution capacity since a high viscosity will hinder the diffusion of EmimAc into the cellulose [105]. Increasing the temperature of EmimAc will increase the dissolution capacity of cellulose. However, degradation processes were found for certain ILs and high cellulose concentration at temperature of 140 and 160 °C, when using microwave heating [106].

Processing parameters that should be considered for cellulose dissolution using the NaOH/urea aqueous solvent system include t_d, pressure at the SIP (P_{SIP}), and P_{HP} [17, 107-109]. A longer t_d will reduce the mechanical properties of the cellulose composites because too much dissolved cellulose will be regenerated as a matrix phase around the cellulosic fibres [16]. A decrease in t_d will also reduce the mechanical properties due to insufficient matrix phase. A decrease in t_d also contributes to the formation of voids within the reinforcement and matrix phases of ACCs. Optimisation of P_{SIP} and P_{HP} is desirable as this will reduce the dissolution time during the dissolution process. Optimal levels of P_{SIP} and P_{HP} are needed to create a vacuum condition before the infusion process, reducing the void formation as the homogeneous cellulose dissolution [24].

2.2.3.3 Cellulose regeneration

Cellulose regeneration involves transforming the dissolved cellulose back into a solid phase. The dissolved cellulose is immersed in the anti-solvent (or coagulant) such as water, ethanol, or methanol in order to remove the solvent from the cellulose through a solvent exchange. Water is an excellent choice for the anti-solvent due to its low in cost and ease of handling. However, the hydrophilicity of cellulose results in significant absorption of water that then requires removal *via* an extensive drying stage. The use of ethanol as an anti-solvent reduces the swelling of the composite although the use of alcohol also results in a decrease in the

crystallinity of the regenerated cellulose due to its fast precipitation rate [4, 23]. In contrast, regeneration of cellulose in water increases the crystallinity of the final ACC due to the slow precipitation rate [23].

2.2.3.4 Mechanical properties

The mechanical properties of bio-based composite materials extend over a wide range, depending on the reinforcement and matrix materials, solvent system, and processing method, processing parameters (dissolution time, solvent temperature, fibre content, fibre orientation), as well as many other variables in the manufacturing process (Tables 2.2 and 2.3). Generally, the mechanical properties of bio-based composites are difficult to compare due to the large variability in manufacturing processes. However, in general, the mechanical properties of ACCs are significantly higher than conventional bio-based composites (Figure 2.10).

Table 2.2 Overview of mechanical properties of ACCs

No	Method	Raw materials	Solvents	Dissolution time	Drying process	Strength (MPa)	Young's modulus (GPa)	Ref
1	2-step method	Refined ramie, and craft pulp	3 wt.% of cellulose in 8 wt.% LiCl/DMAc	24 and 72 h	12 h at RT and 24 h at 60°C in a vacuum	480 ± 50	45	[19]
2	1-step method	Filter paper	Unknown cellulose concentration in 8 wt.% LiCl/DMAc	6 – 12 h	100°C for 12 h and 60°C for 24 h in a vacuum	211	8.2	[21]
3	1-step method	MCC	2 – 4 g of cellulose in 8 g LiCl in 100 ml DMAc	12 h	Dehydration between two sheets of paper	215 – 243	12.6 -14.9	[18]
4	1-step method	Beech pulp	Unknown cellulose in 8 g	10 h	Pressing at 80°C and 200 MPa	154 ± 17	12.2 ± 0.9	[110]

			LiCl in 100 ml DMAc					
5	Hand impreg-nation	Flax	Dissolved in BmimCl	1 min	Hot pressed at 80°C and 7 bar for 30 min	34 ± 2	4.6 ± 0.5	[25]
6	Hand impreg-nation	Lyocell	Dissolved in BmimCl	1 min	Hot pressed at 80°C and 7 bar for 30 min	78 ± 4	7.2 ± 1.0	[25]
7	1-step method	MFC	Dissolved in BmimCl	20 – 160 min	Dried overnight at 60°C under reduced pressure (< 0.1 atm)	124.1	10.8	[22]
8	1-step method	Ramie	LiCl/DMAc	1 – 12 h	Dried at RT for 12 h and then under vacuum at 60°C for 24 h	460 (longitudinal)	28 (longitudinal)	[16]
9	Hand impregna-ted	Cotton fabric	BmimCl	30 min	Dried at 100°C for 24 h	Up to 20	Up to 145	[90]
10	SIP	Cordenka fabric	BmimAc	60 min	Vacuum dried at 60°C at 0.02 MPa for 60 min	91.12	4.1	[17]
11	Hand impreg-nated	Cordenka fabric	BmimAc	80 min	Vacuum dried at 75°C at 0.5 MPa for 2 h	70.16	2.45	[24]
12	1-step method	MCC	1 – 4 wt.% MCC in 8 wt.% LiCl/DMAc	30 min	Dried at RT for 1 day	Up to 35	Up to 2.5	[111]
13	2-step method	Ramie	9 wt.% of NaOH solution	1 h at RT	Vacuum dried at 60°C for 24 h and further dried at 100°C for 1 h	Up to 540	-	[112]
14	Wet spinning method	Cotton linter pulps	7/12/81 wt.% of NaOH, urea, distilled water	5 min	Air-dried at ambient temperature	124	5.1	[113]

15	Hand-impreg-nation	Cotton linter pulps (matrix) and ramie fibre (reinfor-cement)	7/12/81 wt.% of NaOH, urea, distilled water	30 min	Air-dried at ambient temperature	Up to 124.3	Up to 5.9	[114]

Table 2.3 Overview of biocomposites mechanical properties.

No	Matrix	Fibre type	Fibre fraction (vol % or wt %)	Tensile strength (MPa)	Young's modulus (GPa)	Strain to failure (%)	Ref
1	Starch	Ramie	40 (wt.%)	6.9	0.47	13.6	[40]
2	PBS	Jute	30 (wt.%)	16.0	1.1	1.9	[115]
3	PP	Kraft pulps	30 (wt.%)	7.5	1.3	2.0	[116]
4	PBS	Silk (*Bombix Mori*)	50 (wt.%)	50.0	2.3	7.0	[117]
5	PP	Kenaf	60 (wt.%)	27.4	3.0	2.6	[118]
6	PLLA	Kenaf	70 (vol.%)	62.0	6.3	2.0	[119]
7	Polyester	Bagasse (acrylic acid treatment)	20 (wt.%)	229.01	8.09	5.59	[120]
8	PLA	Rayon	30 (wt.%)	57.97	4.85	-	[64]
9	PLA	Flax	30 (wt.%)	54.15	6.31	-	[64]

10	PP	Flax	30 (wt.%)	29.0	5.0	2.7	[121]
11	PLA	Flax	30 (wt.%)	53.0	8.3	1.0	[121]
12	Epoxy	Banana	-	26.1	2.7	-	[122]
13	Polyester	Palm oil	45 (wt.%)	35.1	3.29	3.75	[123]
14	Polyester	Coir	45 (wt.%)	39.8	3.60	5.20	[123]
15	PVC	Bagasse	35 (wt.%)	49.29	0.7	5.93	[124]

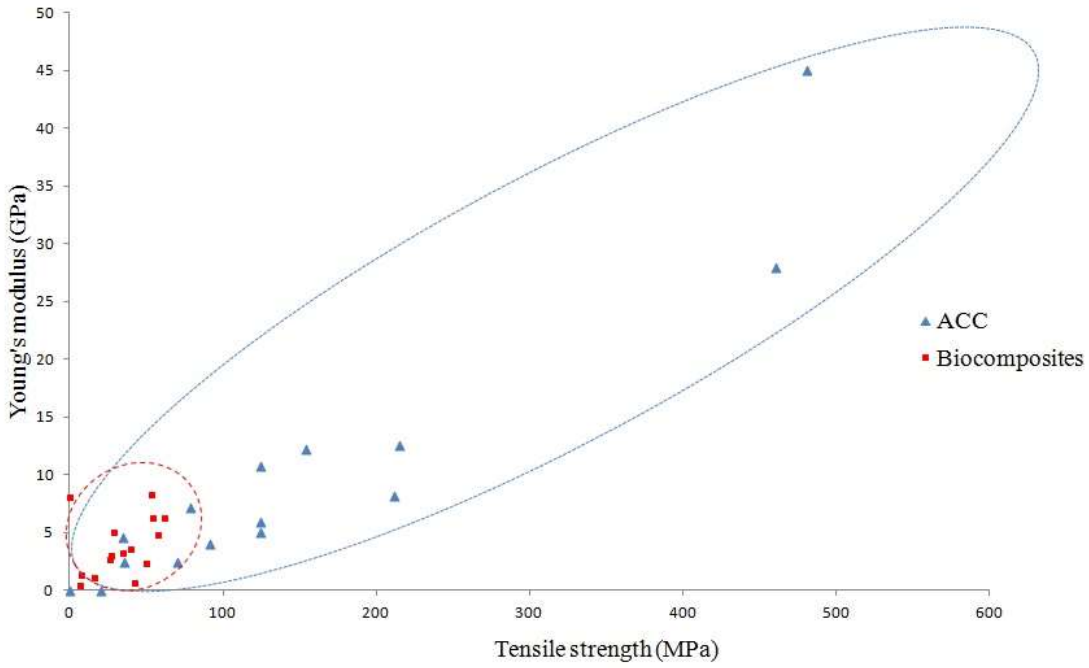

Figure 2.10 Comparison of the mechanical properties of ACCs and biocomposites.

2.2.3.5 Phase characterisation

The crystallinity index (CrI) values depended on the processing parameters including: (i) t_d [16, 21, 22, 68, 81], (ii) cellulose content (c) [68, 111], and (iii) solvent [25]. The effect of t_d was observed to be the most significant factor on the mechanical properties, CrI, and V_f [16, 21, 22, 68, 81]. The CrI decreased with the increase of t_d [16, 21, 22]. A decrease in CrI with the increasing t_d could be observed from wide angle X-ray diffraction (WAXD) diffractograms (Figure 2.11). The non-crystalline phase apparently increased as the t_d increased. This observation indicated that the dissolution of cellulose fibres progressed gradually with t_d, and the resolidified part turned into non-crystalline regions in the composite. The CrI of ACCs at 0, 6 and 12 h were found to be 86, 19, and 14%, respectively [21]. A decrease in CrI was observed from the decreasing peaks at the crystalline plane (grey area) and the increasing non-crystalline scattering (hatched area) (Figure 2.11) [21].

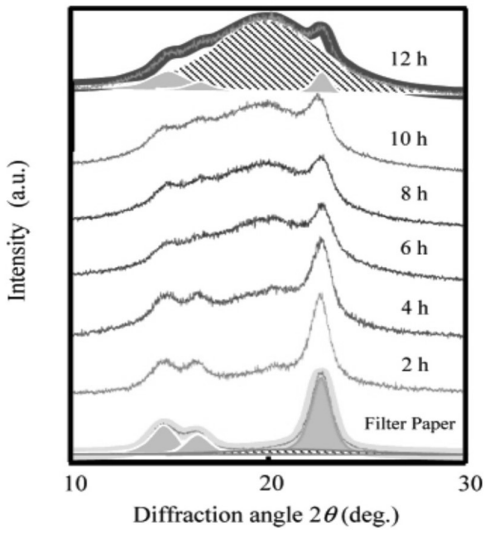

Figure 2.11 WAXD diffractograms of the filter paper and ACCs at different dissolution times up to 12 h [21].

The relationship between CrI and the mechanical properties was observed. Nishino *et al.* found that E and tensile strength of ACCs increased as the CrI decreased [21]. ACCs exhibited brittle

fracture during tensile testing, indicating a strong fibre-matrix interfacial. Duchemin *et al.* also reported the increasing *E* and tensile strength of ACCs as the CrI decreased [22]. However, the effect of V_f on the mechanical properties was not found in the previous studies by Nishino *et al.* and Duchemin *et al.* [21, 22]. Soykeabkaew *et al.* observed that the longitudinal *E* and tensile strength of ACCs decreased as the CrI decreased [16]. The decreasing *E* and tensile strength of ACCs were attributed to the decreasing V_f and increasing matrix volume fraction (V_m). The dissolved fibre core increased which was consistent to the decreasing V_f. The increased matrix phase led to ductile fracture. Soykeabkaew *et al.* found that the maximum mechanical properties could be achieved at shorter t_d (120 min) [16]. However, Nishino *et al.* and Duchemin *et al.* found that the optimal t_d for maximum mechanical properties were 720 [21], and 160 min [22], respectively.

2.3 Viscoelastic properties

Cellulose contains both crystalline and amorphous phases [125]. The viscoelastic behaviour of cellulose is governed by hydrogen bonding [125, 126]. Crystalline cellulose has different interchain links involving hydrogen bonding at the C-6 position [127]. This hydrogen bonding which is in highly ordered crystalline states occurs *via* the C-6 hydroxymethyl group [128]. However, amorphous cellulose differs from crystalline cellulose in its hydrogen bonding pattern. According to previous studies, hydrogen bonding in amorphous cellulose were held together by isotropic intermolecular hydrogen bonds linked to the hydroxyl groups at the C-2 and C-3 positions, resulting in randomly distributed domains [74, 75, 126, 128, 129]. At lower temperature, the molecular mobility is generally considered as localised and this leads to a macroscopic mechanical or dielectric behaviour, the so-called secondary relaxations (γ and β) [130]. Thus, at lower temperature, mechanical relaxations are largely dominated by the amorphous phase and denoted as the secondary relaxations [68]. At higher temperature,

cellulose exhibits three different glass transition temperatures (T_g) (α_1, α_2, and α_3) [131] (Table 2.4).

Table 2.4 Relaxation of cellulose at various range of temperatures

Temperature (°C)	Relaxation	Description	Ref.
-120 to -90	γ	-Associated with a rotation of the hydroxymethyl (CH_2OH) group rather than the rotation of its OH group depending on frequency (*f*), water content and crystallinity.	[130]
-80 to -40	β	-Associated with cooperative but localized motion of segments of the main chain of the cellulose molecule depending on the water content. -Activation energy is in the range of 69-85 kJ/mol.	[132]
30 to 60	α_3	-Attributed to the motion of chains bound water molecules by hydrogen bonding. -Activation energy (10.9 kJ/mol) is consistent with that of hydrogen bonding in the non-crystalline regions.	[126, 133, 134]
140 to 290	α_2	-It is generally acknowledged to a true T_g since *E*' decreases by several order magnitude. -Attributed to the micro-Brownian motion of whole polymer segments with moderate inter- and intramolecular bonding in the amorphous regions with an activation energy of 200-300 kJ/mol.	[68, 133]
285 to 305	α_1	-This region is attributed to the degradation of cellulose at higher temperature. - $\alpha_{1,2}$ and $\alpha_{1,1}$ located at ±300°C and ±320°C.	[68]

2.4 Hygrothermal effect on all-cellulose composites

Hygrothermal effect is attributed from the water/moisture, temperature or the combination of both factors [135]. This issue is a great concern because of the hydrophilic behaviour of cellulose fibres that contain many OH groups [136]. This effect leads to an interaction of hydrogen bonds with water molecules. The quantity of water content depends on the relative humidity (RH) of the surrounding atmosphere, cellulose purity, and CrI [136]. The presence of

OH groups in the amorphous phase is accessible to polar solution; however, only the surface of the crystalline phase is available for water absorption [137].

2.4.1 Water absorption behaviour

The application of bio-based composite materials in an outdoor environment is inevitably exposed to transient, harsh and severely hygrothermal environments [138]. Adhikary *et al.* reported that the exposure of wood flour-reinforced thermoplastic composite to environmental conditions such as humidity, temperature, and sunlight, may alter the chemical and physical properties of the material [139]. The direct comparison of the water diffusion coefficient (D) is difficult to determine due to the inherent variability of manufacturing process (raw materials, processing methods, and test conditions) (Table 2.5). The range of D values for biocomposite materials varies from 10^{-12} to 10^{-14} m^2/s.

Espert *et al.* reported about the effects of temperature and cellulose concentration on water absorption of biocomposite material. The D values increased as the temperature and cellulose concentration increased [116, 140]. The saturation time decreased as the temperature and cellulose concentration increased [116, 140]. The required activation energy was directly proportional to the D values [116]. The D values generally depended on the higher structure of a polymer [141, 142], and was found to have a strong relation with the amorphous fraction of cellulose since the water molecule can diffuse only through the amorphous part of the cellulose [143]. The relationship between water molecules and the water content of cellulose is important to be established [144].

Table 2.5 Water diffusion coefficient of various bio-based materials

No	Materials	D (m^2/s)	Refs.
1	40-50 wt.% sawdust - PP	$2.76 - 9.45 \times 10^{-12}$	[145]
2	50 wt.% rice hull - HDPE	4.63×10^{-13}	[145, 146]
3	30 wt.% starch - natural rubber	$0.65 - 5.61 \times 10^{-14}$	[147]
4	20 wt.% sisal - PP	2.30×10^{-13}	[116]
5	15 wt.% sisal fibre – starch	9.42×10^{-13}	[51]
6	40 wt.% ramie fibre - starch	2.80×10^{-14}	[40]
7	50 wt.% wood - recycled HDPE	5.94×10^{-12}	[145]
8	30 wt.% wood - recycled HDPE	3.24×10^{-12}	[145]

2.4.2 Mechanical properties

Moisture or water acts as a plasticiser [148]. The induced chemical potential between accessible OH and polar water molecules produces an affinity for hydrogen bond formation [138]. The decreasing mechanical properties (tensile strength and Young's modulus) due to water have been reported in previous studies (Table 2.6) [52, 116, 135, 149, 150].

Espert *et al.* found that a significant drop of mechanical properties (tensile strength and Young's modulus) due to water absorption was associated with the fibre content and temperature [116]. The increasing fibre content caused a significant increase in water content because of the highly hydrophilic character of cellulose fibre [116, 151]. At high temperature, the water mobility increased, reducing the entanglement and hydrogen bonding between molecular chains [152].

Kim *et al.* reported on the effects of water on the structure and properties of the cellulose fibre and polymer matrices (*e.g.* epoxy and vinylester) [52]. The fibres swelled when water penetrated into the biocomposite materials [52, 149]. The matrix structures experienced a chain

reorientation and shrinkage. The debonding and weakening of the fibre-matrix interface were expected due to the water absorption.

Adhikary *et al.* explained that the increasing void between the fibre-matrix interface increased the water absorption into the biocomposite materials, inducing water to fill gaps at the fibre-matrix interface [145]. The increasing water content will increase the stress concentration and reduce the transfer capability of the fibre-matrix interface [150]. These results will lead to the reduction of the mechanical properties of biocomposite materials. Mohd Ishak *et al.* found that the absorbed water significantly changed the fracture mode from brittle to a ductile fracture, resulting in the reduction of mechanical properties [135].

However, Dhakal *et al.* found that the tensile strength of a wet sample was higher than the dry sample at specified high cellulose content. This finding could be due to the fact that high amounts of water can cause the swelling of the fibres, filling the gaps between fibre and the matrix. This result led to an increase in the mechanical properties of the hemp fibre reinforced unsaturated polyester composite [140].

Table 2.6 Percentage drop in mechanical properties of bio-based materials

No	Materials	Tensile strength (%)	Young's modulus (%)	Refs.
1	10 wt.% wood reinforced PP	15.4	6.9	[116]
2	30 wt.% wood reinforced PP	46.6	34.6	[116]
3	15 wt.% hemp reinforced PE	25.5	38.0	[140]
4	21 wt.% hemp reinforced PE	9.8	49.2	[140]
5	32 wt.% sisal reinforced epoxy resin	62.0	81.9	[52]
6	32 wt.% sisal reinforced vinyl-Ester	11.7	53.2	[52]
7	40 wt.% *Acacia mangium* reinforced PP	21.1	51.0	[153]
8	40 wt.% wood flour reinforced PP	14.0	29.0	[154]
9	10 wt.% sisal reinforced PP	2.9	23.0	[151]
10	30 wt.% sisal reinforced PP	47.8	61.7	[151]

2.4.3 Viscoelastic properties

The effects of water on the viscoelastic properties of biocomposite materials (storage modulus (*E'*), loss modulus (*E''*), and T_g) have been reported in the previous studies [148, 155-159]. The *E'* and T_g values decreased with the increasing water content [148, 155-160].

Hammiche *et al.* [156] reported on the water molecules retained in the affected matrix phases of biocomposite materials. A decrease in the T_g under hygrothermal condition was due to a plasticisation effect of water in the matrix phase (polyvinyl chloride). The decreasing density but increasing mobility of the matrix phase and free volume were expected due to the absorbed water [158, 161].

The presence of undissolved cellulose counteracted the plasticising effect of water, acting as a rigid reinforcement phase (anti-plasticiser). A restriction in the mobility of cellulose chains was expected. This restriction was due to the strong hydrogen bond interaction between undissolved and dissolved cellulose [162]. Thus, the increasing T_g value of the plasticised amylopectin matrix was expected due to the migration of water molecules from the undissolved to the dissolved cellulose [163].

2.4.4 Molecular deformation

Changes in cellulose structure are due to the interaction between cellulose and water molecules. The intensity of the infrared spectra at 1640 [148] and 3500 cm^{-1} gradually increases with the increasing water content [93, 148, 164-167]. As aforementioned, water acts as a plasticiser, making the material softer. However, water does not easily penetrate into the crystalline domains of cellulose at room temperature. Therefore, the absorbed water is considered to change the mechanical behaviour of the amorphous region. The intensities at 1278, 1268, 1370, 968, and 930 cm^{-1} also increase due to the increasing water content (Figure 2.12). These wavenumbers are assigned to the vibrational modes associated with the OH groups of the cellulose chains.

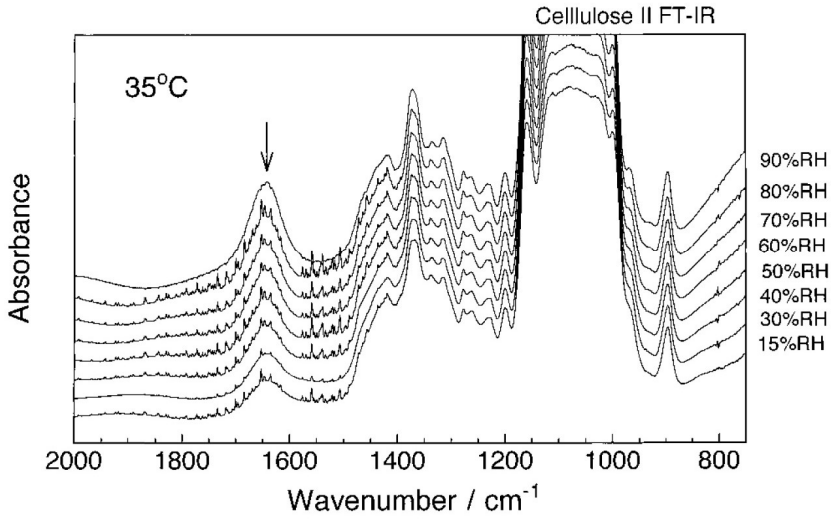

Figure 2.12 Infrared spectra of regenerated cellulose at various relative humidities [148].

A regular arrangement of the hydrogen bonds results in the formation of crystalline regions, alternating with less ordered non-crystalline regions at the surfaces and connection of the crystallites [168]. The intermolecular and intramolecular hydrogen bonds represent the internal structure, control the mechanical properties of cellulose and the behaviour of cellulose materials caused by water change [67, 169]. Water molecules diffuse into the non-crystalline regions when it is brought into contact with cellulose. The cellulose structures swell and form new hydrogen bonds between the water molecules and OH groups [168, 170].

Olsson *et al.* reported that the peak at 3200 cm^{-1} may be associated with more strongly bound water, directly binding with the hydrogen bonds of the OH groups of the cellulose and hemicellulose [166]. The peak at 3600 cm^{-1} is associated with more loosely bound water, indirectly binding with hydrogen bonds of the OH groups of the cellulose *via* other water molecules [166]. Ping *et al.* found that the peaks at 3280 and 3400 cm^{-1} were associated with a lower and higher water content, respectively [167, 171].

Tashiro and Kobayashi found that the peak in the range of 3309-3308 cm^{-1} and 3486-3315 cm^{-1} were associated with intermolecular and intramolecular hydrogen bonds, respectively [171].

For cellulose I, the intramolecular bonding at O(2)H-O6 and O(3)H-O5 are associated with the wavenumber around 3460 and 3340 cm^{-1}, respectively. Meanwhile, the intermolecular hydrogen bonding at O(3)H-O6 is associated to the wavenumber around 3230 cm^{-1} [168, 172]. For cellulose II, the associations of the peak to intramolecular and intermolecular hydrogen bonds are still unidentified. Carillo *et al.* reported that there are three OH stretching intramolecular hydrogen bonds for cellulose II which are at 3488, 3447, and 3175 cm^{-1}. Marchessault and Liang interpreted that the peak at 3305 and 3488 cm^{-1} are associated with intermolecular and intramolecular hydrogen bonds, respectively [173].

The intermolecular hydrogen bond has a lower wavenumber than the intramolecular hydrogen bond [167]. This result is expected due to the weaker intermolecular hydrogen bond than the intramolecular hydrogen bond. At low water content, the bound water is expected to affect the vibration of the intermolecular hydrogen bonding and form a new hydrogen bonding between the water molecules and OH groups of the cellulose [166]. At high water content, the free water is expected to affect the vibration of the intramolecular hydrogen bonding and form a new hydrogen bonding between the water molecules and OH groups of the cellulose [166]. The vibration peak at 3348 cm^{-1} increases to a higher wavenumber with the increasing water content and straining condition [174]. A weakening of intra- and intermolecular hydrogen bond probably changes the vibrational energy of the whole cellulose chain and thus decreases the 1160 cm^{-1} band (C-O-C vibration) to a lower wavenumber [166, 174, 175]. The increase of water content reduces the E values that are strongly governed by the intramolecular hydrogen bond [171].

2.4.5 Phase transformation

Nakamura *et al.* suggested that three different kinds of water appeared as absorbed water in cellulose: (i) free water (Peak I), (ii) freezing bound water (Peak II), and (iii) non-freezing

bound water [144]. For cellulose II, Peak I appeared when the amount of water in cellulose exceeded 23% at 255 K [144]. Peak II was larger than for cellulose I and was found at a higher temperature for cellulose II. The CrI was observed between 42.0 to 46.0% for cellulose II. The findings revealed that water molecules in the amorphous region of cellulose had a strong relationship with the bound water content [144].

The crystallinity of cellulose increased with the increasing water content [176-180]. Creely and Tripp explained the differences of WAXD diffractograms between high water content (100% RH) and low water content (0% RH) [176]. The lower area between the (002) and $(10\bar{1})$ peak associated with the amorphous component was observed at higher water content [176]. Sun *et al.* anticipated that the increase in CrI was due to the increase of molecular mobility, allowing disordered chains to slot into the correct crystal orientation [180]. The presence of water concentrates in the amorphous region raised the water activity.

However, other previous studies reported that some of the CrI value of cellulose decreased as the water content increased [144, 181-185]. The decreasing intensity was observed from WAXD diffractograms at (002), (101) and $(10\bar{1})$ peaks as the water content decreased [184]. The amorphous chain of cellulose took a more released and expanded arrangement in the presence of water molecules, breaking the hydrogen bonds in the crystalline region [184]. The increasing amorphous region due to the presence of water could be observed from the increase of non-freezing water as a function of water content and the angle representing freezing water should be below 45° [184]. The changes of enthalpy for cellulose suggested that the amorphous region of cellulose changed gradually to a more random arrangement with the increasing water content and it then levelled off with the presence of free water [184]. The moles of bound water (M_b) and bound water in amorphous (M_{ba}) per glucose unit could be determined [144]. The M_b

value was inversely proportional to the degree of crystallinity. However, the M_{ba} value was constant as a function of the degree of crystallinity.

Ray reported that there was an increase in total scattering with the increase of water content [181]. The integrated area due to crystalline scatter and amorphous height decreased and increased, respectively, with water content [181]. The presence of free water was observed as a shoulder in the range of 26-28° from WAXD diffractograms as the water content was increased [184]. However, the shoulder did not appear for cellulose containing only bound water. Whether the fraction of the crystalline matter constitutes the paracrystalline regions is yet to be confirmed [181]. NMR can be used to identify the crystalline, paracrystalline and non-crystalline regions.

2.4.6 Creep behaviour

The effects of water content on the mechanical properties of bio-based materials have been widely studied [160, 186-188]. In reality, many materials and structures experience changing hygrothermal conditions. The effects of water on static materials and structures depend on climatic conditions, time of the day, and season of the year [189]. Besides these factors, the effects of water on moving materials and structures also depend on the speed of the structure in relative to the air and the geographical locations the structure is travelling through [186]. For example, the environment of an airplane experience will involve a substantial humidity and moisture absorption fluctuation [189, 190].

From previous studies, creep strain of paper increases as the water content increases (by increasing the relative humidity (RH)). Creep strain is observed under two conditions: (i) constant RH and (ii) cyclic RH. The creep strain for cyclic RH was significantly higher than for the constant RH [160, 186-188]. Adriana *et al.* reported that an increase in creep strain of Kraft and Clupak papers about 120 – 180% under a constant RH of 50%, as compared to a dry

nitrogen atmosphere [160]. An increase in creep compliance about 17 – 19% was also observed with the increasing temperature in a range of 40 – 80 °C [160]. Nunez *et al.* reported that the creep strain of woodflour reinforced polypropylene composites at temperatures of 50 and 80 °C are 2.15 and 3.93 times higher than the creep strain at 20 °C, respectively [191]. Wang *et al.* stated that water molecules diffused into a fibre, breaking its original hydrogen bonds [186]. This hydrogen breakage resulted in a temporary reduction of the rigidity of the material, therefore increasing in deformation under the action load. Water molecules could also bridge between the cellulose chains after the interruption of the interchain bonds. Therefore, an increase in the diameter of the fibre would be expected due to swelling.

Numerous mathematical models have been proposed to describe creep behaviour of polymers including of Schapery and Bürger models. Schapery model is used to described the non-linear creep behaviour. This model is based on irreversible thermodynamic principles and have shown to accurately describe creep performance [192, 193]. On the other hand, a creep behaviour can be represented by simple rheological model, if the material is tested in the linear viscoelastic range. A combination of viscous and elastic components is known as the Bürger model that has been reported to give a satisfactory representation of the creep compliance [194].

Chapter 3

Experimental procedures

3.1 Experimental materials

Cellulose fibre used in this work was based on a woven rayon fibre textile (Cordenka^{TM} K2/2 twill weave, areal weight = 450 g/m^2, thickness = 0.55 mm) of regenerated cellulose in the form of cellulose II (Figure 3.1). The crystallinity of rayon was reported to be in the range of 18 to 45% [195]. The textile was based on a multifilament yarn (Cordenka 700, 1840 dtex, f 1000). The basic properties of a single filament of the Cordenka fibre (as-received) are given below (Table 3.1) [196].

Table 3.1 Properties of rayon fibre (Cordenka 700) [196].

No	Specifications	Single filament of rayon fibre
1	Filament diameter (μm)	12
2	Tensile strength (MPa)	830
3	Young's modulus (GPa)	20
4	Strain to failure (%)	13
5	Density (g/cm^3)	1.5
6	Hygroscopic at 65% RH (%)	13

The ILs, 1-butyl-3-methylimidazoliun acetate (BmimAc) with a purity of > 95%, (BASF, Ludwigshafen, Germany) and aqueous NaOH/urea solution were used as cellulose solvents. The aqueous NaOH/urea solution was prepared by mixing 7 wt.% NaOH, 12 wt.% urea (chemicals of analytical grade, purchased from Sigma Aldrich) and 81 wt.% distilled water in

a glass beaker and stirred with a magnetic stirrer at room temperature until a clear solution was observed, referred to as NaOH/urea.

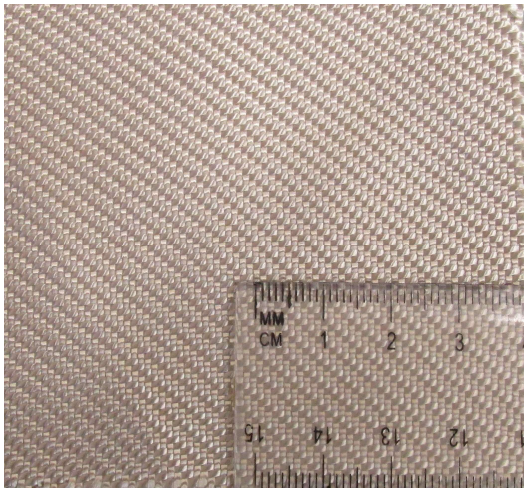

Figure 3.1 As-received woven textile containing multifilament rovings (Cordenka 700) textile.

3.2 Fabrication and processing of all-cellulose composites

An introduction to solvent infusion processing (SIP) was provided in the literature review (Chapter 2) (Section 2.2.3). The fabrication of ACCs was modified based on the type of solvent to be used. All composites were prepared using rectilinear infusion during SIP (Figure 3.2).

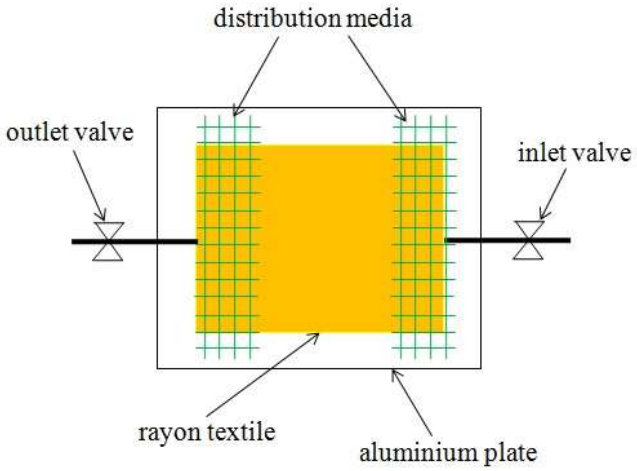

Figure 3.2 A schematic of the top view of the set-up for rectilinear infusion during SIP.

3.2.1 Solvent infusion processing using ionic liquid

The as-received textile was cut into a square shape (120 (*l*) × 120 (*w*) × 55 (*h*) mm). The textile was vacuum dried in a vacuum oven at 80 °C for 24 h prior to processing. The weight of a single layer of the textile after the drying process was 5.0 ± 0.2 g. The IL, BmimAc (BASIONIC BC 02^{TM} supplied by Sigma-Aldrich, St. Louis, USA) was used to dissolve the rayon fibre textile. BmimAc was dried in a vacuum oven at 80 °C for 5 days prior to the usage.

Two flat aluminium plates (270 (*l*) × 270 (*w*) × 2 (*h*) mm) were used as moulds during SIP. A sealant or 'tacky' tape was placed around the edge of the mould to seal the vacuum bag. An outlet valve was connected to the pressure gauge and vacuum pump. Excess solvent was trapped in a beaker. The solvent was introduced to the textile *via* the inlet valve. The laminate stack was assembled by placing the dry textile between two sheets of perforated plastics film (140 (*l*) × 140 (*w*) mm) to improve the distribution of IL through the textile. Distribution media was also used to encourage a uniform flow of the IL across the textile surface. A vacuum bag (300 (*l*) × 300 mm (*w*)) was placed over the laminate stack prior to the infusion process.

Prior to SIP, the assembly was sealed to minimise air entrapment that created voids in the final ACC. Once the mould setup was sealed, a vacuum pressure was applied to the textile. Prior to infusion, vacuum was applied for 5 - 10 min to ensure that no leaks were present. The pressure gauge was monitored until a constant vacuum pressure (88 kPa) was achieved. This vacuum pressure delivered a driving force for the IL to impregnate the textile, while maintaining a compressive force to the textile. The inlet valve was opened to introduce the IL to the textile. The inlet valve was closed when the textile was completely wetted by the solvent. A hot press (Gibitre Instruments, Bergamo, Italy) was used for the dissolution stage of the process. The assembly was placed in the hot press for a specified t_d, T_d, and P_{HP} according to Table 4.5 (subchapter 4.3.1).

Following dissolution, the partially dissolved textile was then removed from the mould and clamped between two aluminium plates (150 (*l*) × 150 (*w*) × 2 (*h*) mm). The partially dissolved textile was then immersed in distilled water in order to regenerate the dissolved cellulose. The distilled water was replaced every 6 h over the first day to ensure rapid removal of the solvent, and replenished once daily over the second and third days. It has been reported that the completion of the solvent removal of ionic liquid and NaOH by washing the ACC laminates in distilled water is indicated by no further increase in conductivity of the washing bath after a total washing time of 48 h in four washing cycles [197]. The regenerated lamina was then wiped to remove excess water. The final step of drying was carried out using the hot press. The drying process was carried out with a constant drying temperature of 60 °C at a drying pressure of 0.1 MPa for 2 days. Upon completion of the drying process, a consolidated ACC was formed (Figure 3.3). Samples were kept in sealed plastic bags prior to further characterisation.

3.2.2 Solvent infusion processing using NaOH/urea

The use of SIP with a NaOH solvent system required some modifications to using BmimAc due to the requirement for a subambient temperature during the dissolution process. Textile was cut into 120 (*l*) × 120 (*w*) mm layers and conditioned at 20 °C and 20% RH for 12 h prior to processing. The average weight of the single layer textile after the conditioning process was 5.3 ± 0.1 g. The aqueous solvent system was based on 7 wt.% NaOH/12 wt.% urea/81 wt.% distilled water and stored at -12 °C.

The conditioned textile was placed in the same mould setup as BmimAc. The mould setup was precooled in the freezer at - 12 °C prior to the infusion process and then removed from the freezer for SIP. Following infusion, the SIP assembly was immersed into a cooling bath held at - 12 °C, leading to a partial dissolution of the textile. The partially dissolved textile was

carefully removed from the mould setup and placed in the hot press at 21 °C for 15 min under pressure. It was then washed in distilled water for a minimum of 72 h, with replacing of the distilled water. Then, the drying process was performed at the hot press. The drying process was the same as the one used for BmimAc-based SIP. Following drying, the partially dissolved textile formed a lamina of ACC (Figure 3.3). Materials were stored in a sealed plastic bag prior to further characterisation.

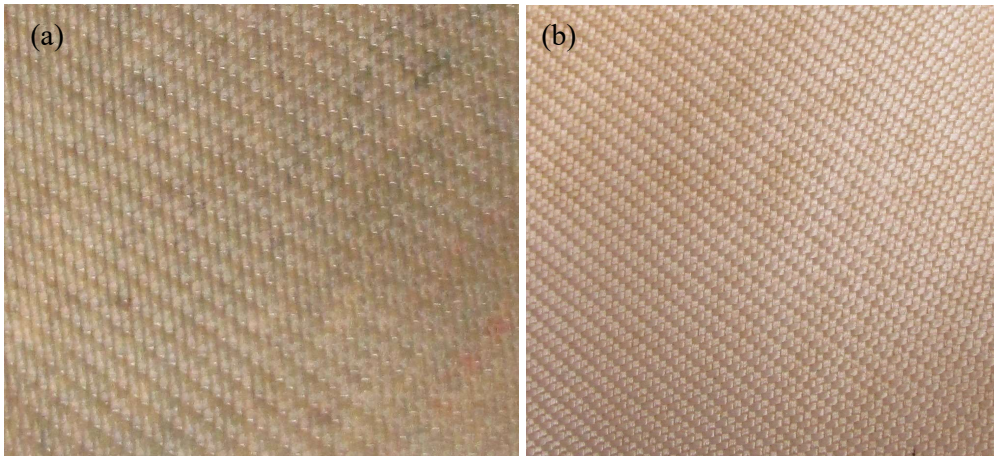

Figure 3.3 An ACC lamina produced *via* (a) BmimAc-based SIP and (b) NaOH/urea-based SIP, respectively.

3.3 Materials characterisation

3.3.1 Microstructural characterisation

Microscopy samples were cut into a rectangular shape with dimensions of 15 (l) × 6 (w) mm and mounted in an Epofix cold-setting embedding resin (Electron Microscopy sciences, Hatfield, PA, USA) according to the ASTM E3-11. Micrographs were obtained from the reflected light microscopy using an Olympus DP-70 Controller digital camera system. ImageJ

software was used to measure the fibre volume fraction (V_f), matrix volume fraction (V_m), and void volume fraction (V_v). V_f, V_m, and V_v were calculated by dividing the number of fibre, matrix, and void pixels, respectively, by the total number of pixels of the full micrograph. An example of procedure for determination of V_f and V_m is shown in Figure 3.4. The red and white colour are considered as the matrix and fibre phases, respectively.

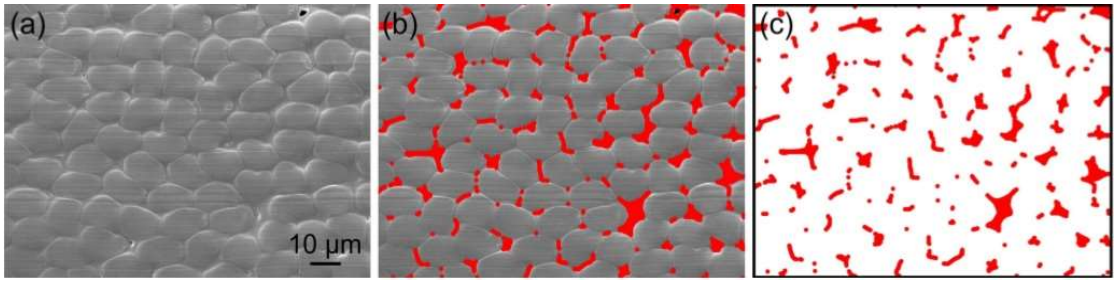

Figure 3.4 Procedure for determination of fibre and matrix volume fraction (Adapted from Dormanns [197].

The determination of the volume fraction of the fibre and matrix phases was complicated by a similar boundary contrast between the reinforcing and matrix phases in reflected light micrographs. Therefore, three reflected light micrographs were analysed for each sample using the ImageJ software. V_f value was determined by the following equation [80]:

$$V_f = \frac{\sum A_{fibre}}{\sum A_{total}} \qquad \text{Eq. 3.1}$$

where V_f is the fibre volume fraction, A_{fibre} the number of fiber pixels and A_{total} the total number of pixels of the full micrograph. V_m and V_v were determined accordingly.

Field emission scanning electron microscopy (FE-SEM) was also used for a microstructural analysis. ACC samples were cut in a wet condition with the dimension of 6 (l) × 5 (w) mm. The samples were mounted in the Epofix cold-setting embedding resin (Electron Microscopy

sciences, Hatfield, PA, USA) according to ASTM E3-11. Cross sectional surfaces of the mounted samples were prepared by cutting a thin layer away from the sample surface using a microtome (Feather Safety Razor Co. Ltd., Japan). The samples were examined using an optical microscopy to check if the cut surface was suitable for an FE-SEM examination. The samples were then dried and sputter-coated with gold for 180 s at 25 mA. Secondary electron images were obtained with a 7000FE-SEM (JOEL, Peabody, USA) using an accelerating voltage of 5 kV.

3.3.2 Determination of crystallinity index and crystallite size

An X-ray diffractometer (XRD) (XPERT-PRO, PANalytical, Almelo, Netherlands) was used to measure the phase composition and crystallinity of the ACCs. Samples were analysed in an XRD using a 1.54 Å copper X-ray source Kα radiation (λ = 1.79031 Å), with 2θ step size 0.05° over the 2θ ranged from 5 to 50°. A voltage of 40 kV and current of 30 mA were used. The details of analysis method are discussed in Chapter 4 (Section 4.2.2.1).

3.3.3 Fourier transform infrared spectroscopy

The ACCs samples were determined with an attenuated total reflectance-Fourier transform infrared (ATR-FTIR) spectroscopy. The spectrum was recorded using an FTIR spectrometer (BrukerOptik GmbH, Ettingen, Germany). The detector was the deuterated triglycine sulfate (DTGS) with a single-reflection diamond ATR sampling module (Platinum ATR QuickSnap™). Air was used as a background for all scanned samples. The scanning range was from 4000 to 600 cm^{-1} with a scanning resolution of 4 cm^{-1} and 64 scans per sample. The results were analysed using the OPUS 6.0 suite (Bruker) software.

3.3.4 Dynamic mechanical analysis

A dynamic mechanical analyser (DMA) Q800 from TA Instruments was used to determine the viscoelastic properties and creep behaviour of ACCs in the tension mode. The samples were cut into a dimension of 20 (l) × 8 (w) × 0.4-0.5 (h) mm. The samples were then conditioned at 23 °C and 50% RH for a week prior to the test. The samples were tested at a frequency of 1 Hz, heating rate of 2 °C/min, and over the temperature range of 30 to 350 °C. TA Universal Analysis and OriginPro 8.5 software were used to analyse the as-received data.

3.3.5 Tensile testing

Tensile testing was used to characterise the mechanical properties of the ACC laminate. Tensile testing was carried out according to ASTM D3039 [198], using an MTS Criterion Model C43.104 load frame equipped with a 2.5 kN load cell. A constant cross head speed of 2 mm/min was used. Rectangular coupons with the dimensions of 100 (l) × 10 (w) mm and gauge length of 35 mm were prepared. Non-contact measurement of the strain was performed using a video extensometer (MTS FVX, TestWorks Axial/Transverse Video Extensometer with Video Traction software). The average E, ultimate tensile strength (UTS), and strain at failure (ε_f) were determined from five replicates.

Chapter 4

Processing-properties relationships of all-cellulose composites

4.1 Introduction

The optimisation of many products and processes has driven manufacturers to use a Design of Experiments (DOE) approach in order to improve quality and reduce costs. Improved quality and cost reductions in order to remain competitive in world markets are achieved by means of design optimisation [199]. Taguchi method is a philosophy for quality control used in the manufacturing industries. Constructed tables (*aka* orthogonal array (OA)) are used in Taguchi DOE, making it an easy yet effective mode of optimising products [199]. The use of DOE approach has not yet been implemented in the processing and production of ACC according to the review from the previous studies [16, 17, 21, 22, 25, 87]. Therefore, a lot of experiments have to be arranged in order to achieve the similar results without DOE.

The main objective of using DOE in this present study was to determine the factorial effect of these control factors on the mechanical properties of ACCs produced *via* BmimAc and NaOH/urea. The CrI, crystallite size, V_f, V_m, V_v, viscoelastic properties, density (ρ), and microstructure images analyses were then investigated. Taguchi DOE was designed using the control factors and levels that had been considered, as shown in Table 4.1 and 4.2. The selection of control factors and their levels were decided based on the previous experimental findings [16, 24, 109]. It has been reported that the mechanical properties of ACCs increase with t_d until a critical point after which the mechanical properties of ACCs may decrease due to the excessive dissolution of cellulose, resulting in an increased volume fraction of the matrix phase. Conversely, the formation of insufficient matrix phase at shorter t_d may lead to poor fibre-

matrix adhesion that decreases the mechanical properties of the final ACC [16]. It is also reported that an increase in T_d would normally decrease the viscosity of the solvent, resulting in enhanced diffusion of the solvent into the cellulose textile that leads to more uniform dissolution of the cellulosic matrix and improved mechanical properties [80]. However, degradation of the cellulose molecule may occur if T_d is too high, resulting in a decrease in the mechanical properties of ACCs [22]. For instance, cellulose is thought to be degraded by most of the cellulose-dissolving ionic liquids at temperatures above ~150 °C [200]. Huber *et al.* observed that increase in P_{HP} improves the mechanical properties of ACCs, presumably due to a more uniform distribution and consolidation of the matrix phase that surrounds the undissolved fibres and the elimination of voids [24]. However, excessive pressure may force the cellulose fibres to separate that reduce the adhesion among fibres, resulting in a decrease in the mechanical properties of ACCs [80].

4.2 Experimental procedures

4.2.1 Taguchi experimental design

Orthogonality of the Taguchi experimental design enables the isolation effects of each control factor at different levels using the *S/N* ratio [201]. In the present study, the *S/N* ratios were used in the analysis. The calculation of *S/N* ratio depends on the experimental objective: (i) higher the better, (ii) lower the better, or (iii) nominal the better [199]. Results were presented in a response table, response graph, and ANOVA, as discussed in subchapter 4.3.1 and 4.3.2. The higher the difference in the *S/N* ratio, the greater the influence that the control factor has on the mechanical properties [201].

The Pareto ANOVA and ANOVA methodologies developed by Fisher [202, 203] can be used to quantify the significance of the control factor. The Pareto ANOVA method simplifies the statistical analysis without considering the *F-test*. Although the percentage contributions can

be easily determined, the error associated within the experimentation is difficult to determine. Therefore, the ANOVA method was more favourable in this present study as it allowed the quantification of the significance of experimental factor by comparing the mean square error of the main factor against an estimate of the experimental error at a specific confidence level [202, 203].

ANOVA was performed to determine the relative influence of control factors on each of the mechanical properties [201]. The relative percentage contribution of all factors was determined by comparing the relative variance. The degrees of freedom (*f*), variance (*V*), *F*-ratio (*F*), sum of squares (*S*), and percentages of contribution (*P*) were also calculated in ANOVA [204]. The comparison of the *F* and critical Fisher ratio (F_{crit}) values can be used to identify the significant control factor in the experimental design. The *F* and F_{crit} values were determined from the (i) ratio of the factor variance to the error variance, and (ii) *F* distribution table. A highly or weakly significant control factor was judged from these events: (i) $F > F_{crit}$ or (ii) $F < F_{crit}$, respectively.

In the present study, three control factors (A, B, and C) and three levels (low (1), medium (2), and high (3)) had been determined. For the ACC produced *via* BmimAc, these three control factors included the t_d, T_d, and P_{HP} (Table 4.1). For the ACC produced *via* NaOH/urea, these three control factors included the t_d, P_{HP}, and P_{SIP} (Table 4.2).

Table 4.1 Control factors and their levels for ACC produced *via* BmimAc

Control factors	Levels		
	1	2	3
A: t_d (min)	30	60	90
B: T_d (°C)	95	105	115
C: P_{HP} (MPa)	0.25	0.5	1.0

Table 4.2 Control factors and their levels for ACC produced *via* NaOH/urea

Control factors	Levels		
	1	2	3
A: t_d (min)	15	30	40
B: P_{HP} (MPa)	0.25	0.5	1.0
C: P_{SIP} (kPa)	86.0	88.0	90.0

The number of experiments was determined using the Taguchi array selector (Table 4.3) based on the number of control factors and levels. The array allowed for each variable and setting to be tested equally. Thus, the current parametric study could be conducted using an L_9 Taguchi orthogonal array in which only 9 trials were required to complete the DOE (Table 4.4) [201, 203]. In comparison, 27 trials would be needed if a full factorial DOE was considered.

Table 4.3 Array selector

		Number of control factors			
		2	3	4	5
Number of levels	2	L_4	L_4	L_8	L_8
	3	L_9	L_9	L_9	L_{18}
	4	L_{16}	L_{16}	L_{16}	L_{16}
	5	L_{25}	L_{25}	L_{25}	L_{25}

Table 4.4 L_9 orthogonal array

Number of trials	A	B	C
1	1	1	1
2	1	2	2
3	1	3	3
4	2	1	2
5	2	2	3
6	2	3	1
7	3	1	3
8	3	2	1
9	3	3	2

In this study, the *S/N* ratio took on 'the higher the better' category for maximising the mechanical properties using Eq. 4.1 [203, 205].

$$S/N = -10\log\left(\frac{1}{n}\sum_{i=1}^{n}\frac{1}{x^2}\right) \quad \text{Eq. 4.1}$$

where n is the number of measurements in each trial and x is the mechanical properties value of E, or UTS. The unit for *S/N* ratio value is dB. The materials, solvent, and processing pathway for ACC preparation had been referred to in Chapter 3.

4.2.2 Material characterisation

Materials characterisation of the ACCs was discussed in Chapter 3, including the mechanical testing, microstructural analysis, and DMA. A detailed description of XRD, ATR-FTIR, and density measurement methods are discussed below. All the ACC samples were conditioned at 23 °C and 50% RH for 24 h prior to mechanical testing.

4.2.2.1 X-ray diffraction analyses

The Wakelin method was used to calculate CrI [206]. In this method, CrI was calculated by the ratio of the area of the crystalline peak over the area of the amorphous background, generally termed as either the subtraction or area method. The curve fitting software Fityk (GNU license) was used to generate the equation for the measured as-received and amorphous background data. The amorphous background data was calculated from the data presented by Duchemin *et al.* [207]. Equations for each fitted curve and the amorphous background were exported from the Fityk software in MATLAB (R2014a, MathWorks, USA) from 2θ (10 to 40°). The CrI value was calculated from the following equation:

$$CrI = \frac{Area_{crystalline} - Area_{amorphous}}{Area_{crystalline}} \qquad \text{Eq. 4.2}$$

From the as-received data, the crystallite size (D) can be calculated based on the Scherrer method [208]. The D was determined from the equation below.

$$D = \frac{K\lambda}{\beta \cos\theta} \qquad \text{Eq. 4.3}$$

where D is the crystal size, λ is the wavelength of X-ray, K is the Scherrer's constant, θ is the Bragg angle, and β is the full width at half of the height.

4.2.2.2 Attenuated total reflectance-Fourier transformed infrared spectroscopy

Total crystallinity index (TCI) was calculated according to Nelson *et al.* from the following equation [129].

$$\text{TCI} = \frac{\alpha_{1372cm^{-1}}}{\alpha_{2900cm^{-1}}} \qquad \text{Eq. 4.4}$$

The TCI was calculated from the absorptivity of the 1372 cm^{-1} band to the 2900 cm^{-1} band. Nelson *et al.* reported that the 1372 cm^{-1} band was assigned to the C-H bending mode and hence should not be affected by the differences in the amount of water absorbed onto the cellulose [129]. Meanwhile, the 2900 cm^{-1} band was assigned to the C-H stretching mode. The absorptivity of the 1372 cm^{-1} band was first trialled as a measure of crystallinity, although it gave a poor correlation. The method of drawing the baseline was used [129]. For the band at 2900 cm^{-1}, the intensity at the adjacent shoulder near 3000 cm^{-1} was chosen as the base. The type of instrument used in this work produced a break in the spectrum at 2800 cm^{-1} that made constructing the usual type of baseline between the transmission maximum on either side of the band to be problematic. For the band at 1372 cm^{-1}, a line was drawn between the maximum at approximately 1290 and 1410 cm^{-1}, giving a common baseline for the group of three bands that occurred in close proximity to each other and were changing simultaneously [129].

4.2.2.3 Density measurements

The ACCs density test was performed by following Archimedes' principle. An XP/XS analytical balance (Mettler Toledo, Switzerland) was used to measure the density. Distilled water was chosen as the immersion liquid. The ACCs samples were vacuum-dried at 60 °C overnight prior to the density measurements. The weight of the sample was measured in air and then completely immersed in the distilled water. Air bubbles that adhered to the samples were removed with a fine brush before determining the weight. The density was calculated based on five replicates using the following equation.

$$\rho = \frac{A}{A-B}(\rho_o - \rho_L) + \rho_L \qquad \text{Eq. 4.5}$$

where ρ is the density of sample, A is the weight of sample in air, B is the weight of sample in the auxiliary liquid (distilled water), ρ_o is the density of the auxiliary liquid ($\rho_{\text{distilled water}}$ = 1 g/cm^3), and ρ_L is the air density (0.0012 g/cm^3).

4.3 Results and discussion

4.3.1 Taguchi and statistical analysis of ACCs produced *via* BmimAc

The best combinations of control factors for E were found at medium t_d (A_2), medium T_d (B_2), and low P_{HP} (C_1) by considering the highest S/N ratio of each control factor (Figure 4.1). Therefore, the most robust setting to achieve a maximum in E was $A_2B_2C_1$, corresponding to 60 min, 105 °C, and 0.25 MPa, respectively. According to the response table (Table 4.6), t_d was the most significant control factor, followed by P_{HP} and finally T_d. The highest E and UTS were found in Trial 6 (Table 4.5). The control factors for t_d and P_{HP} in Trial 6 corresponded with the best combination, identified from the S/N ratio analysis. However, the small difference

between the maximum and minimum *S/N* ratio for P_{HP} and T_d indicated that the effect of these control factors on *E* was insignificant.

Table 4.5 Experimental results for Young's modulus and ultimate tensile strength with their corresponding *S/N* ratios

Trials	Control factors			*E* (GPa)	*S/N* (dB)	UTS (MPa)	*S/N* (dB)
	t_d (min) A	T_d (°C) B	P_{HP} (MPa) C				
1	30	95	0.25	5.79 (0.04)	15.25	75.30 (0.17)	-22.46
2	30	105	0.5	5.86 (0.11)	15.36	74.20 (0.20)	-22.59
3	30	115	1.0	5.45 (0.15)	14.73	73.90 (0.15)	-22.63
4	60	95	0.5	7.10 (0.18)	17.03	76.90 (0.25)	-22.28
5	60	105	1.0	7.21 (0.19)	17.16	77.20 (0.18)	-22.25
6	60	115	0.25	7.32 (0.08)	17.29	77.65 (0.11)	-22.20
7	90	95	1.0	6.90 (0.14)	16.78	72.50 (0.14)	-22.79
8	90	105	0.25	6.80 (0.08)	16.65	71.80 (0.19)	-22.88
9	90	115	0.5	6.79 (0.12)	16.64	71.20 (0.12)	-22.95

*() = standard deviation

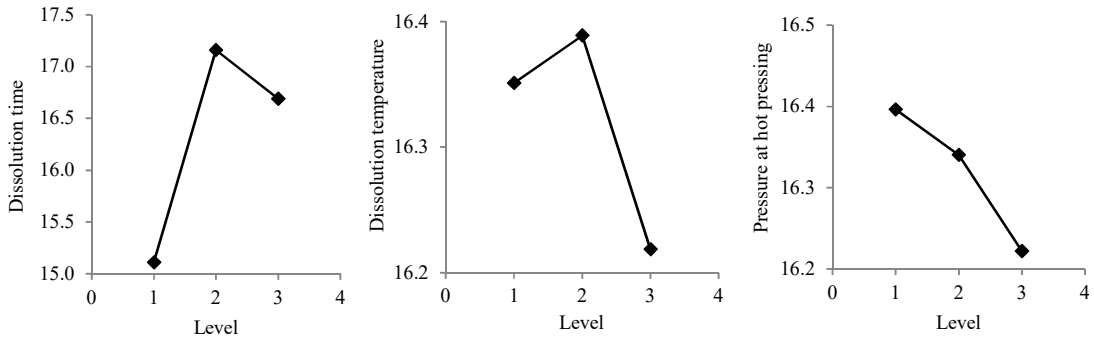

Figure 4.1 Response graphs for Young's modulus, showing the *S/N* ratio as a function of the control factor level.

Table 4.6 Response table for Young's modulus

Level	Control factors		
	t_d (min)	T_d (°C)	P_{HP} (MPa)
1	15.11	16.35	16.40
2	17.15	16.38	16.34
3	16.68	16.21	16.22
Max	17.15	16.38	16.40
Min	15.11	16.21	16.22
Differences	2.04	0.17	0.18
Rank	1	3	2

The t_d had the highest percentage of contribution (P = 96.67%) (Table 4.7). The F value was higher than F_{crit}, indicating the larger effect of t_d on E. Meanwhile, P_{HP} had the lowest F ratio and P values, regardless of the effect of pooled error. The F value for P_{HP} was lower than F_{crit}, indicating little effect on E. The T_d had the lowest F ratio, requiring it to be pooled with a random error related with the experimentation. Thus, t_d was the dominant control factor for E (Tables 4.6 and 4.7).

Table 4.7 ANOVA results for Young's modulus

Control factor	*f*	*S*	*V*	*F*	*P* (%)	Significance
t_d	2	3.71	1.85	41.08	96.6	High
T_d	-	-	-	-	-	No
P_{HP}	2	0.02	0.01	0.22	0.51	Weak
Pooled Error	4	0.10	0.05	1.19	2.79	-
Total	8	3.84	-	-	100.00	-

Note: $F_{crit\ \text{at}\ 2,4} = 6.94$

The highest *S/N* ratio for UTS was associated with a medium t_d (A_2), low T_d (B_1), and low P_{HP} (C_1) (Figure 4.2). The combination of $A_2B_1C_1$ corresponded to the control factor levels of 60 min, 95 °C, and 0.25 MPa. However, the best T_d for UTS was 95 °C, in contrast to 105 °C for *E*. t_d was the most significant control factor for maximising the UTS, followed by P_{HP} and T_d (Table 4.8). However, a small difference between the maximum and minimum *S/N* ratios for P_{HP} and T_d indicated that the effect of these control factors on the UTS was insignificant. The same result was found for *E* (Table 4.6). The *P* for P_{HP} and T_d were 2.16 and 1.50%, respectively, before pooling with the experimental error.

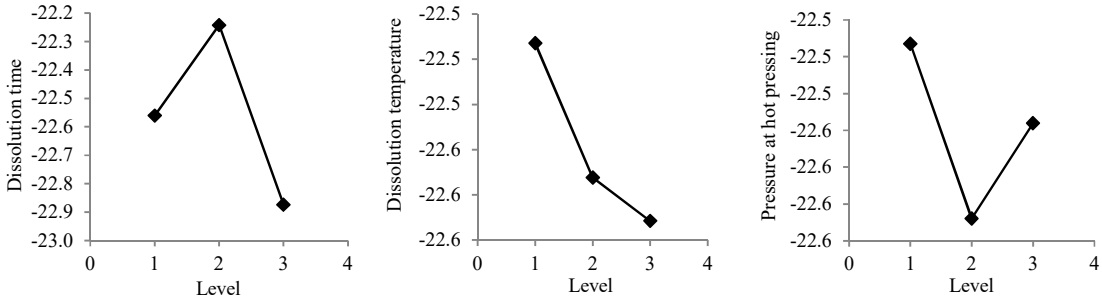

Figure 4.2 Response graphs for ultimate tensile strength, showing the *S/N* ratio as a function of the control factor level.

Table 4.8 Response table for ultimate tensile strength based on *S/N* ratio

Level	Control factors		
	t_d (min)	T_d (°C)	P_{HP} (MPa)
1	-22.56	-22.51	-22.51
2	-22.24	-22.57	-22.60
3	-22.87	-22.59	-22.55
Max	-22.24	-22.51	-22.51
Min	-22.87	-22.59	-22.60
Differences	0.63	0.07	0.09
Rank	1	3	2

The t_d has the highest P (95.20%) (Table 4.9). This result was consistent with the F value which was higher than F_{crit}. The changes in P_{HP} and T_d had no substantial effect on UTS. The smallest value of F ratio for T_d was pooled with a random error related with the experimentation. Therefore, the P for P_{HP} was 2.16% which was considered insignificant. It was concluded that t_d was the dominant control factor for UTS, corresponding to the *S/N* ratio (Table 4.8).

Table 4.9 ANOVA results for the ultimate tensile strength

Control factor	f	S	V	F	P (%)	Significance
t_d	2	4.40×10^{-5}	2.20×10^{-5}	84.38	95.20	High
T_d	-	-	-	-	-	No
P_{HP}	2	1.00×10^{-6}	5.01×10^{-7}	1.92	2.16	Weak
Pooled Error	4	1.21×10^{-6}	6.08×10^{-7}	2.33	2.63	-
Total	8	4.62×10^{-5}	-	-	100.00	-

Note: $F_{crit \text{ at } 2,4} = 6.94$

The findings showed that the best t_d of 60 min was required to maximise the E and UTS of ACCs produced *via* BmimAc. Soykeabkaew *et al.* reported that a shorter t_d led to poor interfacial bonding between fibres in the final composite [16]. However, an extended t_d resulted in excessive dissolution of the fibre core, which can significantly reduce the mechanical properties and lead to the degradation of the cellulose [16, 22]. Duchemin *et al.* reported that the best t_d of 80 min was found to increase the mechanical properties of ACC produced *via* BmimCl [22]. The shorter t_d for cellulose II compared to cellulose I was expected due to the variability of CrI. Klemm *et al.* reported that cellulose I had higher CrI than cellulose II [65]. CrI of cellulose I ranged between 43 and 80%, while that of cellulose II between 34 and 43%, resulting in a more rigid structure for cellulose I.

P_{HP} was expected to encourage a homogeneous distribution of the dissolved cellulose during SIP, helping to fill any voids in the structure. However, high pressure resulted in the compaction of cellulose fibre that may reduce the mechanical properties of ACCs. In this study, a P_{HP} of 0.25 MPa was found to be the best level of P_{HP} as shown in Figure 4.1 and 4.2. This result corresponded closely with findings by Huber *et al.* (0.20 MPa) [17]. The use of Taguchi

DOE helps in determining the best combination of control factors and levels in order to achieve excellent mechanical properties.

4.3.2 Taguchi and statistical analysis of ACCs produced *via* NaOH/urea

The best combination of control factors for E was found at low t_d (A_1), medium P_{HP} (B_2), and low P_{SIP} (C_1) by considering the highest S/N ratio values of control factor (Figure 4.3). Therefore, the most reliable setting to achieve a maximum in E was $A_1B_2C_1$, corresponding to 15 min, 0.5 MPa, and 86.0 kPa, respectively. According to the response table (Table 4.11), t_d was the most dominant control factor, followed by P_{HP} and finally P_{SIP}. The highest E and UTS was found in Trial 2 (Table 4.10). The control factors for t_d and P_{HP} in Trial 2 corresponded with the best combination, identified from the *S/N* ratio analysis. However, the small difference between the maximum and minimum *S/N* ratio for P_{HP} and P_{SIP} indicated that the effect of these control factors on E was insignificant.

Table 4.10 Experimental results for Young's modulus and ultimate tensile strength with their corresponding *S/N* ratios

Trials	Control factors			*E* (GPa)	*S/N* (dB)	UTS (MPa)	*S/N* (dB)
	t_d (min) (A)	P_{HP} (MPa) (B)	P_{SIP} (kPa) (C)				
1	15	0.25	86.00	1.42 (0.10)	3.05	25.63 (0.06)	-31.83
2	15	0.50	88.00	1.49 (0.08)	3.44	27.69 (0.16)	-31.15
3	15	1.00	90.00	1.38 (0.10)	2.78	24.33 (0.10)	-32.28
4	30	0.25	88.00	1.03 (0.09)	0.21	20.13 (0.19)	-33.93
5	30	0.50	90.00	1.12 (0.13)	0.98	19.53 (0.13)	-34.19
6	30	1.00	86.00	1.10 (0.09)	0.79	20.01 (0.25)	-33.97
7	40	0.25	90.00	0.87 (0.17)	-1.21	17.85 (0.17)	-34.97
8	40	0.50	86.00	0.95 (0.08)	-0.45	18.25 (0.20)	-34.77
9	40	1.00	88.00	0.81 (0.15)	-1.83	17.21 (0.15)	-35.29

*() = standard deviation

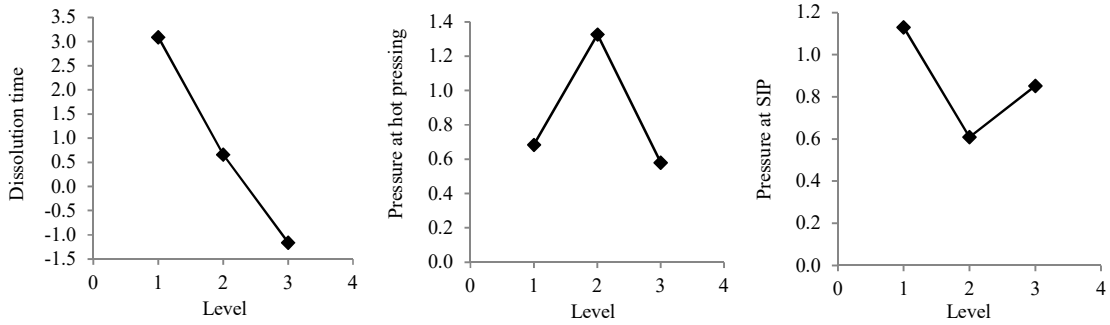

Figure 4.3 Response graphs for Young's modulus, showing the *S/N* ratio as a function of the control factor level.

Table 4.11 Response table for Young's modulus

Level	Control factors		
	t_d (min)	P_{HP} (MPa)	P_{SIP} (kPa)
1	3.08	0.68	1.12
2	0.66	1.32	0.60
3	-1.16	0.57	0.85
Max	3.08	1.32	1.12
Min	-1.16	0.57	0.60
Differences	4.25	0.74	0.52
Rank	1	2	3

The highest *P* for t_d was 95.73% (Table 4.12). The *F* value was higher than F_{crit}, presenting the larger effect of t_d on *E*. Meanwhile, P_{HP} had the lowest *F* ratio and *P* values. The *F* value for P_{HP} was lower than F_{crit}, indicating little effect on *E*. The P_{SIP} had the lowest *F* ratio, requiring it to be pooled with a random error related with the experimentation. Thus, t_d was the dominant control factor for *E*, corresponding to the *S/N* ratio (Tables 4.11 and 4.12).

Table 4.12 ANOVA results for Young's modulus

Control factor	f	S	V	F	P (%)	Significance
t_d	2	0.47	0.23	419.11	95.73	High
P_{HP}	2	0.01	0.01	13.42	3.06	Weak
P_{SIP}	-	-	-	-	-	No
Pooled error	4	0.01	2.90×10^{-3}	5.24	1.19	-
Total	8	0.48	-	-	100.00	-

Note: $F_{crit \text{ at } 2,4} = 6.94$

The best combination of control factors for UTS was found at low t_d (A_1), medium P_{HP} (B_2), and medium P_{SIP} (C_2) (Figure 4.4). The combination $A_1B_2C_2$ corresponded to the control factor levels of 15 min, 0.5 MPa, and 88.0 kPa, respectively. However, the best P_{SIP} for UTS was 88.0 kPa, in contrast to 86.0 kPa for E. According to the response table (Table 4.13), t_d was the most significant control factor for maximising the UTS, followed by P_{HP} and P_{SIP}. However, a small difference between the maximum and minimum S/N ratios for P_{HP} and P_{SIP} indicated that the effect of these control factors on UTS was insignificant. The same result was found for E (Table 4.11). The P for P_{HP} and P_{SIP} were 2.28 and 1.68%, respectively, before pooling with the experimental error (Table 4.14). The dominant effect of t_d on E and UTS is due to the narrow range of other control factors (*e.g.* P_{HP} and P_{SIP}).

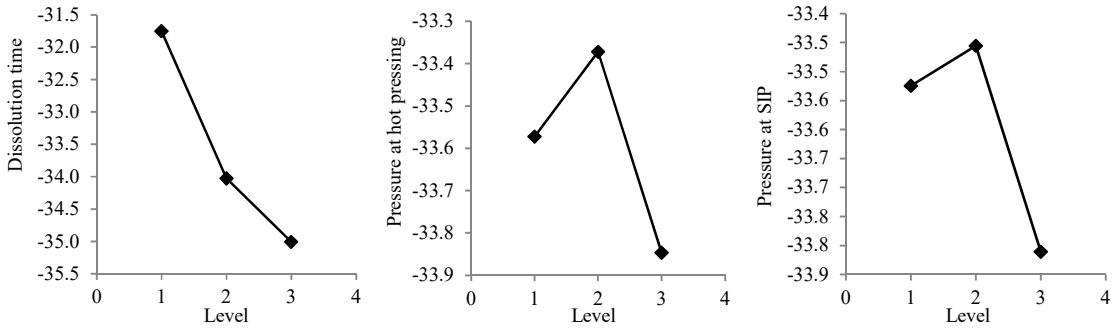

Figure 4.4 Response graphs for ultimate tensile strength.

Table 4.13 Response table for ultimate tensile strength

Level	Control factors		
	t_d (min)	P_{HP} (MPa)	P_{SIP} (kPa)
1	-31.75	-33.57	-33.52
2	-34.02	-33.37	-33.45
3	-35.00	-33.84	-33.81
Max	-31.75	-33.37	-33.45
Min	-35.00	-33.84	-33.81
Differences	3.25	0.47	0.35
Rank	1	2	3

The highest *P* for t_d was 94.22% (Table 4.14). The *F* value for t_d was higher than F_{crit}, indicating the strong effect of t_d on UTS. The P_{HP} was considered as a weak control factor due to its lower *P* values and $F < F_{crit}$. The P_{SIP} had to be pooled with the experimental error because it had the smallest *F* ratio value. Thus, t_d was the dominant control factor that was also consistent to the *S/N* ratio (Tables 4.13 and 4.14).

In this study, t_d of 15 min was found to be the best time to dissolve the rayon textile *via* the NaOH/urea solution. Qi *et al.* reported that cellulose can be dissolved at as short as 2 min in 7 wt.% NaOH/12 wt.% urea/81 wt.% distilled water solution [108]. A vigorous stirring and longer stirring times would increase the cellulose solubility [112]. However, stirring was not possible to be implemented in the SIP setup. Regenerated cellulose fibres have a semicrystalline character with less ordered amorphous regions in line with crystallites along the fibre axis [209]. Dissolution occurs in the amorphous regions, constituting connectors between the crystallites, thereby decreasing the fibre strength. The longer t_d imparts an extensive breakdown of the amorphous regions, decreasing the strength of ACCs. A decrease in fibre strength of lyocell was reported with the NaOH treatment [210]. Jan *et al.* reported that the best t_d for 2 laminae of ACC was 5 min [109]. The shorter t_d was expected due to the additional cooling system during the infusion process. Apart from that, the slightly higher t_d found in this present study may be expected due to the narrow range of t_d. The effect of P_{HP} on mechanical properties is discussed in subchapter 4.3.1.

Table 4.14 ANOVA results for ultimate tensile strength

Control factor	f	S	V	F	P (%)	Significance
t_d	2	6.13×10^{-6}	5.30×10^{-5}	103.62	94.22	High
P_{HP}	2	2.56×10^{-6}	1.28×10^{-6}	2.51	2.28	Weak
P_{SIP}	-	-	-	-	-	No
Pooled error	4	3.94×10^{-6}	1.97×10^{-6}	3.84	3.49	-
Total	8	1.12×10^{-4}	-	-	100.00	-

Note: $F_{crit\ at\ 2,4} = 6.94$

4.3.3 Relationship between control factors and mechanical properties

The relationships between control factors and the mechanical properties were performed using multiple regression analysis (MRA). Hodgskinson *et al.* discussed the nature of power law relating the density on *E* values [211]. The equations for ACCs produced *via* BmimAc (Eq. 4.6) and NaOH/urea (Eq. 4.7) were expressed in terms of the power series equations.

$$Y = C.(t_d)^{\alpha}.(T_d)^{\beta}.(P_{HP})^{\gamma} \quad \text{Eq. 4.6}$$

$$Y = C.(t_d)^{\alpha}.(P_{HP})^{\beta}.(P_{SIP})^{\gamma} \quad \text{Eq. 4.7}$$

where Y is the mechanical properties (E or UTS) and C, α, β, and γ, are the empirical model coefficients. The E and UTS equations for ACC produced *via* BmimAc were expressed in Eq. 4.8 and 4.9, respectively. The E and UTS equations for ACC produced *via* NaOH/urea were expressed in Eq. 4.10 and 4.11, respectively.

$$E = 10^{0.6492} \times (t_d)^{0.1841} \times (T_d)^{-0.0778} \times (P_{HP})^{-0.0144},\ R^2 = 0.62 \quad \text{Eq. 4.8}$$

$$\text{UTS} = 10^{-0.9917} \times (t_d)^{-0.0235} \times (T_d)^{-0.0477} \times (P_{HP})^{-0.0035},\ R^2 = 0.52 \quad \text{Eq. 4.9}$$

$$E = 10^{2.1079} \times (t_d)^{-0.4811} \times (P_{HP})^{-0.0086} \times (P_{SIP})^{-0.7122},\ R^2 = 0.94 \quad \text{Eq. 4.10}$$

$$\text{UTS} = 10^{0.2564} \times (t_d)^{-0.3813} \times (P_{HP})^{-0.0227} \times (P_{SIP})^{-0.7211},\ R^2 = 0.95 \quad \text{Eq. 4.11}$$

For ACC produced *via* NaOH/urea, the coefficients of determination (R^2) for *E* and UTS were 0.94, and 0.95, respectively. For ACC produced *via* BmimAc, the R^2 for *E* and UTS were 0.62, and 0.52, respectively. Thus, the equations for ACC produced *via* NaOH/urea were expected to be more reliable than the ACC produced *via* BmimAc in estimating the *E* and UTS. Further justification regarding these findings will be discussed in subchapters 4.3.4 and 4.3.5.

4.3.4 Validation test

Validation tests were carried out to observe the variation between the experimental and empirical model. A close agreement between empirical model and experimental values was observed, indicating the accuracy of the model developed for the ACC produced *via* BmimAc (Figures 4.5 and 4.6) and NaOH/urea (Figures 4.7 and 4.8). For the ACC produced *via* BmimAc, the average percentage error for *E* and UTS were 5.31 and 1.66%, respectively. For ACC produced *via* NaOH/urea, the average percentage error calculated on *E* and UTS were 4.58 and 2.01%, respectively. Overall, the percentage errors for *E* and UTS between the ACCs produced *via* BmimAc and NaOH/urea were consistent. The percentage error for *E* was higher than UTS for both solvents.

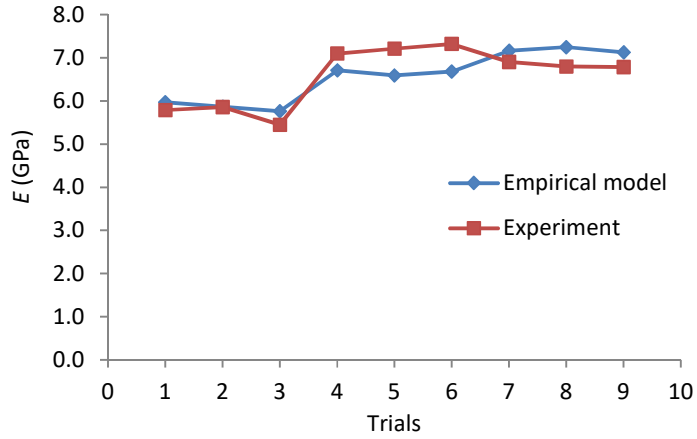

Figure 4.5 Variations of experimental and calculated values for Young's modulus (ACC produced *via* BmimAc).

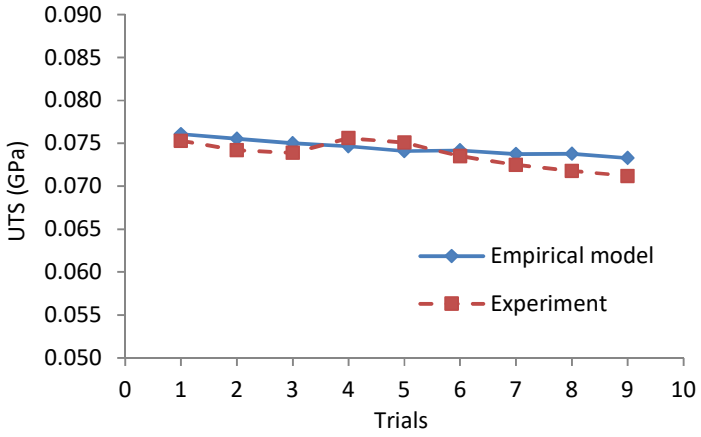

Figure 4.6 Variations of experimental and calculated values for ultimate tensile strength (ACC produced *via* BmimAc).

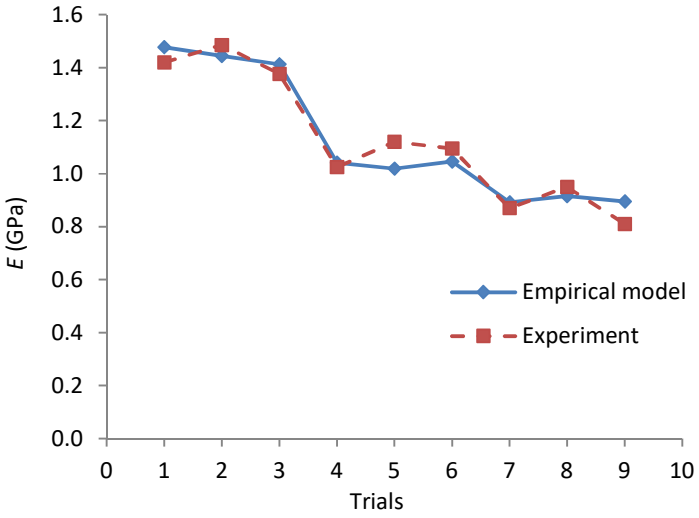

Figure 4.7 Variations of experimental and calculated values for Young's modulus (ACC produced *via* NaOH/urea).

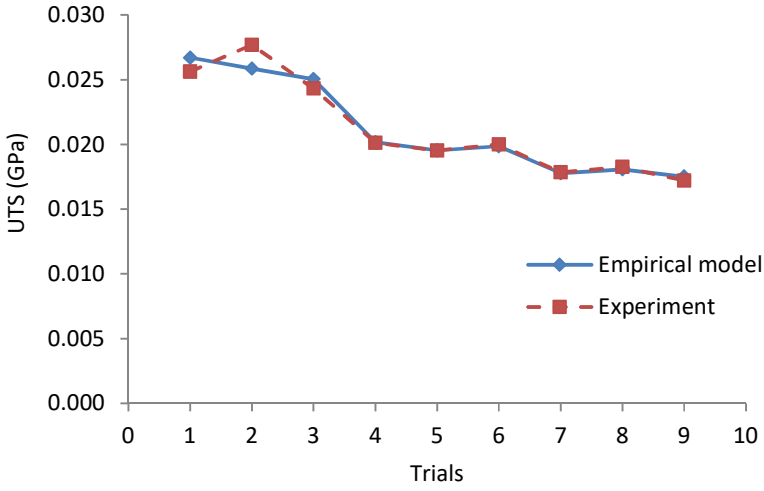

Figure 4.8 Variations of experimental and calculated values for ultimate tensile strength (ACC produced *via* NaOH/urea).

4.3.5 Effect of the main control factors using surface plot

According to the Taguchi analysis, the optimal t_d and P_{HP} were found to be at 60 min and 0.25 MPa to maximise E and UTS. However, t_d of 90 and 30 min increased the E and UTS, respectively (Figure 4.9). The equation models developed using MRA were not quite reliable in predicting the E and UTS, corresponding to the lower R^2 of 0.62 and 0.52, respectively.

This finding was expected due to the nonlinear relationship between t_d and mechanical properties of ACC produced *via* BmimAc. The change of mechanical properties as a function of P_{HP} was insignificant compared to t_d. The use of artificial neural network analyses may impart a good correlation between the experimental and theoretical mechanical properties.

For the ACC produced *via* NaOH/urea, the optimal t_d and P_{HP} were found to be at 15 min and 0.50 MPa to maximise E and UTS (Figure 4.10). These results were consistent with the optimal combination of control factors found for E and UTS according to the Taguchi analysis. The equation models developed using MRA were reliable in predicting the E and UTS, corresponding to the higher R^2 of 0.94 and 0.95, respectively. The linear relationship of the experimental and theoretical values was expected between t_d and the mechanical properties, in contrast to the nonlinear relationship observed for ACC produced *via* BmimAc.

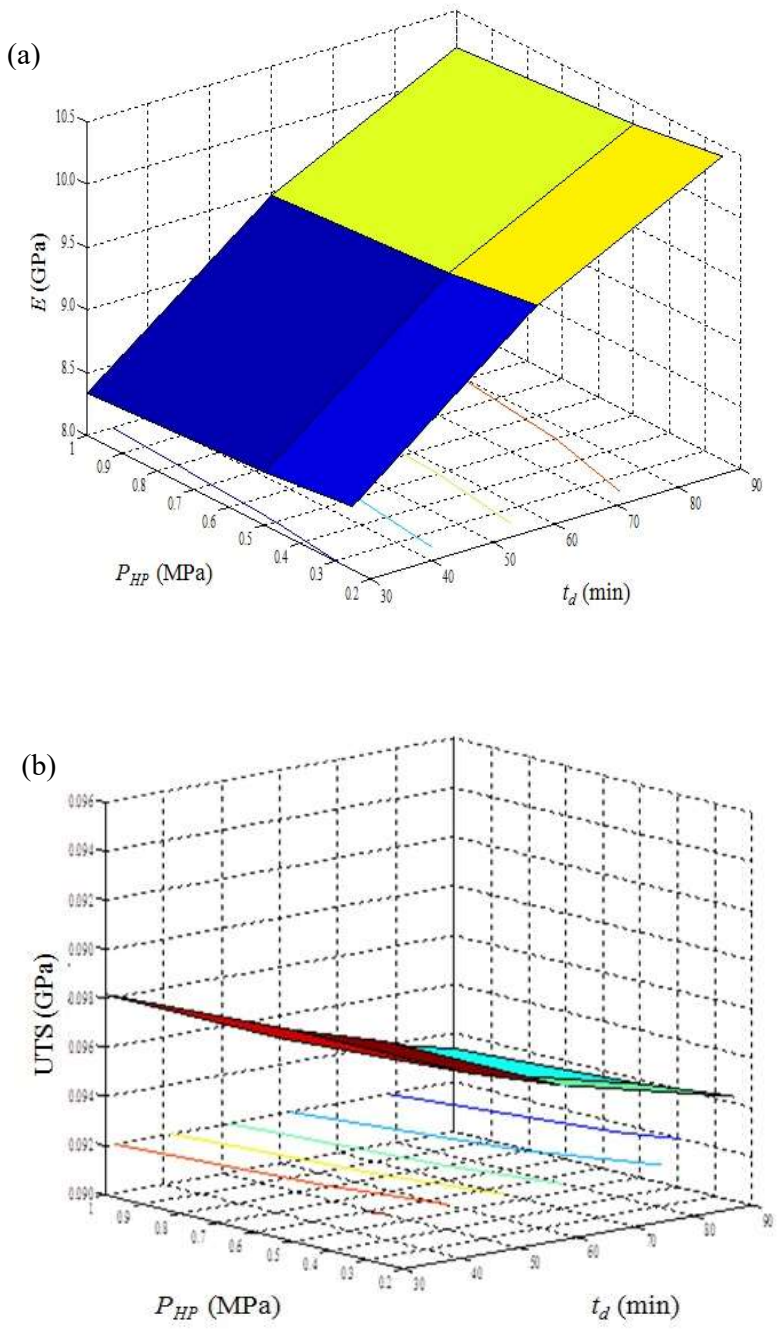

Figure 4.9 Surface plot as a function of dissolution time and pressure at hot press for ACC produced *via* BmimAc: (a) Young's modulus, and (b) ultimate tensile strength.

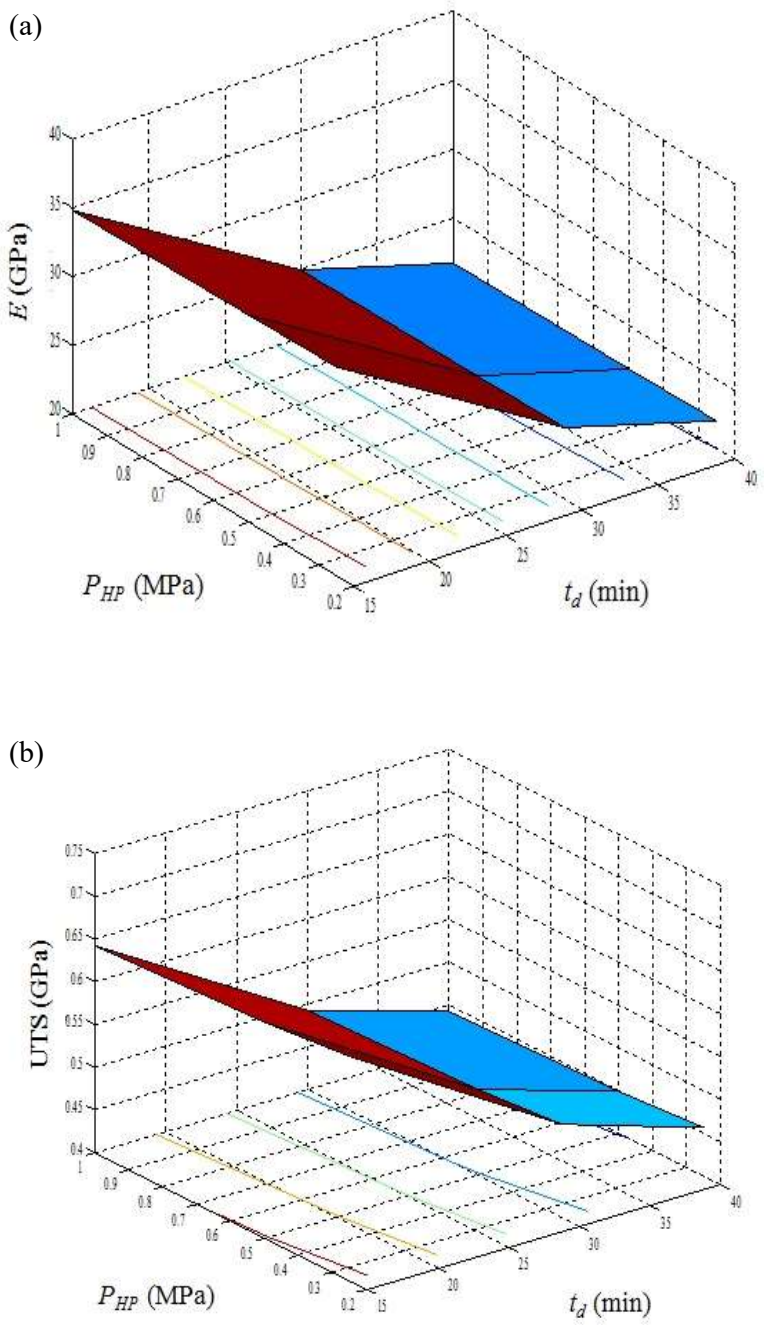

Figure 4.10 Surface plot as a function of dissolution time and pressure at hot press for ACC produced *via* NaOH/urea: (a) Young's modulus, and (b) ultimate tensile strength.

4.3.6 Effect of dissolution time on crystallinity index and crystallite size analyses

For ACC produced *via* BmimAc, the CrI slightly increased at t_d of 60 min (Figure 4.11). The result was expected from the dissolution of the amorphous region by the solvent and reformation of the dissolved cellulose as a paracrystalline phase [17]. The increasing trend of CrI as a function of t_d was also observed for the ACC produced *via* NaOH/urea (Figure 4.12). According to Colom and Carillo [212], an increasing CrI was consistent with a decrease in the water content. The relationship between water content and crystallinity for ACCs will be discussed in Chapter 5. The decrease of CrI at t_d of 90 min was expected due to the increase in the fraction of the amorphous phase (no orientation) at longer t_d, as also observed by Soykeabkaew *et al.* [16]. An increase in matrix phase could also be seen from the volume fraction analyses (Figures 4.21 and 4.22).

The paracrystalline phase is regarded to be a partially disordered structure [213]. Thus, it is expected that the presence of a paracrystalline region could lead to (i) a lower water content due to increasing disorder at the crystallite surface [213] and (ii) a higher CrI because the crystallites surface of the partially dissolved rayon fibre could provide a template for crystal growth during the regeneration of dissolved cellulose portions [109]. Duchemin *et al.* reported that the formation of a paracrystalline phase in cellulose is indicated by the disappearance of the crystalline peak of (004) ($2\theta = 35°$) [68]. The peak from the (004) diffracting planes almost disappears from ACCs produced via BmimAc and NaOH/urea (Figures 4.11 and 4.12), indicating the presence of paracrystalline region for the ACCs produced *via* either solvent.

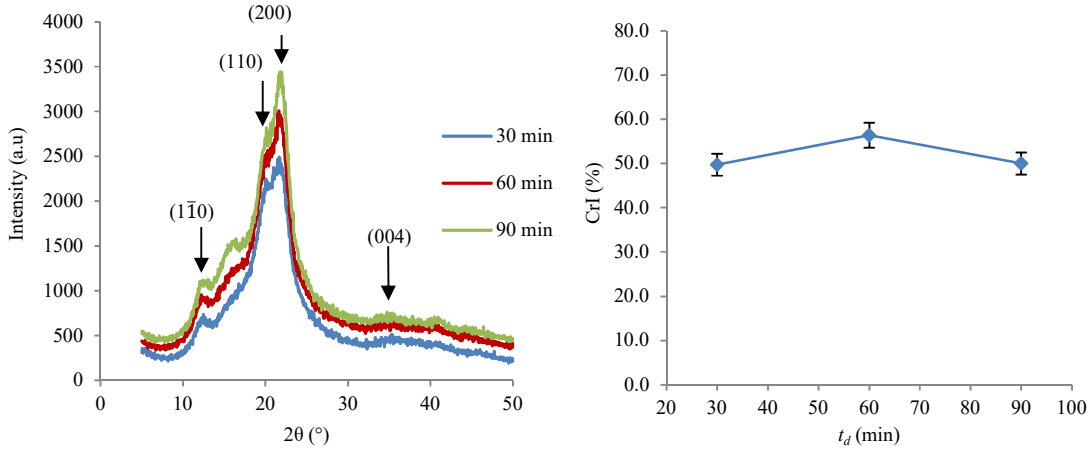

Figure 4.11 XRD diffractogram and crystallinity index for ACC produced *via* BmimAc.

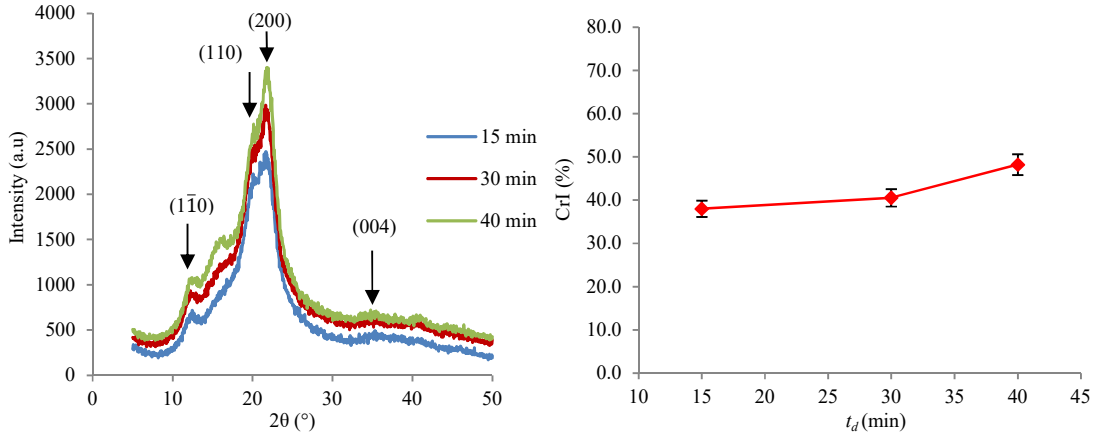

Figure 4.12 XRD diffractogram and crystallinity index for ACC produced *via* NaOH/urea.

The crystallite size at the (1$\bar{1}$0), (200) and (110) planes increased significantly with the increase of t_d (Figures 4.13 and 4.14). These results were expected due to a lateral increase of crystallite thickness perpendicular to the fibre axis, while no recrystallisation occurred at the crystal ends in the fibre axis. Ibbett *et al.* found lateral recrystallisation of regenerated cellulose fibres upon hydrolysis. Similarly, lateral crystallite growth was also reported for NaOH treatment at room temperature [210]. Crystallites of regenerated lyocell fibres grew in the (1$\bar{1}$0) and (200) planes, depending on the alkali concentration. It was argued that the alkali entered the pores and caused interfibrillar swelling, pushing the fibrils closer to each other in

the cross section and short chains which may crystallise at the lateral plane [210]. The swelling rate may be expected to increase as a function of t_d, as will be discussed in Chapter 5.

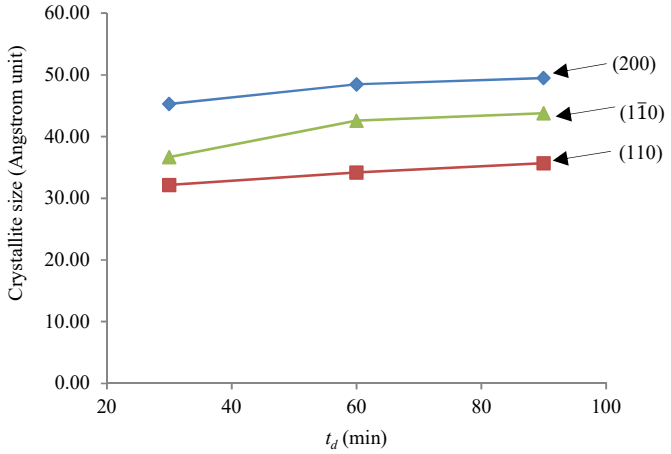

Figure 4.13 Crystallite size as a function of dissolution time for ACC produced *via* BmimAc.

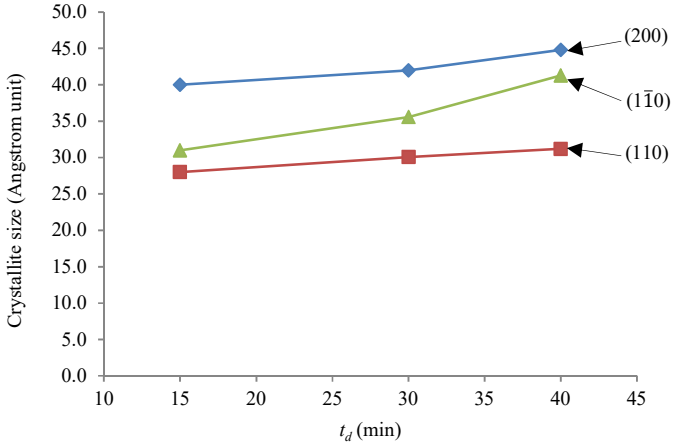

Figure 4.14 Crystallite size as a function of dissolution time for ACC produced *via* NaOH/urea.

In this study, a linear relationship was observed between TCI and CrI (Figure 4.15). The linear relationship between TCI and CrI was also reported for cellulose II by Nelson *et al.* [129]. The increasing TCI and CrI were reported with the increasing dissolution time. The changes of CrI as a function of dissolution time was expected due to the solvent selectively dissolving

amorphous cellulose that subsequently regenerates into a more crystalline (or paracrystalline) phase [17]. The changes of TCI as a function of dissolution time was expected due to the changes in the FTIR bands at 1372 cm^{-1} (C-H bending) and 2900 cm^{-1} (C-H and CH_2 stretching) [129]. ACC produced *via* NaOH/urea had higher R^2 of 0.96 as compared to 0.75 for the ACC produced *via* BmimAc (Figure 4.15), indicating a stronger linear relationship for ACC produced *via* NaOH/urea.

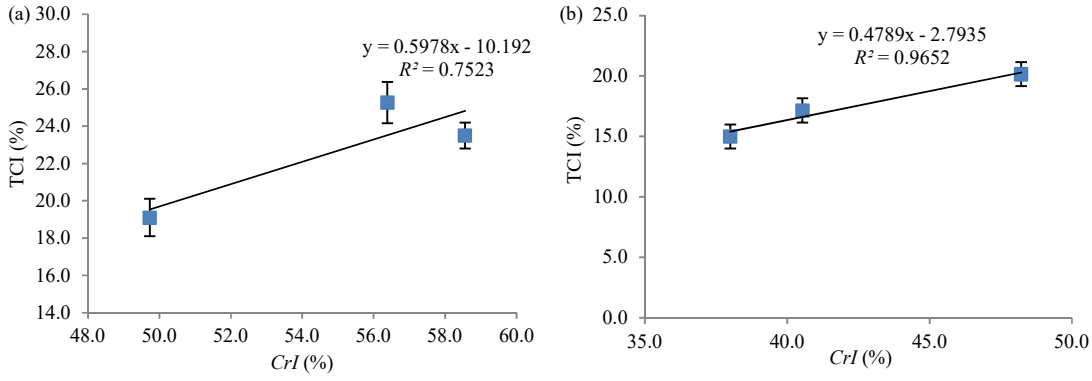

Figure 4.15 Relationship between TCI and CrI for ACC produced *via* (a) BmimAc and (b) NaOH/urea.

4.3.7 Effect of dissolution time on glass transition temperature

T_g for ACC produced *via* BmimAc and NaOH/urea were 266.15 and 267.80 °C, respectively (Figure 4.16). These results were in the range of T_g (140 to 290 °C) for the cellulose that occurred in the α_2 region [126, 214]. The broad peak at around 100 to 200 °C was expected to correspond with the water removal in the ACCs (Figure 4.16).

The degradation temperatures for ACC produced *via* BmimAc and NaOH/urea were 328.89 and 317.30 °C, respectively (Figure 4.16). Both temperatures were found in the range of 250 to 350 °C, which was assigned for α_1 (degradation region) [68]. Manabe *et al.* discussed that

this region was deemed to be the area of strong inter- and intramolecular hydrogen bonding [133].

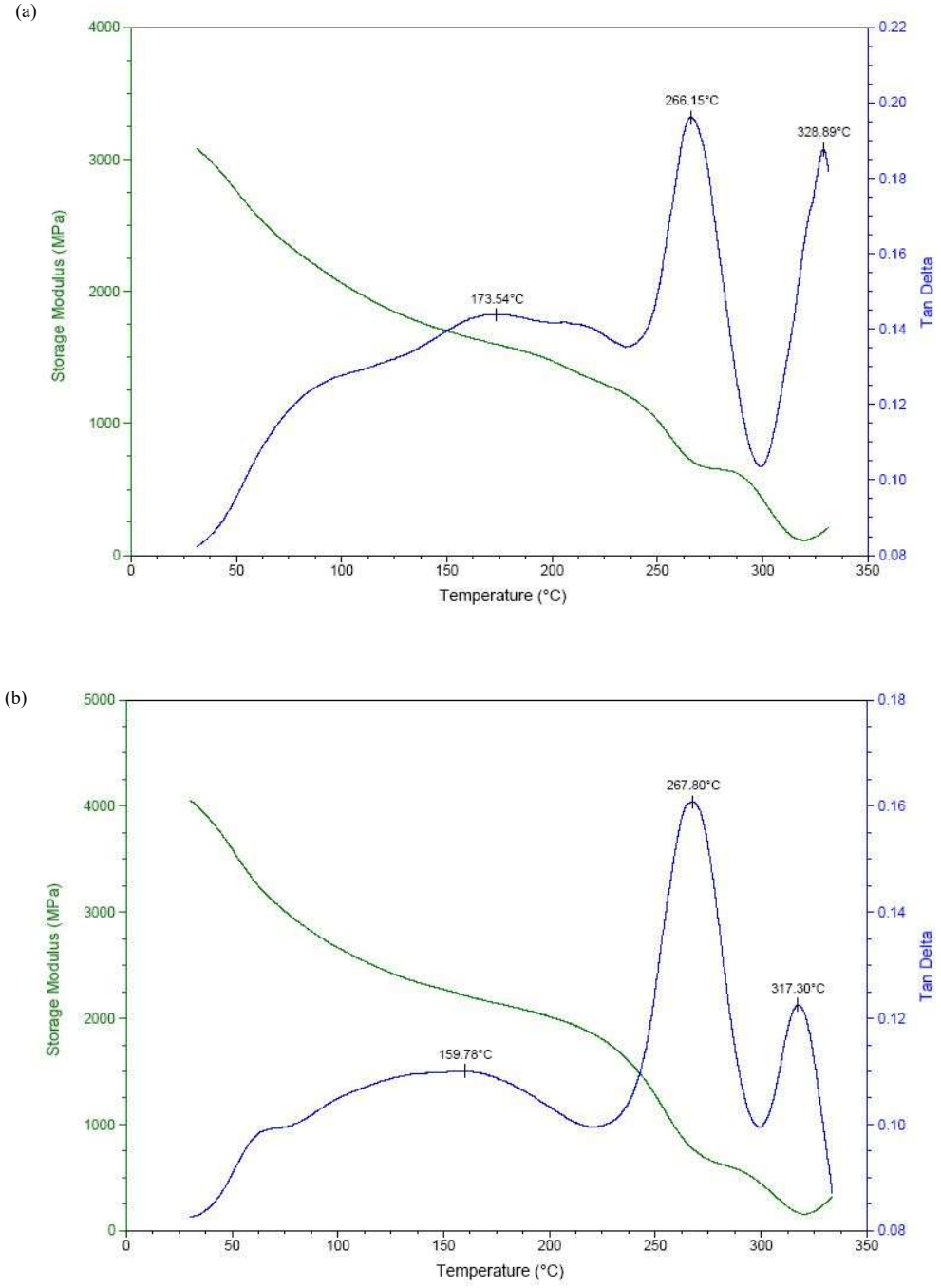

Figure 4.16 The glass transition temperature for ACC produced *via* (a) BmimAc and (b) NaOH/urea.

T_g shifted to a lower temperature with the increase of CrI [126, 215]. The decreasing T_g as a function of CrI was observed for the ACC produced *via* BmimAc and NaOH/urea (Figures 4.19 and 4.20, respectively). For the ACC produced *via* BmimAc, the T_g at t_d of 30, 60 and 90 min were 268.51, 252.75, and 266.15 °C, respectively (Figure 4.17). For the ACC produced *via* NaOH/urea, the T_g at t_d of 15, 30 and 40 min were 267.80, 267.67, and 266.73 °C, respectively (Figure 4.18).

The only slight decrease in T_g was observed as the CrI increased. Nelson *et al.* reported that the infrared spectra for cellulose II and amorphous cellulose are quite similar in the presence of a strong band at 893 – 897 cm^{-1} [129]. Marchessault and Liang pointed out that if the oxygen atoms attached to C_1 participate in a vibrational mode, then changes in hydrogen bonding could affect its intensity at a band range of 893 – 897 cm^{-1} [173]. Thus, the decreasing mobility of the interfacial amorphous phase and smaller volume ratio of true amorphous phase were expected, resulting in lower thermal energy consumption for mechanical relaxation and thus decreasing the T_g of ACCs.

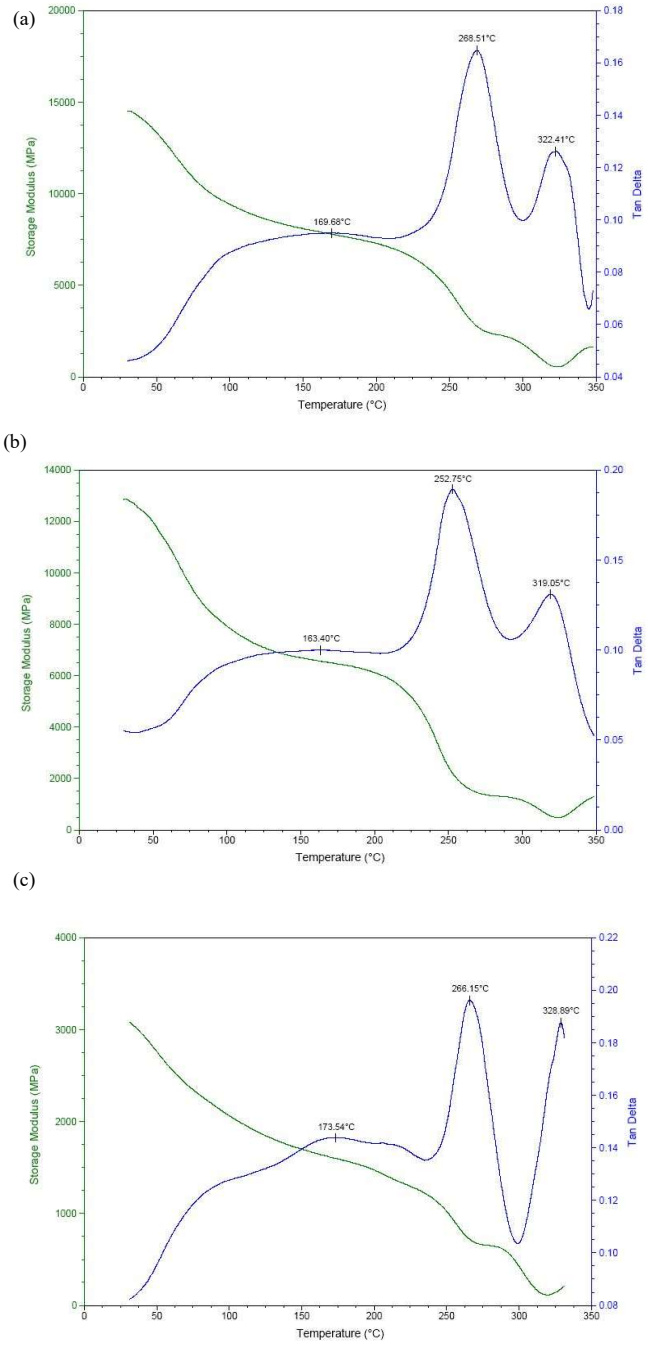

Figure 4.17 The glass transition temperatures for ACCs produced *via* BmimAc at various dissolution times: (a) 30, (b) 60, and (c) 90 min.

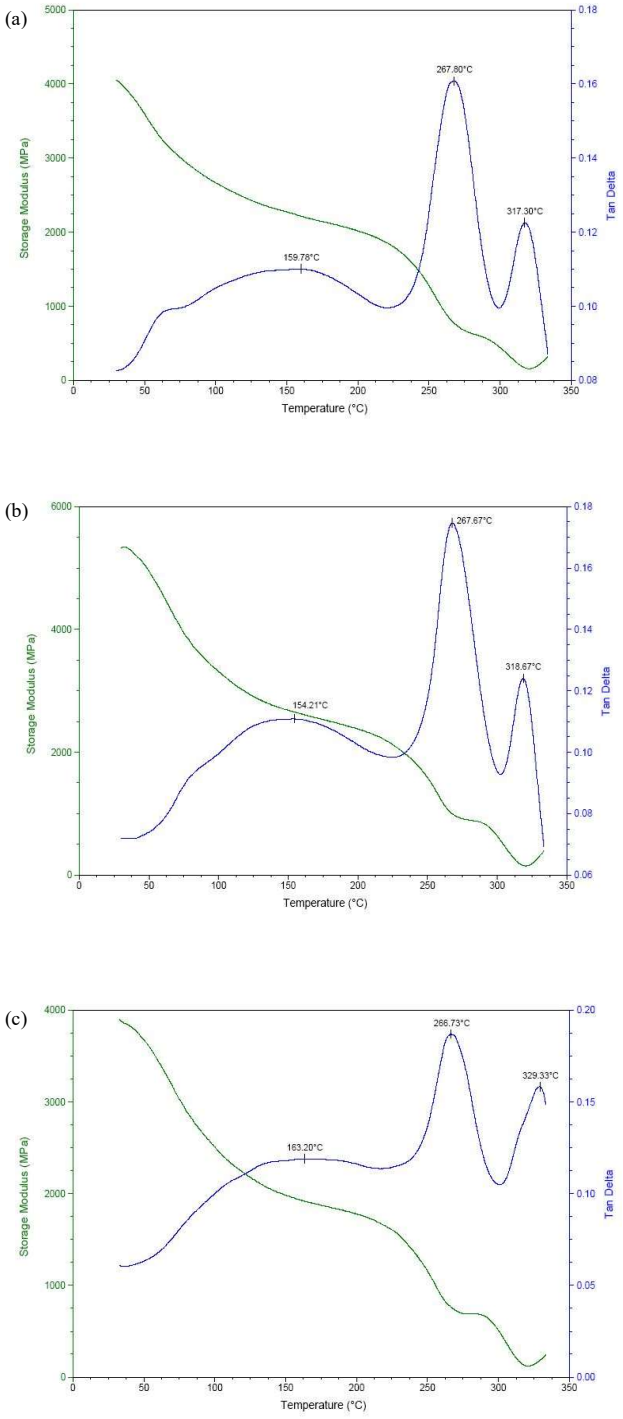

Figure 4.18 The glass transition temperatures for ACC produced *via* NaOH/urea at various dissolution times: (a) 15, (b) 30, and (c) 40 min.

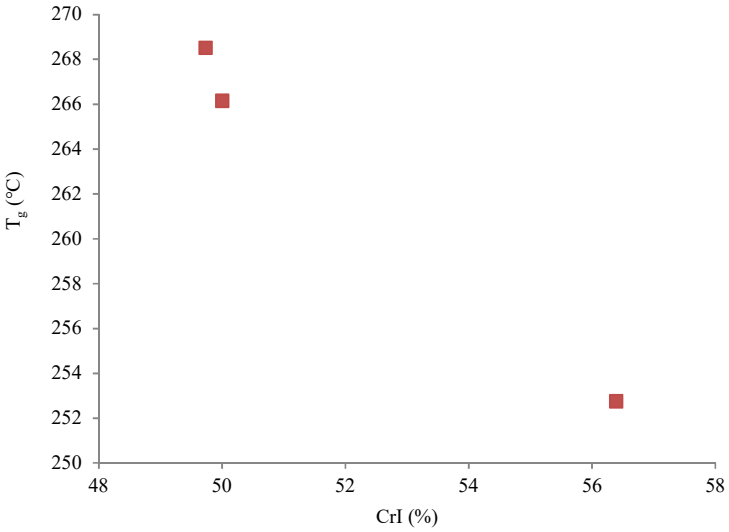

Figure 4.19 Glass transition temperatures as a function of CrI for ACC produced *via* BmimAc.

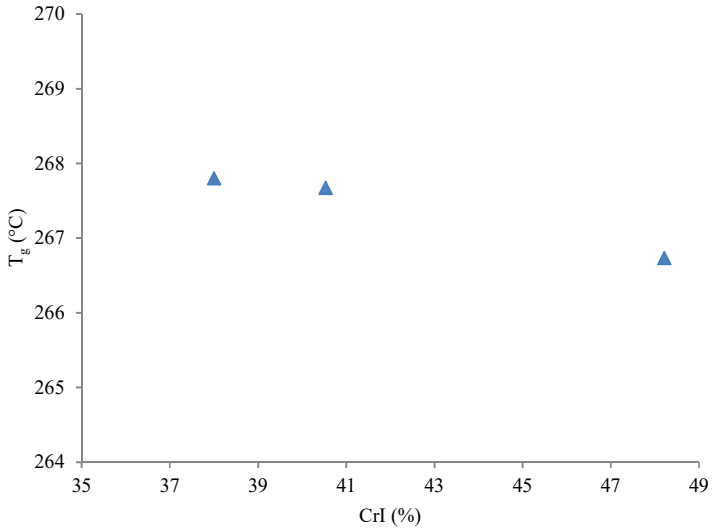

Figure 4.20 Glass transition temperatures as a function of CrI for ACC produced *via* NaOH/urea.

4.3.8 Effect of dissolution time on the fibre volume fraction

In the present study, V_f increases with the increasing t_d (Figures 4.21 and 4.22). This result was observed from the increasing crystallite size at the $(1\bar{1}0)$ and (200) planes (Figures 4.13 and 4.14). The increasing crystallite size was expected due to the dissolved amorphous tie molecules between crystallites in the fibre. The dissolved amorphous tie molecules were assembled onto the lateral surfaces of the neighbouring crystallites perpendicular to the fibre axis [109]. A higher V_f in ACC (~90%) showed that a smaller fraction of the reinforcing fibres was dissolved and transformed into a matrix phase. Although 10% of matrix is often insufficient for wetting of fibres in conventional composites, the matrix is formed in ACCs *in situ*, resulting in the matrix phase being directly adjacent and in close proximity to the fibres surfaces [216]. Attempts to characterise the interface/interphase region are hampered by experimental difficulties due to the small fraction of matrix phase that requires probing by nanoscale characterisation methods [216]. The identification of V_f, V_m, and V_v was difficult due to the both reinforcing and matrix phases that were composed of cellulose II. The boundary between the reinforcing and matrix phases was similar. Thus, the summation of V_f, V_m, and V_v seemed slightly lower than 100%.

The increasing V_m as a function of t_d was observed (Figures 4.21 and 4.22). At a longer t_d, a larger fraction of the reinforcing rayon fibres was dissolved and transformed into a matrix phase, as discussed in the previous study [109]. A higher solvent flow from the outer layer to the inner core of the cellulose fibre was expected at longer t_d, leading to the increase in V_m. Although the increasing V_f and V_m were observed with the increasing t_d, both components should not have greatly differing elastic moduli due to the both reinforcing and matrix phases that are both composed of cellulose II. The lower solubility of NaOH/urea (6.5 wt.%) [112] than IL (20 wt.%) [87] was reported, leading to less transformation of the cellulose fibre to the matrix during partial dissolution [109]. However, higher V_m was found for the ACC produced

with NaOH/urea as compared to BmimAc, leading to a higher swelling rate for the ACC produced *via* NaOH/urea, as will be discussed in Chapter 5. The increase of V_m contributed to the increase of ε_f that was observed for the ACCs produced *via* both solvents. For the ACC produced *via* BmimAc, the ε_f at t_d of 30, 60, and 90 min were found to be at 13.5, 12.3, and 15.3%, respectively. Meanwhile, for the ACC produced *via* NaOH/urea, the ε_f at t_d of 15, 30, and 40 min were 16.6, 17.2, and 19.3%, respectively. These findings show increasing ductility of ACCs as t_d increased. This result may be due to the long-range cohesion of the fibres. It has been reported that the fracture of the matrix leads to the separation of transverse and longitudinal yarns from each other, allowing the latter to straighten from the initial waviness implied by the weave [109].

The increase of V_v was observed as a function of t_d (Figures 4.21 and 4.22). Pressure had an effect on V_v. The increasing V_v was due to the narrow range of P_{SIP} and P_{HP}. The increasing V_v with the increasing t_d may be due to a loss of vacuum pressure at the SIP setup after disconnecting from the vacuum pump. The decreasing density was expected with the increase of V_v. Dormanns *et al.* reported that the density was inversely proportional to the V_v [109]. This relationship will be discussed in subchapter 4.3.9. For the ACC produced *via* BmimAc, a higher V_v was observed at t_d of 90 min. This result was due to the higher amount of dissolved cellulose, requiring higher pressure to impart a homogeneous matrix distribution in the ACC. A higher V_v was also observed at t_d of 30 min. This result was due to the insufficient amount of dissolved cellulose (shorter t_d), leading to an inhomogeneous matrix distribution despite applying sufficient pressure. For the ACC produced *via* NaOH/urea, the increasing V_v with the increasing t_d was observed, requiring a higher pressure for an even matrix distribution.

The increase of V_v decreased the mechanical properties of ACCs. The presence of voids is likely to reduce the overall elastic modulus of the material and the critical stress required for the onset of failure [216]. Dormanns *et al.* reported that a higher void in composites is

associated with a lower strength due to a reduced load bearing volume and by introducing stress concentration [109]. For ACC produced *via* BmimAc, the lower E and UTS values were observed at t_d of 30 and 90 min as compared to the t_d of 60 min, considering a P_{HP} of 0.25 MPa. This result was consistent to the higher V_v at t_d of 30 and 90 min as compared to the t_d of 60 min, corresponding to the V_v of 1.23 and 2.13%, respectively. The decreasing E and UTS at P_{HP} of 0.50 MPa was also observed for ACC produced *via* NaOH/urea, attributing to the increasing V_v. The formation of void in the ACCs introduced a stress concentration [217]. The increasing stress concentration due to the increasing V_v was expected to decrease the E and UTS of ACCs.

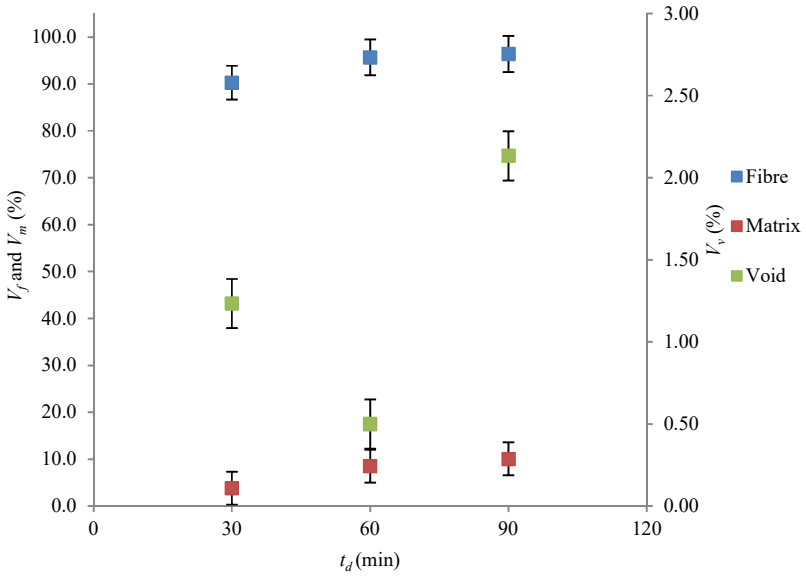

Figure 4.21 Fibre, matrix and void volume fractions for ACC produced *via* BmimAc (P_{HP} = 0.25 MPa).

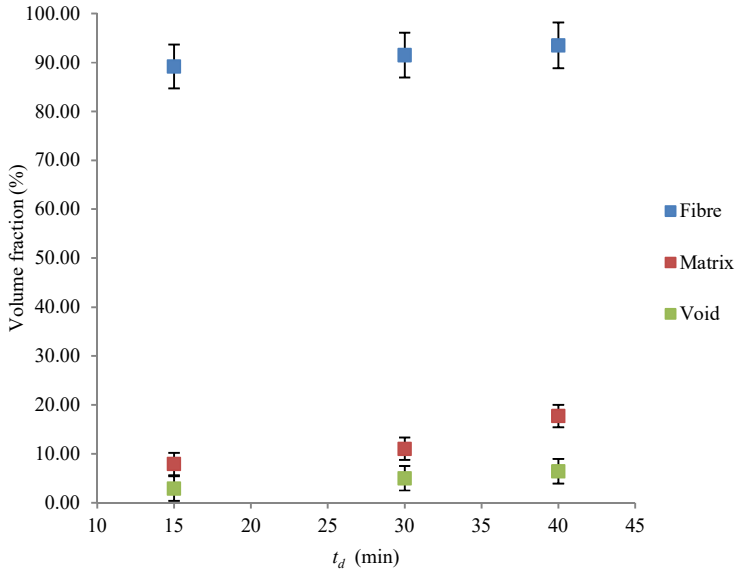

Figure 4.22 Fibre, matrix and void volume fractions of ACC produced *via* NaOH/urea (P_{HP} = 0.50 MPa).

For the ACC produced *via* BmimAc, the highest CrI and V_f of 58.86% and 96.40%, respectively, were observed at t_d of 90 min (Figure 4.23). A strong correlation between the CrI and V_f was observed from a high R^2 of 0.98. The CrI was directly proportional to the V_f. The increase in both CrI and V_f was expected due to the presence of the paracrystallinity phase within the elementary cellulosic fibres with the increasing t_d. However, the increasing V_v decreased the mechanical properties of ACC. The average void content was found at 1.28%.

For the ACC produced *via* NaOH/urea, the CrI was found to be directly proportional to the V_f (Figure 4.24). A strong relationship between CrI and V_f was observed, represented from a high R^2 of 0.89. The decreasing mechanical properties can be seen with the increasing V_v at longer t_d. This result was expected due to the uneven distribution of the matrix phase around the cellulose fibre (Figure 4.30 (b) and (c)). This uneven matrix phase distribution had led to the formation of voids, reducing the mechanical properties of the ACC. The average V_v was found at 4.77%, which was higher than the one reported by Hamami and Gebart (V_v < 1.0%) [84].

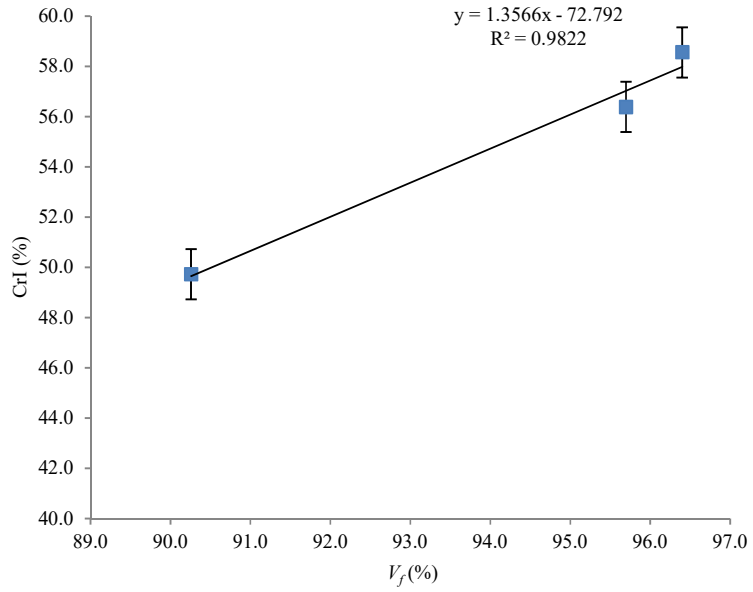

Figure 4.23 Relationship between CrI and V_f for ACC produced *via* BmimAc.

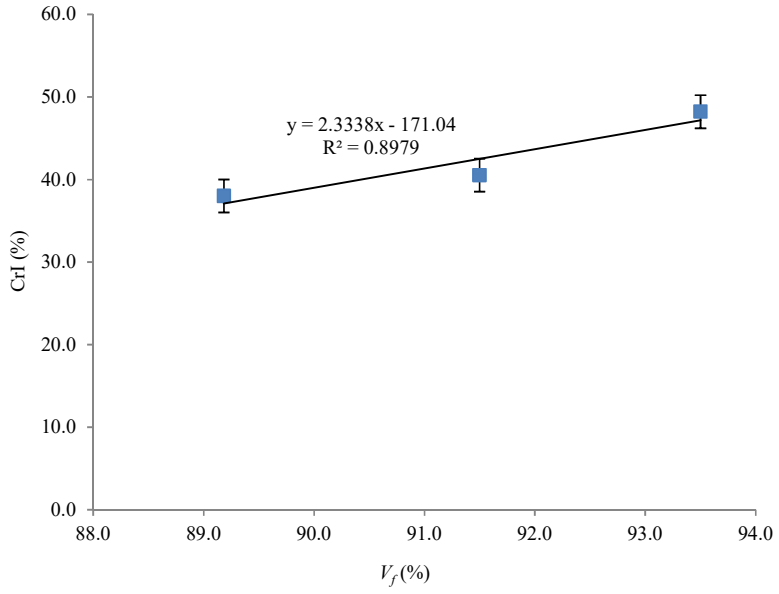

Figure 4.24 Relationship between CrI and V_f for ACC produced *via* NaOH/urea.

4.3.9 Density and microstructural analyses

For the ACC produced *via* BmimAc, the increasing density with the increase of P_{HP} was observed, considering a constant t_d of 60 min (Figure 4.25). This result was consistent to a

previous study carried out by Ignjatovic *et al.* [218]. However, further increase in t_d or P_{HP} caused a degradation effect on the cellulose [218]. The decreasing E with the increasing P_{HP} was observed for the ACC produced *via* BmimAc. The E values at P_{HP} of 0.25, 0.50, and 1.00 MPa were found to be at 7.32, 7.10, and 7.21 GPa, respectively (Table 4.5). The optimal P_{HP} was 0.25 MPa, according to the Taguchi analyses. Although the density increased with the increasing P_{HP}, the use of minimum P_{HP} was preferable. The higher pressure was expected to impart an excessive flow of the matrix phase, leading to the increase of void formation due to inhomogeneous matrix distribution. It has been reported that an excessive pressure may force the cellulose fibres to separate that reduce the adhesion among fibres, resulting in a decrease in the mechanical properties of ACCs [216].

The degradation effect was expected from the decreasing of density by prolonging the t_d (Figure 4.26). Dormanns *et al.* reported that the decrease in density with increasing t_d may be due to a slower loss of vacuum pressure after the setup is disconnected from the vacuum pump [109]. The majority of voids was found in the core yarns, probably due to small volumes of air that have not been replaced by solvent, being trapped in the core yarns [109]. Thus, the resulting gap between the fibres cannot be bridged by the matrix due to a lower matrix phase in ACC. At P_{HP} of 0.25 MPa, the increasing density from 1.50 to 1.59 g/cm^3 was observed at t_d of 30 to 60 min. The decrease in density was observed at t_d of 60 to 90 min. This result was expected due to the degradation effect on ACC above the t_d of 60 min. The V_v at t_d of 30 min was higher as compared to the t_d of 60 min (Figure 4.21). In contrast, the density at t_d of 30 min was lower as compared to the t_d of 60 min. This result indicated that the density was inversely proportional to the V_v, as also stated in the previous studies [109, 217].

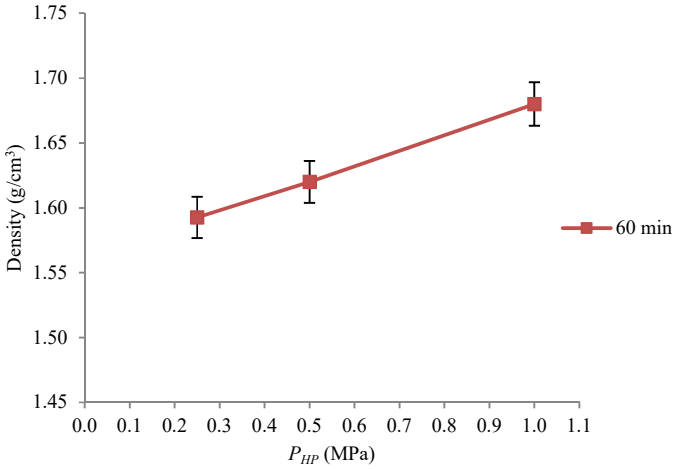

Figure 4.25 Density as a function of P_{HP} for ACC produced *via* BmimAc.

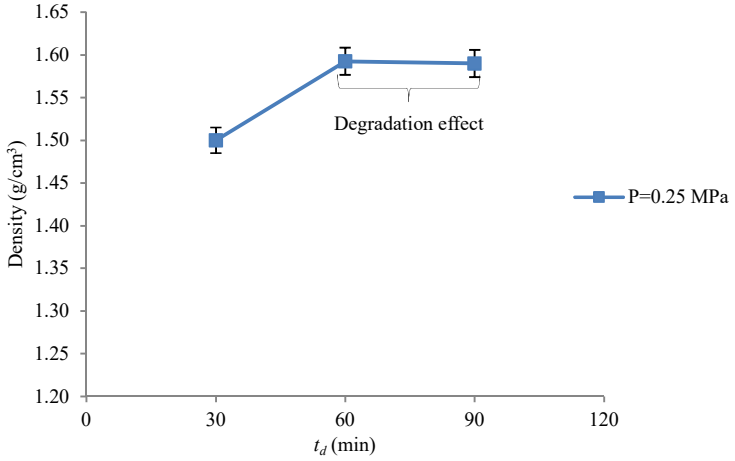

Figure 4.26 Density as a function of dissolution time for ACC produced *via* BmimAc.

The microvoids and intralaminar debonding between the fibres were observed in the ACC produced *via* BmimAc at t_d of 30 and 90 min (Figure 4.27). The diameter of microvoids and intralaminar debonding were in the range of 1-2 and 20 µm, respectively. Due to these defects, the decreasing mechanical properties of the ACC were observed. This result was due to the decreasing stress transfer capability in the ACC. Thus, higher stress concentration was expected at t_d of 30 and 90 min. Thus, the decreasing mechanical properties were significant at t_d of 30 and 90 min. The presence of microvoids is also concomitant with a reduction in the

matrix phase that will reduce the transfer of load from the matrix to the fibres (Figure 4.21). However, the reinforcing and matrix phases that are both composed of cellulose II should not have greatly differing elastic moduli and thus loading sharing is not expected to play a critical role in the final mechanical properties of the ACC. It is more likely that the presence of voids reduces the overall elastic modulus of the material and the critical stress required for the onset failure. Further detailed investigation is required to observe the effects of voids on the E of ACC.

The observation of widespread fibre-matrix interfacial failure tends to suggest that an interface or interphase exists in ACC in spite of the fibres and matrix being chemically similar. A 6.8 and 7.6% decrease in E and UTS are observed with a change of t_d from 60 to 90 min, respectively (Table 4.5). Increased dissolution of fibres is observed as t_d is increased as evidenced by an increase in V_m (Figure 4.21). A decrease in E and UTS is also observed in conjunction with an increase in V_v at a t_d of 30 or 90 min for the reasons as discussed above (Figure 4.21). Although 10.0% matrix is often insufficient for wetting of fibres in conventional composites, the matrix is formed in ACC *in situ*, resulting in the matrix phase being directly adjacent and in close proximity to the fibres surfaces, minimising void formation due to insufficient wetting. It is asserted that an interface and/or interphase do exist since failure does appear to emanate from the fibre-matrix boundary even in a microstructure in which most fibres are wetted by the matrix. It is also rare to observed a transverse failure of a fibre in spite of these ACC consisting solely of cellulose II. The presence of an interphase and/or interface in ACC remains to be clarified. The exact nature of the interface is still unknown in these materials. Attempts to characterise the interface/interphase region are hampered by experimental difficulties due to the small fraction of matrix phase that requires probing by nanoscale characterisation methods.

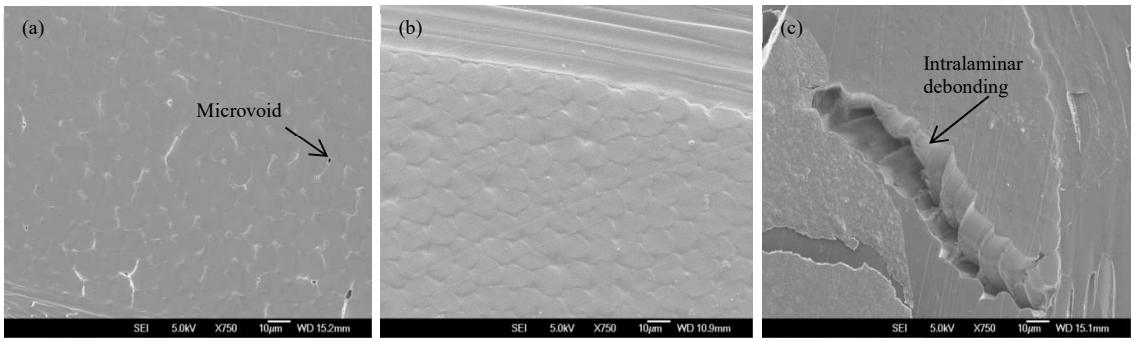

Figure 4.27 Microstructure micrographs for ACC produced *via* BmimAc at various dissolution times: (a) 30, (b) 60, and (c) 90 min.

For the ACC produced *via* NaOH/urea, the increasing density with the increasing P_{HP} was observed, considering a constant t_d of 15 min (Figure 4.28). The degradation effect was observed on the ACC when a constant density was reached (ρ =1.61 g/cm^3). The decreasing E with the increasing P_{HP} was observed at t_d of 15 min. The degradation effect was also observed from the plot of density as a function of t_d (Figure 4.29), considering a constant P_{HP} of 0.50 MPa. The decreasing density from 1.61 to 1.52 g/cm^3 was observed. This result was expected due to the increase of V_v with the increasing t_d (Figure 4.22).

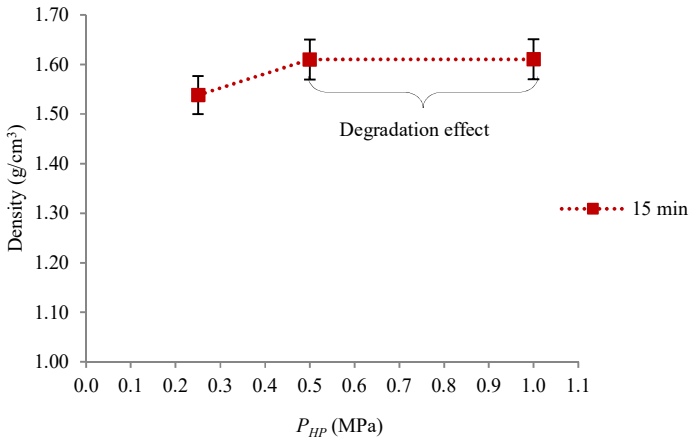

Figure 4.28 Density as a function of pressure at hot press for of ACC produced *via* NaOH/urea.

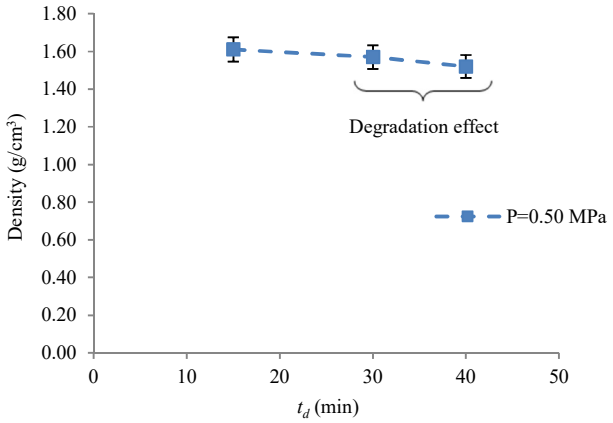

Figure 4.29 Density as a function of dissolution time for ACC produced *via* NaOH/urea.

For the ACC produced *via* NaOH/urea, the microvoids and intralaminar debonding were observed (Figure 4.30). The diameter of microvoid was found in the range of 5-10 µm. Meanwhile, the diameter of intralaminar debonding was found in the range of 30 µm. A larger diameter of microvoids and intralaminar debonding for ACC produced *via* NaOH/urea was observed as compared to BmimAc. The interlaminar debonding was not present due to a single lamina of ACC produced for both solvents. The increasing V_v and decreasing density with the increase of t_d (Figure 4.22 and 4.29, respectively) were observed probably due to the increasing stress concentration, resulting in the decrease of mechanical properties.

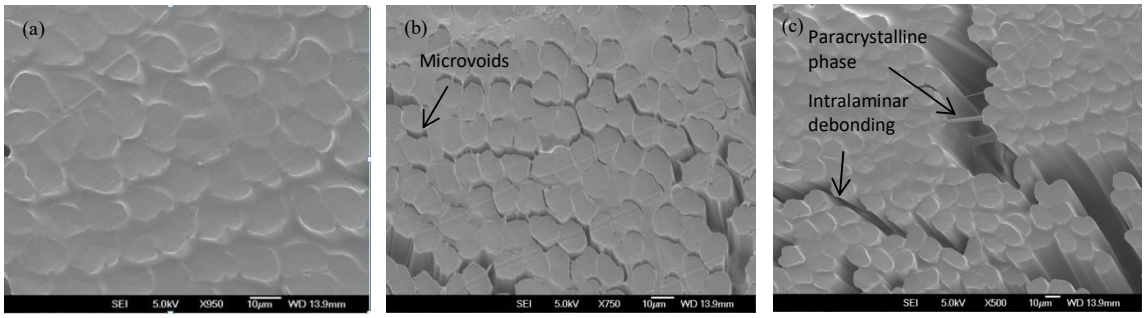

Figure 4.30 Microstructure micrographs for ACC produced *via* NaOH/urea at various dissolution times: (a) 15, (b) 30, and (c) 40 min.

4.4 Summary of findings

This present study presented the effects of control factors on the ACCs behaviour using Taguchi's DOE method. The conclusions are summarised as follows:

- Taguchi orthogonal array can effectively reduce the number of trials from 27 (conventional experimental method) to only 9 trials. t_d imparts the greatest influence on E and UTS of ACC produced *via* BmimAc and NaOH/urea, as shown by a Taguchi fractional factorial experimental design and ANOVA. In contrast, the other control factors (*e.g.* T_d, P_{HP}, and P_{SIP}) had a relatively small effect on the mechanical properties of ACC.

- A t_d of 60 min and 15 min are found to be optimal in maximising E and UTS of the final ACC produced *via* BmimAc and NaOH/urea, respectively. A shorter t_d in ACC produced *via* NaOH/urea is due to a lower viscosity of aqueous NaOH/urea solution than BmimAc. Thus, a faster infusion rate is likely to occur during the infusion process of ACC produced *via* NaOH/urea than BmimAc.

- R^2 for the ACC produced *via* NaOH/urea was higher as compared to BmimAc. This result showed that MRA was a suitable method to predict the E and UTS values for ACC produced *via* NaOH/urea, expecting from their linear relationship between the mechanical properties and control factors.

- The T_g value decreased with the increase of t_d and CrI. The density decreased with the increasing t_d. These results were observed for ACCs produced *via* NaOH/urea. However, the E and UTS values for the ACC produced *via* BmimAc were higher than the ACC produced *via* NaOH/urea, as expected from its lower V_v.

- As a conclusion, BmimAc is a promising solvent to produce ACC *via* SIP. The higher mechanical properties for the ACC produced *via* BmimAc were due to its high ability to dissolve the cellulose, low volatility, low cost, and no requirement for a pretreatment or activation before dissolving the cellulose. This is a good turning point in producing highly efficient ACCs in the future.

Chapter 5

Moisture absorption in all-cellulose composites

5.1 Introduction

Cellulose offers several advantages, including low density, high specific strength and *E*, low in cost and biodegradability [219]. However, cellulose is a hydrophilic material due to its numerous OH groups [65, 136]. These OH groups interact with water molecules by hydrogen bonding, limiting its outdoor usage due to poor environmental and dimensional stability [9, 136]. Thus, it is essential to analyse the mechanical properties of ACCs under the influence of various environmental conditions (Chapter 6). Differential shrinkage and resulting lateral stresses in the ACCs films are known to be caused by water diffusion processes [17, 23]. Thus, a major concern for ACCs is their high water absorption that may degrade the mechanical properties [9, 17].

Three types of water absorption may take place in bio-based materials [116]. The main mechanism is the diffusion of water molecules inside the microgaps between polymer chains. The second mechanism is a capillary transport into the gaps and flaws at the interfaces between the fibres and polymer matrix. Finally, the third mechanism is a water transport by the microcracks in the matrix [220]. The quantity of absorbed water depends on the following factors: RH, purity of cellulose, CrI, V_f, V_v, viscosity of matrix, and water bath temperature [116, 136].

During the dissolution process, the amorphous and the outer layer of cellulose surface are dissolved and transformed into non-crystalline parts. These non-crystalline parts resolidify and act as the matrix phase. As this matrix consists of a disordered region of the cellulose, it tends

to absorb water. Thus, increasing the t_d will increase the matrix phase which subsequently will increase water absorption. The increase of water bath temperature increases the water absorption and shortens the saturation time of the bio-based materials [116]. This is due to the increasing water mobility at higher water bath temperature, indicating a poor compatibility between the fibre and matrix interface. The increasing water mobility also induces more water to fill the gap within the cellulose fibres and matrix structure due to the presence of defects (voids, cracks, and microvoids).

The literature review of the water absorption on bio-based materials has been discussed in Chapter 2 (Section 2.4.1). The water absorption behaviour in bio-based composite materials has been reported in the previous studies [43, 46, 116]. In this present study, the effects of water bath temperature and t_d on the water absorption behaviour of ACCs were observed. The correlation between the theoretical calculations and experimental data was to be determined. The simulation work using ANSYS was used to (i) determine the effect of water bath temperature on water concentration at different thicknesses, and (ii) observe the correlation of saturation time between theoretical calculations and experimental data.

5.2 Theoretical approach

According to the water absorption tests, the type of water transport behaviour and water diffusion coefficient (D) were determined. The water transport behaviour in polymer matrix composites is described by Fickian diffusion, relaxation-controlled diffusion, or non-Fickian diffusion (*aka* anomalous). The types of water transport behaviour can be distinguished by the shape of the absorption curve as represented by Eq. 5.1 [116]:

$$\log\left(\frac{M_t}{M_m}\right) = \log(k) + n\log(t) \qquad \text{Eq. 5.1}$$

where M_t is the moisture content at a specific time (t), M_m is the equilibrium moisture content (EMC), t is time, and k and n are constants. The types of water transport behaviour (n) are summarised in the Table 5.1 [116, 145, 221, 222].

Table 5.1 Types of water transport behaviour

n	Types of diffusion
0.5	Fickian
$n \geq 1$	Relaxation controlled
$0.5 < n < 1.0$	Non-Fickian

The n and k values can be determined from the experiments using the slope and intercept of a log-log plot of M_t/M_m versus t. In the present study, the type of water diffusion will be discussed in a subsequent subchapter.

The determination of D in polymer-matrix composites has been reported by Shen *et al.* [223] for a one-dimensional and unsteady state diffusion through the thickness of the composite panel [223]. The approach by Shen *et al.* is valid for samples having a high surface to volume ratio. In this case, D can be mathematically described by Eq. 5.2:

$$\frac{\partial C}{\partial t} = D\frac{\partial^2 C}{\partial x^2} \qquad \text{Eq. 5.2}$$

where C is the concentration of the water diffusion (g mm^{-3}), t is the time (s), x is the distance through the sample thickness (mm), and D is the water diffusion coefficient (m^2/s).

The analytical solution of Eq. 5.2 for a plane sheet with a uniform distribution of initial moisture concentration through the thickness can be obtained as expressed by Eq. 5.3. This equation was applied for the overall moisture change *via* both faces of the composite panel for a short period of time [145]:

$$M_t = 4M_m\sqrt{\frac{D}{\pi h^2}}\sqrt{t} \qquad \text{Eq. 5.3}$$

where h is the sample thickness, and the other symbols have the same meaning as in Eq. 5.1 and 5.2.

The D value was obtained from the initial slope ($t < t_L$) of M_m versus $t^{1/2}$ curve [223]. The t_L is the point where the curve starts asymptotically approaching the M_m after an extended period of time. Then, the curve tends to plateau when M_m is attained. The following equation had been derived from Eq. 5.3 to calculate the D value (without the edge effect) [223]:

$$D = \pi\left(\frac{h}{4M_m}\right)^2\left(\frac{M_2 - M_1}{\sqrt{t_2} - \sqrt{t_1}}\right)^2 \qquad \text{Eq. 5.4}$$

where the symbols D, M_m, and h represent the same meaning as in Eq. 5.1-5.3. M_1 and M_2 are water contents at the specified times of t_1 and t_2. Eq. 5.4 is modified where the dimension of the sample is incorporated to find D value (with the edge effect) [223].

$$D_{with\ edge\ effect} = D\left(1 + \frac{h}{l} + \frac{h}{w}\right)^2 \qquad \text{Eq. 5.5}$$

The dimension of l, w, and h are the length, width, and thickness of the sample, respectively.

The experimental diffusion results were compared with the theoretical mathematical expression of the Fick's law for a plane sheet, as indicated by Eq. 5.6 [116]:

$$\frac{M_t}{M_m} = 1 - \frac{8}{\pi^2}\sum_{n=0}^{\infty}\frac{1}{(2n-1)^2}\exp\left(-\frac{(2n+1)^2\pi^2}{h^2}Dt\right) \quad \text{Eq. 5.6}$$

The diffusion processes are activated by an increase in water bath temperature, as may be expected for a process that involves mobility of the molecules. In the case of Fickian diffusion, the water diffusion coefficient has been found to follow the exponential Arrhenius-type relationship with the water bath temperature as expressed by Eq. 5.7 [116]:

$$D = D_o \exp\left(-\frac{E_a}{RT}\right) \quad \text{Eq. 5.7}$$

where D_o is the diffusivity index, E_a is the activation energy of the moisture in the composite, T is water bath temperature and R is the universal gas constant.

Thickness swelling (TS) is an important property, representing the stability performance of the composite [145]. The prediction of thickness swelling for the composite panel has been determined by Eq. 5.8 [224]:

$$TS(t) = \left(\frac{h_\infty}{h_o + (h_\infty - h_o)e^{-K_{sr}t}} - 1\right) \quad \text{Eq. 5.8}$$

where h_o is the initial thickness at t = 0, h_∞ is the ultimate thickness of the panel at equilibrium, and K_{sr} is the intrinsic relative swelling rate parameter. The K_{sr} value from the above equation depends on how fast the composite swells and reaches the ultimate thickness swelling at equilibrium [145]. This value can be determined through a nonlinear regression curve that is fitting to the experimental data.

The thermal-moisture diffusion analogy finite element analysis (FEA) is used to determine the water concentration at different thicknesses. The FEA method has the capability of analysing a transient moisture diffusion response [225]. The thermal-moisture analogy follows Fourier's law for the thermal diffusion (Eq. 5.10) that is mathematically equivalent to Fick's law for mass diffusion (Eq. 5.9) [226]:

$$\frac{\partial C}{\partial t} = D\left(\frac{\partial^2 C}{\partial x^2} + \frac{\partial^2 C}{\partial y^2} + \frac{\partial^2 C}{\partial z^2}\right) \quad \text{Eq. 5.9}$$

$$\frac{\partial T}{\partial t} = \frac{k}{\rho c}\left(\frac{\partial^2 T}{\partial x^2} + \frac{\partial^2 T}{\partial y^2} + \frac{\partial^2 T}{\partial z^2}\right) \quad \text{Eq. 5.10}$$

where, C is the moisture concentration which is equivalent to the temperature (T), whereas diffusivity is equivalent to thermal diffusivity $\alpha = k/\rho c$. Due to this similarity, opportunities arise to use the thermal diffusion capabilities to solve Fick's diffusion coefficient equation. The thermal-moisture diffusion analogy input parameters are summarised in the following table [227].

Table 5.2 Thermal-moisture diffusion analogy input parameters

Properties	Thermal	Moisture
Field variable	Temperature, T	Saturation ratio, w
Density	ρ (kg/m^3)	1
Conductivity	k (W/m°C)	D^*M_m (mm^2/h)
Specific gravity	C (J/kg°C)	M_t

In the present study, three assumptions were considered for FEA analyses: (i) 2-dimensional (2D), (ii) boundary conditions, and (iii) solution methods. The 2-dimensional geometry was modelled directly as the mid-plane cross section of the ACC samples, giving a clear representation of the concentration profile through the sample cross section. Cellulose fibres have significant effects on the moisture diffusion parameters of a composite material due to its high hydrophilicity. Therefore, the fibres will not be physically included in the geometry of the finite element model in order to simplify geometry creation, allowing a shorter calculation times due to the reducing the mesh density at the fibre – matrix interfaces.

Properly establishing the boundary conditions is paramount in attaining accurate results. The primary boundary conditions in thermal analyses are temperatures, heat flows, and heat fluxes [227]. In this study, the primary boundary condition that needs to be established is the saturation ratio (temperature in a thermal analysis). Since the cellulose fibres are not physically included in the model, the other primary boundary conditions are not needed. The saturation ratio has a maximum value of one, when $M(t) = M_\infty$, therefore a temperature boundary condition equal to one has to be established along all surfaces of the model which are exposed to moisture. For 2-dimensional model, a temperature of one is applied to all four of the outer edges.

A linear solution method is used once the geometry, and boundary condition have been completely established throughout the model. This method supplies the program with both the ending time, and size of the time step for the transient analysis. The program uses these time parameters and solves the entire system at each step in time until the stopping time is reached at which point further calculations are not needed. The linear solution method works very cleanly, but it can become a game of trial and error in determining the amount of time in order to reach a satisfactory level of model convergence.

ANSYS 13.0 software was used. ANSYS is a well-established FEA package that has built-in capacities for numerically solving a wide variety of problems, including static and dynamic structural systems, acoustics, electromagnetism, fluid flows and most importantly, thermal heat transfer. It has a powerful transient time-dependant solution capabilities, giving a robust and accurate solution to a moisture concentration problem [227].

5.3 Experimental procedures

Water absorption was measured in accordance with ASTM D570-98 [228]. The ACCs were prepared (76.2 (l) × 25.4 (w) × 0.48 (h) mm). Specimens were dried in a vacuum oven at 105 °C for 1 h. After measuring the oven dry weights, samples were completely immersed in distilled water at various temperatures (water bath) of 23 ± 1, 50 ± 1 and 100 ± 1 °C for 168 h. Samples were removed from the distilled water bath, and the water remaining on the sample surface was wiped off with a dry tissue. Samples were then immediately weighed at different specified times. The analysis of the water absorption behaviour was performed similar to previous studies [9, 20].

Water content (W_c) values were calculated by the weight difference between the oven-dry weight (m_o) and weight, following specified immersion times (m_t) (Eq. 5.11) [140, 228]:

$$W_c(\%) = \frac{(m_t - m_o)}{m_o} \times 100 \qquad \text{Eq. 5.11}$$

TS was calculated by the average thickness between the oven-dry thickness (h_0) and thickness following specified immersion times (h_t) (Eq. 5.12) [145]:

$$TS(\%) = \frac{h_t - h_0}{h_0} \times 100 \qquad \text{Eq. 5.12}$$

5.4 Results and discussion

5.4.1 Kinetics of the water absorption

Water content at various temperatures and t_d of 30 min for the ACCs produced *via* BmimAc and NaOH/urea are presented in Figures 5.1 and 5.2, respectively. The samples rapidly absorbed water between 0 and 4 h. Then, the saturation point was reached, indicating that a constant water content was achieved. The EMC increased with the increasing temperature. For the ACC produced *via* BmimAc, the EMC at 23, 50, and 100 °C were 50.5, 51.4, and 51.8%, respectively. For the ACC produced *via* NaOH/urea, the EMC at 23, 50, and 100 °C were 66.8, 69.8, and 71.4%, respectively. Higher EMC was observed for the ACC produced *via* NaOH/urea as compared to those produced *via* BmimAc. These results were expected due to the higher V_v for the ACC produced *via* NaOH/urea (Table 5.6). The saturation time was also shortened with the increasing temperature. The saturation times at 23, 50 and 100 °C were 18, 12, and 5 h, respectively, which were found similar for the ACCs produced *via* both solvents. The result indicated that high kinetics of the absorbed water at high temperature led to a quick saturation time. The increasing slope with the increasing temperature was also observed (Figures 5.1 and 5.2). This result was consistent with the increasing D as the temperature increased (Tables 5.7 and 5.8). At higher temperature, the mobility of water molecules increased. The increasing mobility of water molecules accelerated the water diffusivity along the fibre-matrix and within the defects in the ACCs. The poor ACCs structure and a higher temperature significantly induced water mobility. Thus, the increasing EMC, D and a shorter saturation time were observed.

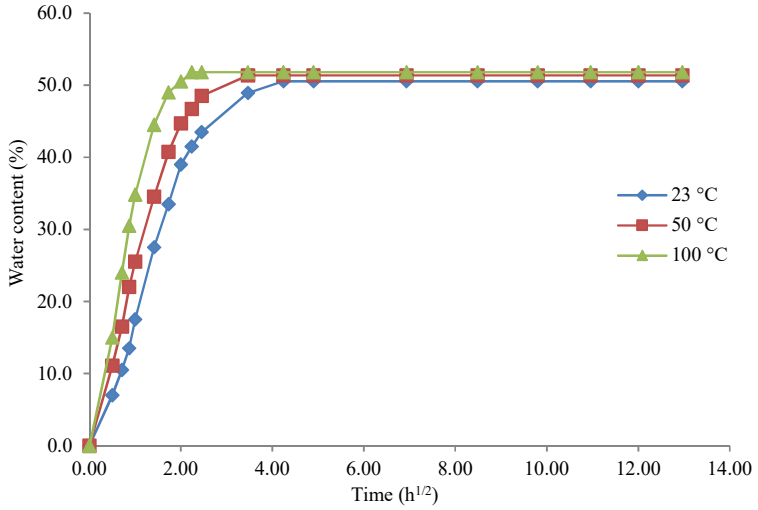

Figure 5.1 Water content for ACC produced *via* BmimAc at various temperatures.

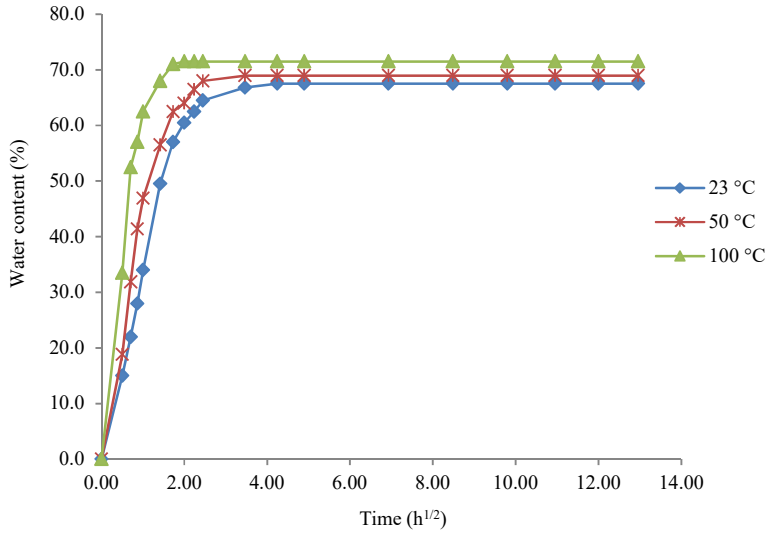

Figure 5.2 Water content for ACC produced *via* NaOH/urea at various temperatures.

Hu *et al.* found three phases of water absorption for biocomposite material (jute fibre reinforced polylactide), which are the (i) first phase (quick water absorption), (ii) second phase (moderate water absorption), and (iii) third phase (rapid water absorption) [46]. The saturation time and EMC were 22 h and 2.0%, respectively [46]. Polylactide had high hydrophobicity, giving lower water absorption and longer saturation time. However, in this present study, only two (first and second) phases were observed (Figure 5.3). The slope (first phase) associated to the *D* value

rapidly increased, expecting an easy capillary transport into the near-surface region of the ACCs. A slower water absorption rate at the second phase was observed as compared to the first phase, indicating water diffusion through the fibres and matrix of ACCs. Higher EMC and shorter saturation time were observed in the ACCs compared to the biocomposite material as reported by Hu *et al.* [46] due to higher hydrophilicity in ACCs, representing the use of cellulose for reinforcement and matrix.

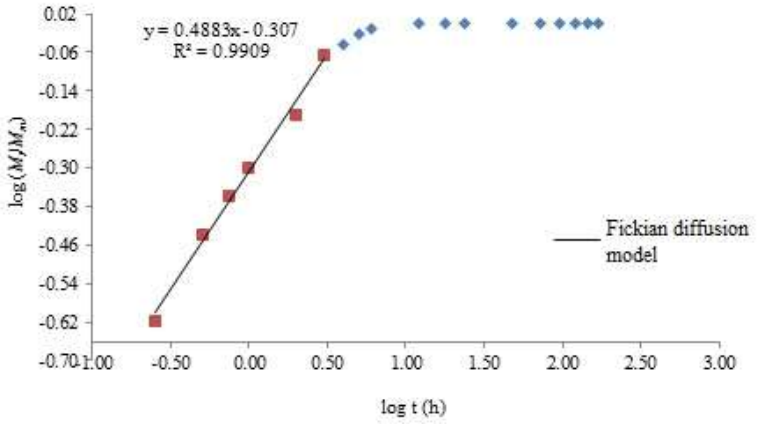

Figure 5.3 Water absorption phases for ACCs.

The ACCs produced *via* BmimAc and NaOH/urea transport water were *via* the Fickian diffusion case, representing from $n = 0.5$ (Tables 5.3 and 5.4, respectively). This result showed that the EMC was rapidly reached and maintained at a constant value at all times. The increasing k with the increase of t_d was observed (Tables 5.3 and 5.4). This result was expected due to the increasing water absorption at longer t_d associated with the increasing V_v, inducing more water to fill the voids. However, k at t_d of 60 min was slightly lower than the other t_d (Table 5.3). This finding was consistent to the lowest V_v found at t_d of 60 min (Table 5.5). From a practical standpoint, the consolidation pressure decreases since the laminae assembly must be disconnected from the vacuum pump prior to the partial dissolution step that takes place in a cooling bath, leading to an increase in V_v as t_d increased.

Table 5.3 Diffusion case selection parameters for ACC produced *via* BmimAc

t_d (min)	Temperature (°C)					
	23 °C		50 °C		100 °C	
	n	k (h^{-n})	n	k (h^{-n})	n	k (h^{-n})
30	0.582	0.466	0.515	0.485	0.510	0.538
60	0.568	0.431	0.559	0.451	0.570	0.482
90	0.581	0.452	0.501	0.493	0.564	0.579

Table 5.4 Diffusion case selection parameters for ACC produced *via* NaOH/urea

t_d (min)	Temperature (°C)					
	23		50		100	
	n	k (h^{-n})	n	k (h^{-n})	n	k (h^{-n})
15	0.582	0.431	0.515	0.485	0.510	0.538
30	0.568	0.452	0.559	0.490	0.570	0.561
40	0.581	0.466	0.501	0.493	0.564	0.579

Table 5.5 Void and fibre volume fraction for ACC produced *via* BmimAc

t_d (min)	V_v (%)	V_f (%)
30	1.2	90.6
60	0.5	95.7
90	2.1	96.4

Table 5.6 Void and fibre volume fraction for ACC produced *via* NaOH/urea

t_d (min)	V_v (%)	V_f (%)
15	2.9	89.2
30	5.0	91.5
40	6.4	93.5

Higher *D* was observed for the ACC produced *via* NaOH/urea than BmimAc (Tables 5.7 and 5.8). This result was due to the higher V_v in ACC produced *via* NaOH/urea. The increasing V_v was associated with the decreasing strength and increasing stress concentration [217]. Dhakal *et al.* reported that the water was presented as free and bound water [140]. Free water travelled through the microvoids and gaps before the saturated-water condition. Thus, the increasing free water was expected with the increase of V_v. Bound water penetrated into the cellulose fibre and capillaries between the fibrils when the saturated-water had been reached. The increasing *D* was also observed with the increasing t_d (Tables 5.7 and 5.8). The lowest *D* for the ACCs produced *via* BmimAc and NaOH/urea were found at an optimal t_d of 60 and 15 min, respectively. These results were due to a good interfacial adhesion between the fibre-matrix at the optimal t_d (Section 4.3.9).

The *D* values may depend on the type of materials, processing methods, and water absorption test conditions. Interestingly, higher *D* with an edge effect was observed for the ACC produced *via* NaOH/urea (17%) as compared to BmimAc (10%). This result was due to the contribution of water from the edges that diffused in parallel directions into the flat surfaces. The elimination of edge effect is obtained without the consideration of dimension of the ACC samples (*e.g.* length (*l*), width (*w*), and thickness(*h*)) during the analysis. Thus, a lower *D* is achieved. As the test samples were relatively small, the effect was substantial. However, with large sheets, the

edge effect was expected to be less significant. The increasing D with the increasing t_d and temperature in the present study was consistent as mentioned in the previous studies [116, 229].

Table 5.7 Water diffusion coefficient for ACC produced *via* BmimAc

t_d (min)	D (10^{-12} m^2/s)					
	23 °C		50 °C		100 °C	
	*With edge effect	**Without edge effect	*With edge effect	**Without edge effect	*With edge effect	**Without edge effect
30	1.82	1.63	1.91	1.72	3.05	2.73
60	1.13	1.01	1.31	1.18	1.59	1.42
90	1.95	1.74	2.11	1.90	3.61	3.22

*With dimension consideration

**Without dimension consideration

Table 5.8 Water diffusion coefficient for ACC produced *via* NaOH/urea

t_d (min)	D (10^{-12} m^2/s)					
	23 °C		50 °C		100 °C	
	*With edge effect	**Without edge effect	*With edge effect	**Without edge effect	*With edge effect	**Without edge effect
15	5.61	4.63	8.77	7.27	12.16	10.11
30	7.33	6.08	12.8	10.69	14.55	12.08
40	7.41	6.13	14.02	11.61	26.55	22.03

*With dimension consideration

**Without dimension consideration

The interaction between water molecules and free OH groups was expected in ACCs. The increasing V_f was found with the increasing t_d (Tables 5.5 and 5.6). Dhakal *et al.* reported that V_f and V_v affected the water absorption behaviour in biocomposite materials [140]. The increasing V_f was consistent with the increasing free OH groups, leading to the increase of the D value. Alvarez *et al.* reported that the peak area at 3100-3800 cm^{-1} increased, indicating the presence of an increased number of OH groups arising due to the cleavage of alkaline-sensitive bonds [230].

In this study, the possible chemical reaction between alkaline-urea solution and the OH group attached with the cellulose fibre is expressed by Eq. 5.13, as discussed in the previous study [231]:

$$\text{Fibre-OH} + \text{Na(OCN)} \longrightarrow \text{Fibre-O}^{-}\text{Na}^{+} + \text{HOCN (cyanic acid)} \qquad \text{Eq. 5.13}$$

For ACC produced *via* BmimAc, the cleavage of BmimAc-sensitive bonds may increase the number of OH groups. Therefore, the possible chemical reaction between BmimAc and the OH group attached with the cellulose fibre is explained by Eq.5.14, as discussed in the previous study [231]:

$$\text{Fibre-OH} + \text{Bmim(Ac)} \longrightarrow \text{Fibre-O-Bmim}^{+} + \text{HAc (acetic acid)} \qquad \text{Eq. 5.14}$$

These free OH groups were anticipated to contact with the water molecules and form new hydrogen bonding, resulting in the increasing water content in the ACCs. The OH group could be observed from the ATR-FTR spectrum analyses, ranging between 3000-3400 cm^{-1} (Figures 5.4 and 5.6). The increasing absorbance of OH stretching region was observed with the increasing t_d (Figures 5.5 and 5.7). This result was consistent with the increasing D in ACCs (Tables 5.7 and 5.8).

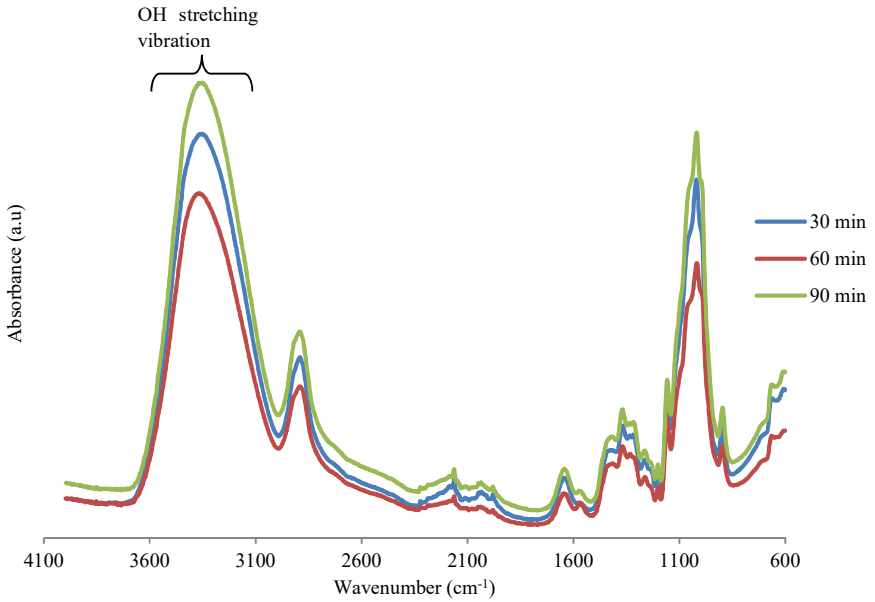

Figure 5.4 ATR-FTIR spectrum at different dissolution times for ACC produced *via* BmimAc.

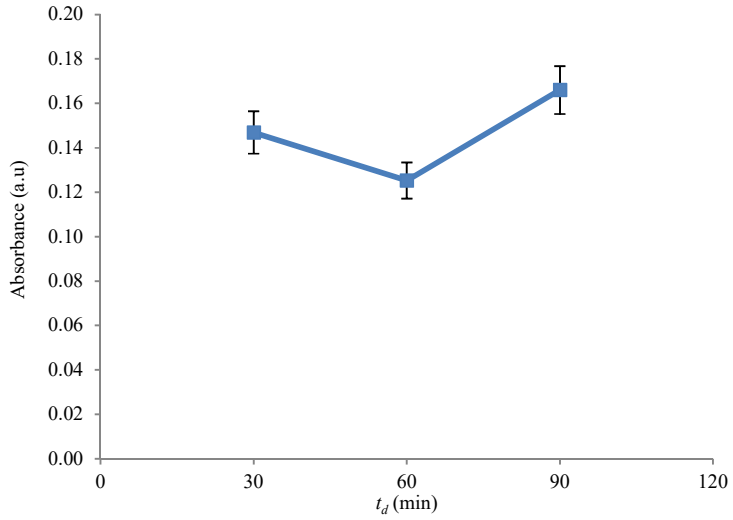

Figure 5.5 Absorbance (OH stretching) at different dissolution times for ACC produced *via* BmimAc.

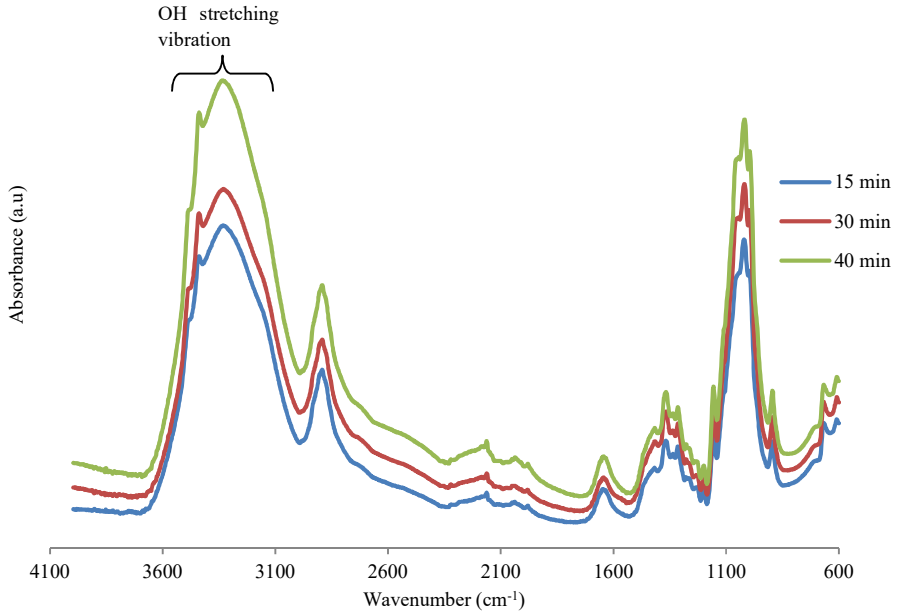

Figure 5.6 ATR-FTIR spectrum at different dissolution times for ACC produced *via* NaOH/urea.

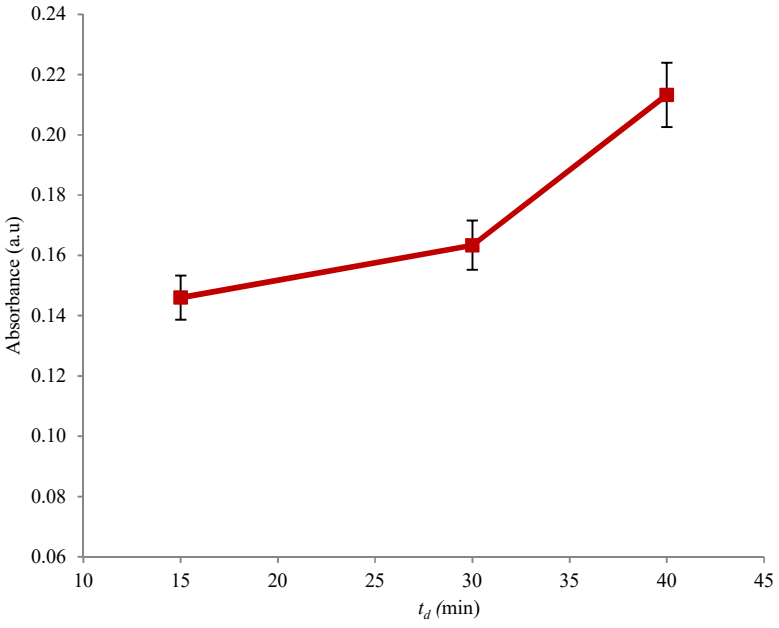

Figure 5.7 Absorbance (OH stretching) at different dissolution times for ACC produced *via* NaOH/urea.

The variability of *D* values was due to the changing molecular structure of cellulose in the ACCs, due to the increasing t_d. Adhikary *et al.* reported that the increasing CrI decreased the water absorption in biocomposite materials [145]. This finding was due to the less accessibility of water into the crystalline region. Ibbett *et al.* reported that the shifts at 89.5 and 88.5 ppm associated to the crystalline region were unchanged, as examined from NMR [213]. The increasing CrI with the increasing t_d was observed (Section 4.3.6), corresponding to the increasing *D* as the t_d increased as discussed previously (Tables 5.7 and 5.8). The increasing *D* was expected due to the increase of the non-crystalline region (partially ordered or disordered region) in the ACC [213]. The non-crystalline region was known to absorb water due to the less ordered cellulose structure as compared to the fully ordered region. The increasing non-crystalline region was consistent with the increasing V_m (Section 4.3.6 and 4.3.8). The increase of the partially ordered (paracrystalline) region was expected with the increase of CrI. The presence of paracrystalline region could be seen from the decreasing (004) plane associated with $2\theta = 35°$ (Section 4.3.6), as also reported in a previous study [68].

The crystallite size was expected to associate with *D*. Chemical modification on cellulose fibre reduced the crystallite size [180, 232]. This result encouraged a large surface area of crystallites, providing sufficient mechanical interlocking between fibre-matrix and reducing water absorption. In the present study, the increasing crystallite sizes in (110), $(1\bar{1}0)$, and (200) planes were observed with the increasing t_d (Section 4.3.6). At higher t_d, the increasing crystallite sizes reduced their surface area. This result was due to the formation of the paracrystalline layer around the cellulose fibres, reducing the mechanical interlocking between the fibre-matrix and increasing the *D* values in ACCs.

The different electronegative characters for both solvents (BmimAc and NaOH/urea) were expected to affect the *D* value in ACCs. The electronegativity effect on the water absorption behaviour had been reported in the previous study by Jacob *et al.* [232]. A higher

electronegative atom provided a higher possibility to draw its surrounding electron, contributing to strong hydrogen bonding between cation and the dissolved cellulose (matrix). Thus, the decreasing *D* was observed in the ACCs. A higher electronegativity in imidazolium ($C_8H_{15}N_2^+$) than sodium (Na^+) were reported to be 2.16 and 0.9 eV, respectively [233]. Thus, the hydrogen bond formed between imidazolium and matrix provided a stronger bonding than the hydrogen bond formed between the sodium and matrix. These results were consistent to the lower *D* found in the ACC produced *via* BmimAc as compared to NaOH/urea. The possible illustration of the interaction between the matrix and cellulose fibre *via* the solvent cation (as a bridge) for ACC produced *via* BmimAc and NaOH/urea are illustrated in Figures 5.8 and 5.9, respectively.

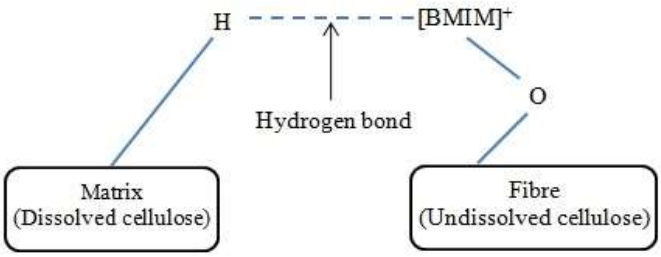

Figure 5.8 Schematic illustration of the interaction between fibre and matrix for ACC produced *via* BmimAc.

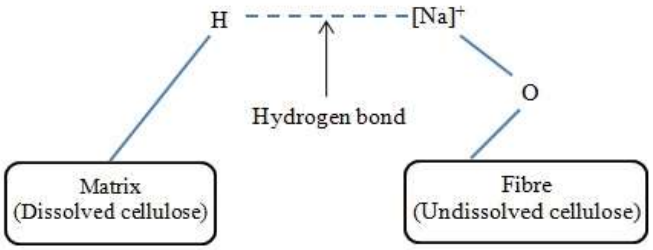

Figure 5.9 Schematic illustration of the interaction between fibre and matrix for ACC produced *via* NaOH/urea.

Interestingly, one to two magnitude orders of higher *D* values were found in ACCs compared to other bio-based composite materials (Table 5.9). The relatively high *D* of ACCs is undoubtedly due to both reinforcing and matrix phases being composed of non-derivatised cellulose. The cellulose molecule is known to be highly hydrophilic due to the presence of three OH groups with each glucose unit [144, 170]. It has been reported that the presence of OH and other polar group in cellulose fibres result in poor compatibility between fibre and matrix, leading to an increase in the water absorption [234]. The observation of widespread fibre-matrix interfacial failure in ACCs [216] suggested that the existence of an interface or interphase due to the presence of OH group, giving an increase in *D*. Nevertheless, the *D* values in ACCs are comparable to those of wood-plastic composites using radiata pine sawdust (30-50 wt.%) reinforced with thermoplastic polymers (PP and HDPE) [145]. A higher *D* is observed in amorphous cellulose than ACCs (Table 5.9), emanating from the highly disordered cellulose system in amorphous cellulose.

Table 5.9 Water diffusion coefficients of various bio-based materials

No	Materials	D (m^2/s)	Refs.
1	ACCs with edge effect	$1.82 - 26.55 \times 10^{-12}$	Present study
2	ACCs without edge effect	$1.63 - 22.03 \times 10^{-12}$	Present study
3	40-50 wt.% sawdust - PP	$2.76 - 9.45 \times 10^{-12}$	[145]
4	50 wt.% rice hull - HDPE	4.63×10^{-13}	[145, 146]
5	30 wt.% starch - natural rubber	$0.65 - 5.61 \times 10^{-14}$	[147]
6	20 wt.% sisal - PP	2.30×10^{-13}	[116]
7	15 wt.% sisal fibre - starch	9.42×10^{-13}	[51]
8	40 wt.% ramie fibre - starch	2.80×10^{-14}	[40]
9	50 wt.% wood - recycled HDPE	5.94×10^{-12}	[145]
10	30 wt.% wood - recycled HDPE	3.24×10^{-12}	[145]
11	30 wt. % flax - polylactide	1.34×10^{-12}	[235]
12	30 wt. % sisal - polylactide	1.7×10^{-12}	[236]
13	Amorphous cellulose	6.7×10^{-11}	[237]

The experimental water concentration results were compared with the theoretical mathematical expression of the Fick's law. The equation was developed in the MATLAB software and the theoretical data were calculated according to the input data in the equation. The comparison between experimental and theoretical data for ACC produced *via* BmimAc and NaOH/urea are presented in Figures 5.10 and 5.11, respectively. The experimental and theoretical data fitted reasonably well at lower temperatures (23 and 50 °C), following the Fickian diffusion mode.

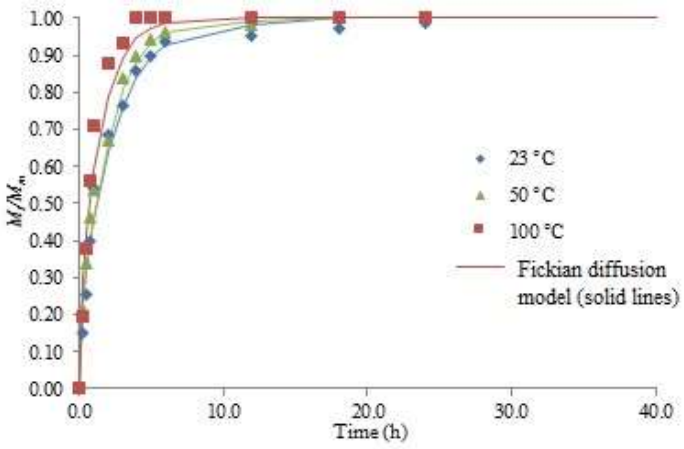

Figure 5.10 A comparison between experimental (data points) and theoretical data (solid line) at dissolution time of 30 min for ACC produced *via* BmimAc.

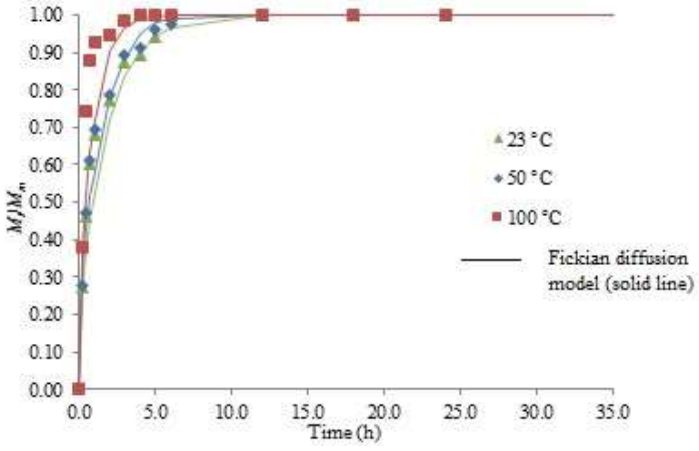

Figure 5.11 A comparison between experimental and theoretical data (solid line) at dissolution time of 30 min for ACC produced *via* NaOH/urea.

For ACC produced *via* BmimAc, the highest slope of ln(D) against 1/T was observed at t_d of 90 min (Figure 5.12). The negative slopes indicated the decreasing D with the increasing temperature. The lowest E_a and D_o values at t_d of 60 min were 0.48 kJ/mol and 0.55×10^{-11} m^2/s, respectively (Figure 5.13). This result was consistent with the lowest EMC of 45.3% at t_d of 60 min. The highest E_a and D_o values at t_d of 90 min were 0.92 kJ/mol and 3.85×10^{-11} m^2/s, respectively (Figure 5.13). This result was consistent with the highest EMC of 53.0% at the same t_d of 90 min. Thus, the increasing D_o with the increasing t_d was associated with the increasing EMC and V_v. Meanwhile, the increasing E_a with the increasing t_d was expected due to the stronger temperature dependence at higher water absorption, leading to the increasing molecular mobility of water [229]. The aging effect was found to be significant at t_d of 90 min, which was expected from its shorter saturation time due to poor fibre-matrix adhesion (Section 4.3.9).

The E_a value depends on the D value. However, Jacob *et al.* discovered that the E_a value is inversely proportional to the D value [232] due to the different fibre (hydrophilic) and matrix (hydrophobic) components. Jacob *et al.* stated that the increasing V_f in the biocomposite increases the water absorption and utilises a relatively lower E_a [232]. However, the lowest E_a and D were reported at t_d of 60 min due to the lowest V_v associated with the decreasing stress concentration. Thus, the lowest E_a was required to fill the least void formation in the ACC at t_d of 60 min.

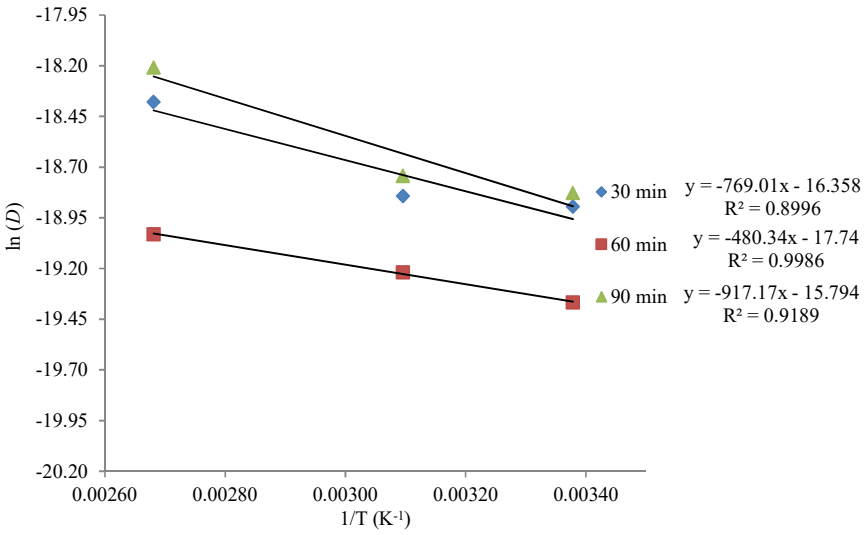

Figure 5.12 Arrhenius dependence of water diffusion coefficients for ACC produced *via* BmimAc.

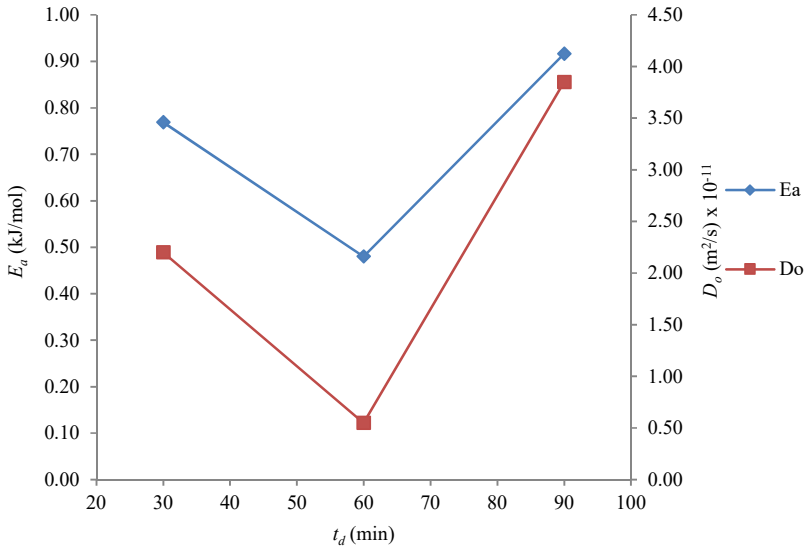

Figure 5.13 Activation energies and diffusivity index at various dissolution times for ACC produced *via* BmimAc.

For ACC produced *via* NaOH/urea, the highest slope of ln(*D*) against 1/T was observed at t_d of 40 min (Figure 5.14). The negative slopes were also observed. The lowest E_a and D_o values at t_d of 15 min were 1.09 kJ/mol and 2.15×10^{-10} m^2/s, respectively (Figure 5.15). This result

was consistent to the lowest EMC of 68.5% at the same t_d. Meanwhile, the highest E_a and D_o values at t_d of 40 min were 1.80 kJ/mol and 32 × 10^{-10} m^2/s, respectively (Figure 5.15). This result was consistent to the highest EMC of 73.9%.

The highest D_o at t_d of 40 min was expected due to the highest V_v. This result represented a driving force for water transportation to reside within the void, leading to the deterioration of mechanical properties. This effect is similar to the aforementioned explanations in the ACC produced *via* BmimAc. Furthermore, the increasing V_f with the increasing t_d was observed, leading to the increase of D. The highest E_a at t_d of 40 min was anticipated due to the molecular mobility, suggesting strong temperature dependence. The increasing E_a with the increasing t_d was expected due to the increasing V_v. Thus, higher stress concentration at longer t_d was expected, consuming higher E_a. The aging effect was found to be significant at t_d of 40 min, which was expected from its shorter saturation time due to poor fibre-matrix adhesion (Section 4.3.9).

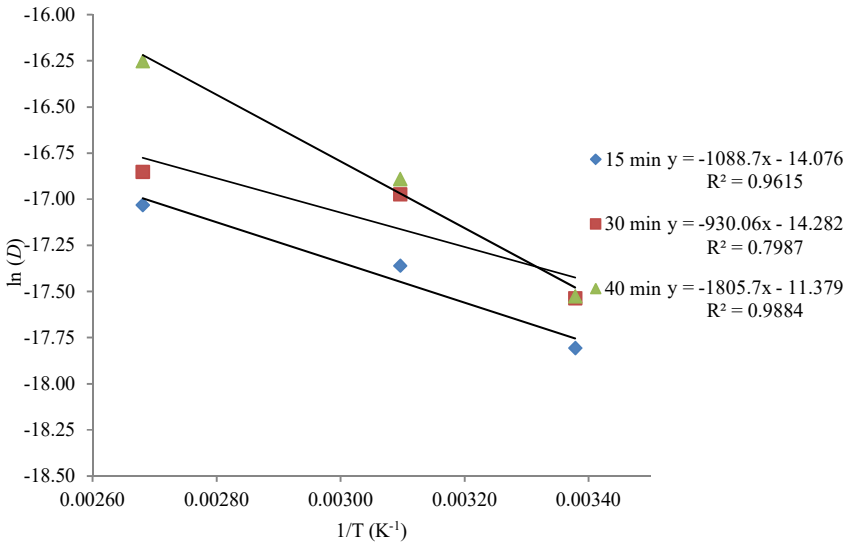

Figure 5.14 Arrhenius dependence of water diffusion coefficients for ACC produced *via* NaOH/urea.

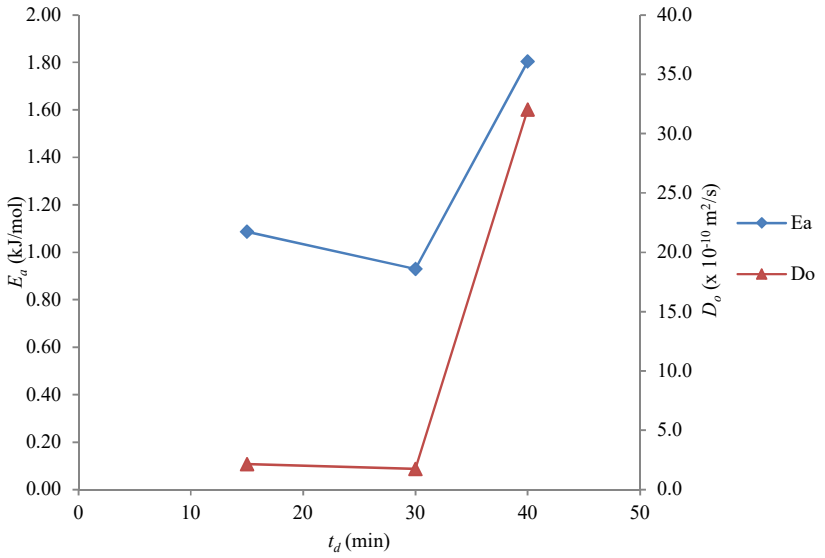

Figure 5.15 Activation energies and diffusivity index at various dissolution times for ACC produced *via* NaOH/urea.

5.4.2 Effects of temperature and dissolution time on thickness swelling behaviour

The shortening saturation time and increasing TS with the increasing temperature were reported for ACC produced *via* BmimAc at t_d of 30 min (Figure 5.16), indicating a similar trend to the water absorption (Figure 5.1). The saturation time at 23, 50, and 100 °C were around 18, 12, and 5 h, respectively. Meanwhile, the TS values at 23, 50, and 100 °C were 35.0, 36.0, and 38.0%, respectively. These results were associated with the high kinetics of the absorbed water at high temperature, leading to a quick saturation time. The increasing slopes with the increasing temperature were also spotted, indicating the increasing water mobility and leading to the increase of TS. A similar result was also observed for ACC produced *via* NaOH/urea at t_d of 30 min.

The increasing K_{SR} was observed with the increasing t_d and temperature (Figure 5.17). The highest K_{SR} was found at t_d of 90 min, followed by 30 and 60 min. Meanwhile, the highest K_{SR} was also seen at the temperature of 100 °C, followed by 50 and 23 °C. The higher value of K_{SR}

was associated with the higher swelling rate, showing that the ACC had a shorter saturation time. This finding corresponded to the aforementioned discussion in the previous paragraph. The shortest saturation time was found at 100 °C. It was also expected that the similar result could be drawn from t_d of 90 min due to its highest K_{SR} observed in Figure 5.17. This result was also possibly due to the poor fibre-matrix adhesion with large intralaminar debonding at t_d of 90 min, allowing water to easily access into the cellulose (Section 4.3.9).

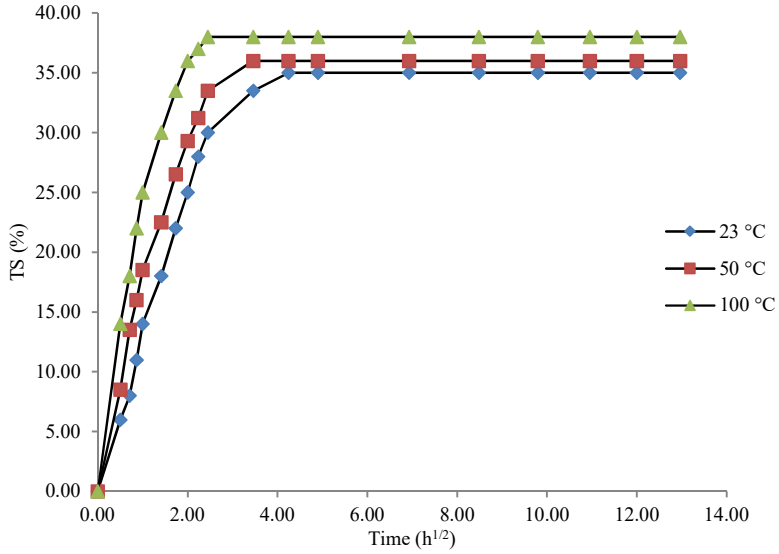

Figure 5.16 Temperature effect on thickness swelling behaviour for ACC produced *via* BmimAc.

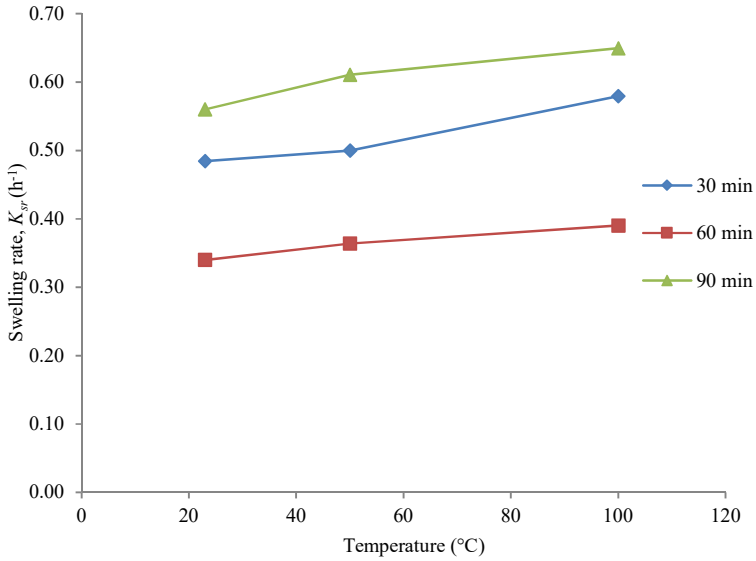

Figure 5.17 Temperature effect on swelling rate for ACC produced *via* BmimAc.

The shortening saturation time and increasing TS with the increasing temperature were reported for ACC produced *via* NaOH/urea at t_d of 30 min (Figure 5.18), showing a similar trend of the water absorption (Figure 5.2). In comparison to ACC produced *via* BmimAc at t_d of 30 min, a similar saturation time at each temperature was observed. The saturation time at 23, 50, and 100 °C were 18, 16, and 6 h, respectively. Meanwhile, the TS values at 23, 50, and 100 °C were 36.5, 40.5, and 41.5%, respectively. The higher TS values were discovered in ACC produced *via* NaOH/urea compared to BmimAc. This result was expected due to the higher V_v, leading to higher TS.

The increasing K_{SR} was observed with the increasing t_d and temperature (Figure 5.19). The highest K_{SR} was found at t_d of 40 min, followed by 30 and 15 min. Meanwhile, the highest K_{SR} was also observed at the temperature of 100 °C, followed by 50 and 23 °C. The higher value of K_{SR} was associated with the higher swelling rate, indicating that the ACC has a shorter saturation time. This finding corresponded to the aforementioned discussion in the previous paragraph. The shortest saturation time was found at 100 °C. The similar result could be drawn

from t_d of 40 min due to its highest K_{SR} observed in Figure 5.17. This result was possibly due to the poor fibre-matrix adhesion with large intralaminar debonding at t_d of 40 min, allowing water to easily access into the cellulose (Section 4.3.9).

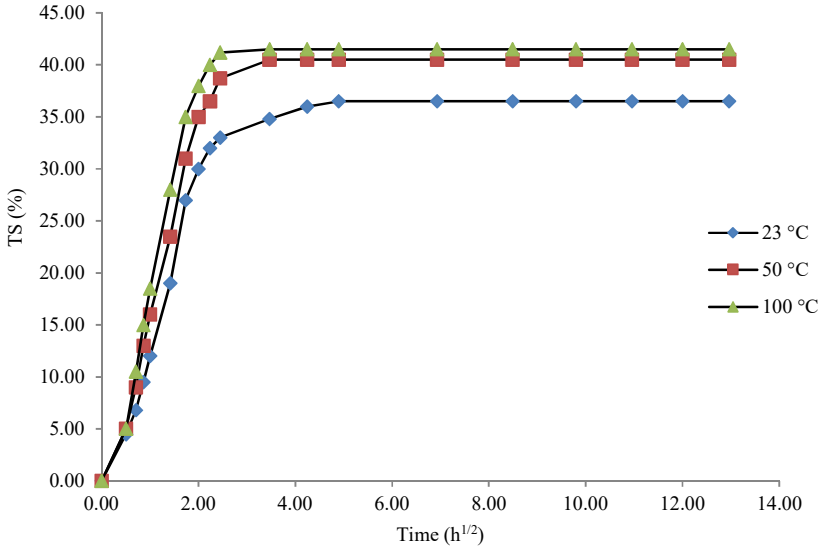

Figure 5.18 Temperature effect on thickness swelling behaviour for ACC produced *via* NaOH/urea.

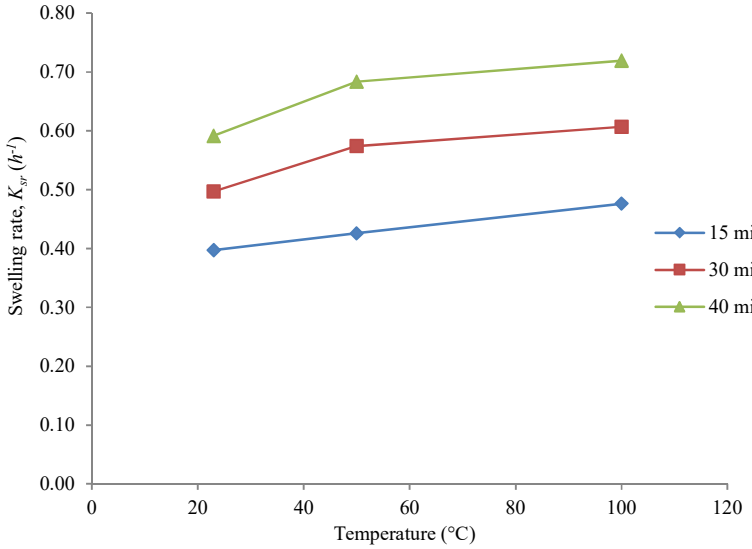

Figure 5.19 Temperature effect on swelling rate for ACC produced *via* NaOH/urea.

Figures 5.20 and 5.21 show the comparison between the empirical model and the experimental TS data for ACCs produced *via* BmimAc and NaOH/urea, respectively. The swelling model fitted reasonably well with the experimental data. A strong correlation between the experimental and empirical model for all ACCs was observed, represented from a higher R^2 of above 0.90.

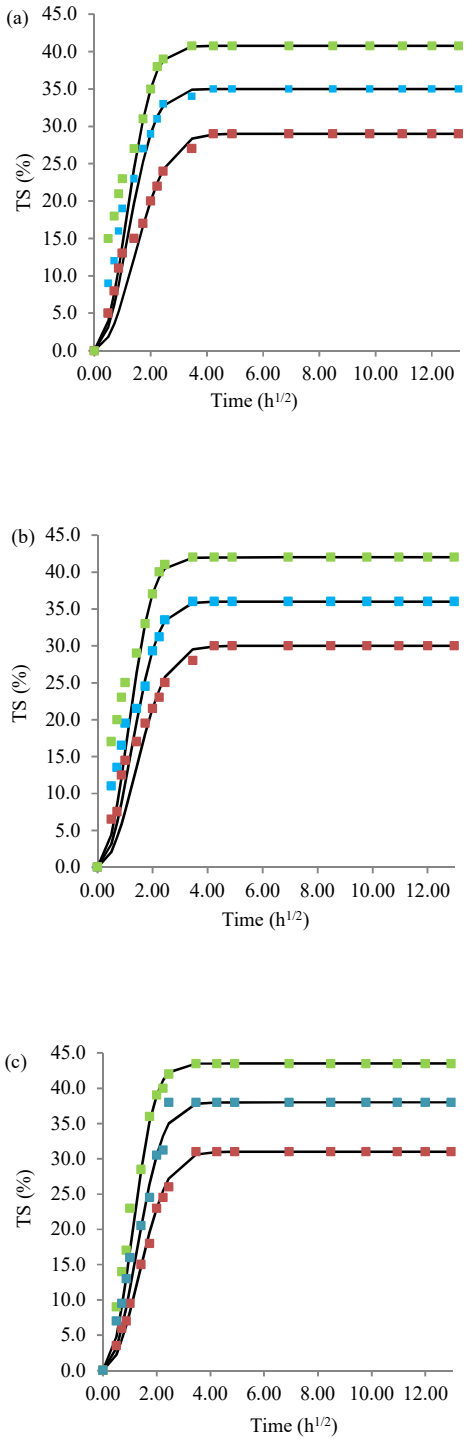

Figure 5.20 Correlation between experimental and theoretical thickness swelling data for ACC produced *via* BmimAc: (a) 23, (b) 50, and (c) 100 °C, respectively.

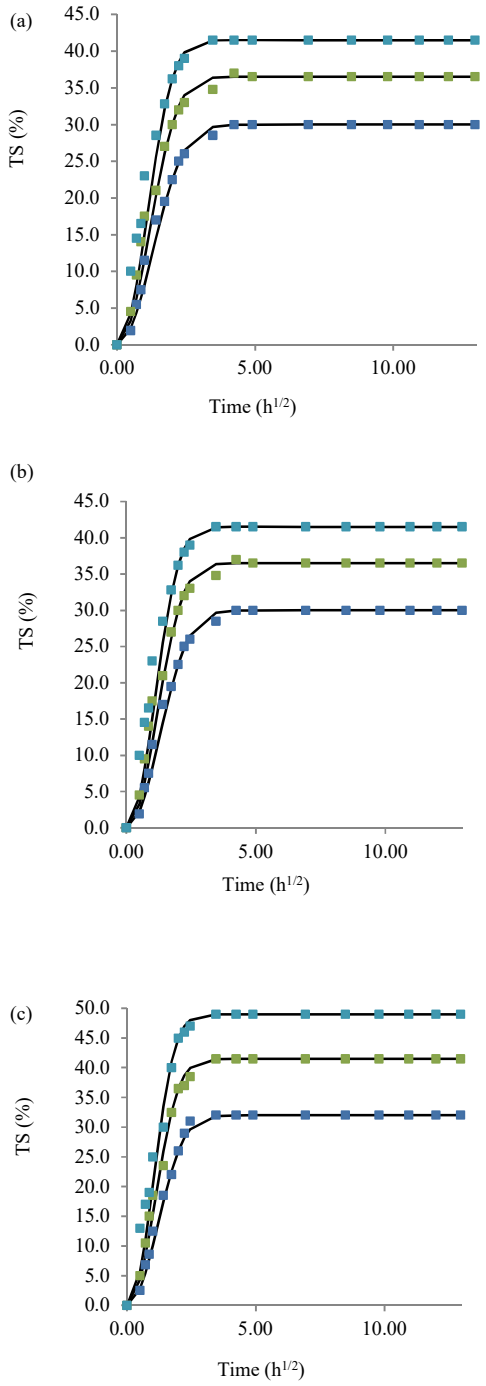

Figure 5.21 Correlation between experimental and theoretical thickness swelling data for ACC produced *via* NaOH/urea: (a) 23, (b) 50, and (c) 100 °C, respectively.

The linear relationships between the equilibrium of TS and EMC for the ACCs produced *via* BmimAc and NaOH/urea are presented in Figures 5.22 and 5.23. This finding correlated to the previous work by Adhikary *et al.* [145]. A stronger relationship was observed in the ACCs produced *via* BmimAc compared to NaOH/urea, as confirmed from R^2. For the ACC produced *via* BmimAc, the R^2 values at 30, 60, and 90 were 0.87, 0.98, and 0.99, respectively. Meanwhile, for the ACC produced *via* NaOH/urea, the R^2 values at 15, 30, and 40 min were 0.87, 0.77, and 0.83, respectively. The linear correlations for ACCs produced *via* BmimAc and NaOH/urea were given by Eq 5.15-5.1, and Eq. 5.18-5.20, respectively.

$$TS_{eq}(\%) = 2.25EMC - 79.08 \quad \text{Eq. 5.15}$$

$$TS_{eq}(\%) = 1.75EMC - 50.26 \quad \text{Eq. 5.16}$$

$$TS_{eq}(\%) = 2.56EMC - 94.61 \quad \text{Eq. 5.17}$$

$$TS_{eq}(\%) = 1.12EMC - 45.48 \quad \text{Eq. 5.18}$$

$$TS_{eq}(\%) = 1.16EMC - 40.66 \quad \text{Eq. 5.19}$$

$$TS_{eq}(\%) = 3.08EMC - 187.75 \quad \text{Eq. 5.20}$$

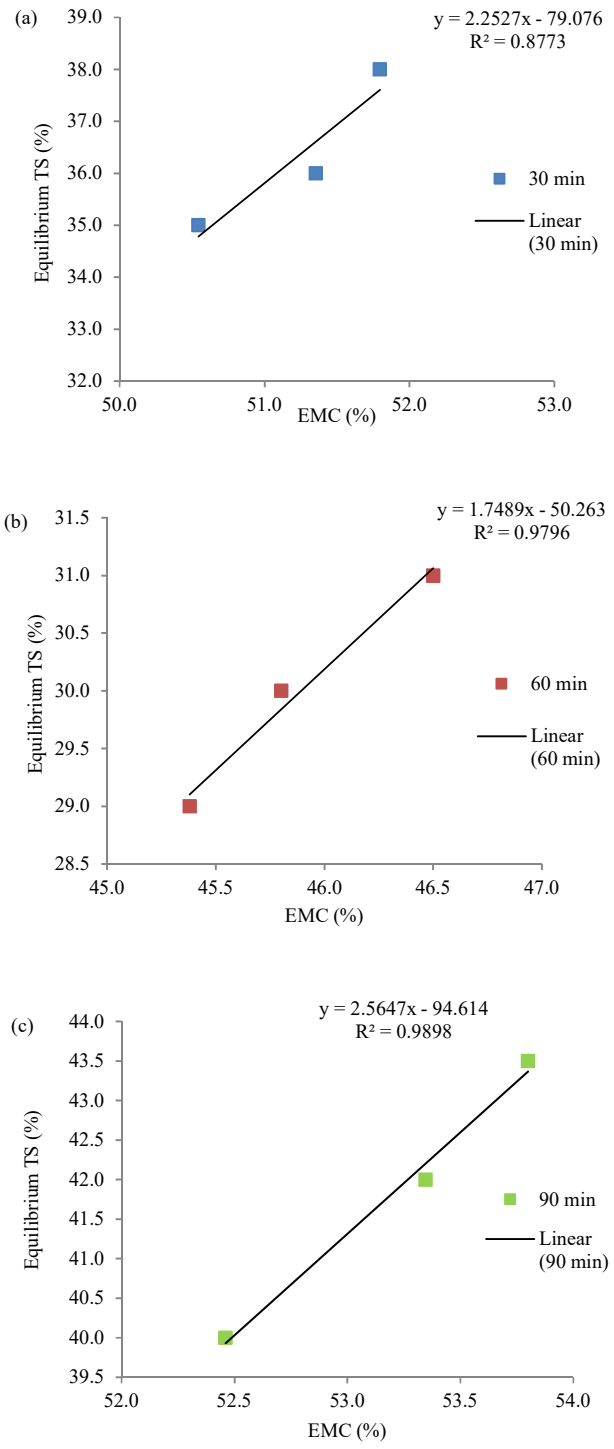

Figure 5.22 Relationship between equilibrium thickness swelling and equilibrium moisture content at various dissolution times for ACC produced *via* BmimAc: (a) 30, (b) 60, and (c) 90 min, respectively.

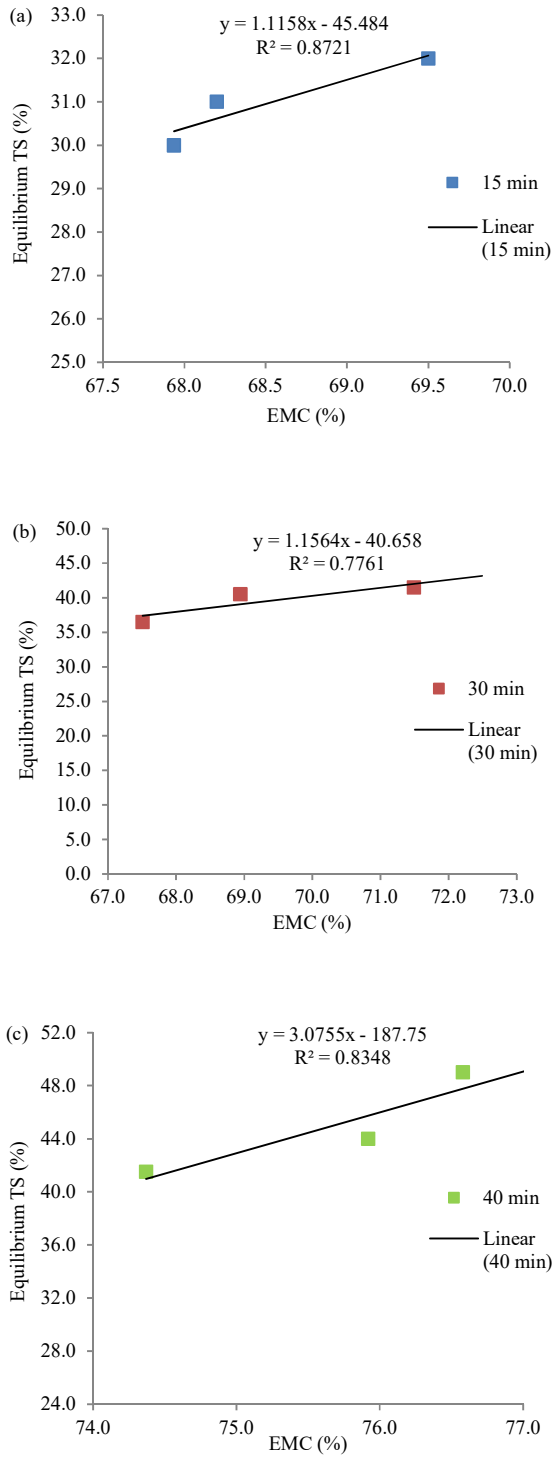

Figure 5.23 Relationship between equilibrium thickness swelling and equilibrium moisture content at various dissolution times for ACC produced *via* NaOH/urea: (a) 15, (b) 30, and (c) 40 min, respectively.

5.4.3 Temperature effect on water concentration

A constant water concentration (M_t/M_m) was observed around the edge (0 and 25 mm) of the samples for the ACCs produced *via* BmimAc and NaOH/urea (Figures 5.24 and 5.27, respectively). The increasing M_t/M_m with the increasing temperatures are presented (Figures 5.24 and 5.27). Mesh sizing of 500 elements is used in ANSYS analyses.

The M_t/M_m patterns varied with the increasing thickness, dividing them into three stages: (i) first stage, (ii) second stage, and (iii) third stage. The M_t/M_m pattern as a function of thickness was similar for the ACCs produced *via* BmimAc and NaOH/urea. In the first stage, the M_t/M_m rapidly decreased from 0 to 1.25 mm. Then, the M_t/M_m maintained at a constant value from 1.25 to 23.75 mm. In the last stage, the M_t/M_m rapidly increased from 23.75 to 25 mm (Figures 5.24 and 5.27). The rapid rises at both ends are due to the numerical singularity.

For the ACC produced *via* BmimAc, the saturation times at 23, 50, and 100 °C were 18, 12, and 6 h, respectively (Figure 5.24). The direction of water concentration is measured in *x*-direction. These results showed that the saturation time at high temperature was quicker than at low temperature. A similar pattern of decreasing saturation times with the increasing temperatures was also observed from the experimental works (Figure 5.1). The examples of the M_t/M_m profiles at temperatures of 23 and 100 °C and t_d of 30 min are presented in Figures 5.25 and 5.26. The saturation times from the M_t/M_m profiles at 23 and 100 °C were consistent with the saturation times observed in Figure 5.1. The increasing M_t/M_m profiles as the time increased was observed, presented by the increase of the blue scale from 0.29 to 1.00 at 1 and 18 h, respectively (Figure 5.25).

For ACC produced *via* NaOH/urea, the saturation times at 23, 50, and 100 °C were 12, 10, and 6 h, respectively (Figure 5.27). A similar result to the ACC produced *via* BmimAc was observed, indicating the decreasing saturation time with the increasing temperature. The

saturation times at 23, 50, and 100 °C were comparable to the saturation times observed in Figure 5.2. The examples of the M_t/M_m profiles at temperatures 23 and 100 °C and t_d of 30 min are presented in Figures 5.28 and 5.29. The saturation times from M_t/M_m profiles at 23 and 100 °C were consistent with the saturation times observed in Figure 5.2. The increasing M_t/M_m profiles as the increasing time was observed, indicated by the increase of the blue scale from 0.67 to 1.00 at 1 and 12 h, respectively (Figure 5.28).

In comparison, higher M_t/M_m was reported for the ACC produced *via* NaOH/urea than BmimAc due to its higher V_v formed during the processing. Thus, the water diffusion was accelerated into the ACC, which experienced a significant decrease in the mechanical properties. From the aforementioned discussion, the D for ACC produced *via* NaOH/urea was one magnitude order higher than the ACC produced *via* BmimAc.

Validation of the model can be done through the water absorption test. The water content at a specified interval time is identified by measuring the weight difference between the dry and wet samples a specified interval time.

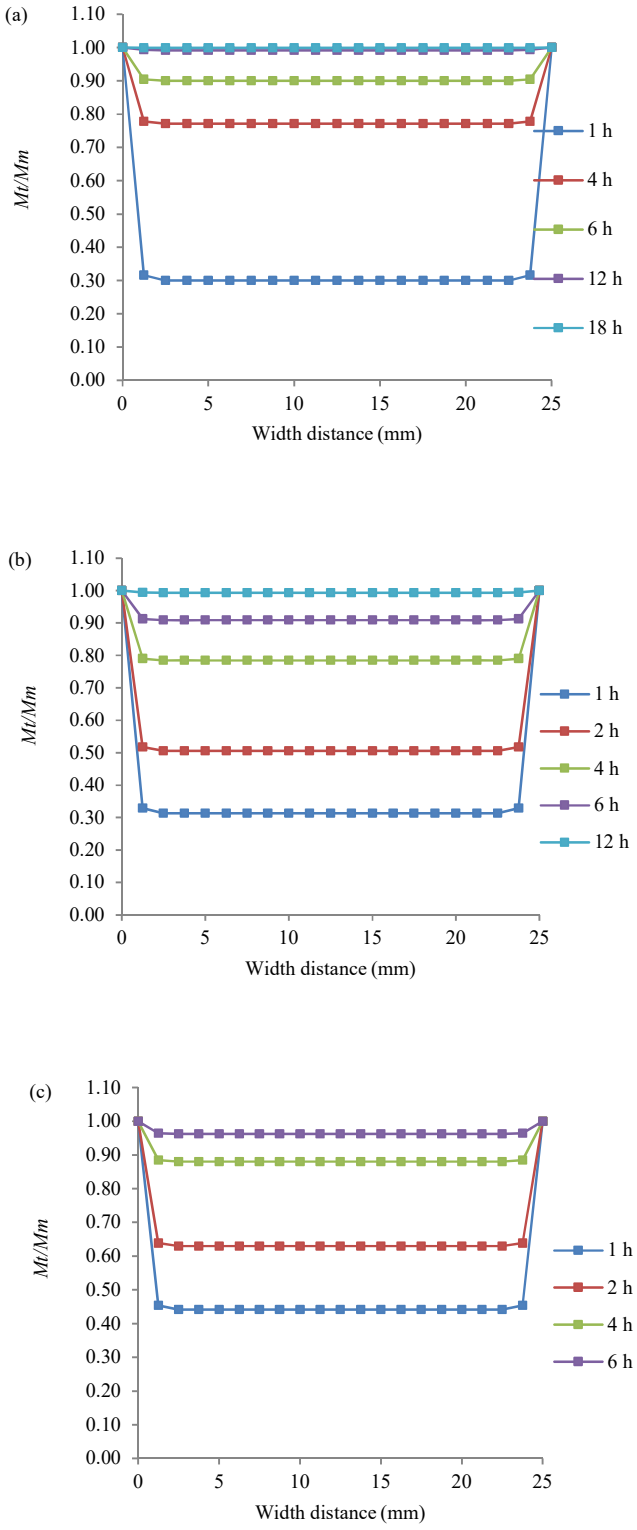

Figure 5.24 Water concentration as a function of width distance for ACC produced *via* BmimAc at various temperatures: (a) 23, (b) 50, and (c) 100 °C.

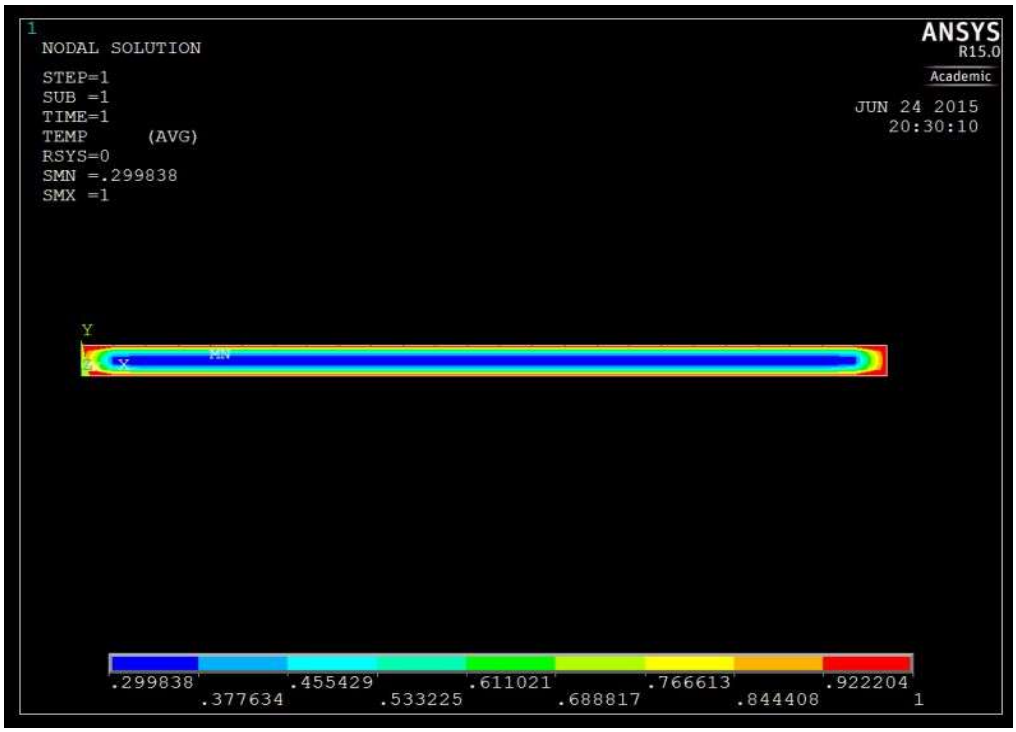
1
NODAL SOLUTION
STEP=1
SUB =1
TIME=1
TEMP (AVG)
RSYS=0
SMN =.299838
SMX =1
ANSYS
R15.0
Academic
JUN 24 2015
20:30:10
Y
MN
.299838
.377634
.455429
.533225
.611021
.688817
.766613
.844408
.922204
1

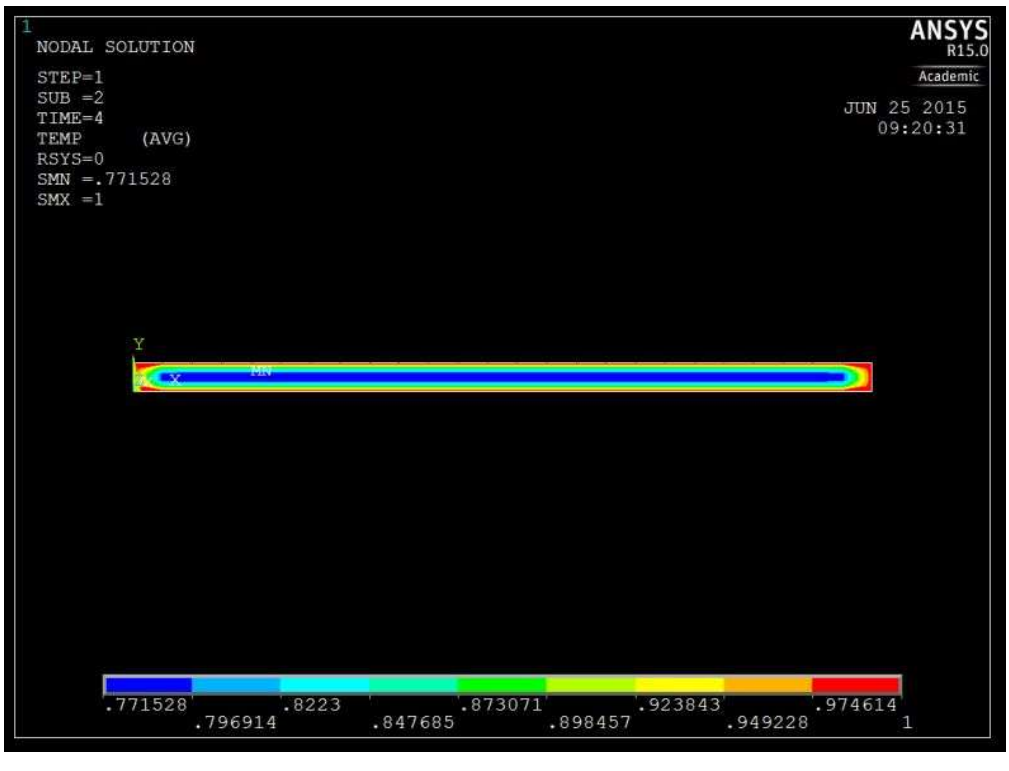
1
NODAL SOLUTION
STEP=1
SUB =2
TIME=4
TEMP (AVG)
RSYS=0
SMN =.771528
SMX =1
ANSYS
R15.0
Academic
JUN 25 2015
09:20:31
Y
MN
.771528
.796914
.8223
.847685
.873071
.898457
.923843
.949228
.974614
1

cont'd.

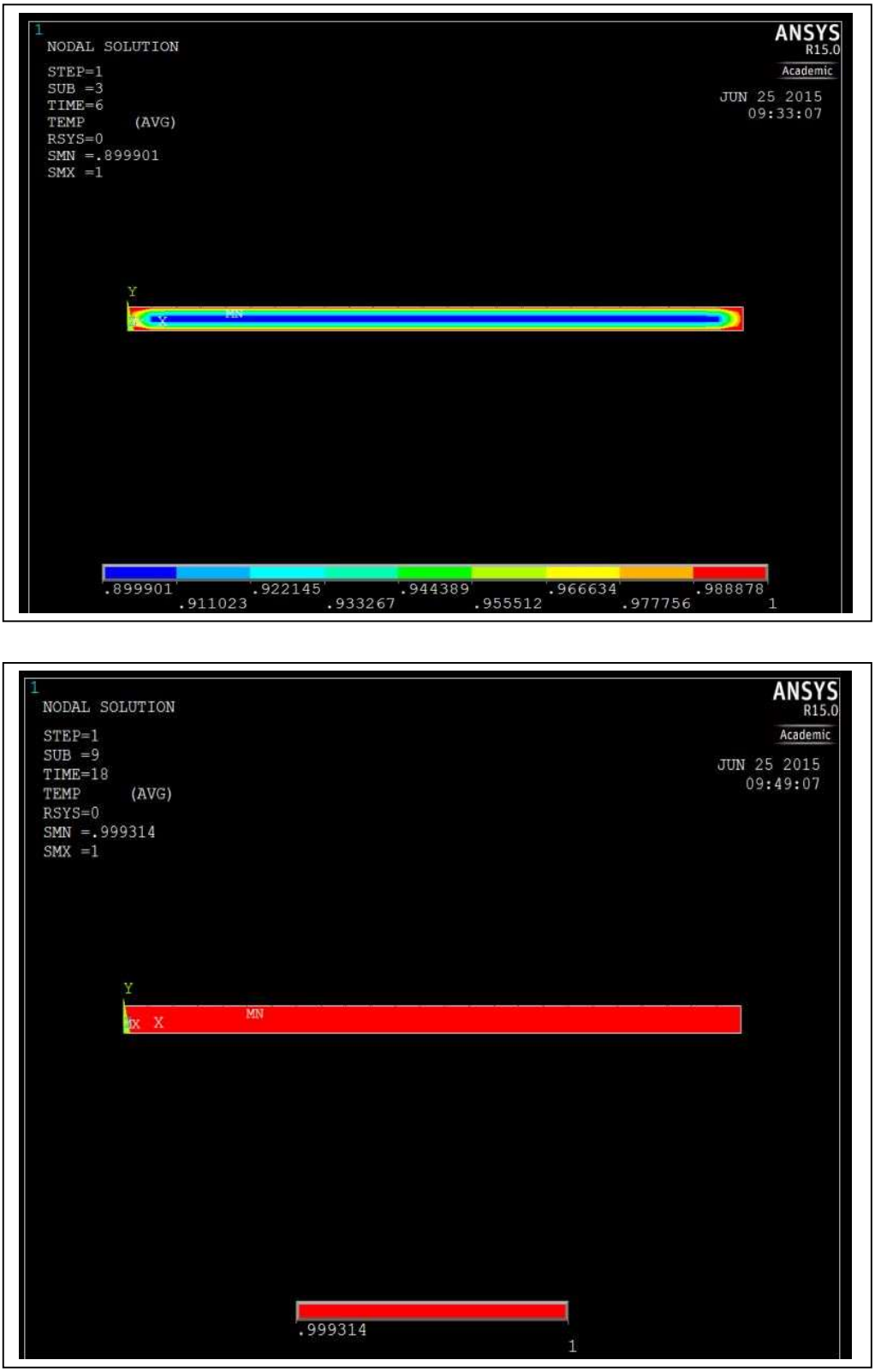

Figure 5.25 Water concentration profiles for ACC produced *via* BmimAc at 23 °C.

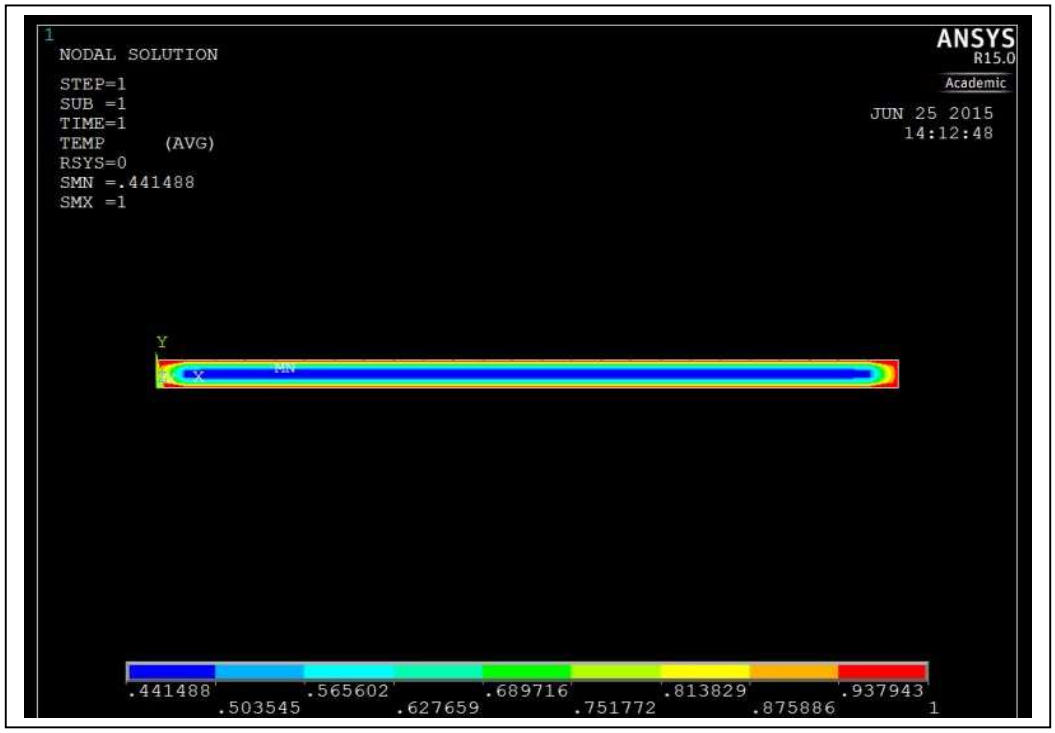
1
NODAL SOLUTION
STEP=1
SUB =1
TIME=1
TEMP (AVG)
RSYS=0
SMN =.441488
SMX =1
ANSYS
R15.0
Academic
JUN 25 2015
14:12:48
Y
MN
.441488
.503545
.565602
.627659
.689716
.751772
.813829
.875886
.937943
1

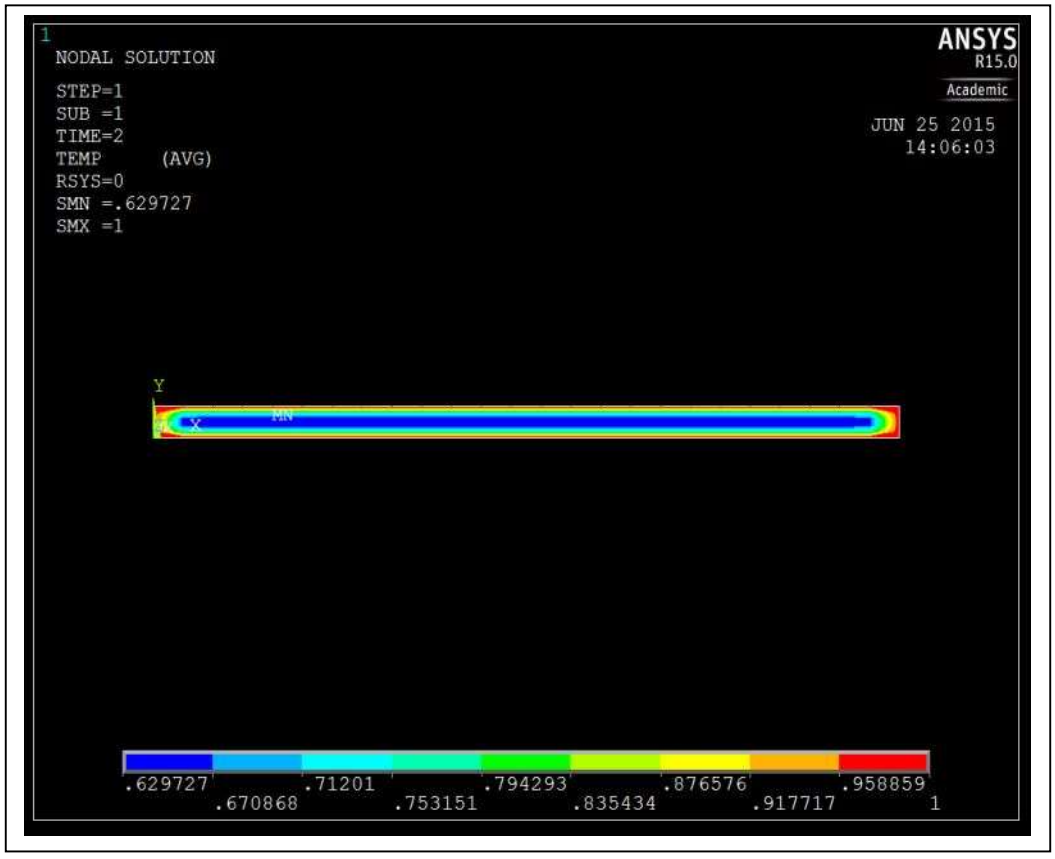
1
NODAL SOLUTION
STEP=1
SUB =1
TIME=2
TEMP (AVG)
RSYS=0
SMN =.629727
SMX =1
ANSYS
R15.0
Academic
JUN 25 2015
14:06:03
Y
MN
.629727
.670868
.71201
.753151
.794293
.835434
.876576
.917717
.958859
1

cont'd.

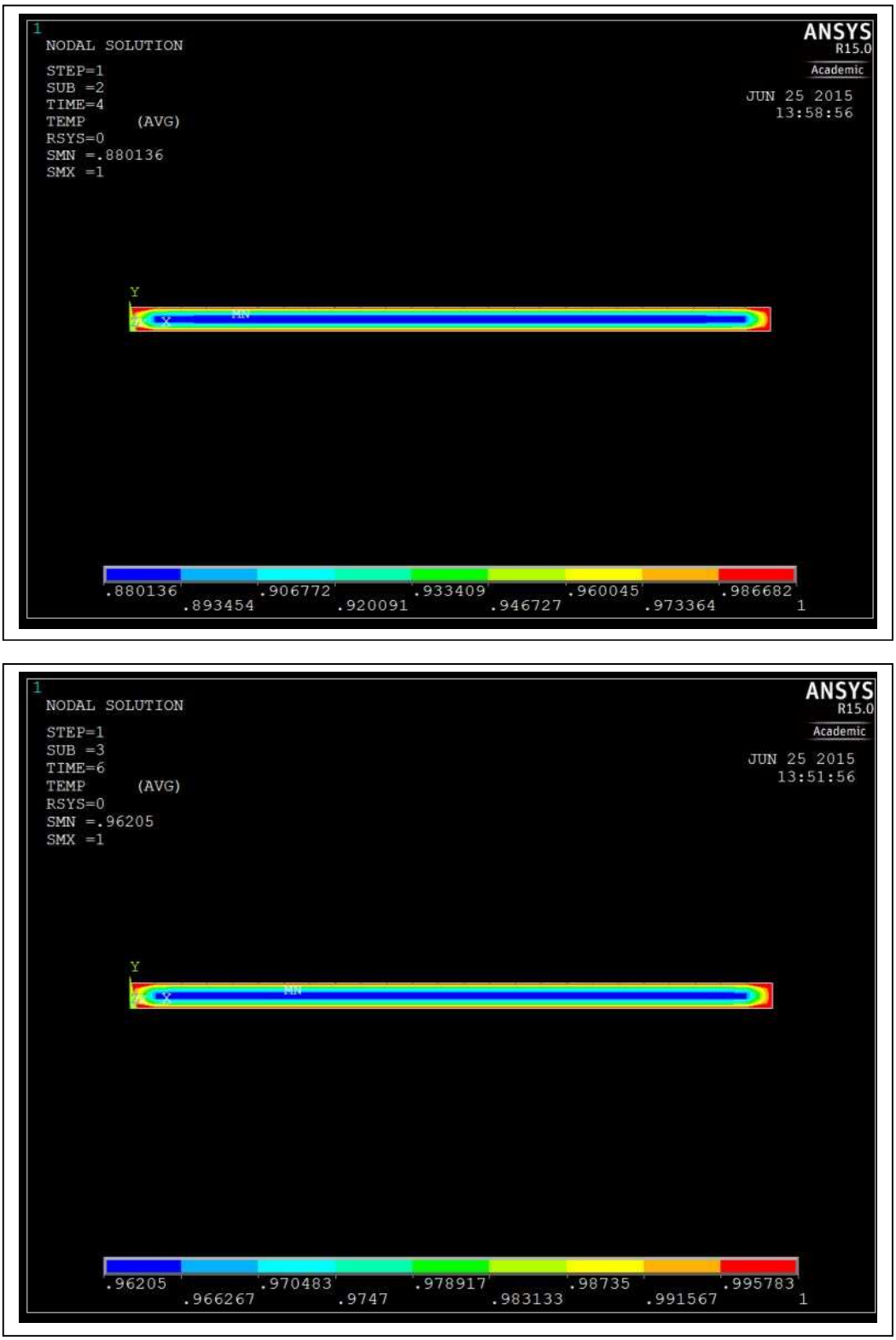

Figure 5.26 Water concentration profiles for ACC produced *via* BmimAc at 100 °C.

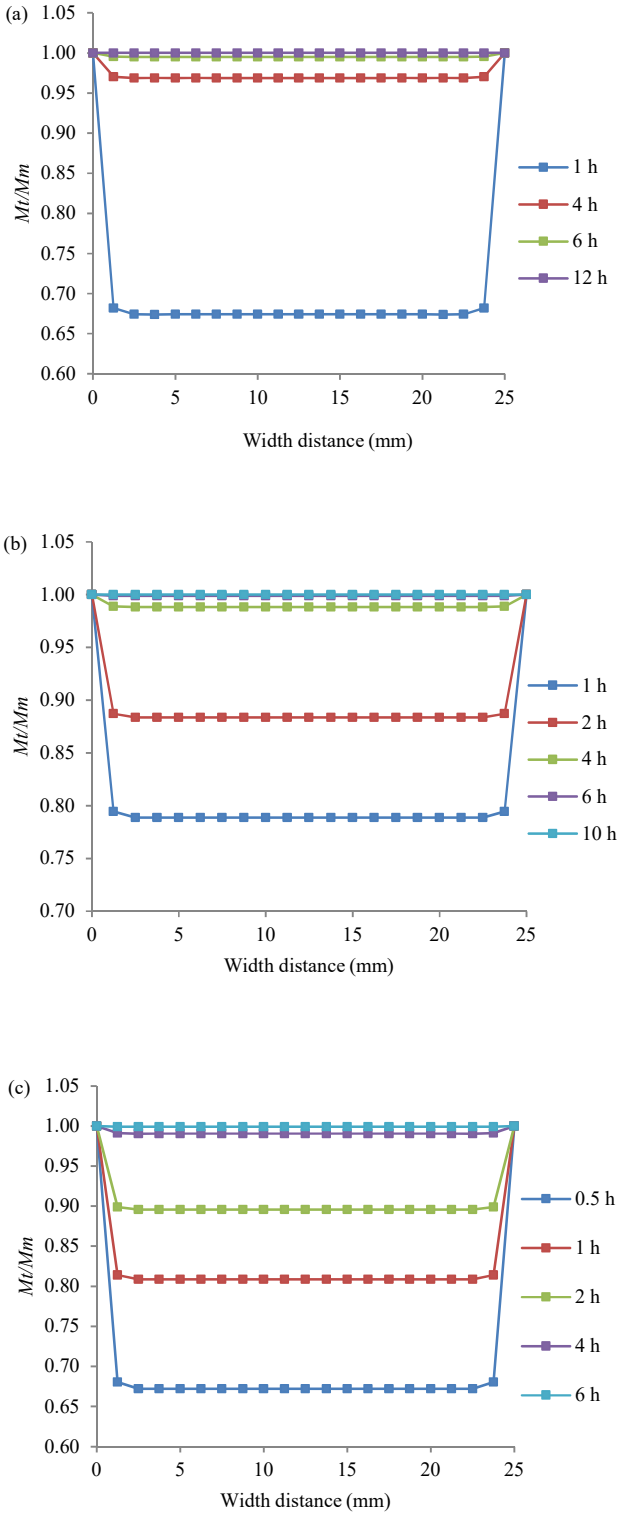

Figure 5.27 Water concentration as a function of width distance for ACC produced *via* NaOH/urea at various temperatures: (a) 23, (b) 50, and (c) 100 °C.

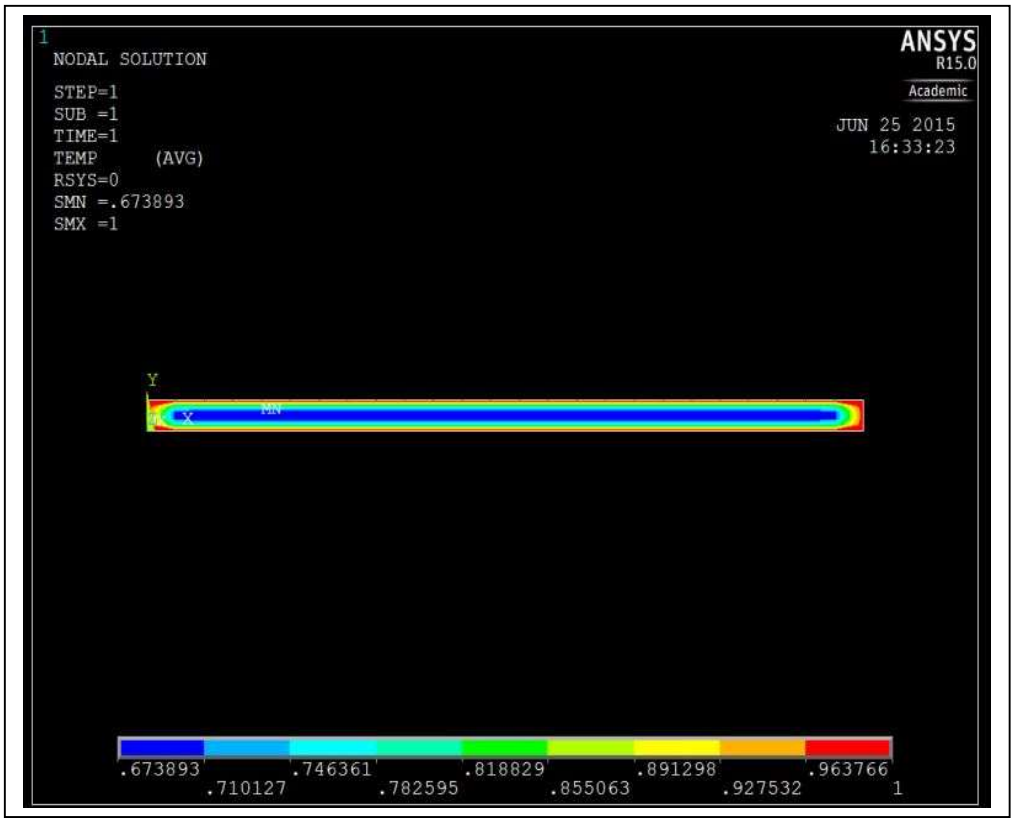
1
NODAL SOLUTION
STEP=1
SUB =1
TIME=1
TEMP (AVG)
RSYS=0
SMN =.673893
SMX =1
ANSYS
R15.0
Academic
JUN 25 2015
16:33:23
Y
MN
.673893
.710127
.746361
.782595
.818829
.855063
.891298
.927532
.963766
1

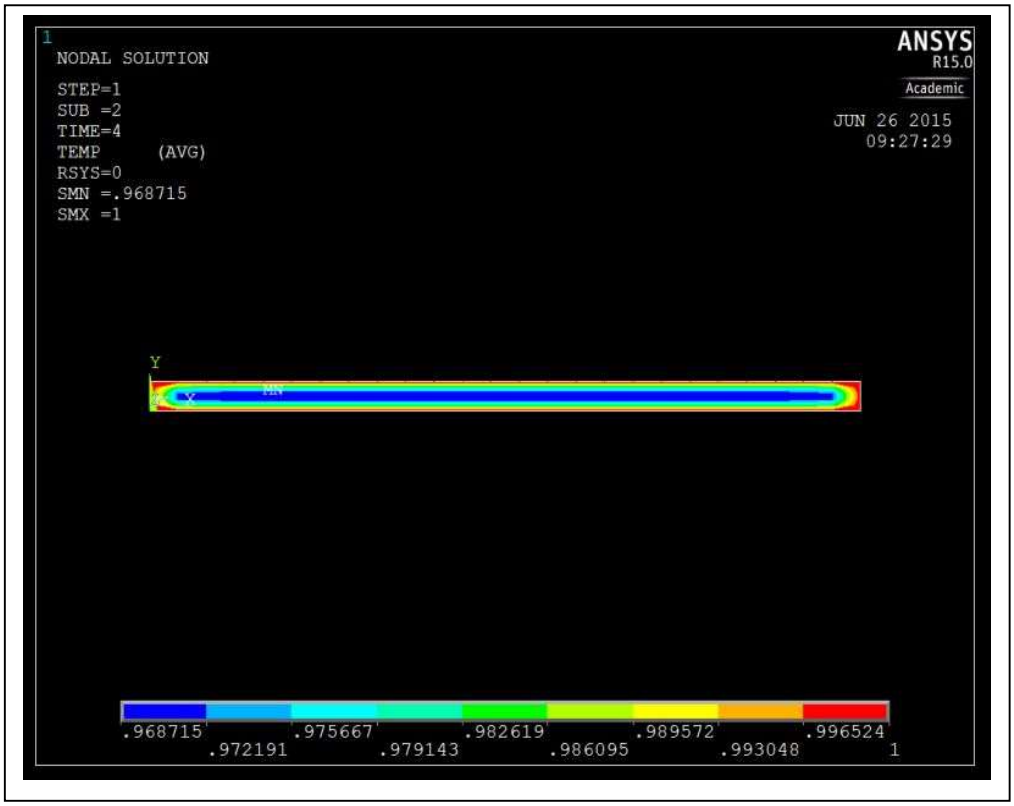
1
NODAL SOLUTION
STEP=1
SUB =2
TIME=4
TEMP (AVG)
RSYS=0
SMN =.968715
SMX =1
ANSYS
R15.0
Academic
JUN 26 2015
09:27:29
Y
MN
.968715
.972191
.975667
.979143
.982619
.986095
.989572
.993048
.996524
1

cont'd.

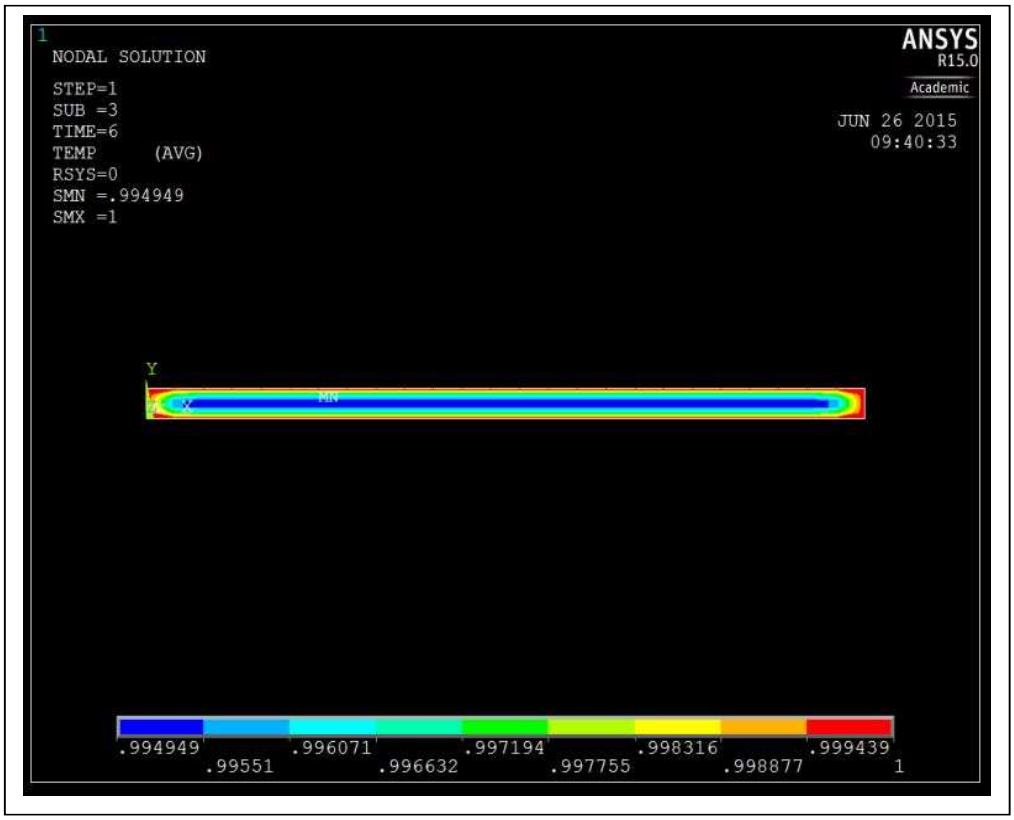

Figure 5.28 Water concentration profiles for ACC produced *via* NaOH/urea at 23 °C.

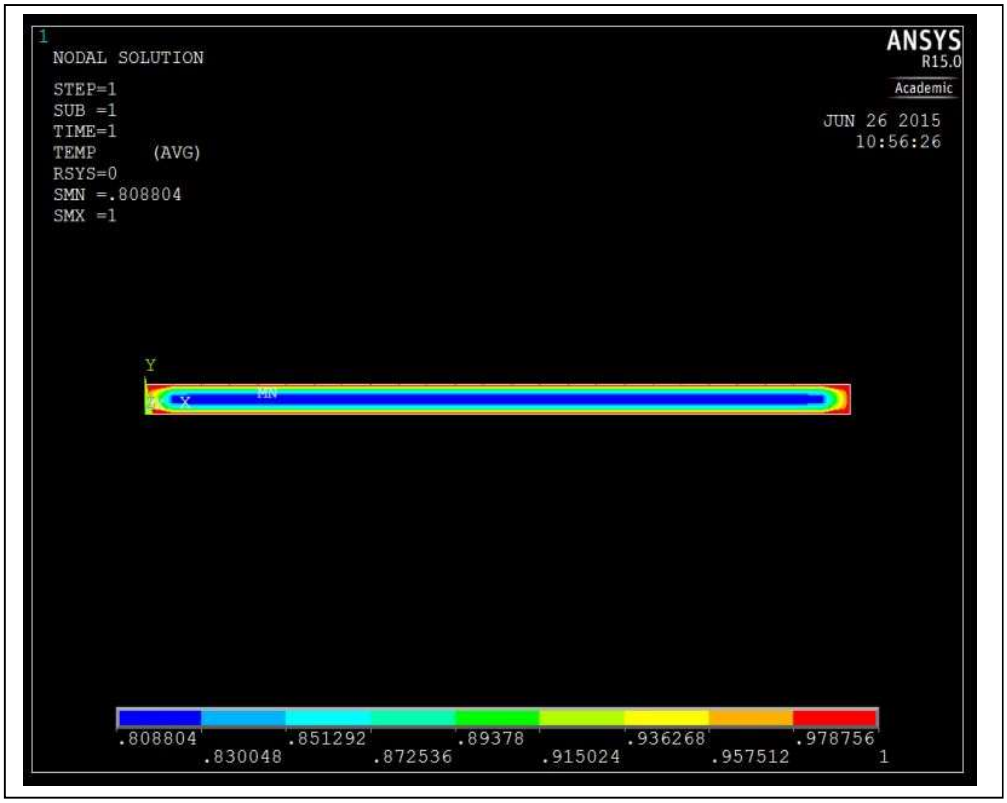
1
NODAL SOLUTION
STEP=1
SUB =1
TIME=1
TEMP (AVG)
RSYS=0
SMN =.808804
SMX =1
ANSYS
R15.0
Academic
JUN 26 2015
10:56:26
Y
MN
.808804
.830048
.851292
.872536
.89378
.915024
.936268
.957512
.978756
1

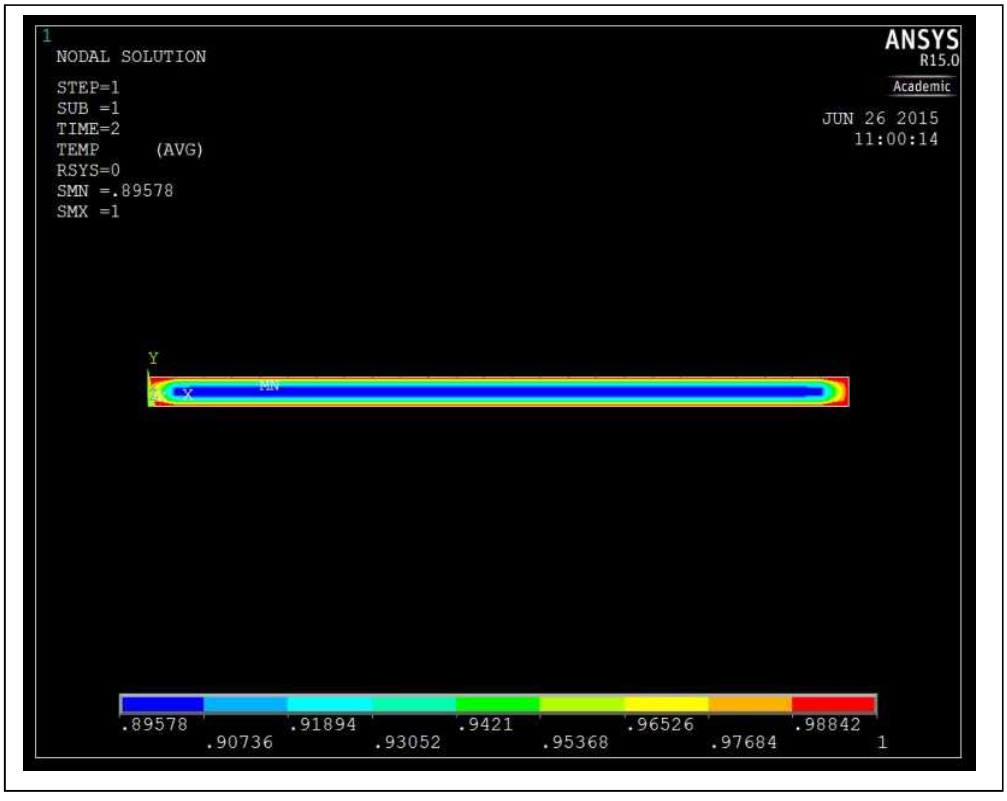
1
NODAL SOLUTION
STEP=1
SUB =1
TIME=2
TEMP (AVG)
RSYS=0
SMN =.89578
SMX =1
ANSYS
R15.0
Academic
JUN 26 2015
11:00:14
Y
MN
.89578
.90736
.91894
.93052
.9421
.95368
.96526
.97684
.98842
1

cont'd.

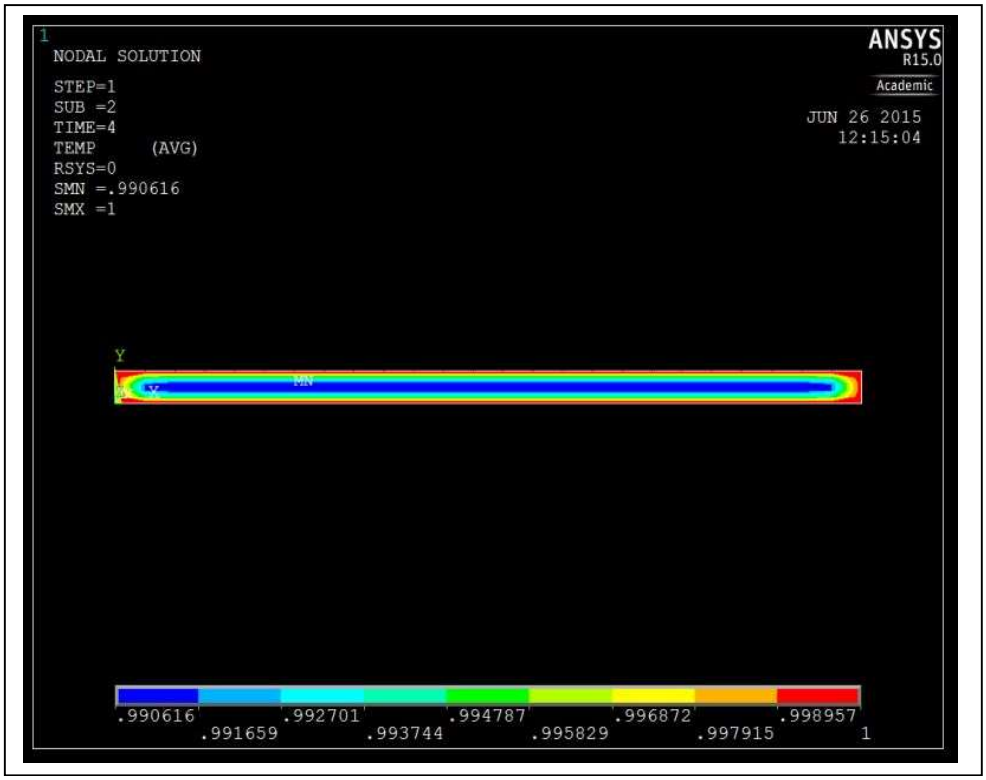

Figure 5.29 Water concentration profiles for ACC produced *via* NaOH/urea at 100 °C.

5.5 Summary of findings

As a conclusion, the summary of the above works are discussed as below:

- The water absorption in ACCs followed the Fickian behaviour because the equilibrium inside the ACCs was rapidly reached and maintained with the independence of time, as shown by the *n* value of 0.5.
- For both ACCs produced *via* BmimAc and NaOH/urea, an increase in temperature was associated with the increase of *D* because a higher temperature will increase water mobility. An increasing *D* on the other hand was associated with an increasing t_d for both ACCs. However, the slight decrease of *D* at t_d of 60 compared to t_d of 30 and 90 min was found for the ACC produced *via* BmimAc because of the lowest V_v at t_d of 60 min, representing a good fibre-matrix adhesion that prevented water penetrating into the ACC. The lowest *D* was observed at t_d of 15 min for the ACC produced *via* NaOH/urea and increased with an increasing t_d for up to 40 min. This result was also associated to the highest V_v observed at t_d of 40 min, thus increasing the *D* for the ACC produced *via* NaOH/urea.
- The increasing D_o with the increase of t_d was associated with the increasing EMC and V_v. Meanwhile, the increasing E_a with the increase of t_d was expected due to the stronger temperature dependence at higher water absorption, leading to the increasing molecular mobility of water. This result was due to the increasing V_v with the increase of t_d, requiring a high E_a to fill the water into the void in the ACC structures. Interestingly, a quite high E_a was also observed at the t_d of 30 min for the ACC produced with BmimAc due to higher V_v.
- The saturation time at 23, 50, and 100 °C for ACC produced *via* BmimAc from the experimental work was consistent with the saturation time observed according to the ANSYS simulation. The saturation time at 23, 50, and 100 °C for the ACC produced

via NaOH/urea from the experimental work was comparable to the ANSYS simulation, although a shorter saturation time was observed at 100 °C. A decrease in M_t/M_m was observed as water diffused from the edge to the centre of the ACC, attaining a constant M_t/M_m in the range of 1.25 to 23.75 mm. Thus, various water concentration profiles were observed with the increasing immersion times and increasing temperatures.

- To conclude, the increasing D in the ACCs was observed with the increasing t_d due to variability in the molecular structure of the ACCs (crystallinity, OH group, crystallite size). The increasing D was also associated with the increasing temperature, as expected with the increasing mobility of the water molecules. A higher D was observed for the ACC produced *via* NaOH/urea compared to BmimAc, because of its higher V_v as compared to the ACC produced *via* BmimAc.

Chapter 6

Effects of water uptake on the mechanical behaviour of all-cellulose composites

6.1 Introduction

Outdoor applications of biocomposite materials are inevitably exposed to severely fluctuating hygrothermal changes [138]. Moisture or water acts as a plasticiser under a static tensile force applied to the composite material [148]. Exposure to water molecules weakens the hydrogen bonding within the cellulose structure by a process of exchange from cellulose/cellulose to cellulose/water hydrogen bonds [180]. This exchange process leads to deterioration in mechanical properties, dimensional instability, and matrix cracking [139]. Previous studies reported that the mechanical properties of conventional composites, bio-based materials and regenerated cellulose decrease due to water absorption [46, 116, 184].

Water threshold is defined as the water in bio-based materials that corresponds with the onset of a plateau in the mechanical properties [170, 184]. The water threshold of cellulose I and II are reported to be 20 and 40 wt.%, respectively [170, 184]. The variation in water threshold for cellulose I and II is due to the differences in the amorphous phase content [170, 184]. The effects of bound and free water on the mechanical properties of cellulose I and II have been determined from differential scanning calorimetry (DSC). Nakamura *et al.* found that the bound water content for cellulose I (19 wt.%) according to DSC was consistent with the water threshold (20 wt.%) observed from the tensile properties [170]. Thus, the conclusion is that the bound water of cellulose I has a significant effect on the mechanical properties in comparison

to cellulose II. The strength, *E* and elongation of cellulose I rapidly increase below a water content of 20 wt.% [170]. In contrast, the *E* value of cellulose II rapidly decreases below a water content of 40 wt.% [184]. However, the effects of bound and free water on the mechanical properties of ACCs have not yet been studied.

Water changes the structural arrangement of the cellulose molecules in wood, according to Salmen *et al.* [174]. A significant spectral shift of the C-O-C glycosidic bond (1160 cm^{-1}) is observed with a high water content [174]. Salmen *et al.* also observed a significant increase in the wavenumber at 3348 cm^{-1} (3OH-O5), associated with the intramolecular hydrogen vibration with the increasing water content of 90 wt.%. The increase of the wavenumber was attributed to the weakening of hydrogen bonding under straining during the deformation test. It has been reported that the determination of stiffness of cellulose nanowhiskers and fibre - matrix interface in a nanocomposite could be done using a Raman spectroscopic measurement [238]. This method involves the measurement of molecular deformation, as seen by a shift in the carbonyl stretch (C-O) mode of cellulose backbone.

In the present study, the relationship between the water threshold and bound water was explored for ACCs. The effects of water on the structural changes were investigated. The relationships between microstructure, crystallinity and viscoelastic properties were examined for the ACCs under various environmentally-controlled conditions.

6.2 Experimental procedures

6.2.1 Preparation of all-cellulose composite samples

The ACCs samples were fabricated using three different t_d using two different solvents (BmimAc and NaOH/urea). The t_d for BmimAc were 30, 60, and 90 min, and 15, 30, and 40

min for NaOH/urea. The P_{HP} for BmimAc and NaOH/urea were 0.25 and 0.50 MPa, respectively.

The samples were conditioned at various RHs including 20, 50, 70, 85, 100%, and wet-saturated conditions at a constant temperature of 23 °C. The water content was calculated using Eq. 6.1 [170]. Three conditions which were (i) 50, (ii) 85% RH, and (iii) wet-saturated were chosen for the experiments in Sections 6.2.4 and 6.2.6.

$$W_c = \left(\frac{W_w}{W_d} - 1 \right) \times 100 \qquad \text{Eq. 6.1}$$

W_c is the water content (%), W_w is the wet sample weight and W_d is the dry sample weight.

6.2.2 Tensile properties

Tensile testing was carried out according to ASTM D3039 [17]. The experimental procedures for tensile testing followed the one used in Section 3.4.5. The number of hydrogen bonds was estimated from the E using Eq. 6.2 [180, 239]:

$$E = kN^{1/3} \qquad \text{Eq. 6.2}$$

where E is Young's modulus (dyn/cm^2), N is the number of effective hydrogen bonds per cm^3, and k for cellulose II is approximately 8×10^3 [180].

6.2.3 Attenuated total reflectance-Fourier transform infrared spectroscopy

Samples at t_d of 60 and 15 min from ACC produced *via* BmimAc and NaOH/urea, respectively, were used. Five replicates were used to observe and measure the effects of water on the OH stretching and bending modes, structural changes and average TCI. For the structural changes analysis, samples were strained in tension using different strains (0.5, 4.0, 6.0, 10.0, 12.0 and

14.0%) which were then immediately examined by ATR-FTIR. Samples were scanned at three different positions. The change in the wavenumber as a function of the tensile strain was used to estimate the elastic modulus of the samples using Eq. 6.3 [238]:

$$\frac{dv}{d\varepsilon} = k_{\varepsilon} E_{ACC} \qquad \text{Eq. 6.3}$$

where $dv/d\varepsilon$ is the change in wavenumber as a function of strain (cm^{-1} $\%^{-1}$), and k_{ε} is a constant of proportionality that is 4.3 cm^{-1} GPa^{-1} for a range of cellulose fibre [238].

6.2.4 Dynamic mechanical analyses

T_g was determined based on five replicates at α_2 transition in the range of 140 to 290 °C.

6.2.5 X-ray diffraction

CrI was calculated from the as-received data for (i) 50% RH at a temperature of 23 °C, and (ii) wet-saturated at a temperature of 23 °C for both solvents.

6.2.6 Differential scanning calorimetry

DSC was performed (PerkinElmer DSC 8000, Waltham, Massachusetts, USA) using samples of approximately 5 mg that were sealed in 50 µL aluminium pans. The wet-saturated samples were lightly pressed against paper towels to remove excess of surface water prior to sample preparation. During DSC, samples were initially held at 30 °C for 5 min, then cooled to -70 °C at a cooling rate of 5 °/min. Samples were held at -70 °C for 3 min and then heated up to 30 °C at a heating rate of 5 °/min. Cooling was achieved using the PerkinElmer PE intracooler 2P and nitrogen was used as a purge gas with a flow rate of 20 ml/min. Pyris software (Version 11.0.3) was used for data analysis. DSC was used to determine the amount of free (W_{P1}), freezing (W_{P2})

and non-freezing bound water (W_{nf}). The W_c from the Peak I and II observed in the DSC thermogram was calculated according to Eq. 6.4 [167]:

$$W_c = \frac{Q}{\Delta H} \quad \text{Eq. 6.4}$$

where Q is the heat absorbed during freezing (J) as calculated from Peak I and II area and ΔH is the melting enthalpy of water (ΔH_{water} = 333.5 J/g) [184]. Water did not move to the outside of an aluminium pan since the first-order transitions were not observed other than the crystallisation and melting in the cooling or heating curves, respectively [144]. Thus, it was assumed that water was tightly bound to the cellulose molecules, permitting the use of Eqs. 6.5 and 6.6 [144]:

$$W_t = W_{P1} + W_{P2} + W_{nf} \quad \text{Eq. 6.5}$$

$$W_t = W_m + W_{nf} \quad \text{Eq. 6.6}$$

where W_t is the total weight of absorbed water in the sample, W_{P1} is the weight of water calculated from the enthalpy of crystallisation due to the free water, W_{P2} is the weight of water calculated from the enthalpy of crystallisation due to the freezing bound water, W_{nf} is the weight of non-freezing bound water calculated from its enthalpy of crystallisation and W_m is the weight of water calculated from the enthalpy of melting. Using Eqs. 6.5 and 6.6, W_m can also be expressed as Eq. 6.7.

$$W_m = W_{P1} + W_{P2} \quad \text{Eq. 6.7}$$

The weight of bound water (W_b) can be expressed as Eq. 6.8.

$$W_b = W_{P2} + W_{nf} \quad \text{Eq. 6.8}$$

The percentage of bound water content was calculated using Eq. 6.9:

$$C_b = \frac{W_b}{W_s} \times 100(\%) \quad \text{Eq. 6.9}$$

where C_b is the percentage of bound water and W_s is the weight of sample. The W_b given by Eq. 6.8 was obtained directly from a DSC cooling curve (Eq. 6.5), while W_{P2} was difficult to evaluate from a DSC heating curve due to the difficulty in separating the melting peaks, W_{P1} and W_{P2} (Eq. 6.7). Therefore, the bound water content (C_b) can only be calculated with the use of DSC cooling curves [144]. The number of moles of water absorbed by a glucose unit ($C_6H_{10}O_5$) was calculated using Eq. 6.10:

$$M_b = \frac{162 \times W_b}{18 \times W_s} = \frac{9 \times W_b}{W_s} = 0.09 C_b \quad \text{Eq. 6.10}$$

where 162 and 18 are the molecular weights of a glucose unit and water, respectively. The number of moles of bound water absorbed by a glucose unit in amorphous cellulose was calculated by Eq. 6.11:

$$M_{ba} = \frac{M_b \times 100}{100 - crystallinity} \quad \text{Eq. 6.11}$$

where M_{ba} is the number of moles of bound water (unit: mol) absorbed by a glucose unit in amorphous cellulose.

6.3 Results and discussion

6.3.1 Hygrothermal effect on the mechanical properties of ACC produced *via* BmimAc

The water content of ACC produced *via* BmimAc used in the present study was comparable to cotton cellulose and slightly lower than wood cellulose (Figure 6.1) [169]. This result was due to its same chemical composition (cellulose) for fibre-matrix components. Wet-saturated condition means that the saturation point of water content, showing that the water content has reached a plateau value.

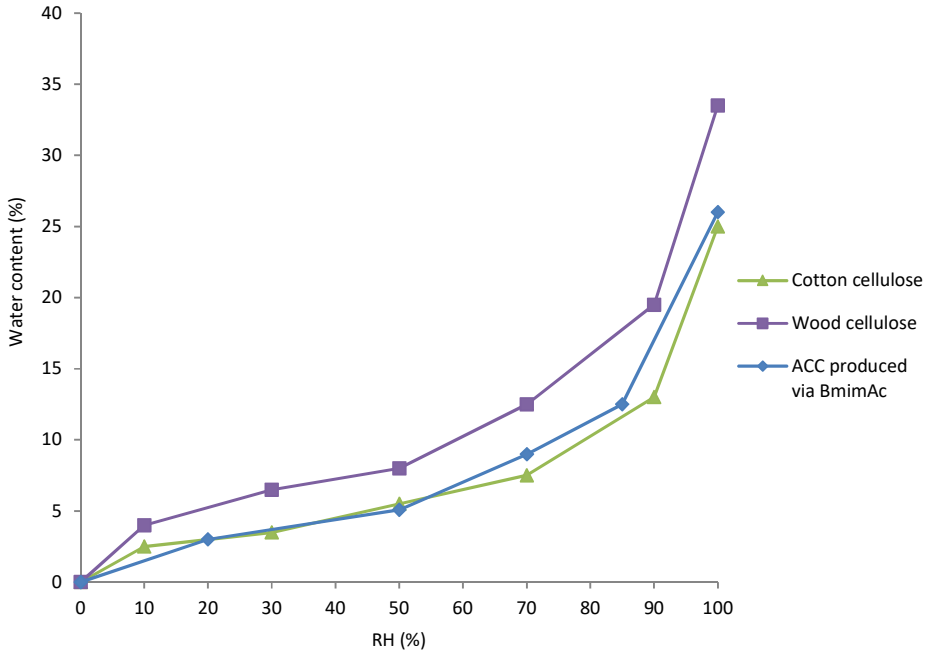

*Wet-saturated = 48.5%

Figure 6.1 Water content of ACC produced *via* BmimAc and various types of cellulose as a function of relative humidity.

The highest amorphous intensity from FTIR was observed for wet-saturated samples (Figure 6.2). The amorphous intensity of the samples conditioned at 85% RH (23 °C) was found in between the wet-saturated and 50% RH (23 °C) conditions. The amorphous intensity of FTIR

decreased slightly up to t_d of 60 min but increased thereafter. As the t_d increased, the amorphous intensity showed V-shaped pattern with the lowest intensity at t_d of 60 min. The same pattern is observed for all the environmental conditions. The increasing trend started at t_d of 60 min, indicating that the increasing amorphous phase in ACCs. This increasing trend of amorphous intensity as a function of t_d was also observed for ACC produced *via* NaOH/urea (Figure 6.17).

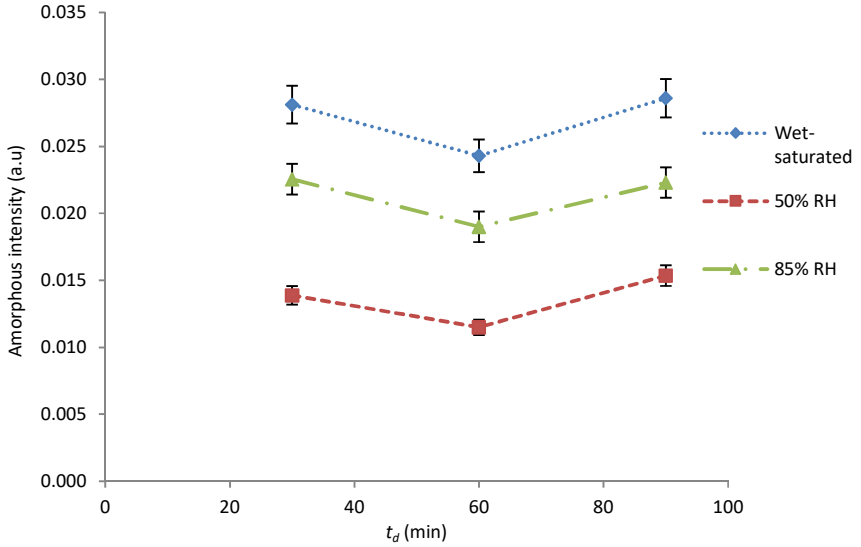

Figure 6.2 The amorphous intensities (893 cm^{-1}) as a function of the dissolution time and water exposure for ACC produced *via* BmimAc.

An increase in the intensity of the OH bending and stretching modes at 1640 cm^{-1} and 3000-3500 cm^{-1}, respectively, was observed with the increasing water absorption for ACCs produced *via* BmimAc and NaOH/urea (Figures 6.3 and 6.18). These results were shown from the sharper and narrower peaks at 1640 cm^{-1} and 3000-3500 cm^{-1} observed with the increasing water absorption, as mentioned in the previous study by Zhou *et al.* [148]. The intensity at 1640 cm^{-1} increased gradually from 50 to 85% RH, and then more dramatically from 85% RH to the wet-saturated condition (Figures 6.3 and 6.18). Thus, an increase in the peak intensity of OH bending mode was observed with a higher water content. A similar result was also reported for

the OH stretching mode. Therefore, it may be speculated that there were some changes in the structure or in the interaction between cellulose and water molecules.

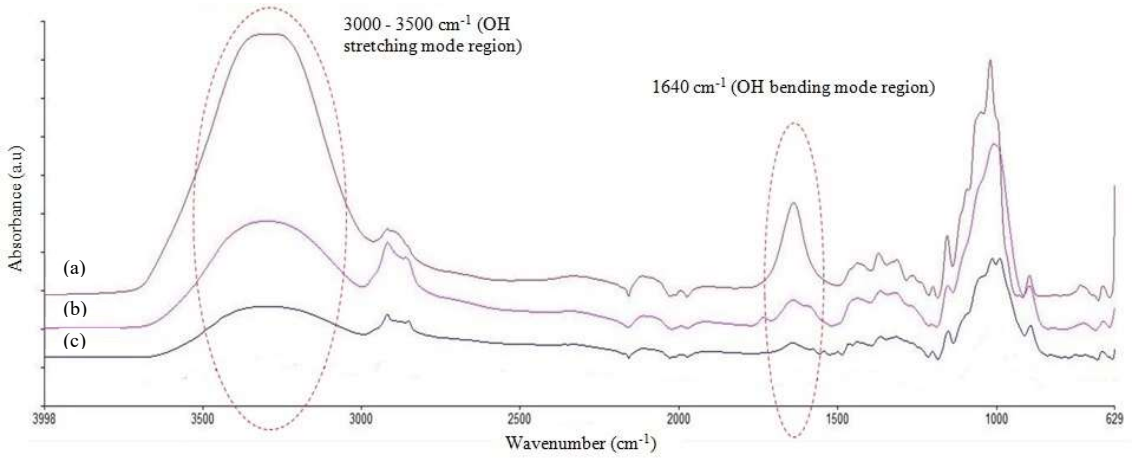

Figure 6.3 FTIR spectra showing the changes in hydroxyl stretching and bending mode for (a) wet-saturated, (b) 85% RH, and (c) 50% RH conditions.

The increasing TCI (1372/2900 cm^{-1}) with the increasing water content was observed for the ACCs produced *via* BmimAc and NaOH/urea, as described by Nelson *et al.* [129]. The TCI values at 50, 85% RH, and wet-saturated sample were 31.4, 36.2, and 87.1%, respectively (Figure 6.4). The increase in the crystallinity was expected due to the relaxation of internal strain of cellulose molecules and a more uniform sharing load was imparted between the cellulose molecules [170]. This result was expected due to an increase in the mobility of disordered phases that facilitated crystallisation [180]. There was no peak observed at 2θ = 35.0° (004) in the XRD diffractograms that would indicate a paracrystalline phase [170], as expected in the ACCs with the increasing water content. On the other hand, the higher-order structure of cellulose II was artificially formed from a concentrated solution [184]. Thus, it was expected that the chain ends and other defects were concentrated in the amorphous phase of the ACCs. The increasing TCI with the increasing water content did not necessarily increase the mechanical properties of ACC, as reported in the previous study [180]. This result was due

to the decreasing hydrogen bonding density (Figure 6.7) and the presence of free water content with the increase of water content (Section 6.3.2). Therefore, it could be concluded that the percentage of crystallinity had a complex relationship with the mechanical properties as a function of water content.

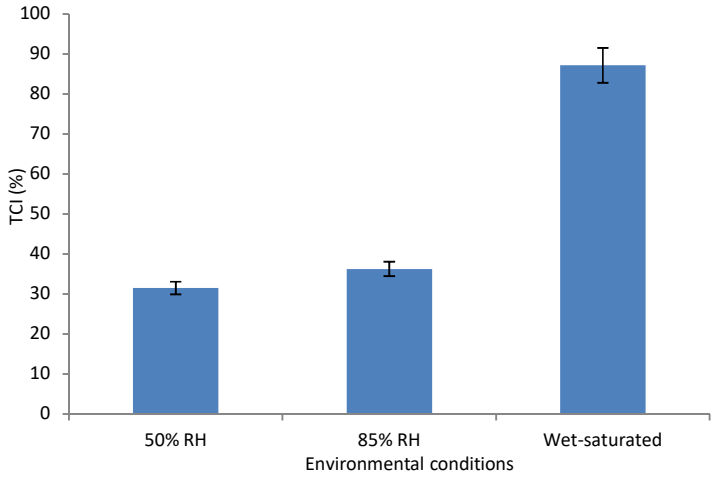

Figure 6.4 Total crystallinity index of ACC produced *via* BmimAc as a function of the environmental conditions.

ACC produced *via* BmimAc in the wet-saturated condition exhibited free water at 26.7° at t_d of 30, 60 and 90 min according to the XRD diffractogram (Figure 6.5). Furthermore, the presence of paracrystalline phase was also observed at $2\theta = 35.0°$. The increasing CrI value was observed from t_d of 30 to 60 min, while the decrease of the CrI value was observed from t_d of 60 to 90 min (Figure 6.6). This result was expected due to the less paracrystalline phase formed at t_d of 90 min, represented from its higher peak at $2\theta = 35.0°$. Duchemin *et al.* obtained results from WAXS and NMR that suggest an exposure of crystalline cellulose to LiCl/DMAc results in peeling away of thin layers from the original crystallites which retain some molecular ordering [240]. After solvent removal, these thin layers can form a paracrystalline phase that is distinct from typical amorphous cellulose. It suggested that the presence of a paracrystalline matrix phase is one of the underlying reasons for the high mechanical properties of ACCs.

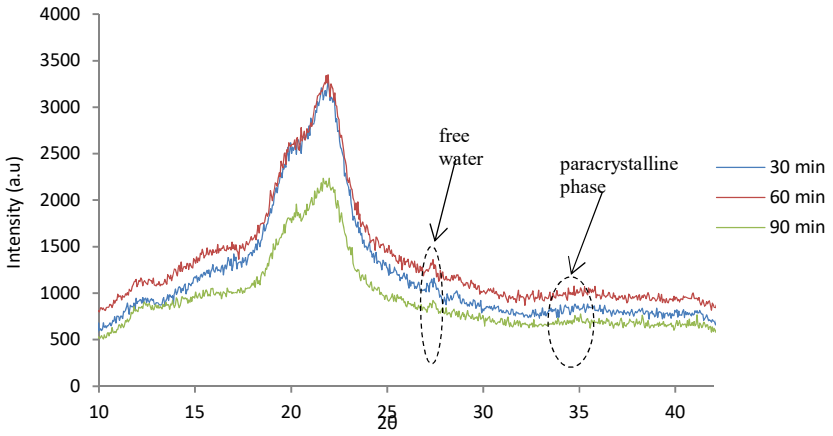

Figure 6.5 XRD diffractograms for ACC produced *via* BmimAc in wet-saturated condition.

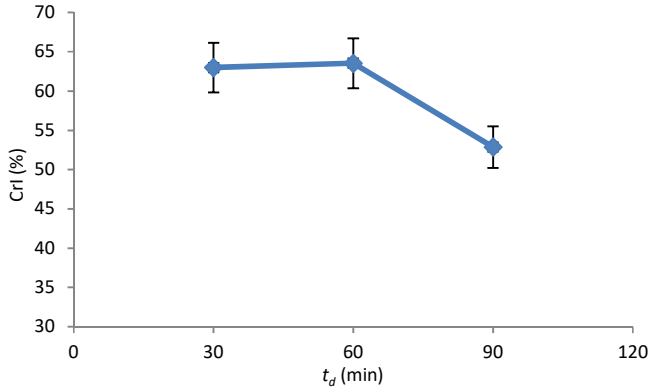

Figure 6.6 Crystallinity index as a function of the dissolution time in wet-saturated condition for ACC produced *via* BmimAc.

The decreasing *E* and UTS were observed with the increase of water content (Figures 6.8 and 6.9). The initial values of *E* at t_d of 30, 60, and 90 min before water absorption testing are 8154 ± 0.3, 8246 ± 0.5, and 7200 ± 0.7 GPa, respectively. Meanwhile, the initial values of UTS at t_d of 30, 60, and 90 min before water absorption testing are 113 ± 0.4, 81 ± 1.2, and 85 ± 0.6 MPa, respectively. Both *E* and UTS decreased rapidly down to a water content of 20% and with a more gradual decrease beyond the water content of 20%. *E* and UTS started to plateau at around 40 and 45%, respectively. The decrease in both *E* and UTS was due to the interruption of inter- and intramolecular hydrogen bonding with the presence of water molecules (Figure

6.7). It has been proposed that changes in *E* and UTS are due to a loosening effect of water on a composite like structure of crystallites embedded in an amorphous phase [180]. Hydrogen bonding is weakened within the cellulose structure due to an exchange of cellulose/cellulose with cellulose/water hydrogen bonds. The exchange of cellulose/cellulose with cellulose/water hydrogen bonds occurs at a water content of 35% (Figure 6.7). This exchange happened slightly lower than the water threshold of *E* (Figure 6.8) and UTS (Figure 6.9) due to the fast exchange of cellulose/cellulose with cellulose/water hydrogen bonds, showing that the remaining bound water beyond the water content of 35%. Various water threshold can be observed in Figure 6.8-6.10. This result was due to the elongation of cellulose II is controlled not only by the break of hydrogen bonding by water, but also by the slipping of individual fibres, as water molecules work as a kind of lubricant [184]. The different patterns are observed in Figure 6.7 and 6.8. The hydrogen bonding density seemed approaching zero value at a water content of 26% (Figure 6.7). This result was due to a smaller *E* at water content of 26%, giving 1-2 orders magnitude lower than *E* at water content of 5.1%.

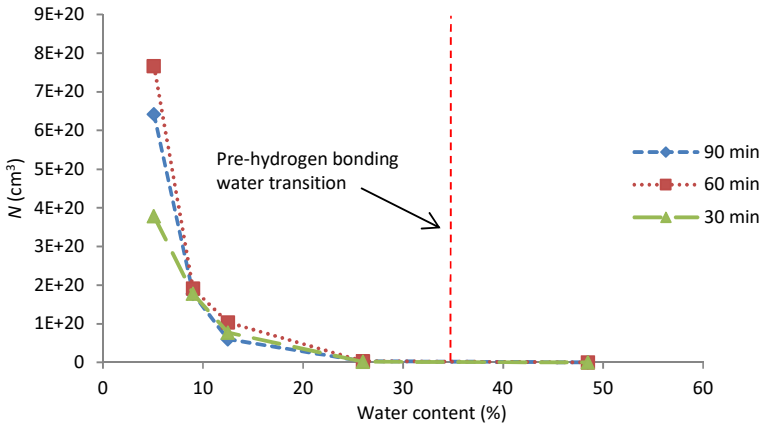

Figure 6.7 Hydrogen bond density of ACC produced *via* BmimAc at various dissolution times.

The rapid decrease of *E* (Figure 6.8) at the initial stage of water absorption was attributed by the increase of the amorphous phase (Figure 6.2). Hatakeyama *et al.* reported that the increasing amorphous phase with the water content may be estimated from the angle of freezing water (< 45°) [184]. A similar drastic decrease of *E* in the initial stages of water absorption was also observed, as mentioned in the previous studies [184, 185]. The decreasing *E* and UTS before the water threshold was due to the effect of bound water on the ACCs (Figures 6.11-6.13). These results will be discussed in Section 6.3.2.

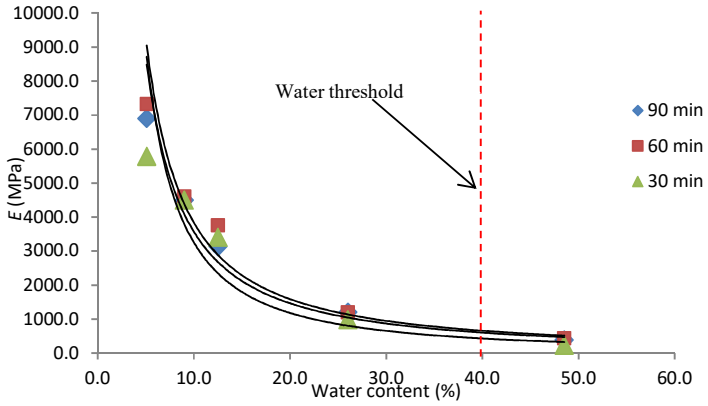

Figure 6.8 Young's modulus of ACC produced *via* BmimAc as a function of water content and dissolution time.

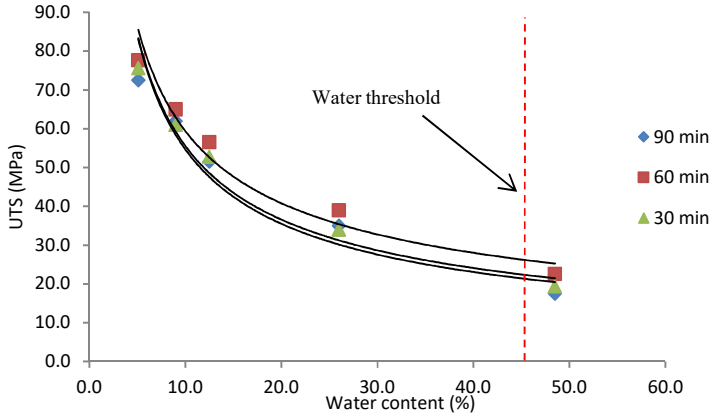

Figure 6.9 Ultimate tensile strength of ACC produced *via* BmimAc as a function of water content and dissolution time.

The ε_f of ACC produced *via* BmimAc increased with the increasing water content (Figure 6.10). Rather the rate is decreasing, the trend seems to reach a constant value at the water content of 45% that corresponded to the water threshold for ε_f. This result showed that no slipping of individual fibres occurred beyond the water threshold. Then, the ε_f approached the constant values of 17.3, 16.4, and 19.5% at t_d of 30, 60, and 90 min, respectively. The increasing ε_f with the increasing water content was due to the interruption of hydrogen bonding and the slipping of individual fibres. The ε_f ratio of wet-saturated to 50% RH at t_d of 30, 60, and 90 min were 1.28, 1.33, and 1.27, respectively. The highest ratio of 1.33 at t_d of 60 min was observed, due to the least significant slippage between the single fibres. The slippage effect will be discussed in Chapter 7.

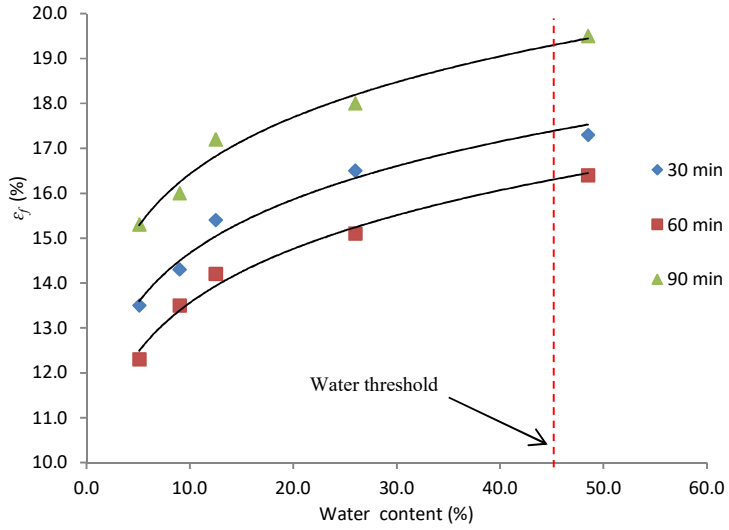

Figure 6.10 Strain to failure of ACC produced *via* BmimAc as a function of water content and dissolution time.

6.3.2 Hygrothermal effect on phase composition of ACC produced *via* BmimAc

According to Figures 6.11-6.13, there was no Peak II observed below a water content of 12.5% (85% RH). This result indicated that the non-freezing bound water was attached at the cellulose chain of ACCs below the water content of 12.5%. Thus, the critical content of non-freezing

water was estimated at the water content of 12.5%. The presence of Peak II with the increasing water content was observed beyond the water content of 12.5%. Peak II (freezing bound water) and I (free water) were observed at a water content of 48.5% at any t_d. The non-freezing and freezing bound water are normally defined as bound water [170]. However, the first order phase transition (Peak II) may appear between the water content of 12.5 and 48.5%. The freezable bound water was difficult to observe due to the large amount of non-freezable bound water.

Considering that an average sample mass was 5 mg, the weight percentages of freezing bound water were 0.55, 0.36, and 0.72% for t_d of 30, 60 and 90 min, respectively, according to Eq. 6.9. It was interesting to note that the percentages of bound water (13.1, 12.9, and 13.2%) did not correlate with the water threshold for E (40.0%), UTS (40.0%), and ε_f (45.0%), respectively. Nakamura *et al.* reported that water does not escape through the sample pan during DSC, so the first order transition is not observed [144]. Thus, it is presumed that water is tightly bound to the cellulose.

In the present study, it was assumed that the difference in bound water was determined from the DSC and that when the mechanical properties reached the constant value, it was due to the large differences in the non-freezing water content between 12.5 and 48.5%. It was also observed that there were various DSC results (Figures 6.11-6.13), suggesting that the size of crystal formed in the amorphous phase of ACCs changed with the increasing water content, as reported elsewhere [184]. It was concluded that the non-freezing bound water significantly affected the mechanical properties of ACC produced *via* BmimAc at a water content below 48.5%. At a higher water content, it was expected that free water was present (Figure 6.15).

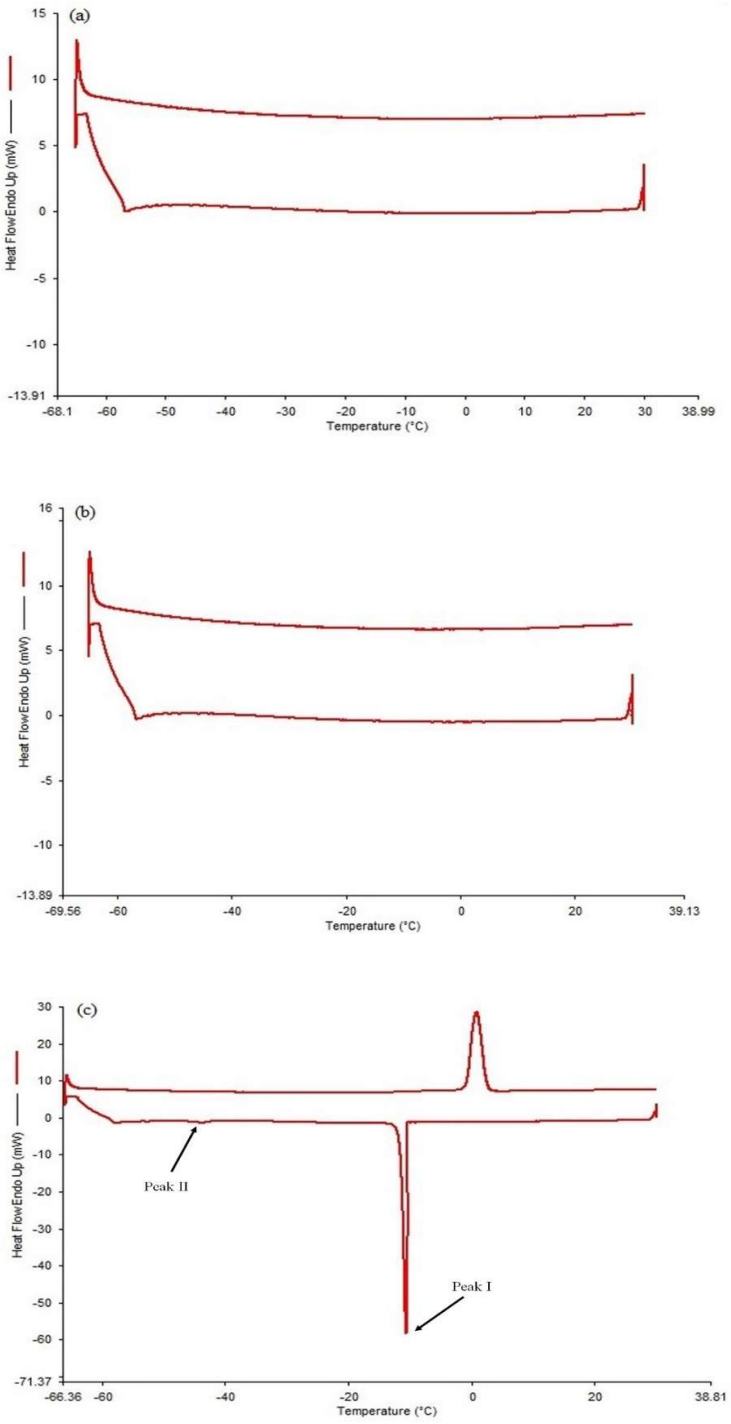

Figure 6.11 DSC thermograms for ACC produced *via* BmimAc at dissolution time of 30 min: (a) 50% RH, (b) 85% RH, and (c) wet-saturated condition.

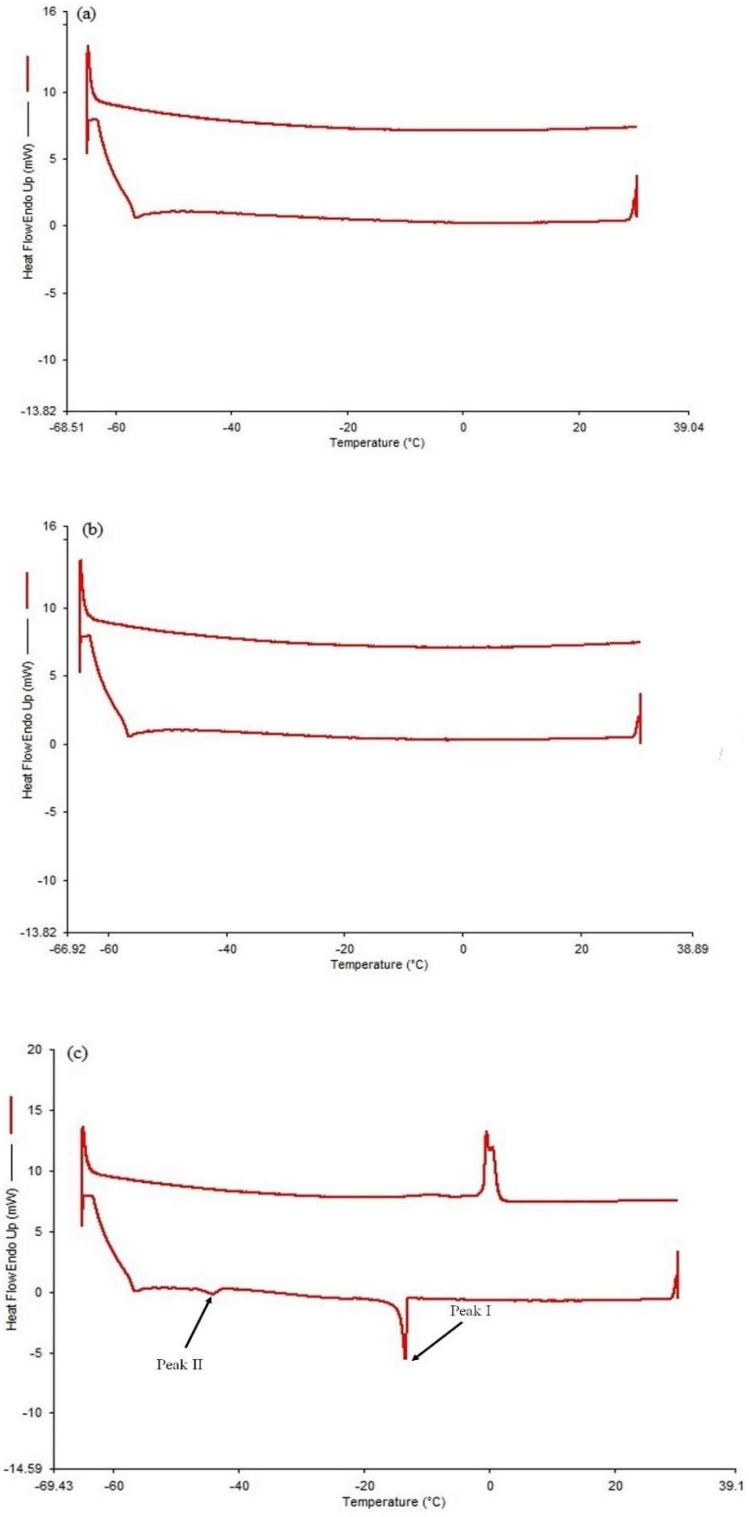

Figure 6.12 DSC thermograms for ACC produced *via* BmimAc at dissolution time of 60 min: (a) 50% RH, (b) 85% RH, and (c) wet-saturated condition.

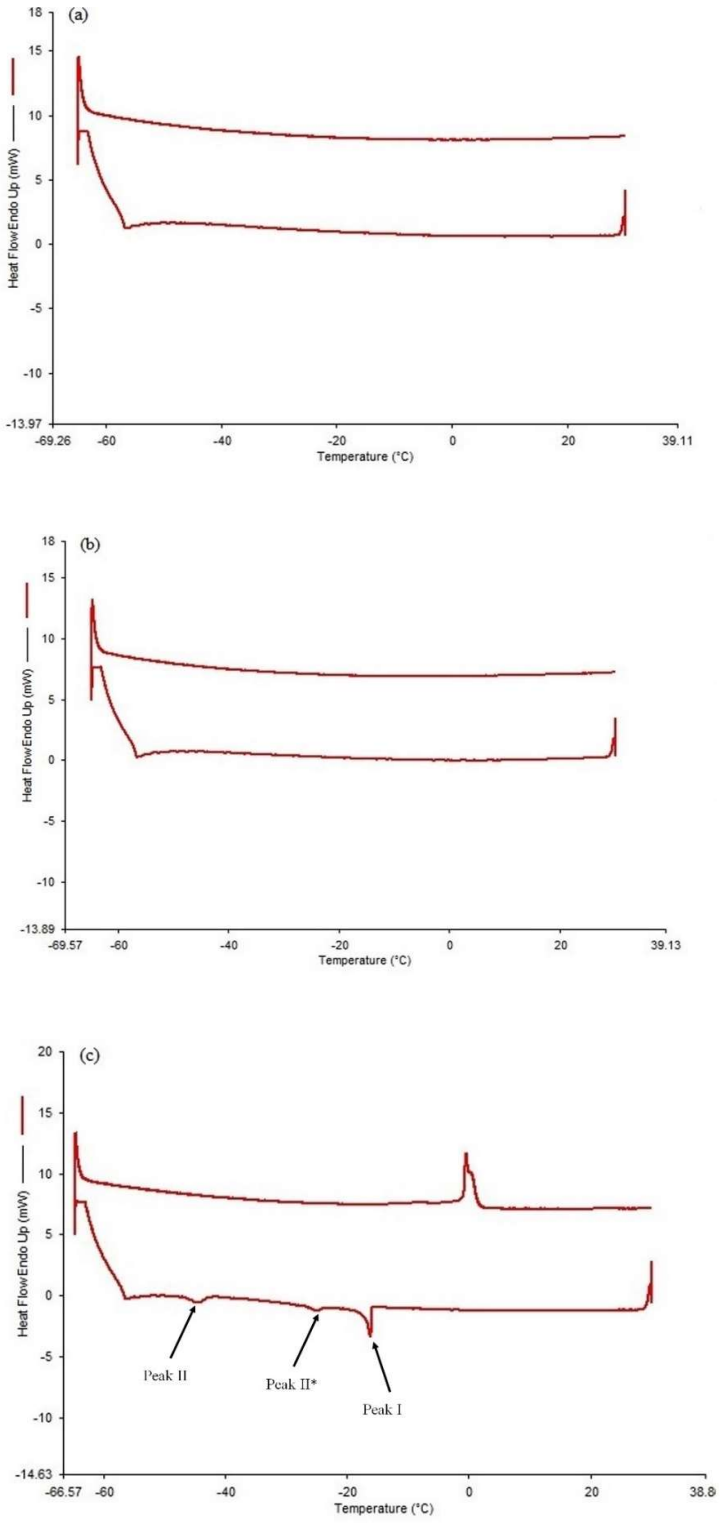

Figure 6.13 DSC thermograms for ACC produced *via* BmimAc at dissolution time of 90 min: (a) 50% RH, (b) 85% RH, and (c) wet-saturated condition.

The angles representing the freezing bound water (Figure 6.14) for t_d of 30, 60, and 90 min were 37, 26 and 45°, respectively. These results indicated that the amorphous phase of ACCs was expected to increase with the presence of water at 30 and 60 min because their slope angles were less than 45°. The amorphous phase at all dissolution times changed to a more random arrangement which could be observed from the increasing enthalpy of freezing water as with increase of water content. The increasing freezing bound water (Figure 6.14) was consistent with the increasing enthalpy (Figures 6.11-6.13). Peak II' was observed at t_d of 90 min (Figure 6.13), representing an intermediate peak. Thus, the amorphous phase at t_d of 90 min became more loosely packed with the increasing water content. The freezing bound water content was inversely proportional to the hydrogen bonding density that can be observed below a water content of 35% (Figure 6.7). Considering the freezing bound water content at a wet-saturated condition (48.5%), the lowest freezing bound water content was observed at t_d of 60 min, followed by 30, and 90 min (Figure 6.14). However, the highest hydrogen bonding density was observed at t_d of 60 min, followed by 90, and 30 min (Figure 6.7).

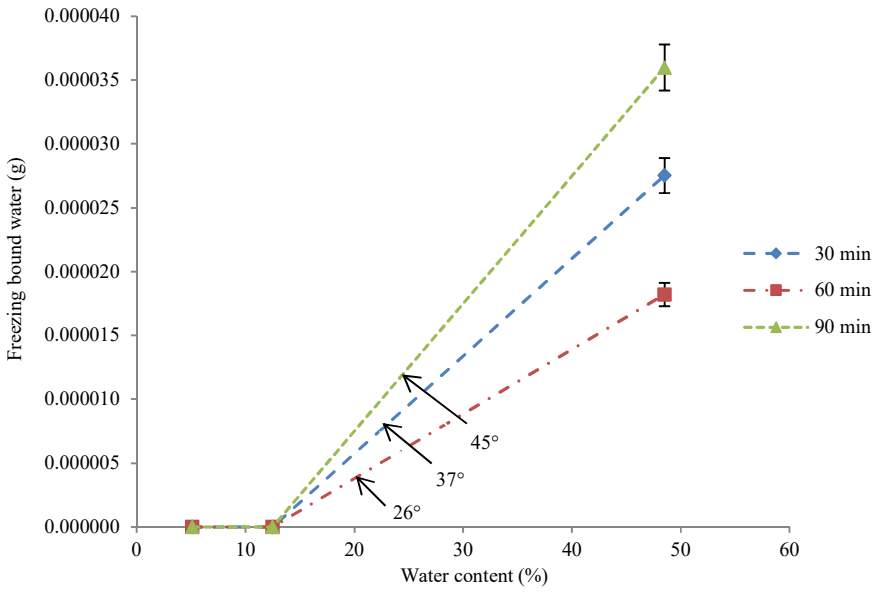

Figure 6.14 Freezing bound water versus water content for ACC produced *via* BmimAc.

The relationship between the free water and V_v was complex (Figure 6.15). The weights of the free water content for the V_v of 0.5 and 2.1% were 7.5×10^{-4} and 1.65×10^{-4} g, respectively. The highest weight of free water was 1.3×10^{-3} g which corresponded to a V_v of 1.2%. The lowest weight of free water was 7.5×10^{-5} g which corresponded to a V_v of 2.1%, due to the existence of the intermediate peak (Peak II'). The temperature of Peak II' approached Peak I at a water content of 48.5% (Figure 6.13). However, Peak II' did not merge with Peak I because the saturation water content had been reached at 48.5%. Thus, less free water content was observed due to the separation of enthalpy between Peak II' and I. However, the decreasing mechanical properties at t_d of 90 min were associated to the significant molecular deformation at high water content.

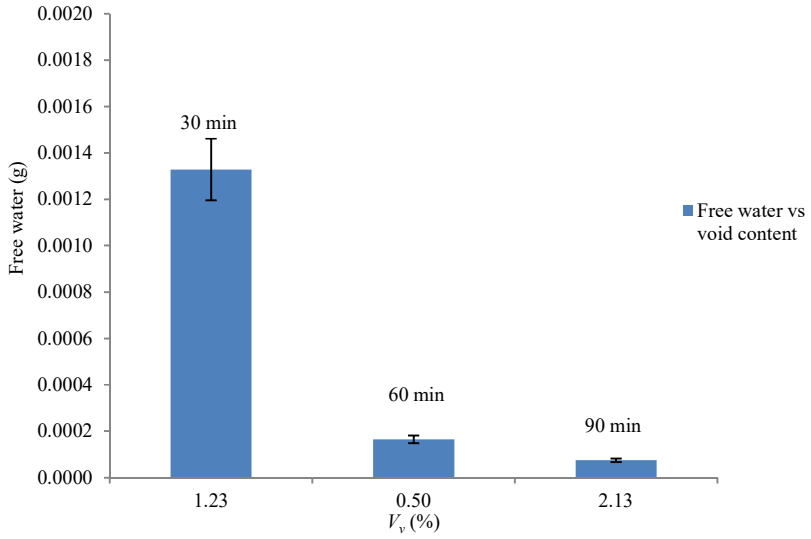

Figure 6.15 Free water content as a function of void content for ACC produced *via* BmimAc.

6.3.3 Hygrothermal effect on mechanical properties of ACC produced *via* NaOH/urea

The water content for ACC produced *via* NaOH/urea was located between the wood and cotton cellulose [169] (Figure 6.16). It was slightly higher than in the ACC produced *via* BmimAc, as observed from its higher V_v.

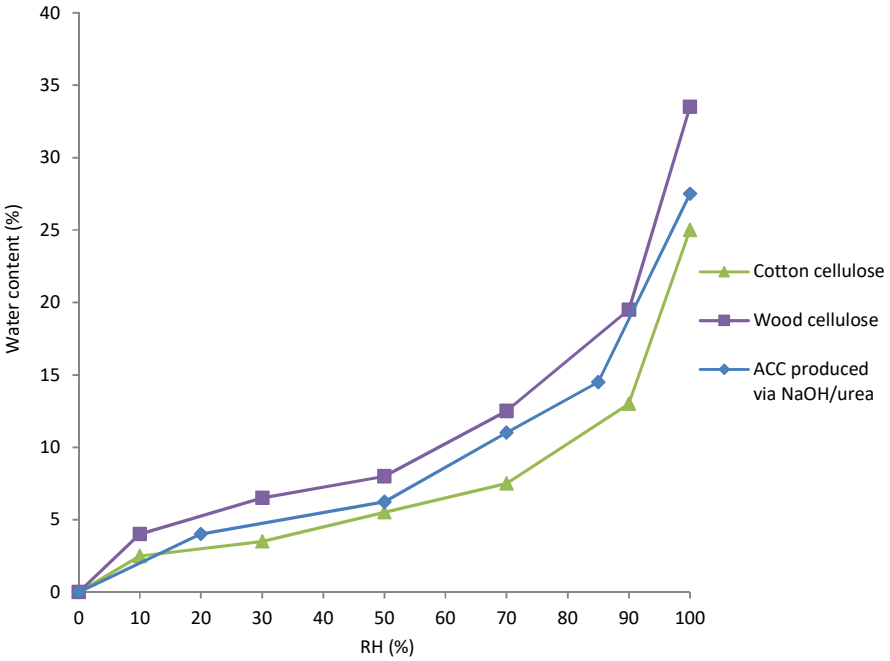

*Wet-saturated = 65.7%

Figure 6.16 Water content of ACC produced *via* NaOH/urea and various types of cellulose as a function of relative humidity.

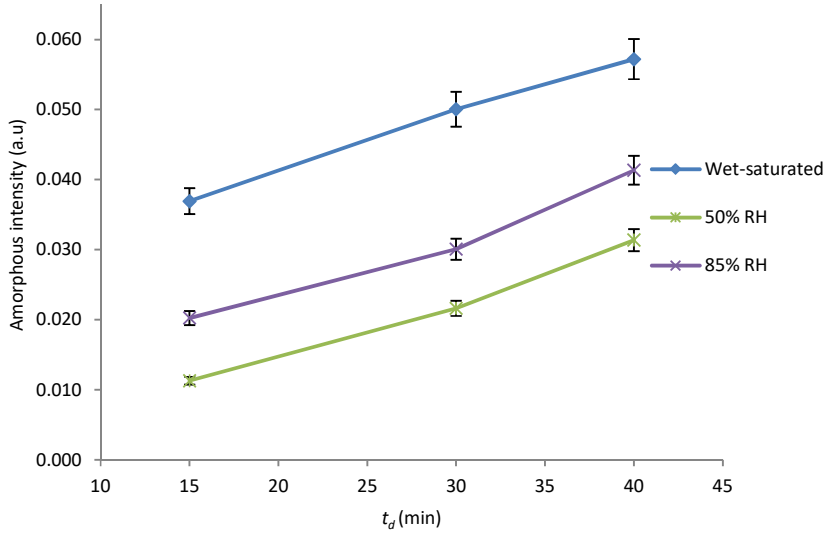

Figure 6.17 The amorphous intensities (893 cm^{-1}) as a function of the dissolution time and water exposure for ACC produced *via* NaOH/urea.

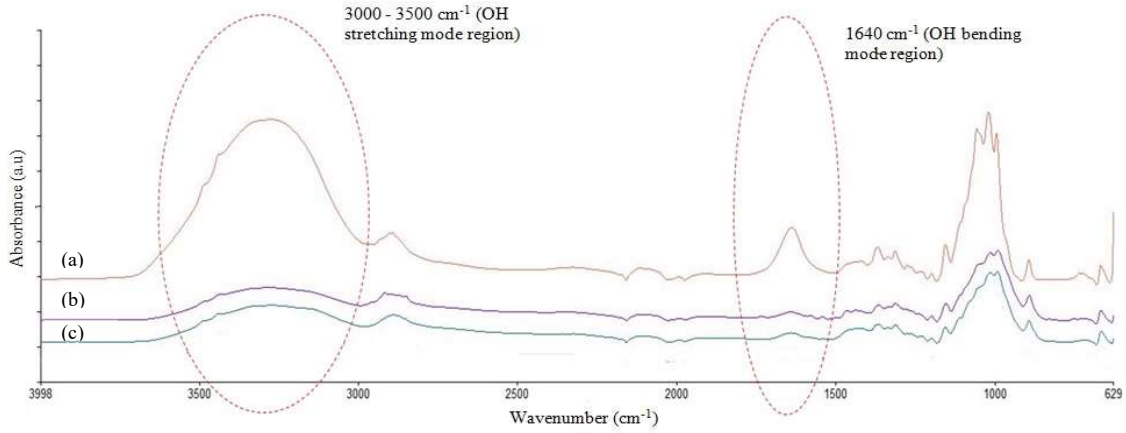

Figure 6.18 FTIR spectra showing the changes in hydroxyl stretching and bending mode for (a) wet-saturated, (b) 85% RH, and (c) 50% RH conditions.

The increasing pattern of TCI was observed with the increasing water content for ACC produced *via* NaOH/urea (Figure 6.19). The results were similar to the ACC produced *via* BmimAc (Figure 6.4). The increasing TCI was expected due to the presence of the paracrystalline phase. The evidence of paracrystalline phase is shown in Figure 6.20. This was due to an increase in the mobility of disordered phases that facilitated crystallisation [180] as

discussed in Section 6.3.1. Ibbett *et al.* characterised the regenerated cellulosic fibre using NMR, indicating that the increasing water content would separate the non-crystalline peak into two sharper peaks (87.0 and 85.2 ppm), representing the paracrystalline phase [213]. The paracrystalline phase was expected to absorb water similar to the amorphous phase due to its non-crystalline phase.

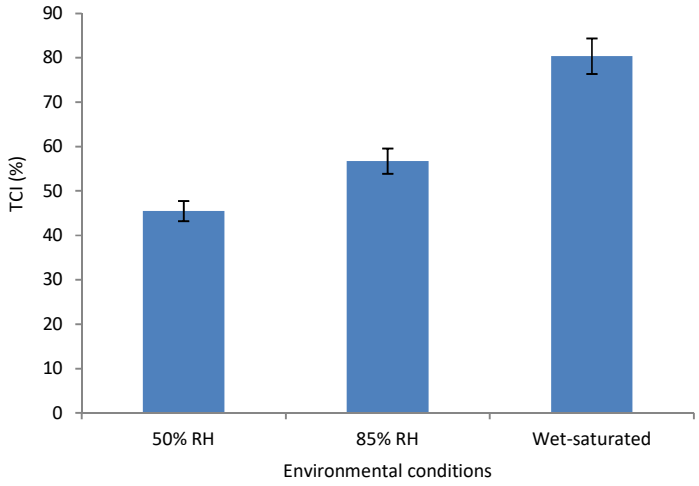

Figure 6.19 Total crystallinity index of ACC produced *via* NaOH/urea as a function of the environmental conditions.

ACC produced *via* NaOH/urea in the wet-saturated condition exhibited free water at 26.7° at t_d of 15, 30 and 40 min according to the XRD diffractogram (Figure 6.20). Furthermore, the presence of paracrystalline phase was also observed at $2\theta = 35.0°$. The increasing CrI value was observed from t_d of 15 to 40 min (Figure 6.21). The increasing CrI with the increase of t_d was due to the increasing paracrystalline phase.

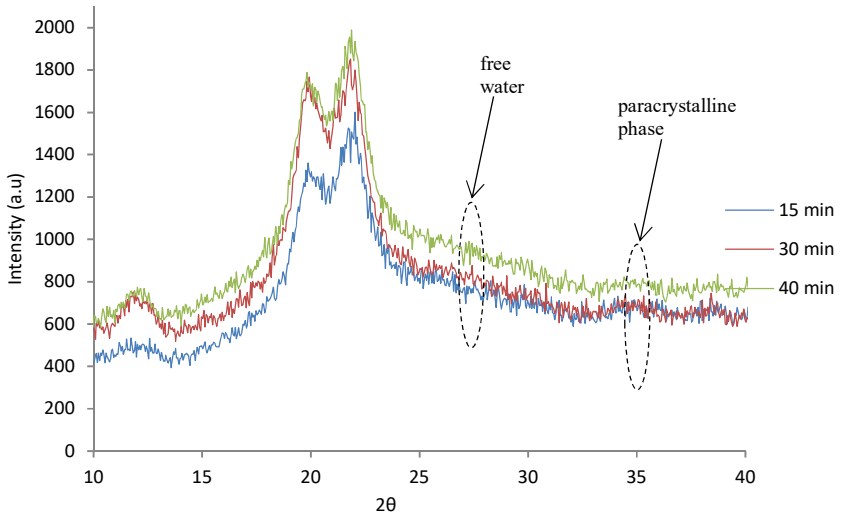

Figure 6.20 XRD diffractograms for ACC produced *via* NaOH/urea in wet-saturated condition.

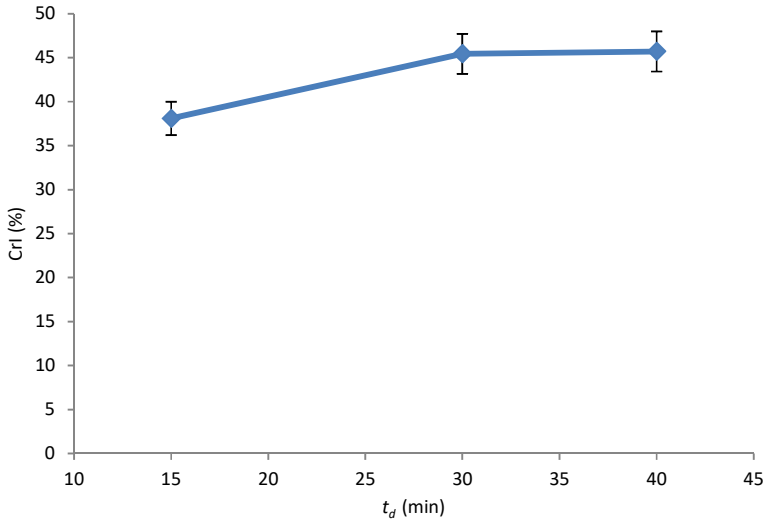

Figure 6.21 Crystallinity index as a function of the dissolution time in wet-saturated condition for ACC produced *via* NaOH/urea.

The decreasing *E* and UTS were observed with the increasing water content (Figures 6.23 and 6.24, respectively). The highest *E* and UTS were achieved with a t_d of 15 min, followed by 30 and 40 min. The initial values of *E* at t_d of 15, 30, and 40 min before water absorption testing are 1489 ± 1.1, 1120 ± 0.5, and 950 ± 0.7 GPa, respectively. Meanwhile, the initial values of

UTS at t_d of 15, 30, and 40 min before water absorption testing are 27.8 ± 1.3, 20.0 ± 0.6, and 18.3 ± 0.4 MPa, respectively. Both *E* and UTS decreased rapidly down to a water content of 15%, with a more gradual decrease beyond the water content of 15%. *E* and UTS started to plateau at the water content of 60%. The decrease in both *E* and UTS was due to the interruption of inter- and intramolecular hydrogen bonding with the presence of water (Figure 6.22). The decreasing *E* and UTS were due to the loosening effect of water and weakening of hydrogen bonding as discussed in Section 6.3.1. The exchange of cellulose/cellulose into cellulose/water hydrogen bonds occurred at a water content of 60% (Figure 6.22) which was similar to the water threshold of 60% for *E* and UTS (Figures 6.23 and 6.24, respectively). Thus, the decreasing water mobility and the presence of free water were expected beyond the water content of 60%.

The rapid decrease of *E* (Figure 6.23) at the initial stage of water absorption was attributed to the increase of the amorphous phase (Figure 6.17). The decreasing *E* and UTS below the water threshold were due to the effect of bound water in the ACCs (Figures 6.26-6.28). These results will be discussed in Section 6.3.4. The increasing matrix fraction of ACC was reported as t_d increased, showing that a larger fraction of reinforcing fibres was dissolved and transformed into the matrix phases [109]. A weaker matrix strength than the laminates in ACC was reported due to the extensive breakage of the amorphous tie molecules, leading to a weakening fibre by their loss. Thus, more water molecules can easily interact with the weakening fibre in the amorphous domain. The increasing V_v enhanced more water to penetrate the cellulose network of the fibres into the capillaries and spaces between the fibrils and into less bound areas of the fibrils, leading to an attachment of water molecules by chemical links to groups in the cellulose molecules. A significant attachment of water-cellulose in ACC is expected due to the hydrophilic behaviour of both reinforcing and matrix phases that are composed of cellulose II [216]. A higher V_v is responsible for a lower fatigue resistance, greater affinity to water

diffusion and variation (scatter) in mechanical properties [231]. The water molecules force the cellulose molecules apart, destroying some of the rigidity of the cellulose structure (*e.g.* hydrogen bonding) and thus permitting the cellulose molecules to move more freely [33]. As a result, the mass of cellulose is softened and changed more easily with an application of force [241].

Interestingly, a higher pre-hydrogen bonding water transition was observed for the ACC produced *via* NaOH/urea in comparison to BmimAc because of its higher amorphous intensity (Figures 6.17 and 6.2, respectively). This result had led to a significant exchange of cellulose/cellulose into cellulose/water in ACC produced *via* NaOH/urea as compared with BmimAc. On the other hand, a higher hydrogen bond density of two order magnitudes for the ACC produced *via* BmimAc as compared to NaOH/urea was observed (Figures 6.7 and 6.22, respectively). As a result, a higher *E* and UTS for the ACC produced *via* BmimAc (Figures 6.8 and 6.9, respectively) was reported (Figures 6.23 and 6.24, respectively).

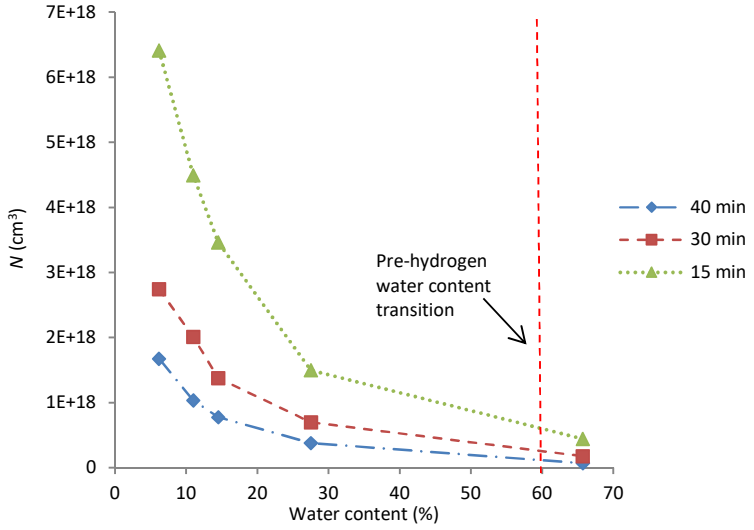

Figure 6.22 Hydrogen bond density of ACC produced *via* NaOH/urea at various dissolution times.

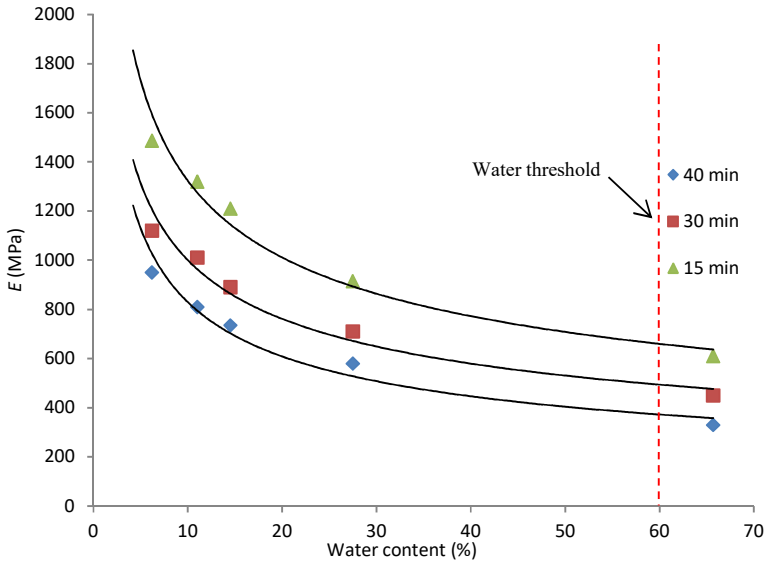

Figure 6.23 Young's modulus of ACC produced *via* NaOH/urea as a function of water content and dissolution time.

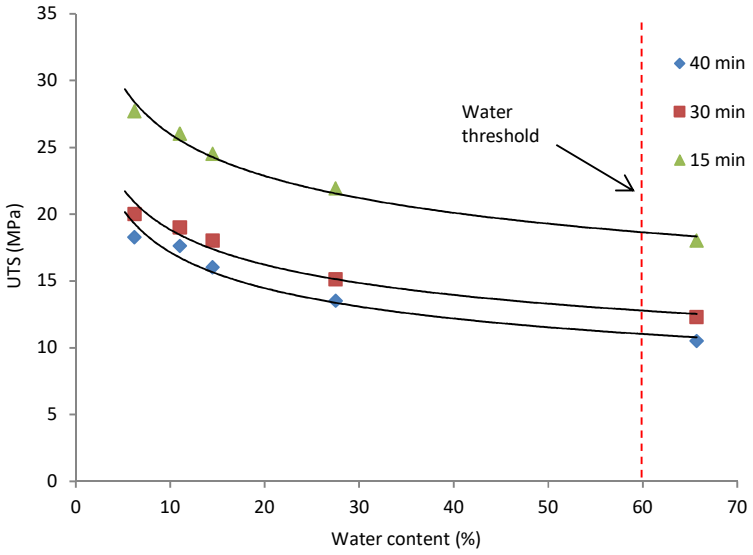

Figure 6.24 Ultimate tensile strength of ACC produced *via* NaOH/urea as a function of water content and dissolution time.

The ε_f of ACC produced *via* NaOH/urea increased with the increasing water content until the water content attained a level of 55% (Figure 6.25). Then, the ε_f approached the constant values of 21.2, 20.7, and 22.5% at t_d of 15, 30, and 40 min, respectively. The increasing ε_f with the increasing water content was due to the interruption of hydrogen bonding and the slipping of individual fibres.

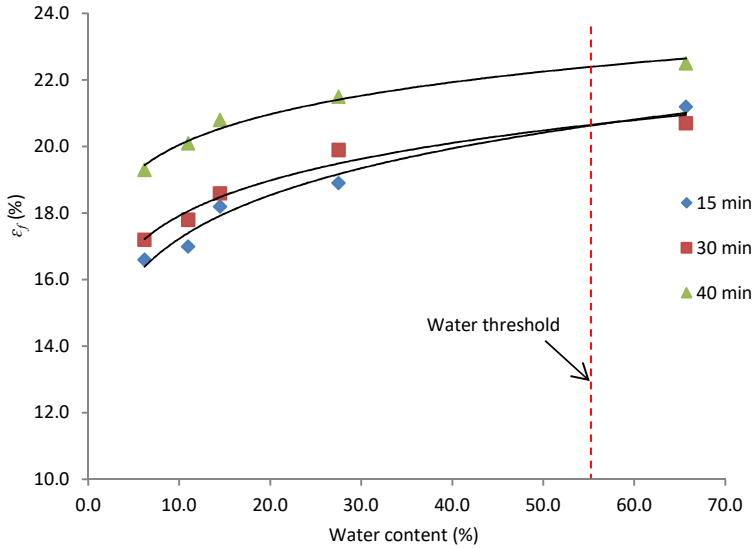

Figure 6.25 Strain to failure of ACC produced *via* NaOH/urea as a function of water content and dissolution time.

6.3.4 Hygrothermal effect on phase composition for ACC produced *via* NaOH/urea

According to Figures 6.26-6.28, there was no Peak II observed below the water content of 14.5% (85% RH), indicating the attachment of non-freezing bound water to the cellulose chain of ACC. Thus, the critical content of non-freezing water was estimated at 14.5%. The presence of Peak II was observed beyond the water content of 14.5%. Peak II (freezing bound water) and I (free water) were observed at the water content of 65.7% at any t_d. The non-freezing and

freezing bound water are normally defined as bound water [170]. However, the first order phase transition (Peak II) may be speculated to be between a water content of 14.5 and 65.7%.

Considering that an average ACCs sample mass was 5 mg, the weight percentages of freezing bound water were 0.08, 0.23, and 0.41% for t_d of 15, 30, and 40 min, respectively. The percentages of bound water (14.6, 14.7, and 14.9%) did not correlate with the water thresholds for E (60.0%), UTS (60.0%), and ε_f (55.0%). In comparison, the non-freezing bound water content for ACC produced *via* NaOH/urea was higher than ACC produced *via* BmimAc which was correlated with a lower hydrogen bonding density.

In the present study, the mechanical properties were attained in the non-freezing bound water phase due to a large difference between the non-freezing water and free water in the range of 14.5 - 65.7%. Thus, the non-freezing bound water significantly affected the mechanical properties of ACC produced *via* NaOH/urea at a water content below 65.7%. At a higher water content, it was expected that free water was present (Figure 6.30).

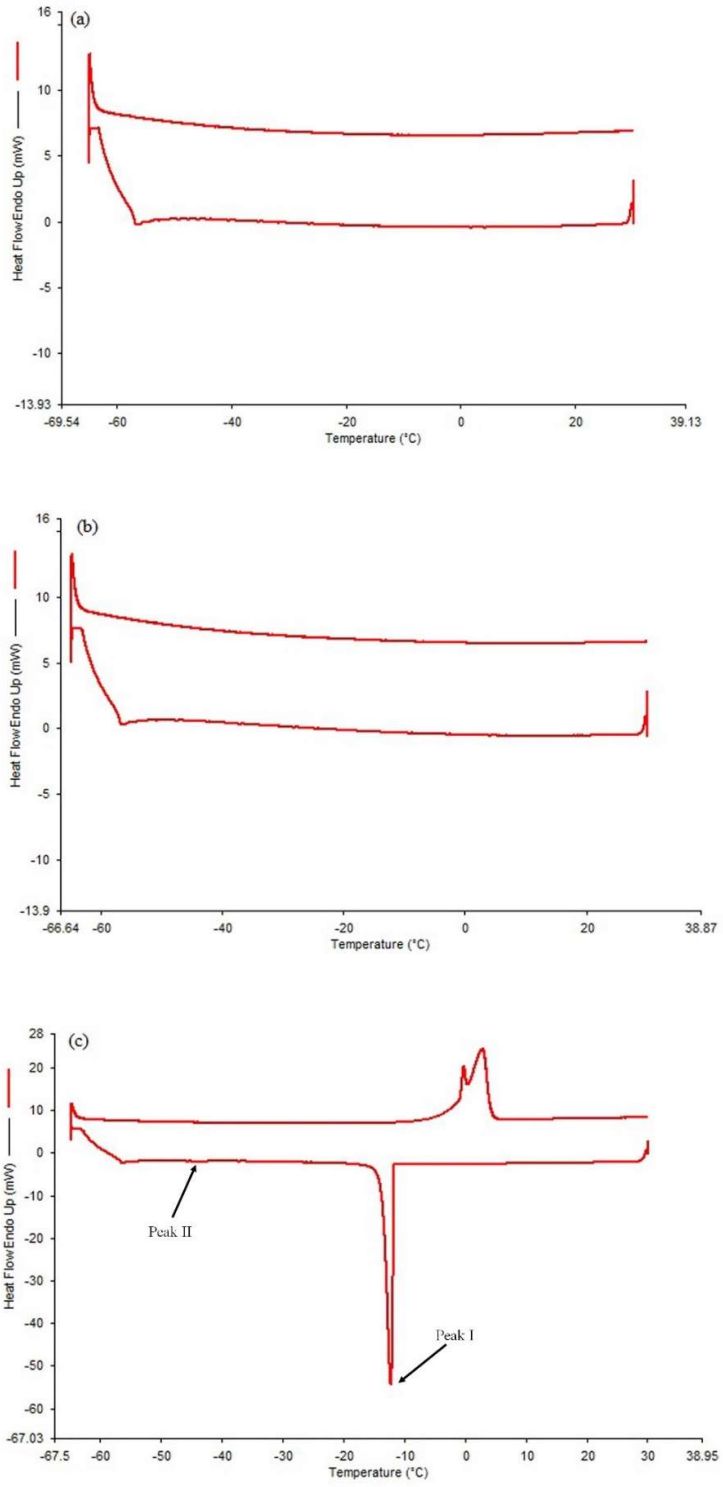

Figure 6.26 DSC thermograms for ACC produced *via* NaOH/urea at dissolution time of 15 min: (a) 50% RH, (b) 85% RH, and (c) wet-saturated condition.

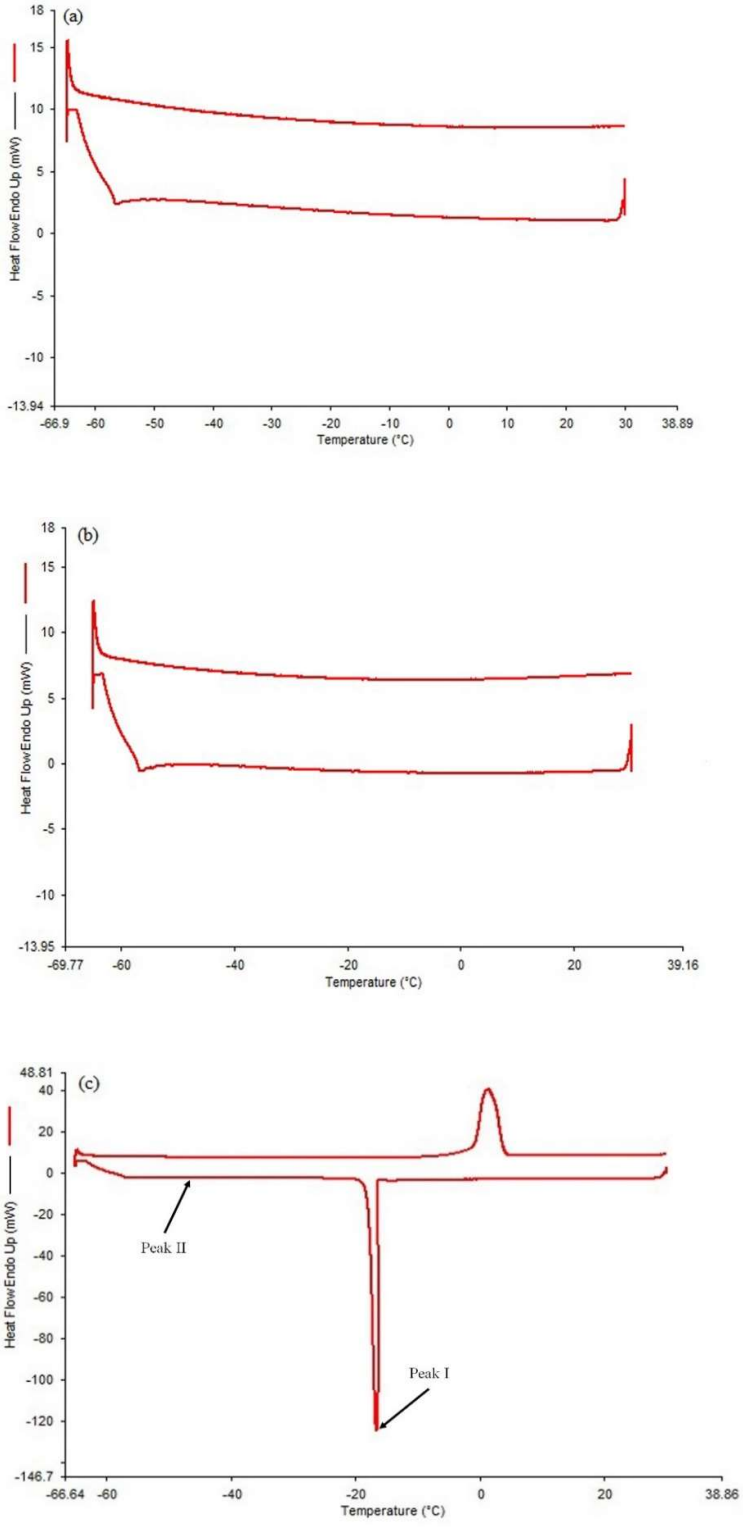

Figure 6.27 DSC thermograms for ACC produced *via* NaOH/urea at dissolution time of 30 min: (a) 50% RH, (b) 85% RH, and (c) wet-saturated condition.

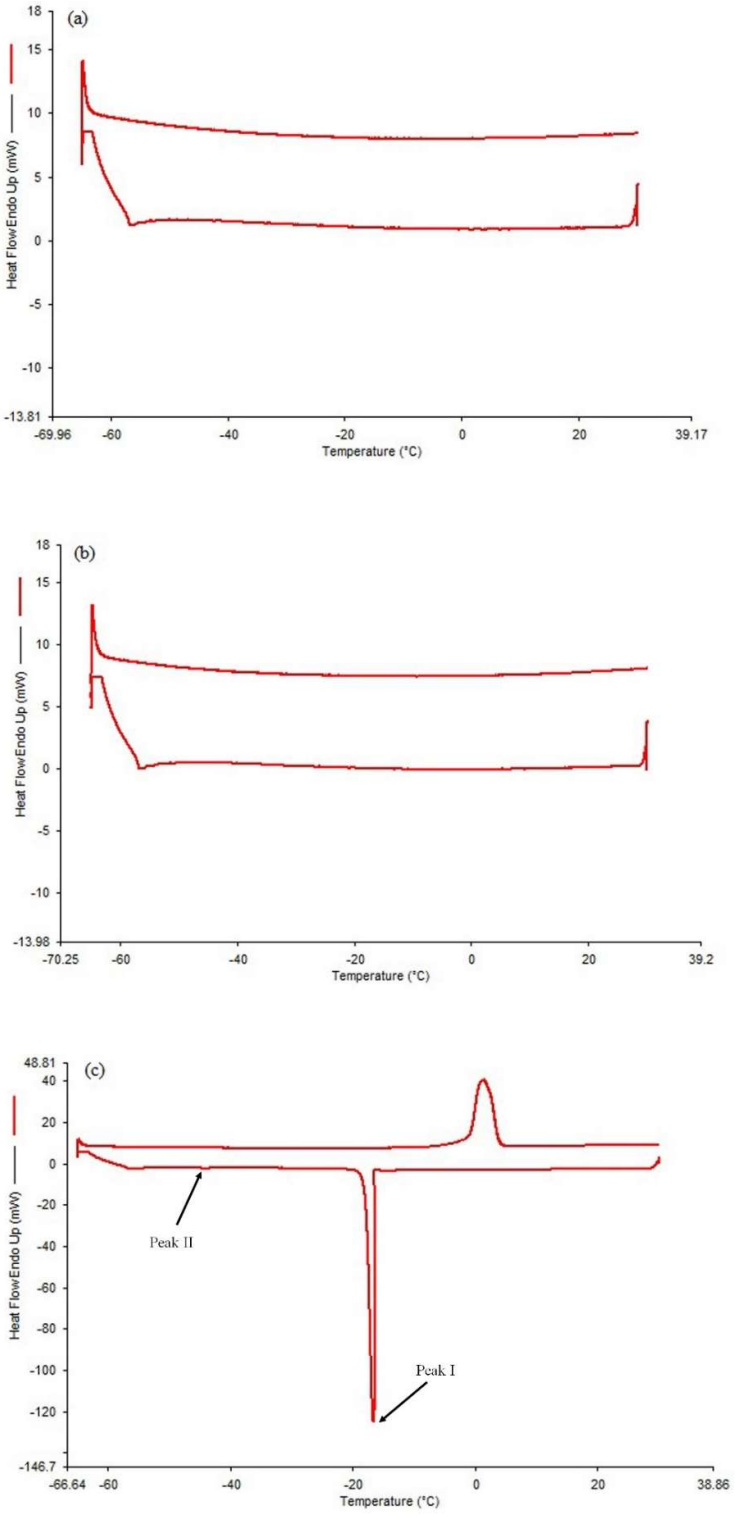

Figure 6.28 DSC thermograms for ACC produced *via* NaOH/urea at dissolution time of 40 min: (a) 50% RH, (b) 85% RH, and (c) wet-saturated condition.

The angles representing the freezing bound water were 4.5, 12.8 and 22.0° for t_d of 15, 30, and 40 min, respectively (Figure 6.29). The increasing amorphous phase was observed from the angle (< 45°). The amorphous phase changed to a more random arrangement, as indicated from the increasing enthalpy (area of Peak II) of freezing bound water with the increasing water content. The increasing enthalpy was correlated to the increasing freezing bound water (Figures 6.26-6.28). Thus, the freezing bound water was inversely proportional to the hydrogen bonding density which was similar to the ACC produced *via* BmimAc. Considering the water content of 65.7%, the lowest freezing bound water was observed for the t_d of 15 min, followed by 30, and 40 min (Figure 6.29). However, the highest hydrogen bonding density was observed for the t_d of 15 min, followed by 30, and 40 min (Figure 6.22).

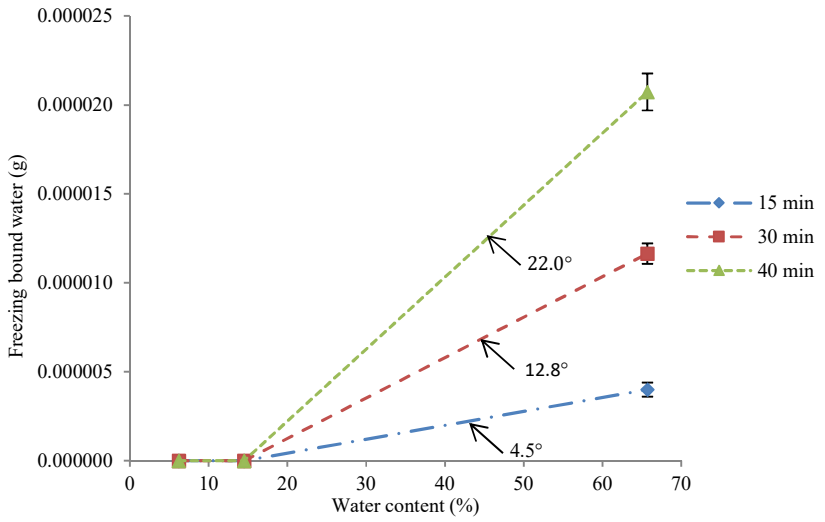

Figure 6.29 Freezing bound water versus water content for ACC produced *via* NaOH/urea.

The increasing free water content with the increasing V_v was observed (Figure 6.30) because of the increasing space for water to reside within the gaps in the ACC structure. The highest free water content was 0.0034 g for V_v at 6.43%. Thus, a significant decrease of E and UTS for the t_d of 40 min was due to the freezing bound water and hydrogen bonding density.

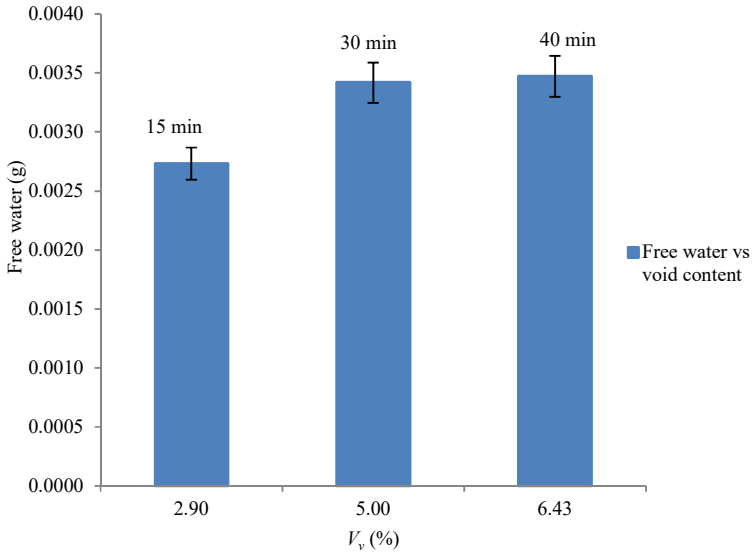

Figure 6.30 Free water content as a function of void volume fraction for ACC produced *via* NaOH/urea.

A higher M_{ba} for ACC produced *via* BmimAc compared to NaOH/urea was observed (Table 6.1). M_{ba} of 9.03 and 6.63 moles were reported for the ACC produced *via* BmimAc and NaOH/urea, respectively. These results suggested that the water molecules of bound water attached on three OH groups in the amorphous region of the cellulose molecules. It was anticipated that three and two moles of water molecules attached on each OH group in each glucose unit for the ACCs produced *via* BmimAc and NaOH/urea, respectively. M_{ba} value depended on the bound water and crystallinity of the ACCs. According to Eq. 6.11, M_{ba} value was directly proportional to the bound water and was inversely proportional to the crystallinity of ACCs. The E value for ACC produced *via* BmimAc was lower than NaOH/urea (Table 6.1). This result was due to the lower hydrogen bonding density and higher M_{ba} observed for the ACC produced *via* BmimAc.

As a conclusion, the non-freezing bound water was associated with the decrease of E and UTS for both ACCs below the water threshold. However, the presence of free water beyond the water threshold was speculated with the decrease of E and UTS. The significant decrease of

hydrogen density was observed below the water threshold; however, it showed a plateau pattern beyond the water threshold.

Table 6.1 Summary of the results for ACCs produced *via* BmimAc and NaOH/urea at the dissolution time of 30 min.

Solvent	t_d (min)	Hydrogen bonding density (cm^3) x10^{17}	Freezing bound water (%)	Non-freezing bound water (%)	Amorphous intensity (a.u)	Bound water (%)	TCI (%)	M_b (mole)	M_{ba} (mole)	E (MPa)
BmimAc	30	0.23	0.55	12.5	0.03	13.05	87	1.17	9.03	229.35
NaOH/urea	30	1.7	0.23	14.5	0.05	14.73	80	1.33	6.63	450

6.3.5 Hygrothermal effect on viscoelastic properties

The broad peaks were observed from 100 to 200 °C for all environmental conditions (Figures 6.31 and 6.32) due to the removal of water in the ACCs. This result was attributed to the motion of chains bound to water molecules by hydrogen bonding, corresponding to the α_3 transition [68]. However, Cristea *et al.* reported that the removal of water occurred at a temperature of 50 °C [242], indicating a lower temperature than the one observed in the present study.

T_g for ACC produced *via* BmimAc conditioned at 50, 85% RH, and wet-saturated condition were 269, 266, and 264 °C, respectively (Figure 6.31). Meanwhile, T_g for ACC produced *via* NaOH/urea conditioned at 50, 85% RH, and wet-saturated condition were 277, 268, and 264 °C, respectively (Figure 6.32). These T_g for both ACCs were in the range as the ones reported in the previous studies [126, 214]. As can be seen, T_g decreased with the increase of water content. This result was due to the plasticisation effect of water, softening the amorphous phase of ACCs. Higher water content in the wet-saturated condition will reduce the flexibility in the

glass transition range, inducing additional hydrogen bonds [242]. The increase of crystallinity with the increasing water content was also observed in the present study (Figures 6.4 and 6.19), which correlated with the previous studies [126, 243].

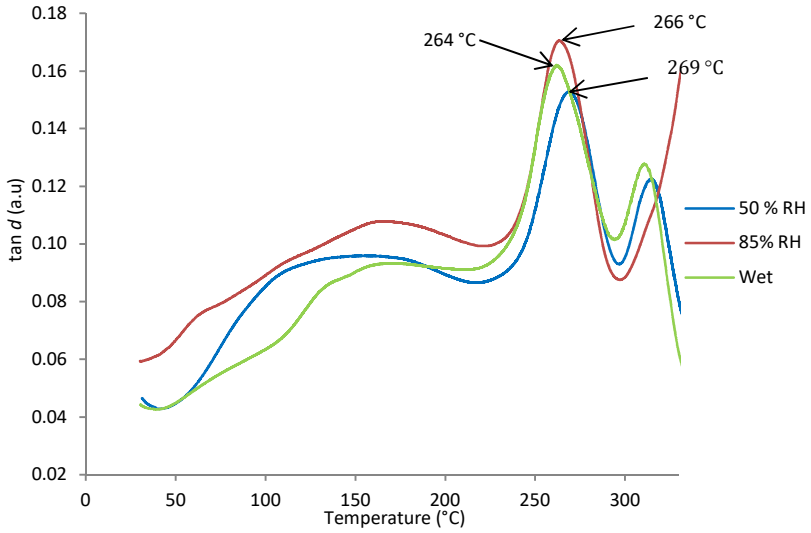

Figure 6.31 tan δ as a function of temperature for ACC produced *via* BmimAc at various environmental conditions.

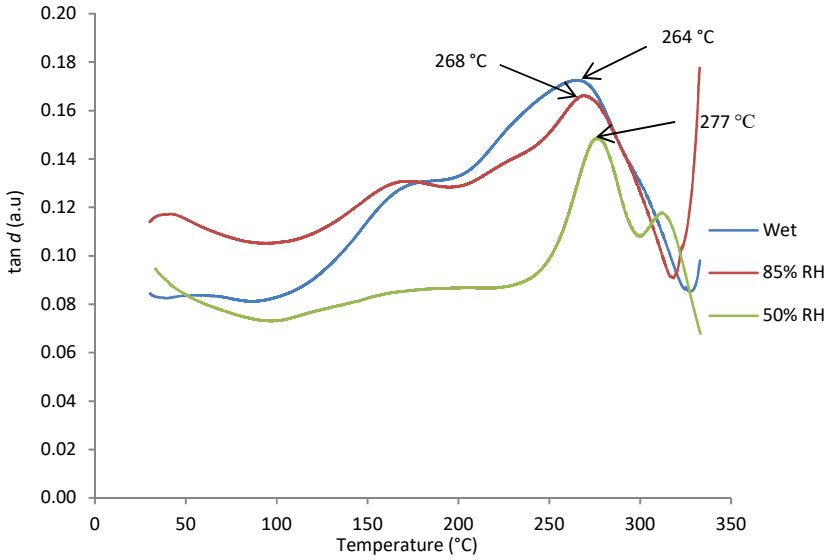

Figure 6.32 tan δ as a function of temperature for ACC produced *via* NaOH/urea at various environmental conditions.

6.3.6 Hygrothermal effect on molecular deformation

The hygrothermal effect on molecular deformation for the ACC produced *via* BmimAc was examined at t_d and P_{HP} of 60 min and 0.25 MPa, respectively. This effect was also examined for the ACC produced *via* NaOH/urea at t_d and P_{HP} of 15 min and 0.50 MPa, respectively. Examples of a peak shift for the C-O-C vibration at 50% RH for the ACCs produced *via* BmimAc and NaOH/urea are presented (Figures 6.33 and 6.38, respectively). These results indicated that the decreasing wavenumber was associated with C-O-C vibration, indicating an increase of the covalent bond length that was involved during the vibration absorption [174]. Thus, the decreasing *E* for the ACCs was presumed to be due to the dependency of stiffness of the C-O-C vibration.

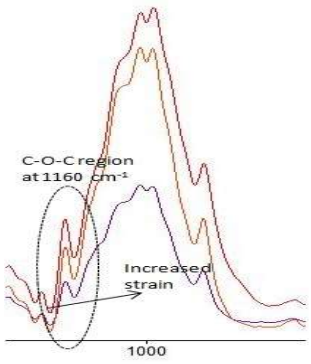

Figure 6.33 FTIR spectra showing the C-O-C vibration peak at 1160 cm^{-1} for ACC produced *via* BmimAc.

The shifting of the absorption peak at the C-O-C region at various environmental conditions of 50, 85% RH, and wet-saturated condition to a lower wavenumber was observed (Figure 6.34). The experimental data were fitted using linear regression. A strong and good correlation was observed with R^2 above 0.85 for all environmental conditions. The highest gradient of -0.28

cm^{-1} $\%^{-1}$ for 50% RH was observed, representing a good stress transfer from the less-stiff to the more-stiff phase in the ACC. The theoretical *E* can be estimated using Eq. 6.3 which is summarised in Table 6.2.

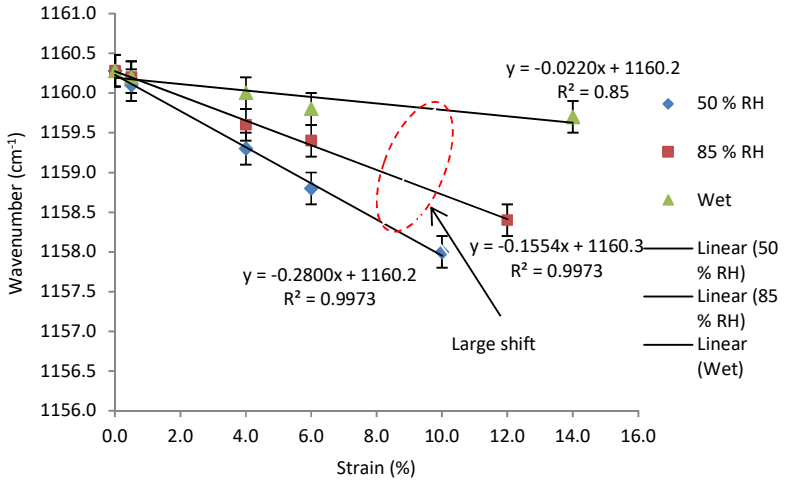

Figure 6.34 Shifting wavenumber at C-O-C region for ACC produced *via* BmimAc at various environmental conditions.

Table 6.2 The comparison between theoretical and experimental values for Young's modulus at various environmental conditions

Environmental conditions	Gradient (cm^{-1} $\%^{-1}$)	*E* (GPa) (Theoretical)	*E* (GPa) (Experimental)		
			Reading 1	Reading 2	Reading 3
50% RH	0.280	5.28	7.32	5.50	6.60
85% RH	0.155	3.60	3.70	4.20	5.50
Wet-saturated	0.022	0.93	0.43	0.42	0.44

A linear equation with the $R^2 = 0.89$ is expressed in Eq. 6.12 between the theoretical data of *E* and EMC:

$$E_{theoretical} = -0.121EMC + 6.221 \quad \text{Eq. 6.12}$$

Based on the R^2, the result from the linear regression analyses proposed that the general equation can predict the *E* values based on the EMC with an acceptable accuracy. The equation above was used to determine the extent of *E* values based on the EMC. The experimental data points (Table 6.2) located within the error of ±15% (Figure 6.35). Eq. 6.12 can estimate accurately the *E* values at any range of EMC. A high accuracy to estimate *E* was due to the single independent variable, EMC, used to calculate *E*.

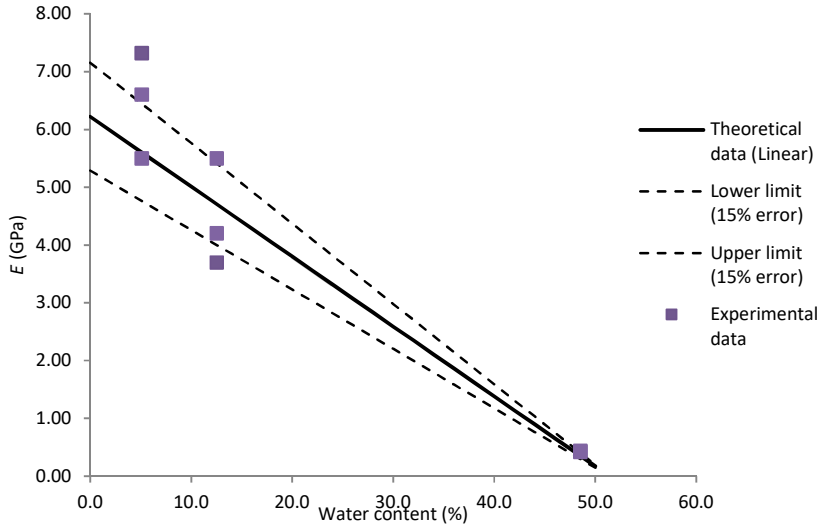

Figure 6.35 A comparison between experimental and theoretical data of Young's modulus for ACC produced *via* BmimAc.

The increasing wavenumbers at 3350 cm^{-1} with the increasing strain for ACCs produced *via* BmimAc and NaOH/urea were observed (Figures 6.36 and 6.41, respectively). These results were associated with the decrease of OH bond length due to the weakening of the hydrogen bonding under straining. A strong influence of the hydrogen bonding on this absorption peak had been demonstrated [244].

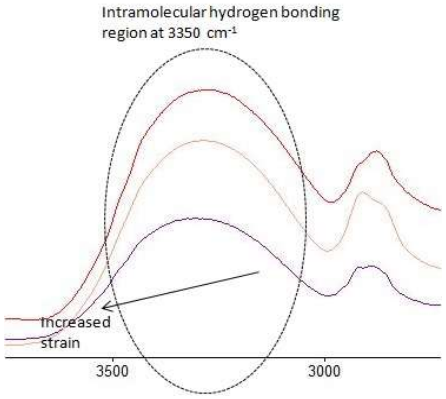

Figure 6.36 FTIR spectra showing the OH vibration peak at 3350 cm^{-1} for ACC produced *via* BmimAc.

The shifting of the peak at 3350 cm^{-1} at various environmental conditions of 50, 85% RH, and wet-saturated condition to higher wavenumbers was observed (Figure 6.37). The experimental data were fitted using linear regression. A strong and good correlation was observed with R^2 above 0.90 for all environmental conditions. The highest gradient for wet-saturated condition was observed, representing a significant weakening of hydrogen bonding at this condition.

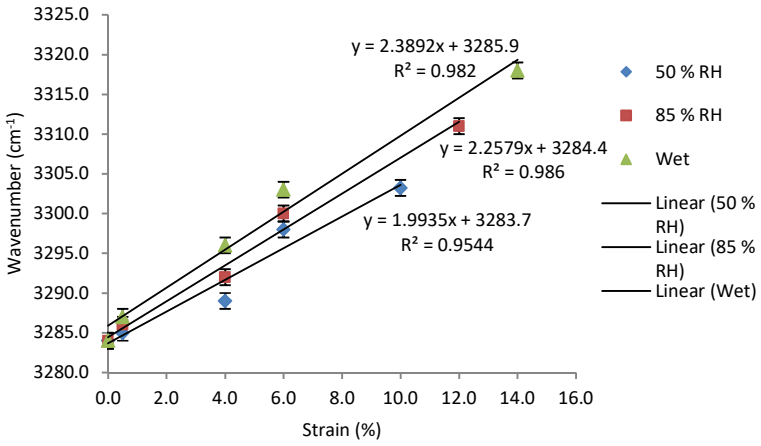

Figure 6.37 Shifting wavenumber at OH region for ACC produced *via* BmimAc at various environmental conditions.

The shifting of the absorption peak at the C-O-C region at various environmental conditions of 50, 85% RH, and wet-saturated condition to lower wavenumbers was observed (Figure 6.39). In comparison, the gradient for the ACC produced *via* NaOH/urea was slightly lower than the ACC produced *via* BmimAc at any environmental condition. A larger difference between 50% RH and wet-saturated condition was found for the ACC produced *via* BmimAc as compared to NaOH/urea (Figures 6.34 and 6.39, respectively). The experimental data were fitted using linear regression, showing a strong and good correlation with R^2 above 0.80 for all environmental conditions. The highest gradient of -0.078 cm^{-1} $\%^{-1}$ for 50% RH was observed, showing a good stress transfer from the less-stiff to the more-stiff phase in the ACC. The theoretical *E* can be estimated using Eq. 6.3, as summarised in Table 6.3.

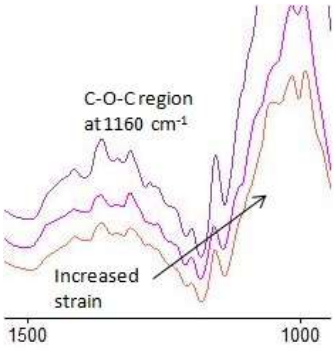

Figure 6.38 FTIR spectra showing the C-O-C vibration peak at 1160 cm^{-1} for ACC produced *via* NaOH/urea.

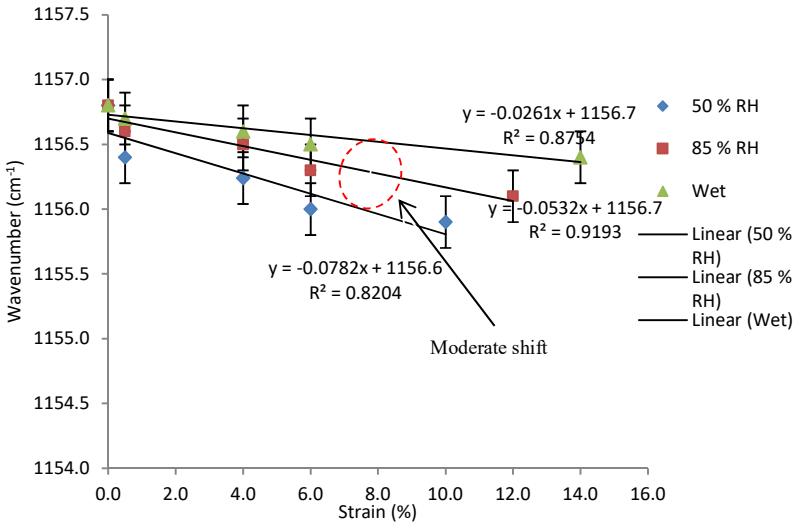

Figure 6.39 Shifting wavenumber at C-O-C region for ACC produced *via* NaOH/urea at various environmental conditions.

Table 6.3 The comparison between theoretical and experimental values for Young's modulus at various environmental conditions.

Environmental conditions	Gradient (cm^{-1} $\%^{-1}$)	*E* (GPa) (Theoretical)	*E* (GPa) (Experimental)		
			Reading 1	Reading 2	Reading 3
50% RH	0.08	1.81	1.49	1.91	1.69
85% RH	0.05	1.23	1.21	1.61	1.32
Wet-saturated	0.03	0.60	0.61	0.51	0.75

A linear equation with the $R^2 = 0.87$ is expressed in Eq. 6.13 between the theoretical data for *E* and EMC:

$$E_{theoretical} = -0.017EMC + 1.720 \qquad \text{Eq. 6.13}$$

The R^2 for ACC produced *via* NaOH/urea was comparable with BmimAc. The experimental data points were located within the error of ±15% (Figure 6.40) according to Eq. 6.13. The equation seemed to accurately estimate the extent of E values within a certain range of water content. The results were similar to the aforementioned discussion for ACC produced *via* BmimAc.

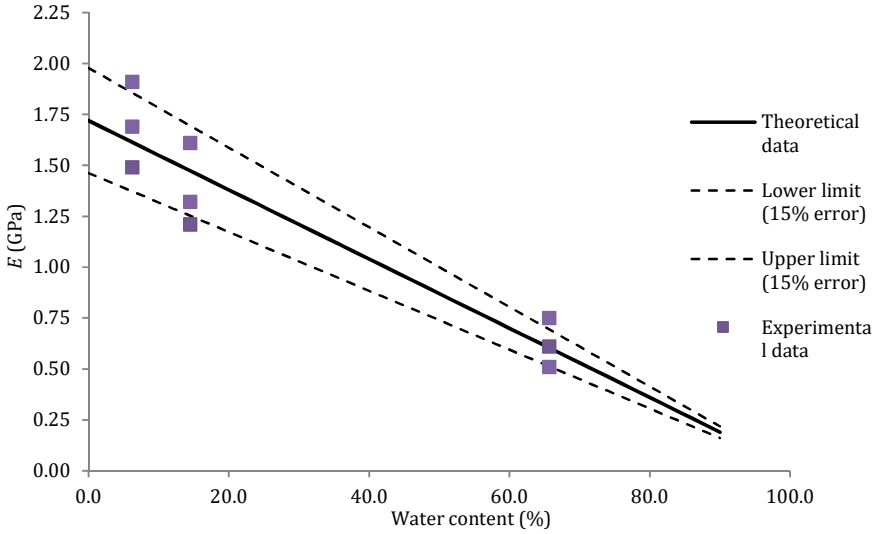

Figure 6.40 A comparison between experimental and theoretical data of Young's modulus for ACC produced *via* NaOH/urea.

The shifting of the absorption peak at the OH region at environmental conditions of 50, 85% RH, and wet-saturated condition for ACC produced *via* NaOH/urea to higher wavenumbers was observed (Figure 6.42), representing a similar result to the ACC produced *via* BmimAc. The fitted experimental data showed that a strong correlation with R^2 was above 0.80 for all environmental conditions. The lowest gradient of 1.38 cm^{-1} $\%^{-1}$ was observed for 50% RH, correlating to the least significant weakening of hydrogen bonding. A lower gradient was observed for ACC produced *via* NaOH/urea than BmimAc, indicating less weakening of hydrogen bonding for the ACCs produced *via* NaOH/urea than BmimAc.

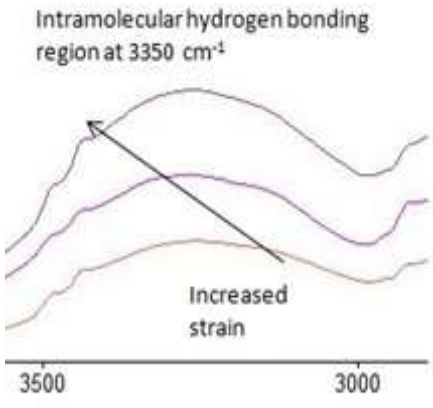

Figure 6.41 FTIR spectra showing the OH vibration peak at 3350 cm^{-1} for ACC produced *via* NaOH/urea.

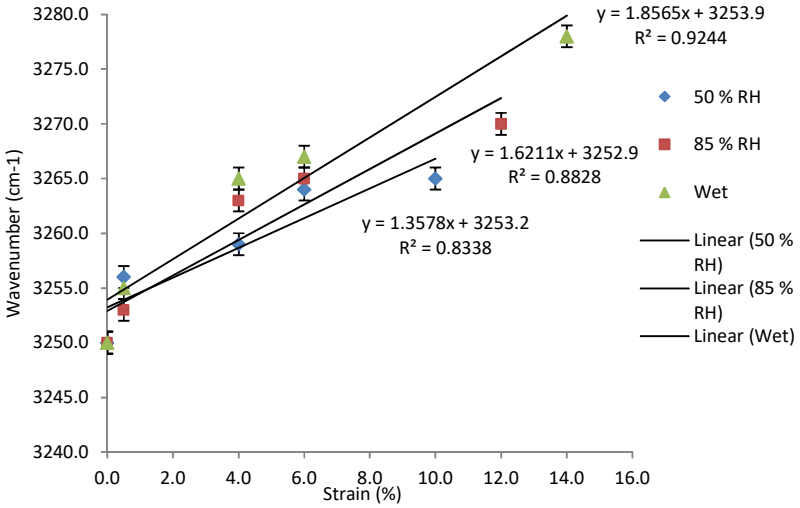

Figure 6.42 Shifting wavenumber at OH region for ACC produced *via* NaOH/urea at various environmental conditions.

6.3.7 Hygrothermal effect on the microstructures

In the present study, different shift patterns of the vibration peaks at C-O-C bond were observed for the environmental conditions of (50, 85% RH, and wet). Water imparted a strong effect on the straining at C-O-C bond, as observed from the shifting peak at 1160 cm^{-1} to a lower

wavenumber. This result was consistent with the lowest gradient, as observed in the wet-saturated condition in comparison to the other conditions. Rafeadah *et al.* [238] elucidated that the shift of wavenumber to a lower value indicated a molecular deformation at the C-O-C bond, representing a stress transfer from the weak to stiff phase. The large deformation can be observed from a larger decrease of wavenumber from its initial strain (Figure 6.34), indicating a good stress transfer in ACC.

In the present study, the molecular deformation of ACCs was observed as an equal stress condition, as shown by a large gap between 50% RH and wet-saturated condition (Figures 6.34 and 6.39, respectively). The equal stress condition was associated with the applied load along the length of cellulose microfibrils, as reported by Salmen *et al.* [174]. As illustrated in Figure 6.43, more amorphous phases were located along the length than the surface of cellulose microfibrils due to the anti-parallel arrangement of ACC, sourced from cellulose II. The findings in this present study were consistent with the previous studies, indicating that the parallel and anti-parallel cellulose packing correlated with cellulose I and II, respectively [78, 245].

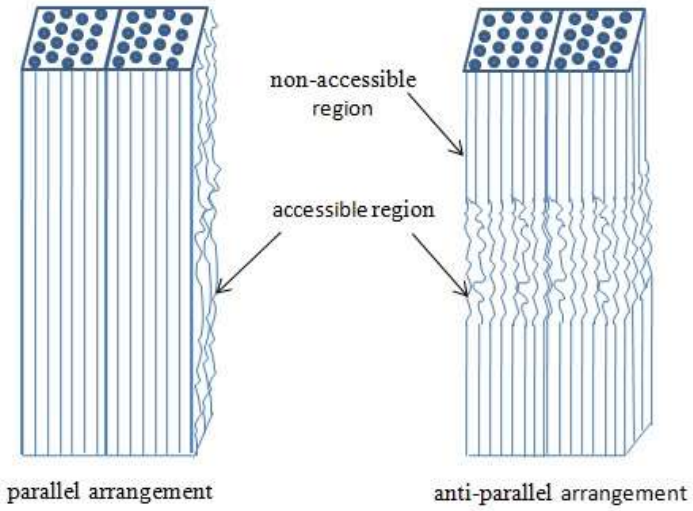

Figure 6.43 Schematic illustration of cellulose microfibril arrangement (Adapted from [174]).

6.4 Summary of findings

As a conclusion, the summary of the above works are discussed below:

- In the present study, the water thresholds of E, UTS and ε_f for the ACC produced *via* BmimAc were 40.0, 45.0, and 45.0%, respectively. The water thresholds of E, UTS and ε_f for the ACC produced *via* NaOH/urea were 60.0, 60.0, and 55.0%, respectively. A higher water threshold was observed for the ACC produced *via* NaOH/urea than BmimAc. This may be due to the higher K_{sr} and V_v observed for the ACC produced *via* NaOH/urea compared to BmimAc. However, further work is required to investigate the accuracy of the water threshold values in the future study.
- The decreasing T_g with the increase of water content was observed. This finding was expected due to the plasticisation effect of water, increasing the cellulose free volume and chain motion. The increasing chain mobility reduced the relaxation time and the hydrogen bonding density, softening the amorphous phase of ACC and reducing the T_g.
- E and UTS values decreased with the increasing water content. This was due to the elongation of the C-O-C bond. Under the wet-saturated condition, the less-stiff components in the cellulose structures were softened and unable to carry much load. The softened cellulose structures led to a lesser stress transfer from the matrix to the reinforcement component in the ACC, as observed from the highest gradient at 50% RH condition. This result presented a strong stress transfer, as represented from the highest E at 50% RH.
- The partially dissolved cellulose interrupted the intra- or intermolecular hydrogen bonds upon dissolving in the solvent. The hydrogen bonding was expected to increase during the regeneration process using distilled water. The surface of the cellulose experienced a higher degree of ordering and formed a hydrogen bonding network with the presence of water, resulting in an increase in the mechanical properties of cellulose

upon drying. The amorphous region was also observed after dissolving it in the solvent. The effect of water on the ACCs was significant on their mechanical properties due to the decreasing *E* and UTS. The presence of water weakened the hydrogen bonding in the ACCs. The increasing wavenumber (3000 – 3500 cm^{-1}) was anticipated due to the weakening of the hydrogen bonding. The broader peak (3000 – 3500 cm^{-1}) was believed to be caused by the association of the cellulose chain through the hydrogen bonds. The increase of water content was indicated by a narrower and sharper peak, showing the splitting of the hydrogen bonds.

Chapter 7

Creep behaviour of all-cellulose composites

7.1 Introduction

Many previous studies have focussed on determining the static mechanical properties of ACCs such as tensile strength, E, and ε_f [191, 246]. However, dynamic mechanical properties such as creep performance of composite materials is an important factor in the consideration of long-term performance [191]. Creep is defined as an increasing strain with time at a constant stress, whereby the strain returns to zero upon releasing the stress if the material is able to undergo recovery [247]. During creep, the material experiences an instantaneous elastic deformation that is completely reversible. Then, the creep rate reaches a steady-state value and finally, the creep rate increases rapidly and the material ruptures. Accurate creep predictions are important, especially in structural applications [248]. However, virtually no information can be found regarding the creep behaviour of ACCs.

Numerous mathematical expressions and models have been proposed to describe the creep behaviour of polymers. Among these models, several attempts have been performed to develop constitutive methods and describe their nonlinear creep behaviour. The most widely used nonlinear viscoelastic model is the Schapery model and its modifications. This model is based on irreversible thermodynamics principles and has shown to accurately describe creep performance [192, 193]. On the other hand, if the material is tested in the linear viscoelastic range, the creep behaviour can be represented by a simple rheological model. The Bürger model is a combination of elastic and viscous elements, providing a satisfactory representation of creep compliance [194, 249]. The model is a combination of Maxwell and Kevin-Voigt

elements [250]. This model is used to present the relationship between the morphology of the composites and their creep behaviour [251]. For most general cases of a linear viscoelastic solid, the total strain ($\varepsilon_{(t)}$) is the sum of three essentially separate parts: (i) immediate elastic deformation (ε_{SM}), (ii) delayed elastic deformation (ε_{KV}), and (iii) Newtonian flow (ε_{∞}). The ε_{∞} value is identical with the deformation of a viscous liquid obeying Newton's law of viscosity [250].

Long-term creep behaviour may also be predicted from short-term test data if the TTS principle is applicable to the material [191]. A master curve is constructed from TTS that provides creep strain over extended periods of time. However, differences between experimental long-term creep data and the master curve at lower creep compliance may occur due to physical aging, particularly in amorphous polymers [191].

A study carried out by Nunez *et al.* [191] investigated the effects of various woodflour contents, interfacial interactions and temperatures on the creep performance of woodflour-polypropylene (PP) composites. The TTS principle was used to generate a master curve. The optimal fitting curve based on the Bürger model was used to determine the Kevin-Voigt and Maxwell parameters (*e.g.* viscous and elastic behaviours) of the material. Creep strain was observed to decrease with the increasing woodflour content [191]. Similarly, Jia *et al.* [250] reported that creep strain of polypropylene/carbon nanotube composites decreases with an increase in the carbon nanotube content. The addition of a small amount of compatibiliser (PP-maleic anhydride copolymer) greatly improved creep resistance, probably due to improvements in the fibre-matrix interfacial strength [191]. Temperature is also an important parameter when designing composites for application, as polymers soften with the increasing temperature due to increasing chain mobility that results in increased opportunity for creep [191, 250].

7.2 Experimental procedures

DMA Q800 from TA Instruments was used for the creep tests. In the present study, a preliminary test was performed to identify a suitable stress for the creep test. The stress had to be within LVR. A short-term creep experiment (test duration = 600 s) was performed in creep mode using a tension film fixture with a gauge length of 12.87 mm. ACCs samples were cut approximately by 20 (l) × 5 (w) × 0.4 (h) mm. Various stresses were used (0.05, 0.1, 0.2, 0.5, 1.0, 2.5, and 5.0 MPa) at a constant temperature (30 °C).

The short-term creep test procedures were followed as the above paragraph to determine the hygrothermal effect on creep behaviour of ACCs. The creep and recoverable strain were determined as the function of the time. The creep time and recovery were set to 180 and 2700 s, respectively. The samples were conditioned at different environmental conditions: (i) 50% RH (23 °C), (ii) 85% RH (23 °C), (iii) wet-saturated, and (iv) dry condition prior to the creep test. A controlled humidity chamber was used to condition the samples. The creep test was performed immediately after taking out from the controlled humidity chamber at three different temperatures: (i) 30, (ii) 60, and (iii) 100 °C.

To construct a master curve, samples were cut into the aforementioned dimension. Samples were vacuum-dried at 95 °C in the oven prior to the test to remove all the moisture from the samples. The short-term creep procedure was followed with the temperature range from 30 to 200 °C and the temperature step of 5 °C. The same creep time as mentioned in the first paragraph was used. The data were analysed using the 'Rheological Advantage Thermal Analysis' software. Long-term creep tests were also performed to investigate physical aging.

Mechanical analogies including viscous elements (dashpots) and elastic elements (springs) are the simplest way to simulate the viscous and elastic behaviour of a material. In order to simulate

the creep behaviour, a viscoelastic liquid model with relaxation times was used. Furthermore, the Bürgers model was used (Figure 7.1) [191, 250].

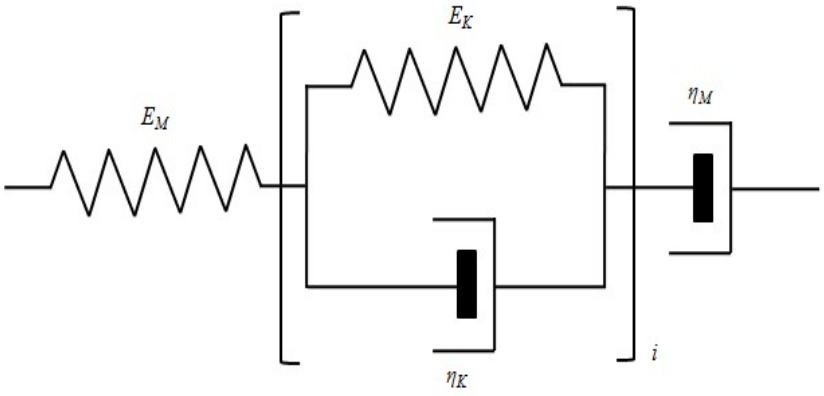

Figure 7.1 Bürgers model (Reproduced from Nunez *et al.* [191]).

The $\varepsilon_{(t)}$ is given by the following equation:

$$\varepsilon_{(t)} = \frac{\sigma}{E_M} + \sum_{i=1}^{n-1} \frac{\sigma}{E_K}.\left[1 - \exp\left(-t.\frac{E_K}{\eta_K}\right)\right] + \frac{\sigma}{\eta_M}.t \qquad \text{Eq. 7.1}$$

where σ is the applied stress, t is the time, E_M and η_M are the modulus and viscosity of the Maxwell spring and dashpot, respectively; E_K and η_K are the modulus and viscosity of the dashpot of the Kelvin-Voigt element, respectively. The ratio η_K/E_K (relaxation time (τ)), is a measure of the time required for the extension of the spring to its equilibrium length while being retarded by the dashpot. Thus, the summation represents the retarded response of the material (decreasing creep rate). Finally, the last viscous element of the Maxwell element largely contributes to the region of steady state creep, where viscous flow is the predominant behaviour.

In order to predict a long-term creep behaviour, it is generally assumed that the polymer does not change its structure with time, so the TTS principle holds. The creep curves obtained at different temperatures are superposed by the horizontal shifts along a logarithmic time scale (ln α_T) to obtain a master curve. The master curve allows a long time-range prediction at the selected reference temperature. Different authors have shown that the approach is viable in some composite systems [194, 252]. If the shifts in the TTS are thought to be a process of matching relaxation times, the shift factors (α_T) are given by:

$$\alpha_T = \frac{\tau(T)}{\tau(T_0)} = \frac{\eta(T)}{\eta(T_0)} \qquad \text{Eq. 7.2}$$

where $\tau(T)$ are the corresponding material relaxation times at a given temperature T, T_0 is the reference temperature and $\eta(T)$ and $\eta(T_0)$ are the viscosities of the material at the temperatures T and T_0. The shift factors can be correlated with temperature using the William-Landel-Ferry (WLF) equation or the Arrhenius equation. The former equation is given by:

$$\log(\alpha_T) = \frac{-C_1.(T - T_0)}{C_2 + (T - T_0)} \qquad \text{Eq. 7.3}$$

where C_1 and C_2 are constants and T_0 is the reference temperature. On the other hand, the Arrhenius equation is:

$$\ln(\alpha_T) = \frac{-E_a}{R}.\left(\frac{1}{T} - \frac{1}{T_0}\right) \qquad \text{Eq. 7.4}$$

where E_a is an activation energy and R is the universal gas constant.

The objective of the present study was to investigate the creep behaviour of ACCs. The hygrothermal effect on the creep performance of ACCs was investigated. The TTS principle

was used to construct the master curve from the short-term creep tests. The long-term creep result was compared with the master curve in order to investigate the physical aging of ACCs. The Bürgers model was used to fit the experimental data in the creep analyses.

7.3 Results and discussion

7.3.1 Determination of linear viscoelastic region

The determination of LVR was essential to ensure that the stress was applied in the range of a linear phase of the LVR during the creep test. Creep strain-stress graphs were plotted from a set of maximum creep results obtained at various stress values after 600 s. The maximum stress for ACCs produced *via* BmimAc (Figure 7.2) and NaOH/urea (Figure 7.3) were 5.0 and 1.0 MPa, respectively.

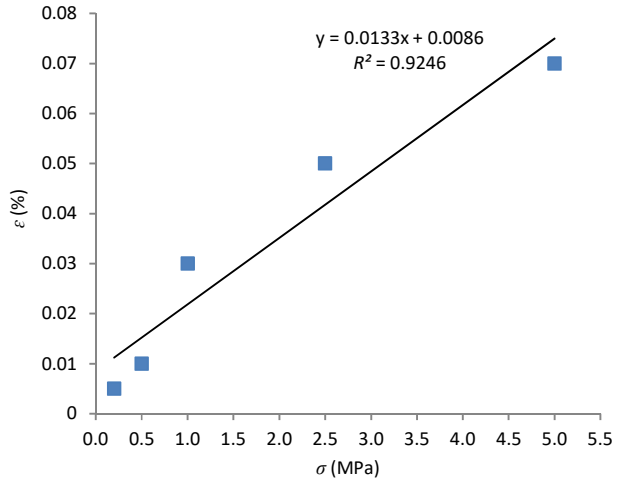

Figure 7.2 Creep strain-stress plot for ACC produced *via* BmimAc.

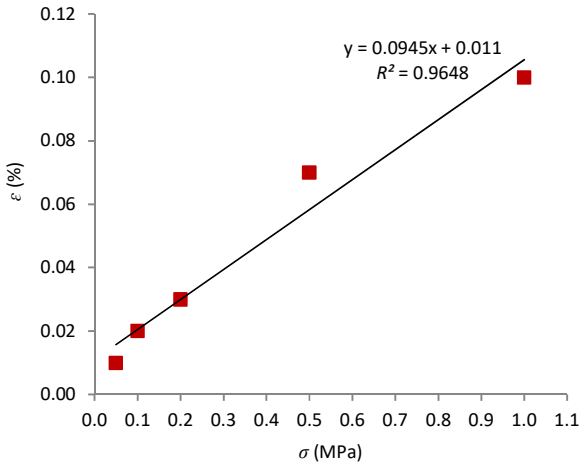

Figure 7.3 Creep strain-stress plot for ACC produced *via* NaOH/urea.

7.3.2 Hygrothermal effect on creep behaviour

In a semicrystalline polymer, the mobility of the amorphous molecules is greatly hindered by the reinforcing effect of the crystalline phase [191]. Nunez *et al.* stated that no change in the mobility of crystalline structure is expected if the creep test is conducted below the melting temperature of a polymer [191]. The creep plots of dry condition for both solvents presented a good curve fitting with the Bürger model (Figure 7.4). For the ACC produced *via* BmimAc, the highest creep strain of 0.044% was observed at 100 °C (Figure 7.4 (a)). Similarly, the highest creep strain of 0.105% was also observed at 100 °C for the ACC produced *via* NaOH/urea (Figure 7.4 (b)). An increasing creep strain with increasing temperature can be seen for both solvents. This result will be reported for other environmental conditions (50, 80% RH, and wet-saturated samples), as summarised in Table 7.5 and 7.6.

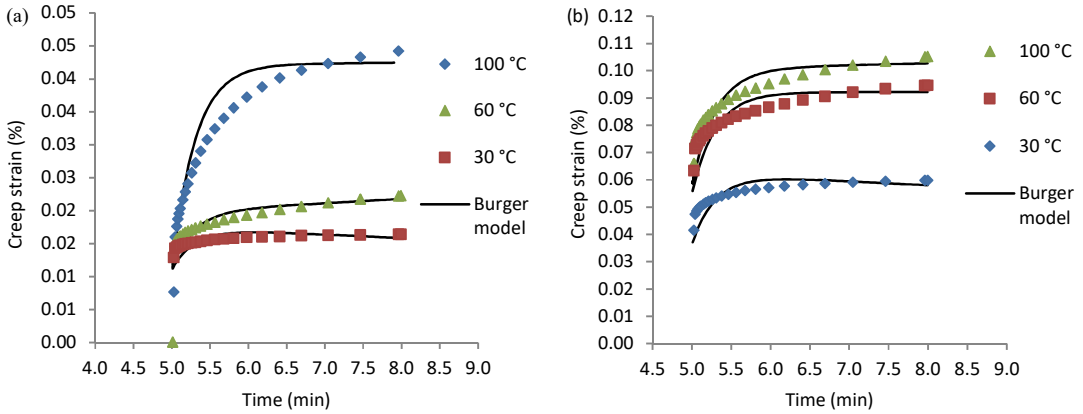

Figure 7.4 Creep strain as a function of times at various temperatures for dry condition: (a) ACC produced *via* BmimAc, and (b) NaOH/urea.

The increasing creep strain with the increasing water content is presented in Figures 7.5-7.7. This result was due to (i) the interruption of the hydrogen bonding by water, (ii) V_v and (iii) microstructures factors. The creep strain for ACC produced *via* NaOH/urea was significantly higher than BmimAc. This finding was consistent with the aforementioned discussion in Chapter 6 (Section 6.3.1 and 6.3.3), indicating that the decreasing hydrogen bonding density with the increasing water content was more pronounced in the ACC produced *via* NaOH/urea than BmimAc. Furthermore, a higher V_v was found in the ACC produced *via* NaOH/urea compared to BmimAc (Section 4.3.8). With the increasing V_v, more water was expected to reside within the cellulose fibre. As a result, higher D was observed for the ACC produced *via* NaOH/urea than BmimAc (Section 5.4.1). Furthermore, less ordered amorphous molecular chain was expected in the ACC produced *via* NaOH/urea than BmimAc. The increasing fibre pull out can be expected from the fibre-matrix interfacial adhesion in wet-saturated condition compared to a dry condition. The homogeneous dispersion of dissolved cellulose (matrixes) around the undissolved cellulose (fibres) can be observed. The increasing creep strain was associated with the increasing amorphous intensity due to the increasing water content (Sections 6.3.1 and 6.3.3). Higher V_m for ACC produced *via* NaOH/urea than BmimAc was

observed (Section 4.3.8), resulting in more significant increase of creep strain for the ACC produced *via* NaOH/urea than BmimAc.

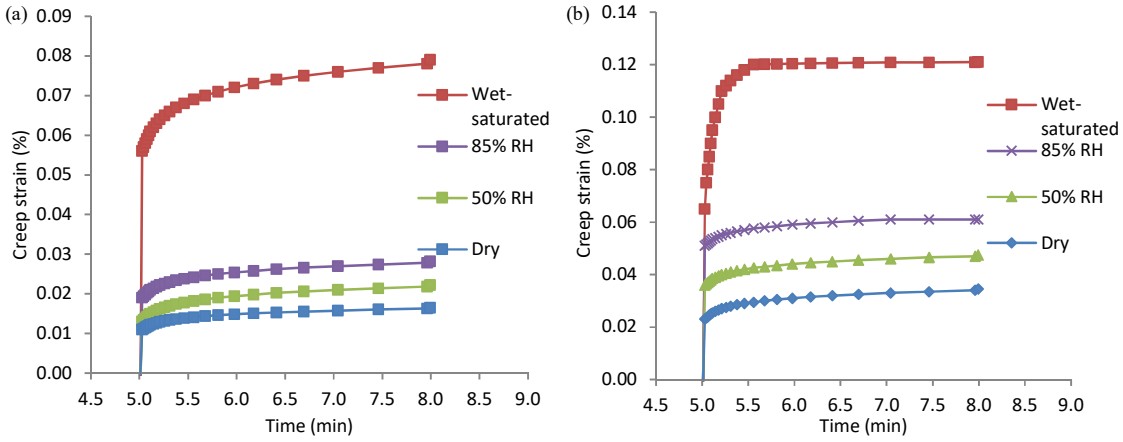

Figure 7.5 Creep strain as a function of time at various environmental conditions (30 °C): (a) ACC produced *via* BmimAc and (b) NaOH/urea.

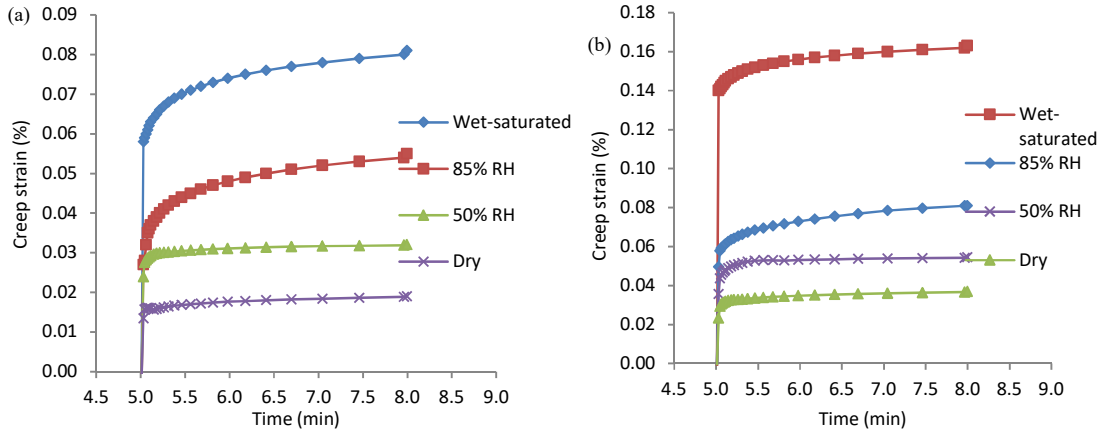

Figure 7.6 Creep strain as a function of time at various environmental conditions (60 °C): (a) ACC produced *via* BmimAc, and (b) NaOH/urea.

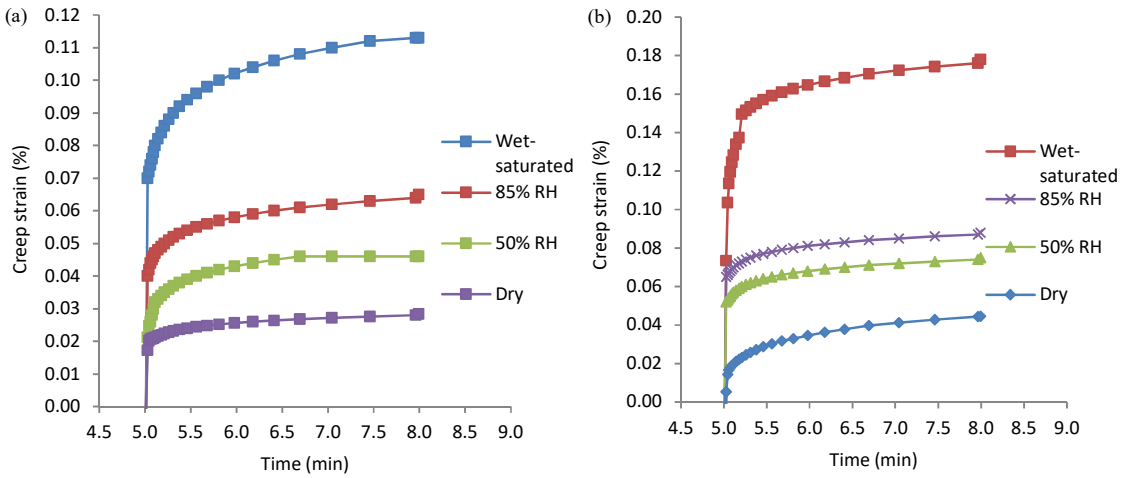

Figure 7.7 Creep strain as a function of time at various environmental conditions (100 °C): (a) ACC produced *via* BmimAc, and (b) NaOH/urea.

The increasing creep strain is observed with the increasing temperature (Figure 7.8). This result was due to the changes in the mobility of amorphous bulk and tie molecules [191, 253, 254]. Furthermore, the increasing creep strain with the increasing water content was also observed (Figure 7.8). The water threshold of 45 and 55% for ε_f were observed for ACCs produced *via* BmimAc and NaOH/urea, respectively (Sections 6.3.1 and 6.3.3). The presence of free water beyond 45 and 55% would impart a significant increase of creep strain (Figure 7.8). The movement of free water would dissipate energy and impart high stress concentrations at the crystallite interface due to the elimination of free water from the anhydrous crystal to the amorphous region [180]. The presence of bound water can be observed at the low creep strain (Figure 7.8). The increasing water mobility was associated with the increasing relaxation time as a function of water content (Figures 7.17 and 7.18), as discussed in the previous study by Sun *et al.* [180].

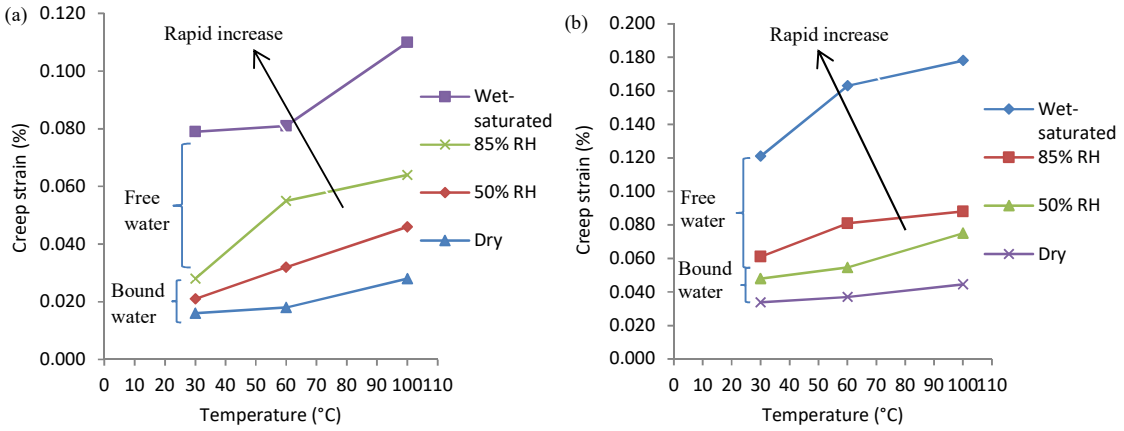

Figure 7.8 The relationship between creep strain and temperature at various environmental conditions for (a) ACC produced *via* BmimAc, and (b) NaOH/urea, respectively.

The recovery strain increased as the water content increased (Figures 7.9-7.11). The increase of recovery strain corresponded to the increase of permanent strain (ε_∞) values as the water content increased. ε_∞ was associated with the slippage effect in the cellulosic fibres of ACCs (Figures 7.9-7.11). The slippage effect was more significant with the increase of water content, as observed from a wider gap (between 85% RH and wet-saturated condition) and the presence of free water for high water content (Figures 7.9-7.11). The slippage of molecular chains of ACCs was expected to occur in the amorphous region. Meanwhile, a narrower gap (between dry and 85% RH) was observed at a low water content (Figures 7.9-7.11), indicating the least significant slippage effect due to the presence of bound water.

The significant slippage effect can also be observed from the differences of recovery strain ($\Delta_{\text{Recovery strain}}$) (Figures 7.12 and 7.13). For the ACC produced *via* BmimAc, the $\Delta_{\text{Recovery strain}}$ values of 0.0171 and 0.0091% for wet-saturated and dry conditions were observed, respectively. Meanwhile, for ACC produced *via* NaOH/urea, the $\Delta_{\text{Recovery strain}}$ values of 0.0465 and 0.0099% for wet-saturated and dry conditions were reported, respectively. A higher $\Delta_{\text{Recovery strain}}$ values for ACC produced *via* NaOH/urea than BmimAc was observed, attributing

to high strain due to the increasing water mobility. Furthermore, the increasing V_v in ACC produced *via* NaOH/urea reduced the ability of the material to return to its initial length due to the increasing local stress concentration. The decreasing recovery strain inhibited the slippage of molecular chain of the ACCs with the decreasing water content. This result contributed to the increasing viscosity and decreasing permanent strain (recovery strain).

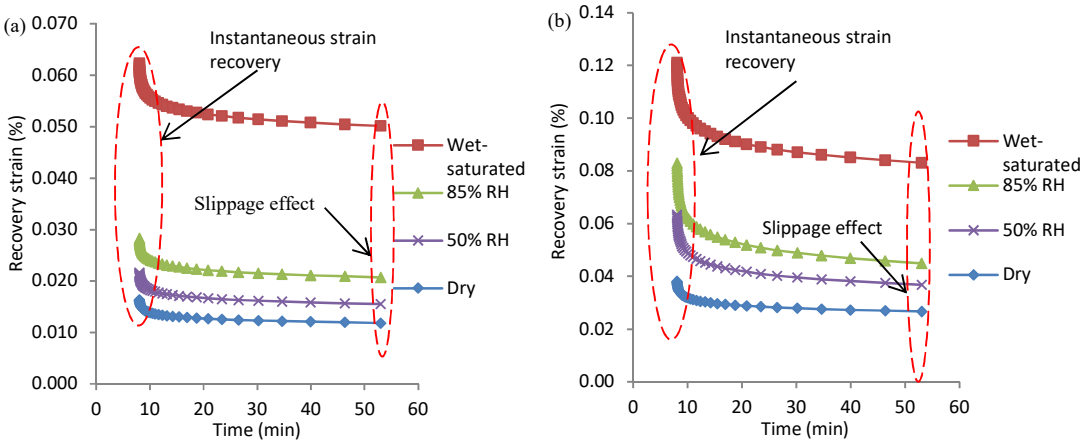

Figure 7.9 Recovery strain as a function of time at various environmental conditions (30 °C): (a) ACC produced *via* BmimAc, and (b) NaOH/urea.

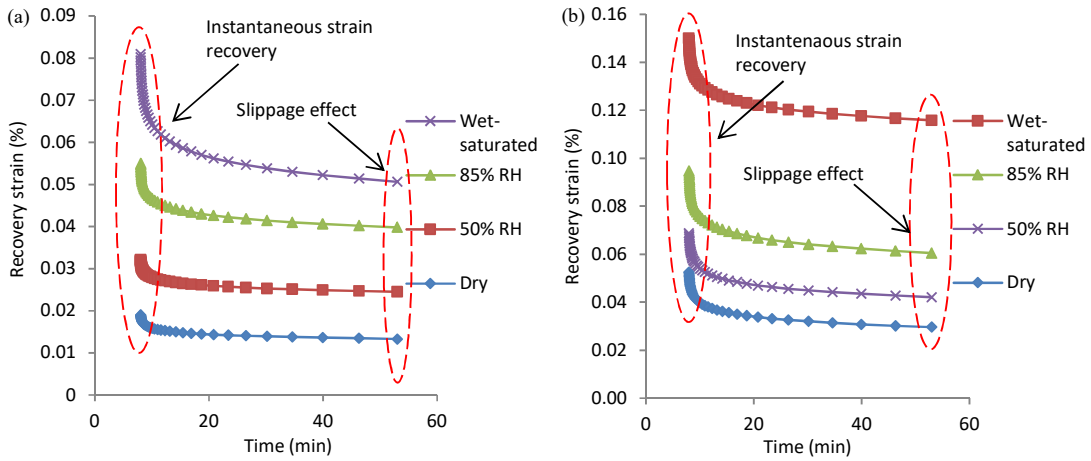

Figure 7.10 Recovery strain as a function of time various environmental conditions (60 °C): (a) ACC produced *via* BmimAc, and (b) NaOH/urea.

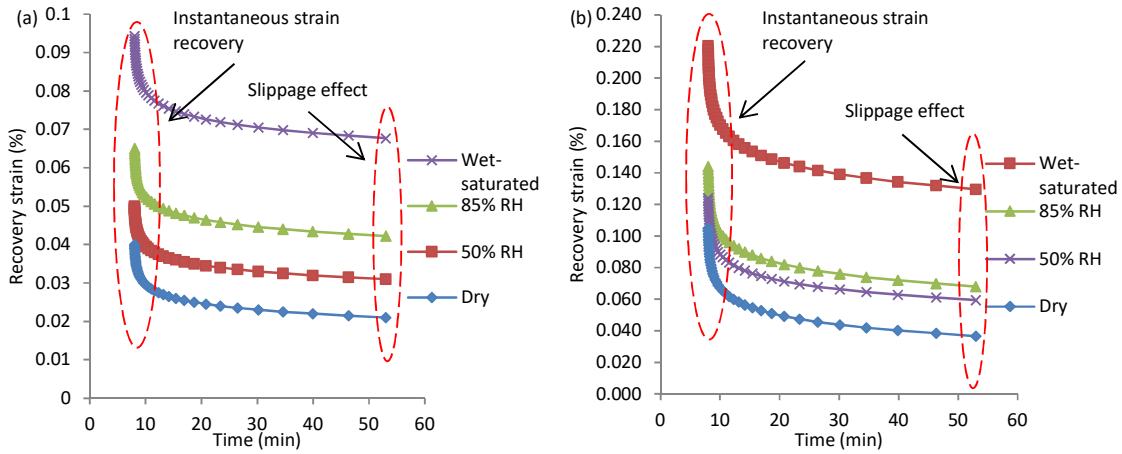

Figure 7.11 Recovery strain as a function of time various environmental conditions (100 °C): (a) ACC produced *via* BmimAc, and (b) NaOH/urea.

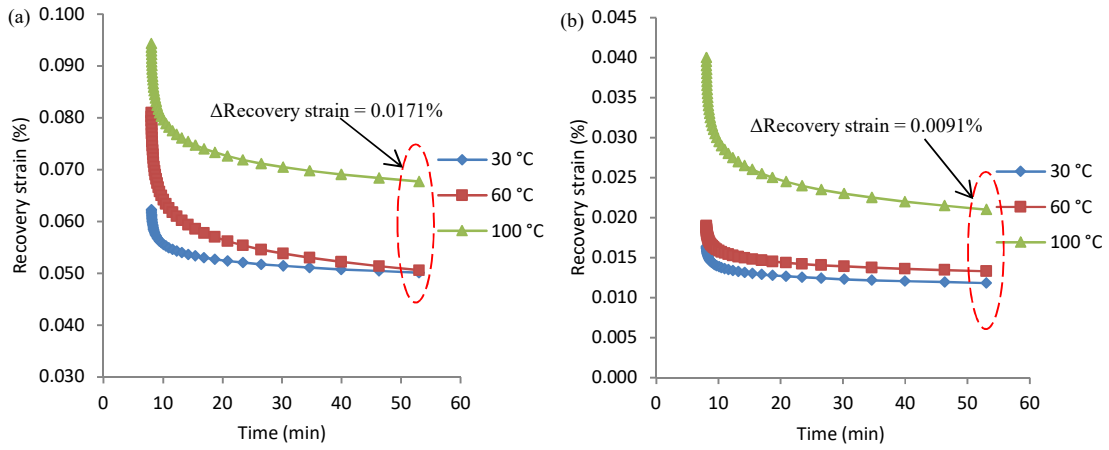

Figure 7.12 Temperature dependant recovery strain for ACC produced *via* BmimAc: (a) wet-saturated, and (b) dry condition.

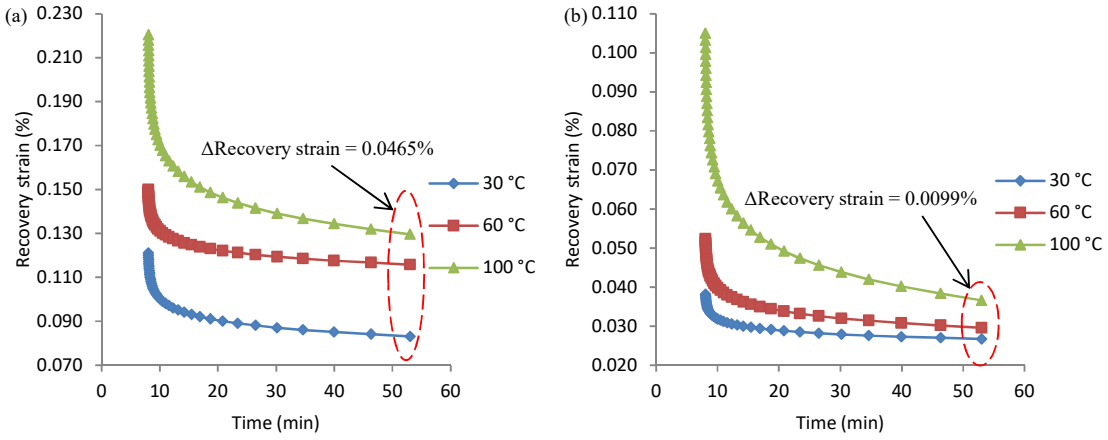

Figure 7.13 Temperature dependant recovery strain for ACC produced *via* NaOH/urea: (a) wet-saturated, and (b) dry condition.

The increasing recovery strain with the increase of temperature is observed (Figure 7.14), indicating the influence of temperature on the slippage between the molecular chains of ACCs. A more significant slippage effect was observed at the temperature of 100 than 30 °C, as indicated from a wider gap at the temperature of 100 than 30 °C (Figure 7.14). Thus, more slippage was observed for ACC produced *via* NaOH/urea than BmimAc, as indicated by a higher creep strain. These findings suggested that both creep and recovery strain can be used

in identifying the slippage effect. This effect can be minimised by utilising a low temperature and less water content.

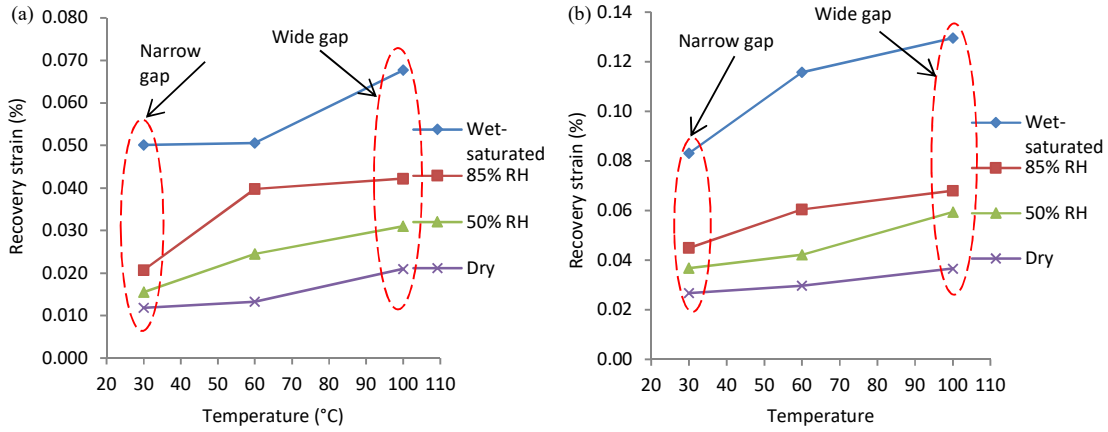

Figure 7.14 The relationship between recovery strain and temperature at various environmental conditions for (a) ACCs produced *via* BmimAc and (b) NaOH/urea, respectively.

The increasing creep compliances with the increasing temperature and water content was reported (Tables 7.1 and 7.2), corresponding to the creep strain analyses (Figures 7.5-7.7). Meanwhile, the increasing recoverable compliances with the increasing temperature water content was also observed (Tables 7.3 and 7.4), corresponding to the recovery strain (Figures 7.9-7.11).

Table 7.1 Creep compliance for ACC produced *via* BmimAc at various temperatures and environmental conditions

	Environmental conditions	Temperature (°C)		
		30	60	100
Creep compliance (m^2/N)	Wet-saturated	1.58×10^{-8}	1.62×10^{-8}	2.20×10^{-8}
	85% RH	5.60×10^{-9}	1.10×10^{-8}	1.28×10^{-8}
	50% RH	4.20×10^{-9}	6.4×10^{-9}	9.20×10^{-9}
	Dry	3.2×10^{-9}	3.60×10^{-9}	5.60×10^{-9}

Table 7.2 Creep compliance for ACC produced *via* NaOH/urea at various temperatures and environmental conditions

	Environmental conditions	Temperature (°C)		
		30	60	100
Creep compliance (m^2/N)	Wet-saturated	1.21×10^{-7}	1.63×10^{-7}	1.78×10^{-7}
	85% RH	6.10×10^{-8}	8.1×10^{-8}	0.88×10^{-7}
	50% RH	4.80×10^{-8}	5.45×10^{-8}	0.75×10^{-7}
	Dry	3.38×10^{-8}	3.69×10^{-8}	0.45×10^{-7}

Table 7.3 Recoverable compliance for ACC produced *via* BmimAc at various temperatures and environmental conditions

	Environmental conditions	Temperature (°C)		
		30	60	100
Recoverable compliance (m^2/N)	Wet-saturated	1.00×10^{-8}	1.01×10^{-8}	1.35×10^{-8}
	85% RH	4.14×10^{-9}	7.96×10^{-9}	8.44×10^{-9}
	50% RH	3.10×10^{-9}	4.90×10^{-9}	6.20×10^{-9}
	Dry	2.36×10^{-9}	2.66×10^{-9}	4.20×10^{-9}

Table 7.4 Recoverable compliance for ACC produced *via* NaOH/urea at various temperatures and environmental conditions

	Environmental conditions	Temperature (°C)		
		30	60	100
Recoverable compliance (m^2/N)	Wet-saturated	8.31×10^{-8}	1.16×10^{-7}	1.30×10^{-7}
	85% RH	4.49×10^{-8}	6.05×10^{-8}	6.80×10^{-8}
	50% RH	3.68×10^{-8}	4.21×10^{-8}	5.94×10^{-8}
	Dry	2.67×10^{-8}	2.96×10^{-8}	3.66×10^{-8}

Relaxation ability was determined from the ratio between the recoverable compliance and the creep compliance. The decreasing relaxation ability was observed with the increasing water content (Figures 7.15 and 7.16), as indicated by the increasing creep compliance with the increase of water content. The relaxation ability for ACC produced *via* NaOH/urea was higher than for the ACC produced *via* BmimAc, as indicated by a higher recoverable compliance for the ACC produced *via* NaOH/urea compared to BmimAc. Adriana *et al.* reported that the

decreasing relaxation ability was due to a high density and low porosity of the cellulosic material [160]. This result was consistent with the low relaxation ability observed for ACC produced *via* BmimAc. The densities of 1.52 and 1.49 g/cm^3 were observed for ACCs produced *via* BmimAc and NaOH/urea, respectively. The relationship between density and V_v was inversely proportional, as discussed in Chapter 4 (Section 4.3.9). Furthermore, a high relaxation ability was associated with low crystallinity.

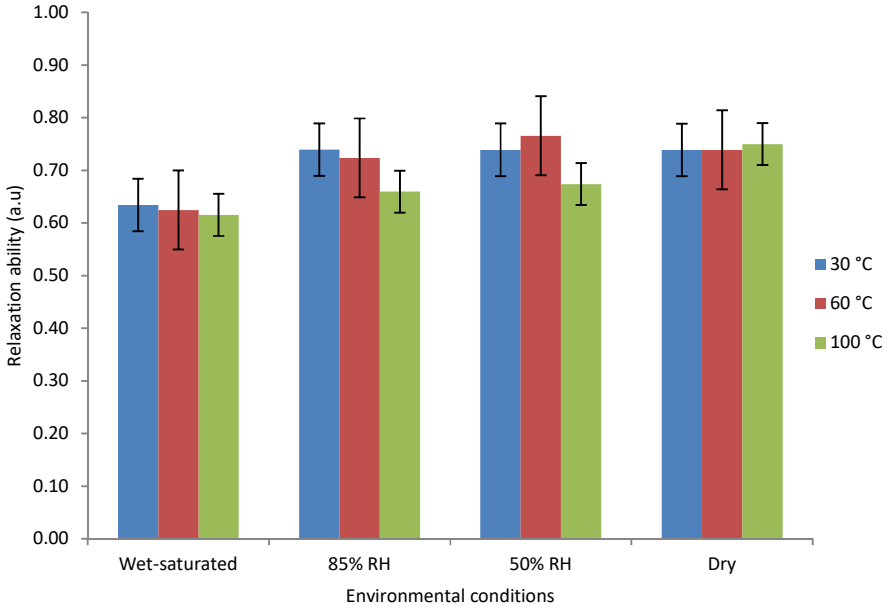

Figure 7.15 Relaxation ability for ACC produced *via* BmimAc at different environmental conditions and temperatures.

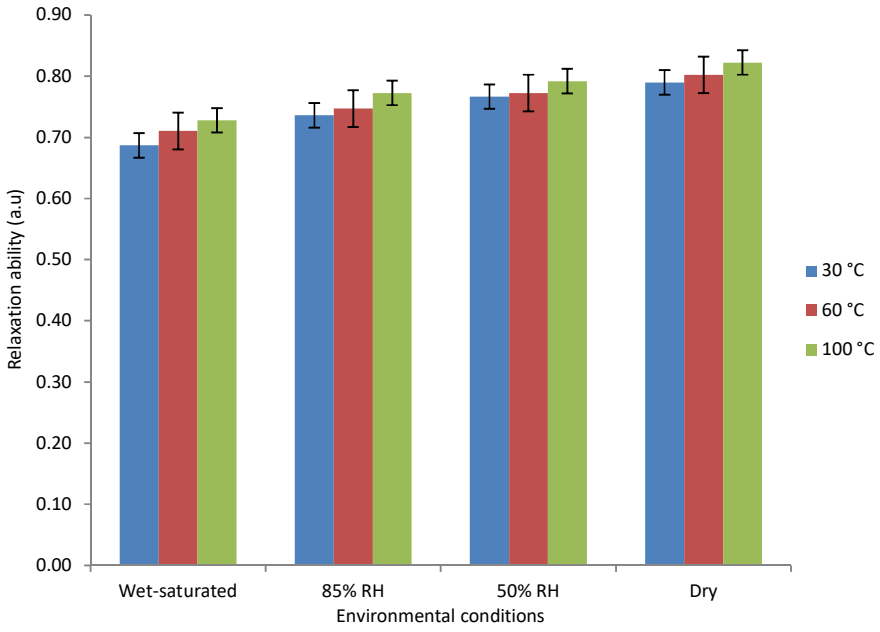

Figure 7.16 Relaxation ability for ACC produced *via* NaOH/urea at different environmental conditions and temperatures.

The decreasing E_M and E_K was observed with the increasing water content (Tables 7.5 and 7.6), indicating the decreasing E, as discussed in Chapter 6 (Section 6.3.1 and 6.3.3). Jia *et al.* reported that E_M was assigned to the Maxwell spring, representing an instantaneous creep strain that would be recovered after releasing the stress [250]. The decreasing instantaneous creep strain with the decreasing water content was observed (Figures 7.9-7.11). Jia *et al.* also reported that E_K was assigned to the Kevin-Voigt spring, associating with the stiffness of amorphous chain in the short-term creep test [250]. Therefore, the increasing stiffness with decreasing water content was expected. This relationship showed an increasing E_K with a decreasing water content (Tables 7.5 and 7.6). The differences between E_M and E_K for ACCs produced *via* BmimAc and NaOH/urea were observed. This result was due to different data for both ACC produced *via* BmimAc and NaOH/urea, used for fitting process of the creep curve.

The decreasing η_M and η_K was observed with the increasing water content (Tables 7.5 and 7.6). Interestingly, η_M was higher than η_K, corresponding to a higher sensitivity of η_M than η_K due to the presence of water [250]. The increasing η_M with the decreasing water content decreased the permanent strain (Figure 7.14). A high viscosity indicated a less significant slippage effect on the ACCs which was due to the less sliding of the Maxwell dashpot.

Table 7.5 Model fitting parameter of ACC produced *via* BmimAc at different environmental conditions (30 °C)

Environmental conditions	E_M (GPa)	E_K (GPa)	η_K (GPa.s)	η_M (GPa.s)	Relaxation time, τ (s)
Wet-saturated	0.2419	1.8257	7.1021	22.00	3.89
85% RH	0.2443	2.0469	7.4510	25.53	3.64
50% RH	0.3232	2.0921	7.5468	26.60	3.61
Dry	0.4822	2.1024	7.5468	27.83	3.59

Table 7.6 Model fitting parameter of ACC produced *via* NaOH/urea at different environmental conditions (30 °C)

Environmental conditions	E_M (GPa)	E_K (GPa)	η_K (GPa.s)	η_M (GPa.s)	Relaxation time, τ (s)
Wet-saturated	0.1676	2.8701	6.1020	45.58	2.13
85% RH	0.2301	3.5500	6.2150	47.12	1.75
50% RH	0.2702	3.8510	6.4130	48.50	1.67
Dry	0.3178	4.1841	6.5121	49.65	1.56

Relaxation time increased with the increasing water content (Figures 7.17 and 7.18). The relationship between relaxation time and water content was directly proportional, as similarly reported in the previous study by Sun *et al.* [180]. The increasing relaxation time was due to the increasing water activity with the increase of water content. The increasing relaxation time was observed between 85% RH and wet-saturated condition due to the presence of free water (Figures 7.17 and 7.18). The increasing relaxation time was also due to the motional decoupling of cellulose hydroxyl groups by fast exchange with added water [213]. The decreasing E_K was observed with the increase of relaxation times (Tables 7.5 and 7.6). This result was consistent with the decreasing stiffness of amorphous polymer chain in a short-term creep as the water content increased.

The increasing crystallinity with the increase of water content was reported due to the plasticisation induced crystallisation (Section 6.3.1 and 6.3.3). In the present study, water was expected to penetrate the paracrystalline region, causing the swelling of ACCs. The increase of the partially ordered crystalline region with the increase of water content was due to the increasing slippage effect. The free water was anticipated to dominantly concentrate in the ribbon-like structure of ACCs at the partially ordered crystalline region, preventing the rupture of ACCs. This was due to the remaining hydrogen bonding that delayed the interruption process. The increasing disordered region with the increasing water content may be observed, as indicated by a broader peak at plane $(1\bar{1}0)$, corresponding to $2\theta = 12.1°$. Thus, the increasing amorphous intensity with the increasing water content had been reported, as discussed in Chapter 6 (Sections 6.3.1 and 6.3.3). However, the presence of paracrystalline region was found at higher water content, resulting in the increase of crystallinity.

A lower relaxation time was observed for the ACC produced *via* NaOH/urea compared to BmimAc (Figures 7.17 and 7.18). A lower crystallinity can be seen for ACC produced *via* NaOH/urea than BmimAc, as discussed in Chapter 4 (Section 4.3.6). Thus, a linear relationship

between relaxation time and crystallinity was expected, as also reported by Ibbett *et al.* [213]. The increasing relaxation time was due to the decreasing free volume, reducing additional space for movement [255]. The lower free volume would be consistent to the higher density. The higher density was reported for the ACC produced *via* BmimAc than NaOH/urea (Section 4.3.9). Although the higher relaxation time was observed for the ACC produced *via* BmimAc than NaOH/urea which was due to the increasing water activity, lower D and EMC were observed for BmimAc than NaOH/urea. This result may be due to the lower V_v observed for the ACC produced *via* BmimAc than NaOH/urea, as discussed in Chapter 5 (Section 5.4.1).

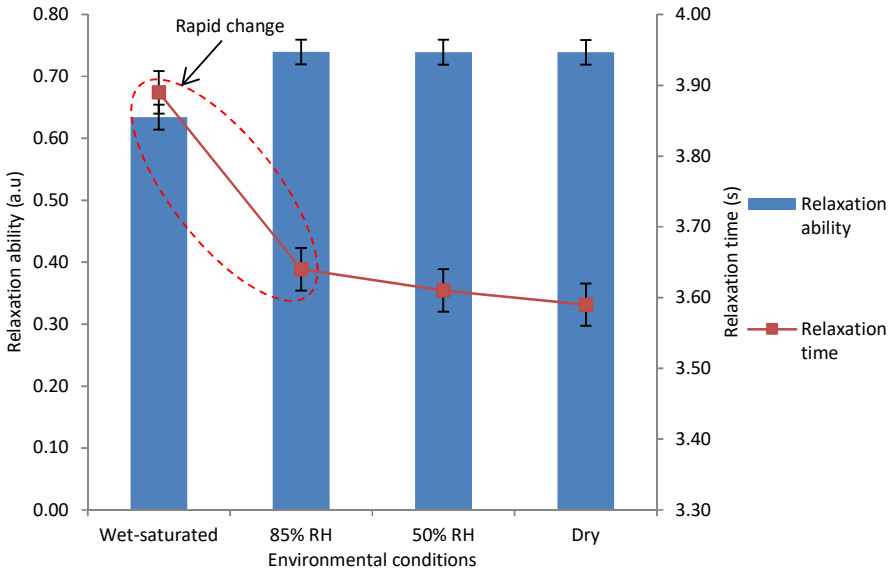

Figure 7.17 The relationship between relaxation ability and relaxation time as a function of different environmental conditions for ACC produced *via* BmimAc.

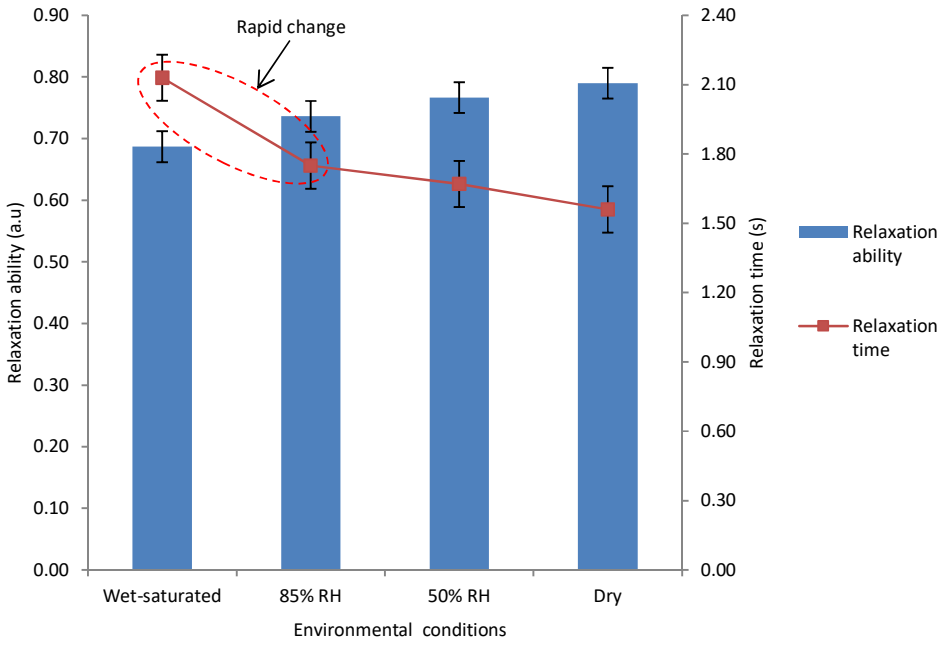

Figure 7.18 The relationship between relaxation ability and relaxation time as a function of different environmental conditions for ACC produced *via* NaOH/urea.

7.3.3 Time temperature superposition and long-term creep test

The TTS technique exploits the sensitivity of the molecular relaxation process to temperature. A quantitative equivalence between time and temperature can be achieved under certain simplifying assumptions. Thus, a long-term creep experiment can be replaced by a shorter one at a higher temperature. The effectiveness of this technique has been shown in the characterisation of different composite materials [191]. The short-term creep compliance data at various temperatures were shifted according to the TTS principle. In the present study, a reference temperature of 70 °C was selected. The master curves for ACC produced *via* BmimAc and NaOH/urea are presented in Figures 7.19 and 7.20, respectively.

Higher creep compliance was observed for ACC produced *via* NaOH/urea than BmimAc. This result was due to a higher V_v, D, and EMC reported for ACC produced *via* NaOH/urea than BmimAc, as discussed in Chapter 5 (Section 5.4.1). Thus, more slippage effect was found for

ACC produced *via* NaOH/urea as compared to BmimAc, indicated by a higher recovery strain differences for ACC produced *via* NaOH/urea (Figures 7.12 and 7.13). This finding was likely due to the inhomogeneous fibre-matrix dispersion and water aggregation at higher V_v, decreasing the mechanical properties (E and UTS) and increasing the creep compliance. Therefore, a better creep resistance was expected for the ACCs produced *via* BmimAc than NaOH/urea. The extended time of up to 10^7 and 10^8 s was observed for ACCs produced *via* BmimAc and NaOH, respectively (Figures 7.19 and 7.20).

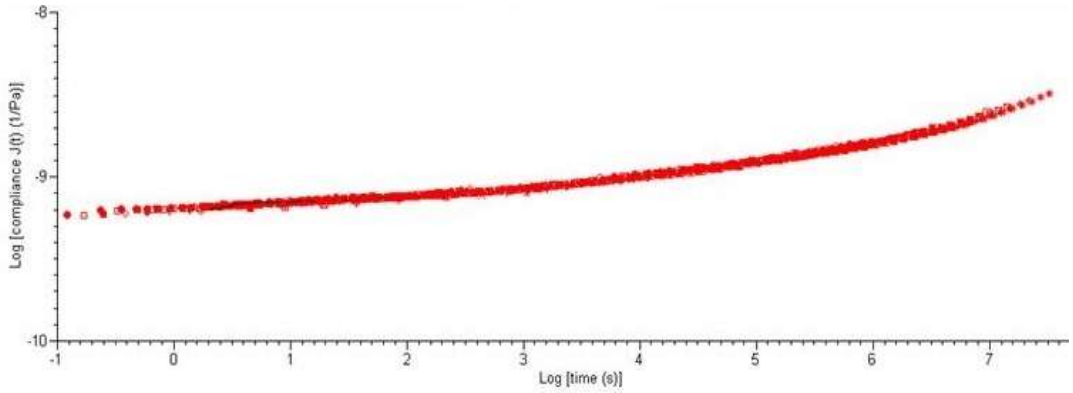

Figure 7.19 Master curve for ACC produced *via* BmimAc at reference temperature of 70 °C.

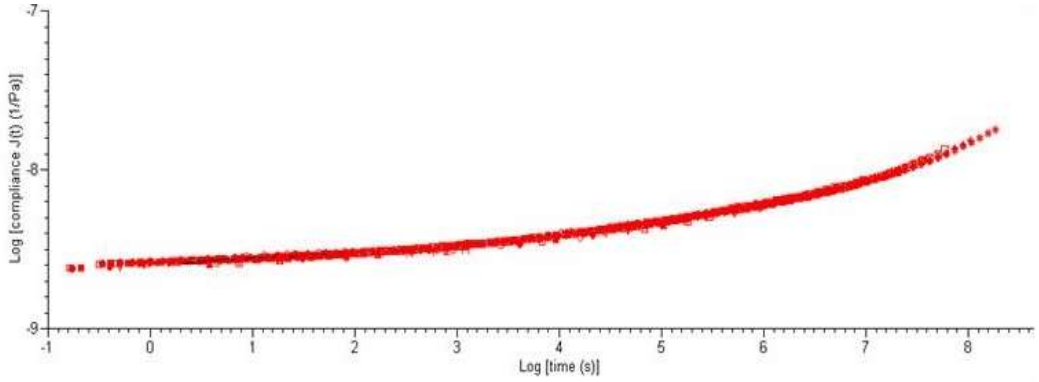

Figure 7.20 Master curve for ACC produced *via* NaOH/urea at reference temperature of 70 °C.

The shift factor values were determined according to the WLF and Arrhenius equations. For ACC produced *via* BmimAc, C_1 and C_2 for WLF were 51.8 and 1131, respectively. Meanwhile, for ACC produced *via* NaOH/urea, C_1 and C_2 for WLF were 3.86×10^7 and 8.32×10^8, respectively. E_a of 13.82 and 12.08 kJ/mol was observed for ACC produced *via* BmimAc and NaOH/urea, respectively, indicating a higher E_a for ACC produced *via* BmimAc than NaOH/urea. This result was due to a closer amorphous fraction to the crystalline region in the ACC produced *via* BmimAc than NaOH/urea. The higher E_a strongly prevented their chain mobility, as also reported in the previous study by Nunez *et al.* [191]. The higher E_a was also consistent with the higher CrI and density, as discussed in Chapter 4 (Sections 4.3.6 and 4.3.9). The increasing density resulted in a decreasing free volume, preventing the molecular chain mobility.

The experimental and theoretical data (WLF and Arrhenius models) were plotted for ACCs produced *via* BmimAc and NaOH/urea (Figures 7.21 and 7.22, respectively). The WLF model showed a better fitting of experimental data than the Arrhenius model. The large shift was observed between the experimental data and Arrhenius model that was due to the lower E_a of the ACC for both solvents. Thus, high E_a was probably required for a better curve fitting between the experimental shift data and Arrhenius model. This may be achieved by minimising the experimental error while running the short-term creep test.

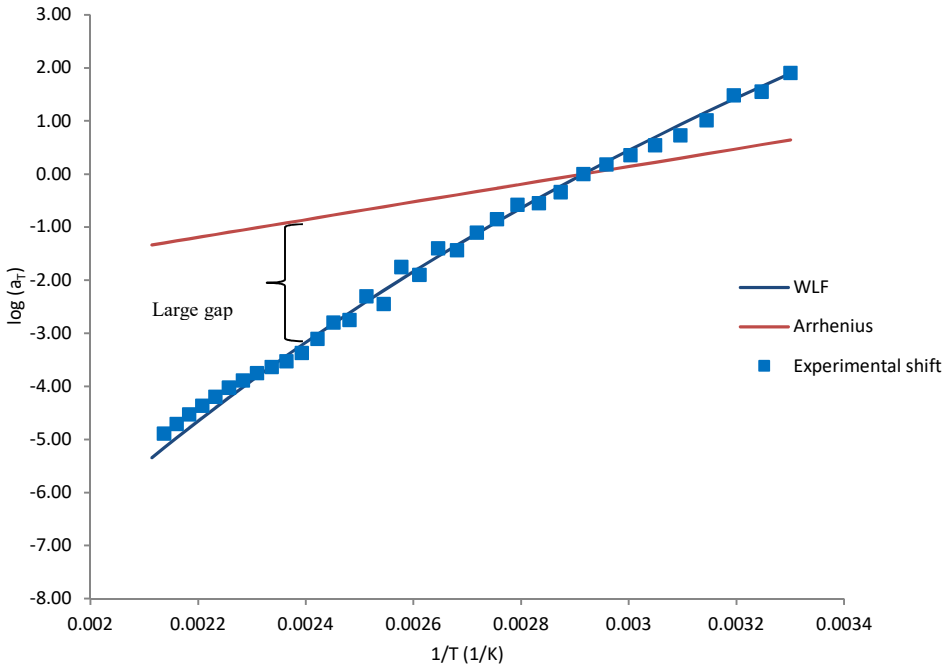

Figure 7.21 Correlation between experimental and theoretical shift factor for ACC produced *via* BmimAc.

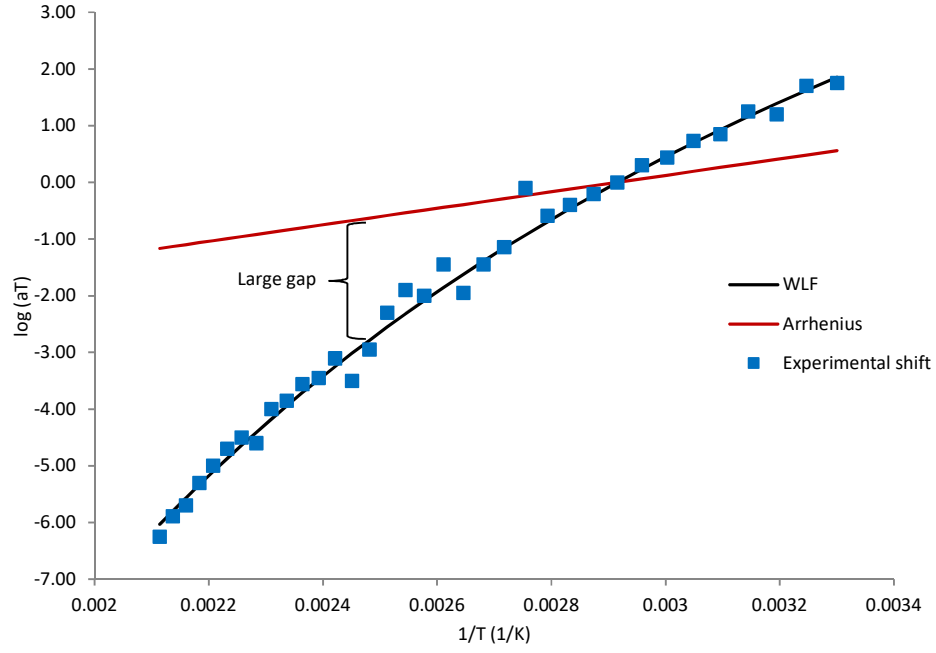

Figure 7.22 Correlation between experimental and theoretical shift factor for ACC produced *via* NaOH/urea.

The master curves were successfully constructed in the present study. However, it was not a sufficient condition to validate the TTS principle. The differences found between the experimental data and the master curves were due to physical aging [254, 256]. Nunez *et al.* reported that in a completely amorphous region, the glass transition occurs in a relatively narrow temperature range, below which physical aging occurs [191]. However, this is not the case in semicrystalline polymers, where the amorphous fractions are closer to the crystalline region that may be partially incorporated in both phases and consequently hinder their mobility.

The long-term creep test data for ACCs produced *via* BmimAc and NaOH/urea were shifted according to the shift factor at a reference temperature of 70 °C. The mismatch between the master curve and long-term creep was observed at a temperature of 30 °C due to physical aging (Figures 7.23 and 7.24). The mobility of molecular chain parts (free volume) was ceased, leading to a higher local density and a higher stiffness, and impeding the free mobility of surrounding chain parts [257]. Therefore, the free volume decreased but the rate of aging slowed down, which was also known as the self-retarding process [257]. On the other hand, the creep strain for long-term creep curves at temperatures of 150 and 200 °C were higher than the short-term master curve. Therefore, no physical aging effect was observed at the higher temperature (Figures 7.23 and 7.24). Both temperatures were required to effectively erase the physical aging effect due to the strong molecular chain of ACCs that prevented their mobility.

In comparison, a lower long-term creep strain at a temperature of 30 °C was observed for ACC produced *via* BmimAc compared to NaOH/urea. This result was due to the lower free volume surrounding the molecular chain parts for the ACC produced *via* BmimAc than NaOH/urea, resulting in a higher density and stiffness for the ACC produced *via* BmimAc. In addition, a comparable creep strain was found for the ACCs produced *via* BmimAc and NaOH/urea at the temperatures of 150 and 200 °C at longer creep time. However, a higher long-term creep strain was observed at the temperatures of 150 and 200 °C than 30 °C. This result was due to the

lower density and stiffness, resulting in higher free volume surrounding the molecular chain parts of ACCs for both solvents at 150 and 200 °C, as discussed previously. Thus, lower mechanical properties were presumed at higher temperatures.

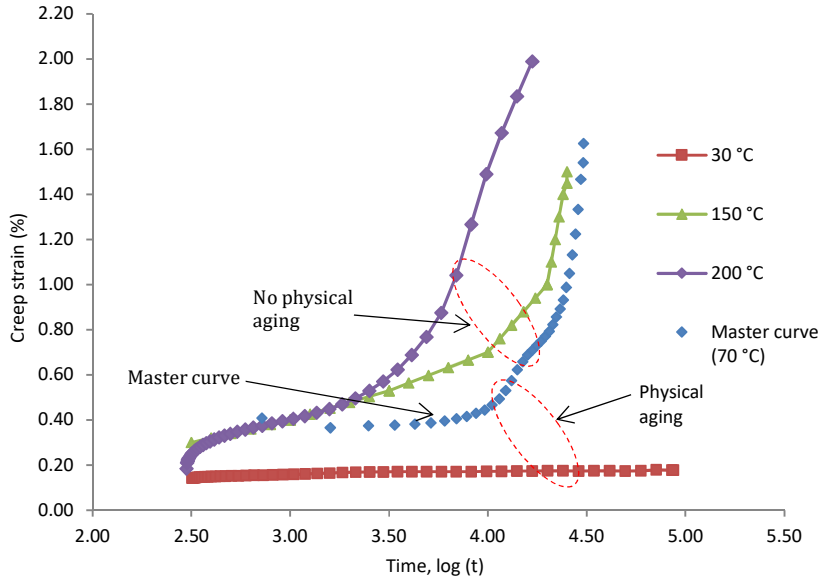

Figure 7.23 Physical aging effect at various temperatures for ACC produced *via* BmimAc.

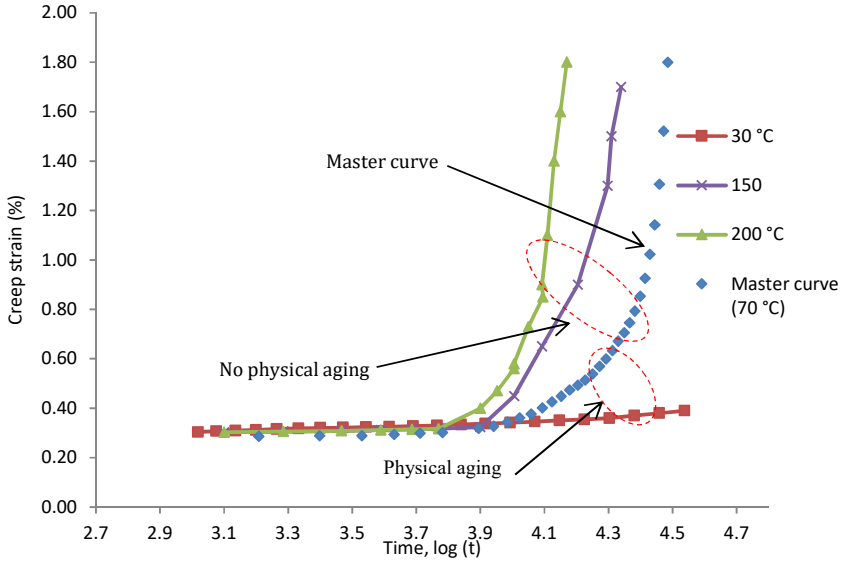

Figure 7.24 Physical aging effect at various temperatures for ACC produced *via* NaOH/urea.

7.4 Summary of findings

This chapter has presented and discussed the hygrothermal effects on the creep behaviour of ACCs. The following conclusions can be drawn based on the results of the present study:

- The increasing creep strain with the increasing water content and temperature was observed. This result was due to the increasing water activity at an extreme environmental condition.
- Lower creep strain was observed at lower water content and temperature. This result was due to the less slippage of molecular chain that was consistent with the increasing of viscosity and decreasing of the permanent strain at low water content and temperature.
- The increasing relaxation time with the increase of water content was reported. This finding was due to the decreasing of free volume, reducing its additional space for movement. Apart from that, the increasing CrI required a longer relaxation time, leading to a higher density and stiffness. However, with the increasing water content, the increase of the relaxation time had not promised to impart a higher stiffness. The decreasing hydrogen bonding density with the increase of water content was reported due to the interruption of hydrogen bonding. In addition, more slippage effect was found at higher water content. The presence of less hydrogen bonding density at higher water content would prevent the ACCs from rupturing, despite having excessive slipping of molecular chain.
- However, longer relaxation time was observed for the ACC produced *via* BmimAc than NaOH/urea. The relaxation time was inversely proportional with V_v. A higher V_v allowed more free water to reside within the gap. The effect of free water had significantly increased the creep strain at higher water content. This result may be due to the increase of water mobility at high water content due to the presence of free water.

More free water was observed for the ACC produced *via* NaOH/urea than BmimAc. The higher relaxation time observed for ACC produced *via* BmimAc was consistent with its higher density and CrI.

- The experimental shift factor was successfully fitted using the WLF compared to the Arrhenius model. The physical aging effect was observed at the temperature of 30 °C and eliminated at the temperatures of 150 and 200 °C. The physical aging effect was observed at a lower temperature due to its lower strain than the expected strain (master curve). This effect was neglected at higher temperature due to its higher strain than the expected strain, although it was not superimposed to the master curve.

Chapter 8

Conclusions and Future work

8.1 Conclusions

Generally, it is possible to approach the optimisation of all-cellulose composite through the use of a Taguchi-type analysis. The results of the Taguchi analysis could be correlated with microstructural changes that are found to be sensitive to the processing conditions used to fabricate an ACC laminae. t_d imparts the greatest influence on E and UTS of ACC laminae as shown by a Taguchi fractional factorial experimental design and ANOVA. At the optimal t_d of 60 and 15 min for both ACC produced *via* BmimAc and NaOH/urea, respectively, the optimisation of the mechanical properties was associated with a more homogeneous, void-free microstructure in the ACC laminae. It is observed that the presence of voids reduces the overall elastic modulus of the material and the critical stress required for the onset of failure. The decreasing E and UTS is reported beyond the optimal t_d due to the presence of microstructure failure (*e.g.* curved crack, void, and etc.).

It is observed that the moisture diffusion mechanism in ACCs follows the Fickian diffusion behaviour (n = 0.5). D increased with the increasing V_v and water temperature. The lowest V_v is found to be an optimum parametric control factor to minimise D. The significant increase in V_v results in more water to fill the gaps within the ACC structures. D increased as the water temperature increased due to the increasing mobility of the water molecules. The increasing E_a was observed with the increasing V_v. This result showed that a stronger dependence of diffusion coefficient of water on the water temperature, showing by a steeper slope of ln (D) versus 1/T due to a significant increase in V_v.

The negative water effect on the mechanical properties of ACC is clearly observed in this present study, leading to a decrease in the mechanical properties. It is likely to be due to the interaction between water-cellulose molecules. The significant disruption of the rigidity of cellulose structure (*e.g.* hydrogen bonding) is expected due to the increasing V_v that enhanced more water penetration into cellulose structure. The increasing CrI is observed as V_v increases. However, the increasing CrI is expected to counterbalance the increasing D due to the regeneration of more crystalline phase.

The decreasing E and UTS are observed with the increasing water content due to the elongation of the C-O-C bonding. This can be observed from the shifting of the wavenumber at 1160 cm^{-1} to a lower wavenumber region. The softening effect of cellulose structure under wet-saturated condition reduces the stress transfer from matrix to reinforcing phase, resulting in the decreasing E. This is shown by the lowest slope value of a plot of wavenumber versus strain. Apart from that, the weakening of hydrogen bonding is observed from the increasing wavenumber in a range of 3000 – 3500 cm^{-1} due to the presence of water that is associated with the hydrogen bonding. Thus, the decreasing of mechanical properties of ACC is reported.

Interestingly, a higher creep strain is reported with the increasing water content. This result is due to the increasing water activity and more slippage of molecular chain at an extreme environmental condition. A longer relaxation time is required at a higher CrI. This result is due to the decreasing free volume, thus reducing its additional space for movement.

The optimisation approach taken in this study may be applied to a multiaxial all-cellulose laminates that are expected to be significantly different due to changes in failure mechanisms. The application of ACC in engineering field depends on the different environmental conditions, which are likely to influence the mechanical properties. The findings in this present study prove that the ACC produced with the optimum parametric control factors can be successfully used

to produce a stable ACC that is suitable for exterior application due to its lower *D*. However, further study is still required to minimise the formation of void through a proper selection of control factors and their range during SIP.

The objectives of the present study were to (i) investigate the critical control factors for ACCs production, (ii) investigate the effect of the significant control factor on water absorption behaviour of ACCs, and (ii) determine the hygrothermal effects on the mechanical properties and creep behaviour of ACCs. The main contributions of the entire research are summarised as follows:

a) Parametric study

- For the ACCs produced *via* BmimAc and NaOH/urea, t_d was the most significant control factor, followed by P_{HP}.
- The equation developed from MRA showed that the mechanical outputs (*E* and UTS) equations were successfully developed for the ACC produced *via* NaOH/urea. This result was shown from a higher R^2 values for both *E* and UTS. A linear relationship between the desirable control factors and the mechanical outputs was observed. However, for ACC produced *via* BmimAc, lower R^2 than the ACC produced *via* NaOH/urea was observed. This result may be due to the nonlinear relationship between the control factors and the mechanical properties. Thus, the use of MRA may be inappropriate to predict the *E* and UTS for the ACC produced *via* BmimAc.
- In comparison, the ACC produced *via* BmimAc imparted better mechanical properties than NaOH/urea. This result can be observed from the higher *E* and UTS for ACC produced *via* BmimAc than NaOH/urea, which was correlated with the higher V_f for ACC produced *via* BmimAc than NaOH/urea. Shorter t_d was required for ACC produced *via* NaOH/urea than BmimAc. This result may be due to a lower viscosity for the ACC produced *via* NaOH/urea than BmimAc, contributing to a higher dissolution

rate for ACC produced *via* NaOH/urea than BmimAc. Higher P_{HP} was observed for the ACC produced *via* NaOH/urea than BmimAc. This result was consistent with the higher V_m in ACC produced *via* NaOH/urea, thus requiring higher pressure to impart a homogeneous fibre-matrix distribution.

- Overall, the decreasing E and UTS was observed with the increase of t_d for the ACC produced *via* NaOH/urea. However, the increasing E and UTS was observed at t_d of 60 min compared to t_d of 30 min for ACC produced *via* BmimAc. This result was consistent with the increasing V_f and decreasing V_v at t_d of 60 min. Furthermore, the highest density was also reported at t_d of 60 min, resulting in the increase of E and UTS. For ACC produced *via* NaOH/urea, the decreasing density with the increasing t_d was observed which corresponded with the increasing V_v.

b) Water absorption behaviours

- The water absorption in ACCs followed the Fickian behaviour because the water equilibrium state was reached, resulting in n equal to 0.5.

- The increasing D with the increasing temperature was observed for ACCs produced *via* BmimAc and NaOH/urea. The lowest D was reported at t_d of 15 and 60 min for ACCs produced *via* NaOH/urea and BmimAc, respectively. This result was due to the highest density and lowest V_v found at t_d of 15 and 60 min, inhibiting water penetration and resulting in the highest E and UTS.

- The lowest E_a of 0.48 kJ/mol was observed at t_d of 60 min for the ACC produced *via* BmimAc. However, for ACC produced *via* NaOH/urea, a comparable E_a of 1.09 and 0.93 kJ/mol was observed at t_d of 15 and 30 min, respectively. The higher E_a was observed for ACC produced *via* NaOH/urea, consistent to the higher D in ACC produced *via* NaOH/urea compared to BmimAc. The higher V_v in ACC produced *via*

NaOH/urea than BmimAc was observed, resulting in the increase of stress concentration. The increasing V_v imparted high barrier for the water diffusion, leading to a higher E_a for the ACC produced *via* NaOH/urea than BmimAc.

- The saturation time at 23, 50, and 100 °C for ACC produced *via* BmimAc from experimental work was consistent to the saturation time observed according to the ANSYS simulation. However, the saturation time at 23, 50, and 100 °C for the ACC produced *via* NaOH/urea from the experimental work was comparable to the ANSYS simulation; despite the shorter saturation time observed at 100 °C. The decreasing M_t/M_m was observed as water diffused from the edge to the centre of the ACC, maintaining at a constant M_t/M_m in the range of 1.25 to 23.75 mm. Thus, various water concentration profiles were observed with the increasing immersion times and increasing temperatures.

- To conclude, the increasing D in ACCs was observed with the increasing t_d, which caused from the variability in the molecular structures of ACCs (crystallinity, OH group, cryastallite size). The increasing D also was associated with the increasing temperature, resulting from the increasing water molecules mobility. A higher D was observed for the ACC produced *via* NaOH/urea than BmimAc, attributed from its higher V_v than the ACC produced *via* BmimAc.

c) Hygrothermal effects on mechanical properties

- In the present study, the water threshold of E, UTS and ε_f for ACC produced *via* BmimAc were 40.0, 45.0, and 45.0%, respectively. The water threshold of E, UTS and ε_f for ACC produced *via* NaOH/urea were 60.0, 60.0, and 55.0%, respectively. A higher water threshold was observed for ACC produced *via* NaOH/urea than BmimAc. This result may be due to the higher K_{sr} and V_v observed for ACC produced *via* NaOH/urea than BmimAc. The decreasing E and UTS below the water threshold was associated

with the presence of bound water. However, *E* and UTS approached almost a constant value beyond the water threshold, indicating the presence of free water.

- The decreasing T_g was observed with the increasing water content. This finding was expected due to the plasticisation effect of water, leading to an increase of cellulose free volume and chain motion. The increasing chain mobility reduced the relaxation time and the hydrogen bonding density, softening the amorphous phase of ACC, leading to the decreasing of T_g.
- *E* and UTS values decreased with the increasing water content. This result was due to the elongation of the C-O-C bond. Under the wet-saturated condition, the less-stiff components in the cellulose structures were softened and unable to carry much load. The softened cellulose structure led to less stress transfer from the matrix to the reinforcement component in ACC, resulting in the decreasing *E* during a wet-saturated condition.
- The partially dissolved cellulose interrupted the intra- or intermolecular hydrogen upon dissolving cellulose in the solvent. The hydrogen bonding was expected to increase during the regeneration process using distilled water. The surface of the cellulose experienced a higher degree of ordering and formed a hydrogen bonding network in the presence of water, resulting in an increase in the mechanical properties of cellulose upon drying. The amorphous region was also observed after dissolving in the solvent. The effect of water on the ACCs was found to be significant to their mechanical properties due to the decrease of *E* and UTS. The presence of water weakened the hydrogen bonding in the ACCs. The increasing wavenumber (3000 – 3500 cm^{-1}) was anticipated due to the weakening of the hydrogen bonding. The broader peak (3000 – 3500 cm^{-1}) was believed to be caused by the association of the cellulose chain through

the hydrogen bonds. The increase of water content was indicated by a narrower and sharper peak, showing the splitting of the hydrogen bonds.

d) Hygrothermal effects on creep behaviour

- The increasing creep strain was observed with the increasing water content and temperature. This result was due to the increasing water activity at an extreme environmental condition.
- Lower creep strain was observed at lower water content and temperature. This result was due to the less slippage of molecular chain that was consistent with the increase of viscosity and the decrease of permanent strain at lower water content and temperature.
- The increasing relaxation time was found with the increase of water content. This was due to the decrease of free volume, reducing its additional space for movement. Apart from that, the increasing CrI required longer relaxation time, leading to a higher density and stiffness. However, with the increasing water content, the increasing relaxation time had not promised to impart a higher stiffness. The decreasing hydrogen bonding density with the increasing water content was reported because of the interruption of hydrogen bonding. In addition, more slippage effect was found at higher water content. The presence of less hydrogen bonding density at higher water content would prevent the ACCs from rupturing, despite having excessive slipping of molecular chain.
- Longer relaxation time was observed for the ACC produced *via* BmimAc than NaOH/urea. The relationship between relaxation time and V_v was inversely proportional. A higher V_v allowed more free water to reside within the gap. The effect of free water had significantly increased the creep strain at higher water content. This result may be due to the increase of water mobility at high water content due to the presence of free water. More free water was observed for ACC produced *via*

NaOH/urea than BmimAc. The higher relaxation time observed for ACC produced *via* BmimAc was consistent with its higher density and CrI.

- The experimental shift factor was successfully fitted using the WLF compared to the Arrhenius model. The physical aging effect was observed at a temperature of 30 °C and was eliminated at temperatures of 150 and 200 °C. The physical aging effect was observed at lower temperature due to its lower strain than the expected strain (master curve). This effect was neglected at higher temperature due to its higher strain than the expected strain, although it was not superimposed to the master curve.

8.2 Future works

The understandings of the hygrothermal effects on the ACCs had been performed in this present study. However, some improvements are suggested the future study. The following recommendations are outlined:

- Other types of ILs may be useful to use in the ACCs production in the future. It is recommended to use a cheaper, easy to handle, high recyclability, high dissolubility, and environmentally friendly ILs solvent. The NaOH/urea solvent system can be added with thiourea in order to increase its effectiveness and dissolution capacity for ACCs production in future. Apart from that, the optimisation of (i) regeneration and washing, and (ii) drying process may be needed, to observe the effects of these control factors on the ACCs properties.
- The results discussed in the present study were limited to only one type of cellulose II. Therefore, other types of cellulose polymorphs (cellulose I, III, or IV) should be considered as a comparison with the present study.
- ACCs are known to absorb more water due to its hydrophilicity characteristic. Therefore, an environmentally friendly coating system is required to prevent the moisture uptake into the ACCs due to its extensive usage in extreme environmental

conditions. The mechanical properties, water uptake, and creep behaviour would be required in order to observe any significant changes upon applying the coating system. The effects of thermoforming and recyclability should be performed in future studies.

- Nonlinear modelling (artificial neural network and fuzzy logic) may be required to predict the theoretical mechanical outputs and experimental data due to its ability to fit the experimental data with a high degree of accuracy.
- The potential application of ACCs should be focussed through a collaboration work of the present study with interested industries, providing a development of ACCs from the lab-scaled to the up-scaled ACCs manufacturing.
- The effects of water uptake on the paracrystalline region should be addressed on ACCs. The relationship between paracrystalline regions on the mechanical properties would be performed on ACCs.
- Further analyses of the water content effects on the long-term creep behaviour should be done thoroughly in order to observe any possible physical aging effects at various water contents.

8.3 List of publications

Refereed International Journals

- Paper title: “Parametric optimisation of the processing of all-cellulose composite laminae”, Advanced Manufacturing: Polymer & Composite Science Journal - (Accepted on 9 April 2017).
- Paper title: “The influence of moisture on the mechanostability of all-cellulose composite laminae”, Polymer and Degradation Stability Journal - (Under review process).

International Conference Presentations

- International Conference on Frontiers of Polymers and Advanced Materials 2013, 8-13 December 2013, University of Auckland, New Zealand, Poster presentation: “The study of water transport behaviour in all-cellulose composites (ACCs)”.
- Composite Australia 2015 Conference, 21-23 April, 2015, Gold Coast, Australia, Oral presentation: “Optimisation of Critical Processing Parameters in the Preparation of All-Cellulose Composites”.

International Conference/Proceeding Paper

- Paper title: “Optimisation of Critical Processing Parameters in the Preparation of All-Cellulose Composites”, Composite Australia 2015 Conference, 21-23 April, 2015, Gold Coast, Australia.

References

1. Mohanty, A., M. Misra, and L. Drzal, *Sustainable bio-composites from renewable resources: opportunities and challenges in the green materials world.* Journal of Polymers and the Environment, 2002. **10**(1-2): p. 19-26.
2. John, M.J. and S. Thomas, *Biofibres and biocomposites.* Carbohydrate polymers, 2008. **71**(3): p. 343-364.
3. Gray, D., *Polypropylene transcrystallization at the surface of cellulose fibers.* Journal of Polymer Science: Polymer Letters Edition, 1974. **12**(9): p. 509-515.
4. Huber, T., Mussig, J., Curnow, O., Pang, S., Bickerton, S., and Staiger, M.P., *A critical review of all-cellulose composites.* Journal of Material Science, 2012. **47**: p. 1171-1186.
5. Dufresne, A., *Monomers, Polymers and Composites from Renewable Resources: Chapter 19: Cellulose-based composites and nanocomposites*. 2008, United Kingdom: Elsevier.
6. Pothan, L.A., Z. Oommen, and S. Thomas, *Dynamic mechanical analysis of banana fiber reinforced polyester composites.* Composites Science and Technology, 2003. **63**(2): p. 283-293.
7. Saha, A.K., Das, S., Bhatta, D., and Mitra, B.C., *Study of jute fiber reinforced polyester composites by dynamic mechanical analysis.* Journal of Applied Polymer Science, 1998. **71**: p. 1505-1513.
8. Ouajai, S. and R.A. Shanks, *Preparation, structure and mechanical properties of all-hemp cellulose biocomposites.* Composites Science and Technology, 2009. **69**(13): p. 2119-2126.
9. Adhikary, K.B., S. Pang, and M.P. Staiger, *Dimensional stability and mechanical behaviour of wood-plastic composites based on recycled and virgin high-density polyethylene (HDPE).* Composites Part B: Engineering, 2007. **39**: p. 807-815.
10. Le Duigou, A., P. Davies, and C. Baley, *Seawater ageing of flax/poly(lactic acid) biocomposites.* Polymer degradation and stability, 2009. **94**(7): p. 1151-1162.
11. Araujo, J.R., W.R. Waldman, and M.A.D. Paoli, *Thermal properties of high density polyethylene composites with natural fibres: Coupling agent effect.* Polymer degradation and stability, 2008. **93**: p. 1770-1775.
12. Facca, A.G., M.T. Kortschot, and N. Yan, *Predicting the tensile strength of natural fibre reinforced thermoplastics.* Composites Science and Technology, 2007. **67**: p. 2454-2466.
13. Kumar, A.P., R.P. Singh, and B.D. Sarwade, *Degradability of composites, prepared from ethylene–propylene copolymer and jute fiber under accelerated aging and biotic environments.* Materials Chemistry and Physics, 2005. **92**(2): p. 458-469.
14. Meredith, J., Coles, S.R., Powe, R., Collings, E., Cozien-Cazuc, S., Weager, B., Mussig, J., and Kirwan, K., *On the static and dynamic properties of flax and Cordenka epoxy composites.* Composites Science and Technology, 2013. **80**: p. 31-38.
15. Cristaldi, G., Latteri, A., Recca, G., and Cicala, G., *Composites based on natural fibre fabrics.* Woven Fabric Engineering, 2010: p. 317-342.
16. Soykeabkaew, N., Arimoto, N., Nishino, T., and Peijs, T., *All-cellulose composites by surface selective dissolution of aligned ligno-cellulosic fibres.* Composites Science and Technology, 2008. **68**(10): p. 2201-2207.
17. Huber, T., Bickerton, S., Mussig, J., Pang, S., and Staiger, M.P., *Solvent infusion processing of all-cellulose composite materials.* Carbohydrate polymers, 2012. **90**: p. 730-733.
18. Gindl, W. and J. Keckes, *All-cellulose nanocomposites.* Polymer, 2005. **46**: p. 10221-10225.
19. Nishino, T., I. Matsuda, and K. Hirao, *All-cellulose composite.* Macromolecules, 2004. **37**: p. 7683-7687.
20. Yousefi, H., Nishino, T., Shakeri, A., Faezipour, M., Ebrahimi, G., and Kotera, M., *Water-repellent all-cellulose nanocomposites using silane coupling treatment.* Journal of Adhesion Science and Technology, 2012: p. 1-11.
21. Nishino, T. and N. Arimoto, *All-cellulose composite prepared by selective dissolving of fiber surface.* Biomacromolecules, 2007. **8**: p. 2712-2716.

22. Duchemin, B.J.C., A.P. Mathew, and K. Oksman, *All-cellulose composites by partial dissolution in the ionic liquid 1-butyl-3-methylimidazolium chloride* Composites: Part A, 2009. **40**: p. 2031-2037.
23. Duchemin, B.J.C., R.H. Newman, and M.P. Staiger, *Structure-property relationship of all-cellulose composites.* Journal of Composites Science and Technology, 2009. **69**: p. 1225-1230.
24. Huber, T., S. Pang, and M.P. Staiger, *All-cellulose composites laminates.* Composites: Part A, 2012. **43**(10): p. 1738-1745.
25. Gindl-Altmutter, W., Keckes, J., Plackner, J., Liebner, F., Englund, K., and Laborie, M.P., *All-cellulose composites prepared from flax and lyocell fibres compared to epoxy–matrix composites.* Composites Science and Technology, 2012. **72**(11): p. 1304-1309.
26. Belgacem, M.N. and A. Gandini, *Monomers, Polymers and Composites from Renewable Resources: Chapter 18: Surface modification of cellulose fibres*. 2008, United Kingdom: Elsevier.
27. Heijenrath, R. and T. Peijs, *Natural-fibre-mat-reinforced thermoplastic composites based on flax fibres and polypropylene.* Advanced composites letters, 1996. **5**: p. 81-86.
28. Peijs, T., Garkhail, S., Heijenrath, R., Van Den Oever, M., and Bos, H., *Thermoplastic composites based on flax fibres and polypropylene: influence of fibre length and fibre volume fraction on mechanical properties*. in *Macromolecular Symposia*. 1998. Wiley Online Library.
29. Luo, S. and A. Netravali, *Interfacial and mechanical properties of environment-friendly "green" composites made from pineapple fibers and poly (hydroxybutyrate-co-valerate) resin.* Journal of Materials Science, 1999. **34**(15): p. 3709-3719.
30. Garkhail, S., R. Heijenrath, and T. Peijs, *Mechanical properties of natural-fibre-mat-reinforced thermoplastics based on flax fibres and polypropylene.* Applied Composite Materials, 2000. **7**(5-6): p. 351-372.
31. Mohanty, A., M.A. Khan, and G. Hinrichsen, *Surface modification of jute and its influence on performance of biodegradable jute-fabric/Biopol composites.* Composites Science and Technology, 2000. **60**(7): p. 1115-1124.
32. Peijs, T., *Natural fiber based composites.* Materials Technology(UK)(UK), 2000. **15**(4): p. 281-285.
33. Stamboulis, A., Baillie, C.A., Garkhail, S.K., Van Melick, H.G.H., and Peijs, T., *Environmental durability of flax fibres and their composites based on polypropylene matrix.* Applied Composite Materials, 2000. **7**(5-6): p. 273-294.
34. Peijs, T., *Composites turn green.* Department of Materials, Queen Mary, University of London, 2002.
35. Mohanty, A., Wibowo, A., Misra, M., and Drzal, L.T., *Development of renewable resource–based cellulose acetate bioplastic: Effect of process engineering on the performance of cellulosic plastics.* Polymer Engineering & Science, 2003. **43**(5): p. 1151-1161.
36. Singleton, A., Baillie, C., Beaumont, P., and Peijs, T., *On the mechanical properties, deformation and fracture of a natural fibre/recycled polymer composite.* Composites Part B: Engineering, 2003. **34**(6): p. 519-526.
37. Toriz, G., Arvidsson, R., Westin, M., and Gatenholm, P., *Novel cellulose ester–poly (furfuryl alcohol)–flax fiber biocomposites.* Journal of Applied polymer Science, 2003. **88**(2): p. 337-345.
38. Averous, L. and N. Boquillon, *Biocomposites based on plasticized starch: thermal and mechanical behaviours.* Carbohydrate polymers, 2004. **56**(2): p. 111-122.
39. Wibowo, A.C., Mohanty, A.K., Misra, M., and Drzal, L.T., *Chopped industrial hemp fiber reinforced cellulosic plastic biocomposites: thermomechanical and morphological properties.* Industrial & engineering chemistry research, 2004. **43**(16): p. 4883-4888.

40. Lu, Y., L. Weng, and X. Cao, *Morphological, thermal and mechanical properties of ramie crystallites-reinforced plasticized starch biocomposites.* Carbohydrate Polymers, 2006. **63**: p. 198-204.
41. Shanks, R., A. Hodzic, and D. Ridderhof, *Composites of poly (lactic acid) with flax fibers modified by interstitial polymerization.* Journal of Applied polymer Science, 2006. **99**(5): p. 2305-2313.
42. Abedin, M., Beg, M., Pickering, K.L., and Khan, M., *Study on the mechanical properties of jute/glass fiber-reinforced unsaturated polyester hybrid composites: effect of surface modification by ultraviolet radiation.* Journal of Reinforced Plastics and Composites, 2006. **25**(6): p. 575-588.
43. Akil, H.M., Cheng, L.W., Ishak, M., Bakar, A.B., and Rahman, M.A.A, *Water absortipn study on pultruded jute fibre reinforced unsaturated polyester composites.* Composites Science and Technology, 2009. **69**: p. 1942-1948.
44. Alam, M.K., M.A. Khan, and E.H. Lehmann, *Comparative study of water absorption behavior in biopol® and jute-reinforced biopol® composite using neutron radiography technique.* Journal of Reinforced Plastics and Composites, 2006. **25**(11): p. 1179-1187.
45. Dash, B.N., Rana, A.K., Mishra, H.K., Nayak, S.K., Mishra, S.C., and Tripathy, S.S., *Novel, low-cost jute-polyester composites. Part 1: Processing, mechanical properties, and SEM analysis.* Polymer Composites, 1999. **20**(1): p. 62-71.
46. Hu, R., M. Sun, and J. Lim, *Moisture absorption, tensile strength and microstructure evolution of short jute fiber/polylactide composite in hygrothermal environment.* Material and Design, 2010. **31**: p. 3167-3173.
47. Kafi, A., Abedin, M.Z., Beg, M.D.H., Pickering, K.L., and Khan, M.A., *Study on the mechanical properties of jute/glass fiber-reinforced unsaturated polyester hybrid composites: Effect of surface modification by ultraviolet radiation.* Journal of Reinforced Plastics and Composites, 2006. **25**: p. 575-587.
48. Mohanty, S., S.K. Verma, and S.K. Nayak, *Dynamic mechanical and thermal properties of MAPE treated jute/HDPE composites.* Composites Science and Technology, 2006. **66**(3–4): p. 538-547.
49. Munikenche Gowda, T., A.C.B. Naidu, and R. Chhaya, *Some mechanical properties of untreated jute fabric-reinforced polyester composites.* Composites Part A: Applied Science and Manufacturing, 1999. **30**(3): p. 277-284.
50. Abdullah, H.H., Asa'ari, A.Z.M., Zawawi, N.I.M., Abdullah, L.C., and Zakaria, S., *Effects of physical treatments on the hydrophobicity of kenaf whole stem paper surface using stearic acid.* Bioresources, 2013. **8**(3): p. 4088-4100.
51. Alvarez, V.A., A.N. Fraga, and A. Vazquez, *Effects of the moisture and fiber content on the mechanical properties of biodegradable polymer-sisal fiber biocomposites.* Journal of Applied Polymer Science, 2003. **91**(6): p. 4007-4016.
52. Kim, H.J. and D.W. Seo, *Effect of water absorption fatique on mechanical properties of sisal textile-reinforced composites.* International Journal of Fatigue, 2006. **28**: p. 1307-1314.
53. Soykeabkaew, N., T. Nishino, and T. Peijs, *All-cellulose composites of regenerated cellulose fibres by surface selective dissolution.* Composites Part A: Applied Science and Manufacturing, 2009. **40**(4): p. 321-328.
54. Ward, I. and P. Hine, *Novel composites by hot compaction of fibers.* Polymer Engineering & Science, 1997. **37**(11): p. 1809-1814.
55. Ward, I. and P. Hine, *The science and technology of hot compaction.* Polymer, 2004. **45**(5): p. 1413-1427.
56. Peijs, T., *Composites for recyclability.* Materials today, 2003. **6**(4): p. 30-35.
57. Cabrera, N., Alcock, B., Loos, J., and Peijs, T., *Processing of all-polypropylene composites for ultimate recyclability.* Proceedings of the Institution of Mechanical Engineers, Part L: Journal of Materials Design and Applications, 2004. **218**(2): p. 145-155.

58. Alcock, B., Cabrera, N.O., Barkoula, N.M., Loos, J., and Peijs, T., *The mechanical properties of unidirectional all-polypropylene composites.* Composites Part A: Applied Science and Manufacturing, 2006. **37**(5): p. 716-726.
59. Alcock, B., Cabrera, N.O., Barkoula, N.M., Spoelstra, A.B., Loos, J., and Peijs, T., *The mechanical properties of woven tape all-polypropylene composites.* Composites Part A: Applied Science and Manufacturing, 2007. **38**(1): p. 147-161.
60. Matabola, K., De Vries, A.R., Moolman, F.S., and Luyt, A.S., *Single polymer composites: a review.* Journal of Materials Science, 2009. **44**(23): p. 6213-6222.
61. Ho, M., Wang, H., Lee, J., Ho, C., Lau, K., Leng, J., and Hui, D., *Critical factors on manufacturing processes of natural fibre composites.* Composites: Part B, 2011.
62. Woodings, C., *Regenerated cellulose fibres*. Vol. 18. 2001: Woodhead Publishing.
63. Ganster, J. and H.-P. Fink, *Novel cellulose fibre reinforced thermoplastic materials.* Cellulose, 2006. **13**(3): p. 271-280.
64. Bax, B. and J. Müssig, *Impact and tensile properties of PLA/Cordenka and PLA/flax composites.* Composites Science and Technology, 2008. **68**(7): p. 1601-1607.
65. Klemm, D., Heublein, B., Fink, H.P., and Bohn, A., *Cellulose: Fascinating biopolymer and sustainable raw material.* Angew Chem-Int, 2005. **44**(22): p. 3358-3393.
66. Perepelkin, K. *Polysaccharides as renewable plant polymers for fibers: their today position and future forecast*. in *4th International Symposium Materials from Renewable Resources*. 2003.
67. O'SULLIVAN, A.C., *Cellulose: the structure slowly unravels.* Cellulose, 1997. **4**(3): p. 173-207.
68. Duchemin, B.J.C., *Structure, property and processing relationship of all-cellulose compossites*, in *Mechnical Engineering*. 2008, University of Canterbury: Christchurch. p. 240.
69. Pullawan, T., *Interfacial micromechanics of all-cellulose nanocomposites using Raman spectroscopy*, in *Faculty of Engineering and Physical Science*. 2012, University of Manchester: United Kingdom.
70. Staudinger, H., *Über polymerisation.* Berichte der deutschen chemischen Gesellschaft (A and B Series), 1920. **53**(6): p. 1073-1085.
71. Atalla, R.H. and D.L. Vanderhart, *Native cellulose: a composite of two distinct crystalline forms.* Science, 1984. **223**(4633): p. 283-285.
72. Heiner, A.P., J. Sugiyama, and O. Teleman, *Crystalline cellulose Iα and Iß studied by molecular dynamics simulation.* Carbohydrate Research, 1995. **273**(2): p. 207-223.
73. Sugiyama, J., Okano, T., Yamamoto, H., and Horii, F., *Transformation of Valonia cellulose crystals by an alkaline hydrothermal treatment.* Macromolecules, 1990. **23**(12): p. 3196-3198.
74. Nishiyama, Y., P. Langan, and H. Chanzy, *Crystal structure and hydrogen-bonding system in cellulose Iß from synchrotron X-ray and neutron fiber diffraction.* Journal of the American Chemical Society, 2002. **124**(31): p. 9074-9082.
75. Nishiyama, Y., Sugiyama, J., Chanzy, H., and Langan, P., *Crystal structure and hydrogen bonding system in cellulose Iα from synchrotron X-ray and neutron fiber diffraction.* Journal of the American Chemical Society, 2003. **125**(47): p. 14300-14306.
76. Šturcová, A., His, I., Apperley, D.C., Sugiyama, J., and Jarvis, M.C., *Structural details of crystalline cellulose from higher plants.* BIOMACROMOLECULES, 2004. **5**(4): p. 1333-1339.
77. Rånby, B.G., *Fibrous macromolecular systems. Cellulose and muscle. The colloidal properties of cellulose micelles.* Discussions of the Faraday Society, 1951. **11**: p. 158-164.
78. French, A.D. and G.P. Johnson, *Cellulose shapes. Cellulose: Molecular and Structural Biology*. 2007.
79. Zugenmaier, P., *Conformation and packing of various crystalline cellulose fibers.* Progress in polymer science, 2001. **26**(9): p. 1341-1417.
80. Huber, T., *Processing of all cellulose composites via an ionic liquid route*, in *Mechanical Engineering*. 2013, University of Canterbury: Christchurch. p. 343.

81. Ciolacu, D., F. Ciolacu, and V.I. Popa, *Amorphous cellulose—structure and characterization.* Cellulose Chemistry and Technology, 2011. **45**(1): p. 13.
82. Ciolacu, D., L. Pitol-Filho, and F. Ciolacu, *Studies concerning the accessibility of different allomorphic forms of cellulose.* Cellulose, 2012. **19**(1): p. 55-68.
83. Richardson, S. and L. Gorton, *Characterisation of the substituent distribution in starch and cellulose derivatives.* Analytica Chimica Acta, 2003. **497**(1): p. 27-65.
84. Hammami, A. and B.R. Gebart, *Analysis of the vacuum infusion molding process.* Polymer Composites, 2000. **21**(1): p. 28-40.
85. Forsyth, S.A., J.M. Pringle, and D.R. MacFarlane, *Ionic liquids—an overview.* Australian Journal of Chemistry, 2004. **57**(2): p. 113-119.
86. Graenacher, C., *Cellulose solution*. 1934, Google Patents.
87. Swatloski, R.P., Spear, S.K., Holbrey, J.D., and Rogers, R.D., *Dissolution of cellose with ionic liquids.* Journal American Chemical Society, 2002. **124**: p. 4974-4975.
88. Zhang, H., Wu, J., Zhang, J., and He, J., *1-Allyl-3-methylimidazolium chloride room temperature ionic liquid: a new and powerful nonderivatizing solvent for cellulose.* Macromolecules, 2005. **38**(20): p. 8272-8277.
89. Liu, Z., Sun, X., Hao, M., Huang, C., Xue, Z., and Mu, T., *Preparation and characterization of regenerated cellulose from ionic liquid using different methods.* Carbohydrate polymers, 2015. **117**: p. 99-105.
90. Shibata, M., Teramoto, N., Nakamura, T., and Saitoh, Y., *All-cellulose and all-wood composites by partial dissolution of cotton fabric and wood in ionic liquid.* Carbohydrate polymers, 2013. **98**(2): p. 1532-1539.
91. Parviainen, H., Parviainen, A., Virtanen, T., Kilpelainen, I., Ahvenainen, P., Serimaa, R., Gronqvist, S., Maloney, T, and Maunu, S.L., *Dissolution enthalpies of cellulose in ionic liquids.* Carbohydrate polymers, 2014. **113**: p. 67-76.
92. Bochek, A., Murav'ev, A., Novoselov, N., Zaborski, M., Zabivalova, N., Pertova, V., Vlasova, E., Volcheck, B., and Lavrent'ev, V., *Specific features of cellulose and chitin dissolution in ionic liquids of varied structure and the structural organization of regenerated polysaccharides.* Russian Journal of Applied Chemistry, 2012. **85**(11): p. 1718-1725.
93. Singh, S., B.A. Simmons, and K.P. Vogel, *Visualization of biomass solubilization and cellulose regeneration during ionic liquid pretreatment of switchgrass.* Biotechnology and Bioengineering, 2009. **104**(1): p. 68-75.
94. Remsing, R.C., Swatloski, R.P., Rogers, R.D., and Moyna, G., *Mechanism of cellulose dissolution in the ionic liquid 1-n-butyl-3-methylimidazolium chloride: a 13 C and 35/37 Cl NMR relaxation study on model systems.* Chemical communications, 2006(12): p. 1271-1273.
95. Zhao, Q., Yam, R.C.M., Zhang, B., Yang, Y., Cheng, X., and Li, R.K.Y., *Novel all-cellulose ecocomposites prepared in ionic liquids.* Cellulose, 2009. **16**(2): p. 217-226.
96. Dawsey, T. and C.L. McCormick, *The lithium chloride/dimethylacetamide solvent for cellulose: a literature review.* Journal of Macromolecular Science—Reviews in Macromolecular Chemistry and Physics, 1990. **30**(3-4): p. 405-440.
97. Cao, Y., Wu, J., Zhang, J., Li, H., Zhang, Y., and He, J., *Room temperature ionic liquids (RTILs): a new and versatile platform for cellulose processing and derivatization.* Chemical Engineering Journal, 2009. **147**(1): p. 13-21.
98. Mohsenzadeh, A., Jeihanipour, A., Karimi, K., and Taherzadeh, M.J., *Alkali pretreatment of softwood spruce and hardwood birch by NaOH/thiourea, NaOH/urea, NaOH/urea/thiourea, and NaOH/PEG to improve ethanol and biogas production.* J Chem Technol Biotechnol, 2011. **87**: p. 1209-1214.
99. Zhang, S., Li, F., Yu, J., and Hsiah, Y., *Dissolution behaviour and solubility of cellulose in NaOH complex solution.* Carbohydrate Polymers 2010. **81**: p. 668-674.

100. Li, M.-F., Sun, S.N., Xu, F., and Sun, R.C., *Cold NaOH/urea aqueous dissolved cellulose for benzylation: Synthesis and characterization.* European Polymer journal, 2011. **47**(9): p. 1817-1826.
101. Zhou, J. and L. Zhang, *Solubility of cellulose in NaOH/urea aqueous solution.* Polymer journal, 2000. **32**(10): p. 866-870.
102. Yang, G., X. Xiong, and L. Zhang, *Microporous formation of blend membranes from cellulose/konjac glucomannan in NaOH/thiourea aqueous solution.* Journal of Membrane Science, 2002. **201**: p. 161-173.
103. Zhang, P., L. Zhang, and S. Cheng, *Effects of urea and sodium hydroxide on the molecular weight and conformation of α-(1→ 3)-d-glucan from< i> Lentinus</i>< i> edodes</i> in aqueous solution.* Carbohydrate Research, 2000. **327**(4): p. 431-438.
104. Pinkert, A., Marsh, K.N., Pang, S., and Staiger, M.P., *Ionic liquids and their interaction with cellulose.* Chem. Rev., 2009. **109**: p. 6712-6728.
105. Gericke, M., Schlufter, K., Liebert, T., Heinze, T., and Budtova, T., *Rheological properties of cellulose/ionic liquid solutions: from dilute to concentrated states.* BIOMACROMOLECULES, 2009. **10**(5): p. 1188-1194.
106. Vitz, J., Erdmenger, T., Haensch, C., and Schubert, U.S., *Extended dissolution studies of cellulose in imidazolium based ionic liquids.* The Royal Society of Chemistry, 2009. **11**: p. 417-424.
107. Cai, J. and L. Zhang, *Rapid dissolution of cellulose in LiOH/urea and NaOH/urea aqueous solutions.* Macromolecular Bioscience, 2005. **5**(6): p. 539-548.
108. Qi, H., C. Chang, and L. Zhang, *Effects of temperature and molecular weight on dissolution of cellulose in NaOH/urea aqueous solution.* Cellulose, 2008. **15**(6): p. 779-787.
109. Dormanns, J.W., Schuermann, J., Mussig, J., Duchemin, B.J.C, and Staiger, M.P., *Solvent infusion processing of all-cellulose composite laminates using an aqueous NaOH/urea solvent system.* Composites Part A: Applied Science and Manufacturing, 2016. **82**: p. 130-140.
110. Gindl, W., T. Schöberl, and J. Keckes, *Structure and properties of a pulp fibre-reinforced composite with regenerated cellulose matrix.* Applied Physics A, 2006. **83**(1): p. 19-22.
111. Govindan, V., Hussiensyah, S., Leng, T.P., and Amri, F., *Preparation and characterization of regenerated cellulose using ionic liquid.* Advances in Environmental Biology, 2014. **8**(8): p. 2620-2625.
112. Qin, C., Soykeabkaew, N., Xiuyuan, N., and Peijs, T., *The effect of fibre volume fraction and mercerization on the properties of all-cellulose composites.* Carbohydrate polymers, 2008. **71**(3): p. 458-467.
113. Qi, H., Cai, J., Zhang, L., and Kuga, S., *Properties of films composed of cellulose nanowhiskers and a cellulose matrix regenerated from alkali/urea solution.* BIOMACROMOLECULES, 2009. **10**(6): p. 1597-1602.
114. Yang, Q., A. Lue, and L. Zhang, *Reinforcement of ramie fibers on regenerated cellulose films.* Composites Science and Technology, 2010. **70**(16): p. 2319-2324.
115. Liu, L., Yu, J., Cheng, L., and Qu, W., *Mechanical properties of poly (butylene succinate)(PBS) biocomposites reinforced with surface modified jute fibre.* Composites Part A: Applied Science and Manufacturing, 2009. **40**(5): p. 669-674.
116. Espert, A., F. Vilaplana, and S. Karlsson, *Comparison of water absorption in natural cellulosic fibres from wood and one-year crops in polypropylene composites and its influence on their mechanical properties.* Composites Part A: Applied Science and Manufacturing, 2004. **35**: p. 1267-1276.
117. Lee, S.M., Cho, D., Park, W.H., Lee, S.G., Han, S.O., and Drzal, L.T., *Novel silk/poly (butylene succinate) biocomposites: the effect of short fibre content on their mechanical and thermal properties.* Composites Science and Technology, 2005. **65**(3): p. 647-657.
118. Karnani, R., M. Krishnan, and R. Narayan, *Biofiber-reinforced polypropylene composites.* Polymer Engineering & Science, 1997. **37**(2): p. 476-483.

119. Nishino, T., Hirao, K., Kotera, M., Nakamae, K., and Inagaki, H., *Kenaf reinforced biodegradable composite.* Composites Science and Technology, 2003. **63**(9): p. 1281-1286.
120. Vilay, V., Mariatti, M. Mat Taib, R., and Todo, M., *Effect of fiber surface treatment and fiber loading on the properties of bagasse fiber–reinforced unsaturated polyester composites.* Composites Science and Technology, 2008. **68**(3): p. 631-638.
121. Oksman, K., M. Skrifvars, and J.-F. Selin, *Natural fibres as reinforcement in polylactic acid (PLA) composites.* Composites Science and Technology, 2003. **63**(9): p. 1317-1324.
122. Sapuan, S.M., Leenie, A., Harimi, M., and Beng, Y.K., *Mechanical properties of woven banana fibre reinforced epoxy composites.* Materials & design, 2006. **27**(8): p. 689-693.
123. Hill, C. and H. Abdul Khalil, *Effect of fiber treatments on mechanical properties of coir or oil palm fiber reinforced polyester composites.* Journal of Applied polymer Science, 2000. **78**(9): p. 1685-1697.
124. Zheng, Y.-T., Cao, D.R., Wang, D.S., and Chen, J.J., *Study on the interface modification of bagasse fibre and the mechanical properties of its composite with PVC.* Composites Part A: Applied Science and Manufacturing, 2007. **38**(1): p. 20-25.
125. Herman, P., *Physics and Chemistry of Cellulose Fibers*. 1949, Elsevier: New York.
126. Yano, S., H. Hatakeyama, and T. Hatakeyama, *Effect of hydrogen bond formation on dynamic mechanical properties of amorphous cellulose.* Journal of Applied polymer Science, 1976. **20**(12): p. 3221-3231.
127. Kondo, T., E. Togawa, and R.M. Brown, *"Nematic ordered cellulose": a concept of glucan chain association.* Biomacromolecules, 2001. **2**(4): p. 1324-1330.
128. Kondo, T. and C. Sawatari, *A Fourier transform infra-red spectroscopic analysis of the character of hydrogen bonds in amorphous cellulose.* Polymer, 1996. **37**(3): p. 393-399.
129. Nelson, M.L. and R.T. O'Connor, *Relation of certain infrared bands to cellulose crystallinity and crystal lattice type. Part II. A new infrared ratio for estimation of crystallinity in celluloses I and II.* Journal of Applied polymer Science, 1964. **8**(3): p. 1325-1341.
130. Montes, H., K. Mazeau, and J. Cavaillé, *Secondary mechanical relaxations in amorphous cellulose.* Macromolecules, 1997. **30**(22): p. 6977-6984.
131. Nissan, A. and S. Sternstein, *Cellulose as a viscoelastic material.* Pure and Applied Chemistry, 1962. **5**(1-2): p. 131-146.
132. Jafarpour, G., Dantras, E., Boudet, A., and Lacabanne, C., *Study of dielectric relaxations in cellulose by combined DDS and TSC.* Journal of non-crystalline solids, 2007. **353**(44): p. 4108-4115.
133. Manabe, S.-I., M. Iwata, and K. Kamide, *Dynamic mechanical absorptions observed for regenerated cellulose solids in the temperature range from 280 to 600 K.* Polymer journal, 1986. **18**(1): p. 1-14.
134. Haughton, P. and D. Sellen, *Stress relaxation in regenerated cellulose.* Journal of Physics D: Applied Physics, 1973. **6**(17): p. 1998.
135. Ishak, Z.M., A. Ariffin, and R. Senawi, *Effects of hygrothermal aging and a silane coupling agent on the tensile properties of injection molded short glass fiber reinforced poly (butylene terephthalate) composites.* European Polymer journal, 2001. **37**(8): p. 1635-1647.
136. Beg, M. and K. Pickering, *Mechanical performance of Kraft fibre reinforced polypropylene composites: Influence of fibre length, fibre beating and hygrothermal ageing.* Composites Part A: Applied Science and Manufacturing, 2008. **39**(11): p. 1748-1755.
137. Gauthier, R., Joly, C., Coupas, A.C., Gauthier, H., and Escoubes, M., *Interfaces in polyolefin/cellulosic fiber composites: chemical coupling, morphology, correlation with adhesion and aging in moisture.* Polymer Composites, 1998. **19**(3): p. 287-300.
138. Srubar III, W. and S. Billington, *A micromechanical model for moisture-induced deterioration in fully biorenewable wood–plastic composites.* Composites Part A: Applied Science and Manufacturing, 2013. **50**: p. 81-92.

139. Adhikary, K.B., S. Pang, and M.P. Staiger, *Effects of the accelerated freeze-thaw cycling on physical and mechanical properties of wood flour-recycled thermoplastic composites.* Polymer Composites, 2010. **31**(2): p. 185-194.
140. Dhakal, H.N., Z.Y. Zhang, and M.O.W. Richardson, *Effect of water absorption on the mechanical properties of hemp fibre reinforced unsaturated polyester composites.* Composites Science and Technology, 2007. **67**(7–8): p. 1674-1683.
141. Long, F. and D. Richman, *Concentration gradients for diffusion of vapors in glassy polymers and their relation to time dependent diffusion phenomena1, 2.* Journal of the American Chemical Society, 1960. **82**(3): p. 513-519.
142. Crank, J., *The mathematics of diffusion*. 1979: Oxford university press.
143. Hatakeyama, H. and T. Hatakeyama, *Structural change of amorphous cellulose by water-and heat-treatment.* Die Makromolekulare Chemie, 1981. **182**(6): p. 1655-1668.
144. Nakamura, K., T. Hatakeyama, and H. Hatakeyama, *Studies on bound water of cellulose by differential scanning calorimetry.* Textile research journal, 1981. **51**(9): p. 607-613.
145. Adhikary, K.B., S. Pang, and M.P. Staiger, *Long-term moisture absorption and thickness swelling behaviour recycled thermoplastics reinforced with Pinus radiata sawdust.* Chemical Engineering Journal, 2007. **142**: p. 190-198.
146. Wang, W., M. Sain, and P.A. Cooper, *Study of moisture absorption in natural fiber plastic composites.* Composites Science and Technology, 2006. **66**(3–4): p. 379-386.
147. LeCorre, D., J. Bras, and A. Dufresne, *Influence of the botanic origin of starch nanocrystals on the morphological and mechanical properties of natural rubber nanocomposites.* Macromolecular Journals, 2012. **297**: p. 969-978.
148. Zhou, S., Tashiro, K., Hongo, T., Shirataki, H., Yamane, C., and Ii, T., *Influence of water on structure and mechanical properties of regenerated cellulose studied by an organized combination of infrared spectra, X-ray diffraction, and dynamic viscoelastic data measured as functions of temperature and humidity.* Macromolecules, 2001. **34**(5): p. 1274-1280.
149. Rahman, N.M.M.A., A. Hassan, and R. Yahya, *Plasticisation effect on thermal, dynamic mechanical and tensile properties of injection-moulded glass-fibre/polyamide 6,6.* Journal of Science and Technology, 2011. **3**(1): p. 1.
150. Thomason, J., *The influence of fibre length, diameter and concentration on the impact performance of long glass-fibre reinforced polyamide 6, 6.* Composites Part A: Applied Science and Manufacturing, 2009. **40**(2): p. 114-124.
151. Chow, C., X. Xing, and R. Li, *Moisture absorption studies of sisal fibre reinforced polypropylene composites.* Composites Science and Technology, 2007. **67**(2): p. 306-313.
152. Kohan, M., *Nylon Plastics Handbook*. 1995, New York: Hanser Gardner Publications Inc.
153. Taib, R.M., Ishak, Z.A.M., Rozman, H.D., and Glasser, W.G., *Effect of Moisture Absorption on the Tensile Properties of Steam-exploded Acacia mangium Fiber–Polypropylene osites.* Journal of Thermoplastic Composite Materials, 2006. **19**(5): p. 475-489.
154. Stark, N., *Influence of moisture absorption on mechanical properties of wood flour-polypropylene composites.* Journal of Thermoplastic Composite Materials, 2001. **14**(5): p. 421-432.
155. Mazuki, A.A.M., Akil, H.M., Safiee, S., Ishak, Z.A.M., and Bakar, A.A., *Degradation of dynamic mechanical properties of pultruded kenaf fiber reinforced composites after immersion in various solutions.* Composites Part B: Engineering, 2011. **42**(1): p. 71-76.
156. Hammiche, D., Boukerrou, A., Djidjelli, H., Corre, Y.M., Grohens, Y., and Philin, I., *Hydrothermal ageing of alfa fiber reinforced polyvinylchloride composites.* Construction and Building Materials, 2013. **47**: p. 293-300.
157. Milinkovic, A., P. Miroslav, and A. Gregorova, *Humidity response of poly (butylene adipate-co-butylene terephthalate) copolyesters and their composites with wood flour determined by dynamic mechanical analysis.* Thermochimica acta, 2014. **590**: p. 40-50.

158. Aitken, D., Burkinshaw, S.M., Cox, R., Catherall, J., Litchfield, R.E., Price, D.M., and Todd, N.G., *Determination of the Tg of wet acrylic fibers using DMA.* Journal of Applied polymer Science, 1991. **47**(0): p. 263-269.
159. Roohani, M., Habibi, Y., Belgacem, N.M., Ebrahim, G., Karimi, A.N., and Dufresne, A., *Cellulose whiskers reinforced polyvinyl alcohol copolymers nanocomposites.* European Polymer journal, 2008. **44**(8): p. 2489-2498.
160. Adriana, G., Jussi, L., Robert, S., and Franz, S., *Humidity response of Kraft papers determined by dynamic mechanical analysis.* Thermochimica acta, 2013. **570**: p. 33-40.
161. Sanyang, M.L., Sapuan, S.M., Jawaid, M., Ishak, M.R., and Sahari, J., *Effect of plasticizer type and concentration on tensile, thermal and barrier properties of biodegradable films based on sugar palm (Arenga pinnata) starch.* Polymers, 2015. **7**(6): p. 1106-1124.
162. Peresin, M.S., Habibi, Y., Vesterinen, A.H., Rojas, O.J., Pawlak, J.J., and Seppala, J.V., *Effect of moisture on electrospun nanofiber composites of poly (vinyl alcohol) and cellulose nanocrystals.* BIOMACROMOLECULES, 2010. **11**(9): p. 2471-2477.
163. Mathew, A.P. and A. Dufresne, *Morphological investigation of nanocomposites from sorbitol plasticized starch and tunicin whiskers.* BIOMACROMOLECULES, 2002. **3**(3): p. 609-617.
164. Hinterstoisser, B. and L. Salmén, *Application of dynamic 2D FTIR to cellulose.* Vibrational Spectroscopy, 2000. **22**(1): p. 111-118.
165. Hinterstoisser, B. and L. Salmén, *Two-dimensional step scan FTIR: a tool to unravel the OH valency range of the spectrum of Cellulose I.* Cellulose, 1999. **6**(3): p. 251-263.
166. Olsson, A.-M. and L. Salmén, *The association of water to cellulose and hemicellulose in paper examined by FTIR spectroscopy.* Carbohydrate research, 2004. **339**(4): p. 813-818.
167. Ping, Z., Nguyen, Q.T., Chen, S.M., Zhou, J.Q., and Ding, Y.D., *States of water in different hydrophilic polymers—DSC and FTIR studies.* Polymer, 2001. **42**(20): p. 8461-8467.
168. Hofstetter, K., B. Hinterstoisser, and L. Salmén, *Moisture uptake in native cellulose–the roles of different hydrogen bonds: a dynamic FT-IR study using Deuterium exchange.* Cellulose, 2006. **13**(2): p. 131-145.
169. Fengel, D. and G. Wegener, *Wood: chemistry, ultrastructure, reactions*. 1983: Walter de Gruyter.
170. Nakamura, K., T. Hatakeyama, and H. Hatakeyama, *Effect of bound water on tensile properties of native cellulose.* Textile research journal, 1983. **53**(11): p. 682-688.
171. Tashiro, K. and M. Kobayashi, *Theoretical evaluation of three-dimensional elastic constants of native and regenerated celluloses: role of hydrogen bonds.* Polymer, 1991. **32**(8): p. 1516-1526.
172. Carrillo, F., Colom, X., Sunol, J.J., and Saurina, J., *Structural FTIR analysis and thermal characterisation of lyocell and viscose-type fibres.* European Polymer Journal, 2004. **40**: p. 2229-2234.
173. Marchessault, R. and C. Liang, *Infrared spectra of crystalline polysaccharides. III. Mercerized cellulose.* Journal of Polymer Science, 1960. **43**(141): p. 71-84.
174. Salmén, L. and E. Bergström, *Cellulose structural arrangement in relation to spectral changes in tensile loading FTIR.* Cellulose, 2009. **16**(6): p. 975-982.
175. Eichhorn, S., J. Sirichaisit, and R. Young, *Deformation mechanisms in cellulose fibres, paper and wood.* Journal of Materials Science, 2001. **36**(13): p. 3129-3135.
176. Creely, J., V.W. Tripp, and dquo, *The effect of humidity on the crystallinity of cellulose.* Textile Research Journal, 1971. **41**(4): p. 371-373.
177. Heyn, A., *Crystalline state of cellulose in fresh and dried mature cotton fiber from unopened bolls as studied by x-ray diffraction.* Journal of Polymer Science Part A: General Papers, 1965. **3**(4): p. 1251-1265.
178. Segal, L., Creely, J.J., Martin, A.E., and Conrad, C.M., *An empirical method for estimating the degree of crystallinity of native cellulose using the X-ray diffractometer.* Textile Research Journal, 1959. **29**(10): p. 786-794.

179. Seitsonen, S. and I. Mikkonen, *X-ray study on the effect of moisture on the crystalline state of cellulose.* Journal of Polymer Science Part A-2: Polymer Physics, 1972. **10**(9): p. 1743-1748.
180. Sun, S., Mitchell, J.R., MacNaughtan, W., Foster, T.J., Harabagiu, V., Song, Y., and Zheng, Q., *Comparison of the mechanical properties of cellulose and starch films.* Biomacromolecules, 2009. **11**(1): p. 126-132.
181. Ray, P., *On the Degree of Crystallinity in Some Cellulose Fibers Under Different Moisture Conditions.* Textile Research Journal, 1967. **37**(5): p. 434-436.
182. Ray, P., *On the degree of crystallinity in jute and mesta fibers in different states of purifications and moisture conditions.* Journal of Applied Polymer Science, 1969. **13**(12): p. 2593-2600.
183. Ray, P. and S. Bandyopadhyay, *Some observations on the concept of the degree of crystallinity in cellulose fibers with reference to moisture effects.* Journal of Applied Polymer Science, 1975. **19**(3): p. 729-733.
184. Hatakeyama, T., Y. Ikeda, and H. Hatakeyama, *Effect of bound water on structural change of regenerated cellulose.* Die Makromolekulare Chemie, 1987. **188**(8): p. 1875-1884.
185. Harris, M., *Handbook of textile fibers.* Washington.: Harris Research Labs.. Seen in Esau, K.(1969) Phloem, 1954.
186. Wang, J.Z., Dillard, D.A., Wolcott, M.P., Kamke, F.A., and Wilkes, G.L., *Transient moisture effects in fibers and composite materials.* Journal of Composite Materials, 1990. **24**(9): p. 994-1009.
187. Olsson, A.M. and L. Salmén, *Molecular mechanisms involved in creep phenomena of paper.* Journal of applied polymer science, 2001. **79**(9): p. 1590-1595.
188. Olsson, A.M., Salmen, L., Eder, M., and Bulgert, I., *Mechano-sorptive creep in wood fibres.* Wood Science and Technology, 2007. **41**(1): p. 59-67.
189. Tenney, D. and J. Unnam, *Analytical prediction of moisture absorption in composites.* Journal of Aircraft, 1978. **15**(3): p. 148-154.
190. Dvoskin, N., V. Jordan, and W. Wolter, *Collaborative BAe/GAC Environmental Fatigue Test Programme, Environmental Definition*. 1979, Grunman AC Technical Report AC-79.5.
191. Nunez, A.J., N.E. Marcovich, and M.I. Aranguren, *Analysis of creep behavior of polypropylene-woodflour composites.* Polymer Engineering And Science, 2004. **44**(8): p. 1594-1602.
192. Strganac, T.W. and H.J. Golden, *Predictions of nonlinear viscoelastic behavior using a hybrid approach.* International journal of solids and structures, 1996. **33**(30): p. 4561-4570.
193. Beijer, J. and J. Spoormaker, *Solution strategies for FEM analysis with nonlinear viscoelastic polymers.* Computers & structures, 2002. **80**(14): p. 1213-1229.
194. Marais, C. and G. Villoutreix, *Analysis and modeling of the creep behavior of the thermostable PMR-15 Polyimide.* Journal of Applied Polymer Science, 1998. **69**: p. 1983-1991.
195. Hindeleh, A. and D. Johnson, *Crystallinity and crystallite size measurement in cellulose fibres: 2. Viscose rayon.* Polymer, 1974. **15**(11): p. 697-705.
196. Wunderlich, D. and B. Zimmerer, *Technical rayon: Present and future*. 2011, Cordenka GmbH. p. 1-20.
197. Dormanns, J., *All-cellulose composite laminates: The processing-structure-property relationship from the micro- to the nanoscale*, in *Mechanical Engineering*. 2015, University of Canterbury: Christchurch, New Zealand. p. 1-313.
198. D3039, A., *Standard Test Method for Tensile Properties of Polymer Matrix Composite Materials*. 2008, ASTM International: United States.
199. Roy, R.K., *A primer on the Taguchi method*. 2010, US: Society of Manufacturing Engineers. 245.
200. Anderson, J.L., D.W. Armstrong, and G.-T. Wei, *Ionic liquids in analytical chemistry.* Analytical Chemistry, 2006. **78**(9): p. 2892-2902.

201. Azmi, A.I., R.J.T. Lin, and D. Bhattacharyya, *Machinability study of glass fibre-reinforced polymer composites during end milling.* International Journal Advanced Manufacturing Technology, 2012. **64**: p. 247-261.
202. Park, S.H., *Robust Design and Analysis for Quality Engineering*. 1996, London, UK: Chapman & Hall.
203. Ross, P.J., *Taguchi Techniques for Quality Engineering*. Vol. 2nd Edition. 1996, US: McGraw-Hill. 327.
204. Shayfull, Z., Fathullah, M., Nasir, M.S., Shuaib, N.A., and Abdul Manan, M.S., *Warpage analyses on thin plate in three-plate mold by Taguchi Method and Analysis of Variance (ANOVA) for PC, ABS and PC/ABS.* International Review of Mechanical Engineering 2012. **6**: p. 1-10.
205. Roy, R.K., *Design of experiments using the Taguchi approah: 16 steps to product and process improvement*. 2001, New York: John Wiley and Sons.
206. Wakelin, J.H., H.S. Virgin, and E. Crystal, *Development and Comparison of Two X-Ray Methods for Determining the Crystallinity of Cotton Cellulose.* Journal of Applied physics, 1959. **30**(11): p. 1654-1662.
207. Duchemin, B., Thuault, A., Vicente, A., Rigaud, B., Fernandez, C., and Eve, S., *Ultrastructure of cellulose crystallites in flax textile fibres.* Cellulose, 2012. **19**(6): p. 1837-1854.
208. Nieduszynski, I. and R. Preston, *Crystallite size in natural cellulose.* Nature, 1970. **225**: p. 273-274.
209. Eichhorn, S., R. Young, and W.-Y. Yeh, *Deformation processes in regenerated cellulose fibers.* Textile Research Journal, 2001. **71**(2): p. 121-129.
210. Öztürk, H.B., Potthast, A., Rosenau, T., Abu-Rous, M., MacNaughtan, B., Schuster, K.C., Mitchell, J.R., and Bechtold, T., *Changes in the intra-and inter-fibrillar structure of lyocell (TENCEL®) fibers caused by NaOH treatment.* Cellulose, 2009. **16**(1): p. 37-52.
211. Hodgskinson, R. and J. Currey, *Young's modulus, density and material properties in cancellous bone over a large density range.* Journal of Materials Science: Materials in Medicine, 1992. **3**(5): p. 377-381.
212. Colom, X. and F. Carrillo, *Crystallinity changes in lyocell and viscose-type fibres by caustic treatment.* European Polymer journal, 2002. **38**(11): p. 2225-2230.
213. Ibbett, R.N., D. Domvoglou, and M. Fasching, *Characterisation of the supramolecular structure of chemically and physically modified regenerated cellulosic fibres by means of high-resolution Carbon-13 solid-state NMR.* Polymer, 2007. **48**(5): p. 1287-1296.
214. Yamane, C., Mori, M., Saito, M., and Okajima, K., *Structures and mechanical properties of cellulose filament spun from cellulose/aqueous NaOH solution system.* Polymer journal, 1996. **28**(12): p. 1039-1047.
215. Salmen, N. and G. Back, *The influence of water on the glass transition temperature of cellulose.* Tappi, 1977. **60**(12): p. 137-140.
216. Mat Salleh, M., Magniez, K., Pang, S., Dormanns, J., and Staiger, M.P., *Parametric optimisation of the processing of all-cellulose composite laminae.* Advanced Manufacturing: Polymer & Composites Science, 2017. **18**: p. 1-7.
217. Madsen, B. and H. Lilholt, *Physical and mechanical properties of unidirectional plant fibre composites—an evaluation of the influence of porosity.* Composites Science and Technology, 2003. **63**(9): p. 1265-1272.
218. Ignjatović, N., Tomic, S., Dakic, M., Miljkovic, M., Plavsic, M., and Uskokovic, D., *Synthesis and properties of hydroxyapatite/poly-L-lactide composite biomaterials.* Biomaterials, 1999. **20**(9): p. 809-816.
219. Karmarkar, A., Chauhan, S., Modak, J., and Chanda, M., *Mechanical properties of wood–fiber reinforced polypropylene composites: Effect of a novel compatibilizer with isocyanate functional group.* Composites Part A: Applied Science and Manufacturing, 2007. **38**(2): p. 227-233.

220. Lin, Q., X. Zhou, and G. Dai, *Effect of hydrothermal environment on moisture absorption and mechanical properties of wood flour-filled polypropylene composites.* Journal of Applied polymer Science, 2002. **85**: p. 2824.
221. Chiou, J. and D. Paul, *Sorption equilibria and kinetics of ethanol in miscible poly (vinylidene fluoride)/poly (methyl methacrylate) blends.* Polymer Engineering & Science, 1986. **26**(17): p. 1218-1227.
222. Comyn, J., *Polymer permeability*. 2012: Springer Science & Business Media.
223. Shen, C. and G.S. Springer, *Moisture absorption and desorption of composite materials.* Journal of Composite Materials, 1975. **10**: p. 2-20.
224. Shi, S.Q. and D.J. Gardner, *Effect of density and polymer content on the hygroscopic thickness swelling rate of compression molded wood fiber/polymer composites.* Wood and Fiber Science, 2005. **38**(3): p. 520-526.
225. Wang, Q., Zhang, B., Qu, M., Zhang, J., and He, D., *Fabrication of superhydrophobic surfaces on engineering material surfaces with stearic acid.* Applied Surface Science, 2008. **254**: p. 2009-2012.
226. Wong, E., Koh, S., Lee, K., and Rajoo, R., *Advanced moisture diffusion modeling and characterisation for electronic packaging*. in *Electronic Components and Technology Conference, 2002. Proceedings. 52nd*. 2002. IEEE.
227. Stoffels, M.T., Miller, D.A., Samborsky, D.D., and Mandell, J.F., *Effects of Tensile Stresses On The Moisture Diffusion Characteristics Of Epoxy Glass Composites.* 2014.
228. International, A., *Standard Test Method for Water Absoprtion of Plastics*. 2010, American National Standard Institute: United States. p. 1-3.
229. Fiorentini, C., Demarchi, S., Ruiz, N., Irigoyen, R., and Giner, S., *Arrhenius activation energy for water diffusion during drying of tomato leathers: The concept of characteristic product temperature.* Biosystems Engineering, 2015. **132**: p. 39-46.
230. Alvarez, V.A. and A. Vázquez, *Influence of fiber chemical modification procedure on the mechanical properties and water absorption of MaterBi-Y/sisal fiber composites.* Composites Part A: Applied Science and Manufacturing, 2006. **37**(10): p. 1672-1680.
231. Kabir, M., Wang, H., Lau, K., and Cardona, F., *Chemical treatments on plant-based natural fibre reinforced polymer composites: An overview.* Composites Part B: Engineering, 2012. **43**(7): p. 2883-2892.
232. Jacob, M., K.T. Varughese, and S. Thomas, *Water sorption studies of hybrid biofiber-reinforced natural rubber biocomposites.* Biomacromolecules, 2005. **6**: p. 2969-2979.
233. Flickinger, M.C., *Downstream Industrial Biotechnology: Recovery and Purification*. 2013: John Wiley & Sons.
234. Shakeri, A. and M. Raghimi, *Studies on mechanical Performance and water absorption of recycled Newspaper/Glass fiber-reinforced polypropylene hybrid composites.* Journal of Reinforced Plastics and Composites, 2010. **29**(7): p. 994-1005.
235. Le Duigou, A., P. Davies, and C. Baley, *Seawater ageing of flax/poly (lactic acid) biocomposites.* Polymer degradation and stability, 2009. **94**(7): p. 1151-1162.
236. Gil-Castell, O., Badia, J., Kittikorn, T., Stromberg, E., Martinez-Felipe, A., Ek, M., Karlsson, S., and Ribes-Greus, A., *Hydrothermal ageing of polylactide/sisal biocomposites. Studies of water absorption behaviour and Physico-Chemical performance.* Polymer degradation and stability, 2014. **108**: p. 212-222.
237. Mazeau, K., *The hygroscopic power of amorphous cellulose: a modeling study.* Carbohydrate polymers, 2015. **117**: p. 585-591.
238. Rusli, R. and S.J. Eichhorn, *Determination of the stiffness of cellulose nanowhiskers and the fiber-matrix interface in a nanocomposite using Raman spectroscopy.* Applied Physics Letters, 2008. **93**(3): p. 033111.
239. Nissan, A.H., *H-bond dissociation in hydrogen bond dominated solids.* Macromolecules, 1976. **9**(5): p. 840-850.

240. Benoît, J.-C.D., R.H. Newman, and M.P. Staiger, *Phase transformations in microcrystalline cellulose due to partial dissolution.* Cellulose, 2007. **14**(4): p. 311-320.
241. Cook, J.G., *Handbook of textile fibres: man-made fibres*. 1984: Elsevier.
242. Cristea, M., D. Ionita, and B.C. Simionescu, *Dynamic Mechanical Analysis on Regenerated Cellulose.* REVISTA DE CHIMIE, 2008. **59**(10): p. 1088-1091.
243. Baley, C., *Analysis of the flax fibres tensile behaviour and analysis of the tensile stiffness increase.* Composites Part A: Applied Science and Manufacturing, 2002. **33**(7): p. 939-948.
244. Maréchal, Y. and H. Chanzy, *The hydrogen bond network in I β cellulose as observed by infrared spectrometry.* Journal of molecular structure, 2000. **523**(1): p. 183-196.
245. Klemm, D., Philip, B., Heinze, T., Heinze, U., and Wagenknecht, W., *Comprehensive Cellulose Chemistry*. Vol. Volume 1: Fundamental and analytical methods. 1998, Weinheim, Germany: Wiley-VCH.
246. Sain, M., J. Balatinecz, and S. Law, *Creep fatigue in engineered wood fiber and plastic compositions.* Journal of Applied Polymer Science, 2000. **77**(2): p. 260-268.
247. McCrum, N.G., C. Buckley, and C.B. Bucknall, *Principles of polymer engineering*. 1997: Oxford University Press, USA.
248. Park, B.D. and J.J. Balatinecz, *Short term flexural creep behavior of wood-fiber/polypropylene composites.* Polymer composites, 1998. **19**(4): p. 377-382.
249. Lu, J.P., L.S. Burn, and B.E. Tiganis, *Creep modeling of ABS pipes at variable temperature.* Polymer Engineering Science, 2000. **40**: p. 2407.
250. Jia, Y., Peng, K., Gong, X., and Zhang, Z., *Creep and recovery of polypropylene/carbon nanotube composites.* International Journal of Plasticity, 2011.
251. Findley, W.N. and F.A. Davis, *Creep and relaxation of nonlinear viscoelastic materials*. 2013: Courier Dover Publications.
252. Cyras, V., Martucci, J., Iannace, S., and Vacquez, A., *Influence of the fiber content and the processing conditions on the flexural creep behavior of sisal-PCL-starch composites.* Journal of Thermoplastic Composite Materials, 2002. **15**(3): p. 253-265.
253. Read, B. and P. Tomlins, *Creep and physical aging of injection molded, fiber reinforced polypropylene.* Polymer Engineering & Science, 1997. **37**(9): p. 1572-1581.
254. Matsumoto, D., *Time-temperature superposition and physical aging in amorphous polymers.* Polymer Engineering & Science, 1988. **28**(20): p. 1313-1317.
255. Daniels, C.A., *Polymers: structure and properties*. 1989: CRC Press.
256. Dean, D., M. Husband, and M. Trimmer, *Time–temperature-dependent behavior of a substituted poly (paraphenylene): Tensile, creep, and dynamic mechanical properties in the glassy state.* Journal of Polymer Science Part B: Polymer Physics, 1998. **36**(16): p. 2971-2979.
257. Powell, P.C. and A.I. Housz, *Engineering with polymers*. 1998: CRC Press.